School of Civil and Mechanical Engineering

Structural Response of Modular Buildings to Multiple Hazards

Andrew William Lacey

0000-0003-1171-5282

This thesis is presented for the Degree of
Doctor of Philosophy
of
Curtin University

August 2020

Declaration

To the best of my knowledge and belief this thesis contains no material previously published by any other person except where due acknowledgment has been made.

This thesis contains no material which has been accepted for the award of any other degree or diploma in any university.

Signature: ……

Date: 15 August 2020

Abstract

Modular building is a new type of construction in which buildings are assembled from prefabricated volumetric modules. Prefabrication leads to a shorter construction schedule, improved quality, and reduced resource wastage, and, therefore, has great potential to enhance building construction practice. While low-rise transportable buildings are used extensively in the existing industry, the application is being extended to taller medium- and high-rise structures, for which there is a lack of knowledge of the structural behaviour. Due to the lacking knowledge, there is a risk of economic loss due to overconservative structural design, or avoidance of the new construction technique. The aim of this thesis is, therefore, to study the structural performance of modular buildings subjected to the multiple hazards of wind and earthquake ground motion.

This thesis begins with a state-of-the-art review, which introduces the structural forms of modular buildings. The structural response to different hazards is then considered, followed by the design practice. It is observed that the structural performance of modular buildings may be different to that of similar traditional structures, and that the performance is dependent on the inter-module connections (IMCs) which join the modules together onsite. The IMCs are shown to have important structural behaviours, i.e., shear, axial, and moment-rotation, which are simplified and input into a global numerical model of the structure for design purposes. Therefore, the numerical and experimental behaviours of three existing IMCs are compared with the behaviours predicted by the existing models developed to simplify the traditional connection modelling. When applied to the IMCs, the existing models are shown to be unable to accurately predict the IMC behaviours, hence, further study of the structural behaviour of IMCs is conducted to enable the development of improved models.

To study the importance of the IMC behaviours to the overall building response, a six-storey apartment building with 72 modules is selected for a case study. A numerical model is developed using the software SAP2000, in which basic bi-linear and tri-linear models are adopted for the translational and rotational behaviours of the IMCs, respectively. Then, by varying the initial stiffness of the input IMC model, it is established that the IMCs significantly influence the overall response to simulated time-varying wind loads and earthquake ground accelerations. Moreover, it is found that the shear behaviour of the IMC has the greatest effect on the global building response.

Before moving on to the shear behaviour of IMCs, an experimental program is performed to establish the shear behaviour of slip factor test specimens, which are a traditional type of bolted connection. Australian grade 350 steel is adopted and the surface finish is varied to establish

the effect on the shear behaviour. To verify the accuracy of the experiments and to investigate the effect of the relevant parameters including the slip factor and bolt preload, numerical simulations are carried out using the software ABAQUS. An empirical formula is proposed for the initial shear behaviour based on the numerical results, which are calibrated with reference to the experimental data. In addition, the accuracy of the torque controlled bolt preload and the digital image correlation (DIC) displacement measurements are demonstrated prior to application in the subsequent experiments on IMCs.

Next, as the design and construction of reliable IMCs is identified as a major challenge, two new IMCs are proposed: the post-tensioned (PT) connection, and the interlocking (IL) connection. The PT connection reduces the requirement for working at heights during construction and improves the initial shear behaviour. In comparison, the IL connection offers easy site installation and improves the safety during construction. For each new connection, experiments are conducted to investigate the shear behaviour considering the effect of the surface finish, contact area, interlocking element, bolt preload, and hole tolerance. Experimental setups are developed which allow the shear behaviours to be determined by loading the specimens in compression using a universal testing machine. To support the experiments, numerical simulations are carried out using ABAQUS, and empirical models are proposed for the initial shear behaviour based on the calibrated numerical results.

Although the shear behaviour is relatively more important, the axial and moment-rotation behaviours are still required to define the performance of the connections. Therefore, extended numerical models are prepared for the PT and IL connections using ABAQUS. Whereas the previous numerical models of the IMCs were based on the experimental specimens, the extended models reflect the geometry and loading conditions of the IMCs which are incorporated in a modular building structure. The extended numerical models are calibrated based on the experimental shear behaviours, after which the empirical models for the shear behaviour are refined and extended to the bearing/yield stage. Axial forces and bending moments are then applied to the numerical models, and simplified analytical and semi-empirical models are derived for the axial and moment-rotation behaviours.

Finally, the simplified models developed for the PT and IL connections are implemented in the global model of the case study building. The simplified IMC models are demonstrated to be suitable for application in global numerical simulations, while different connection geometries are accommodated by the analytical derivation of the key parameters. The effect of more accurate IMC models on the overall building responses to the wind and earthquake loads is examined and compared to the previous analysis of a case study building. Based on the numerical results, inter-storey drift ratio limits are suggested according to the simplified

IMC models. Moreover, the possibility of horizontal gaps between modules is identified which may lead to the detrimental impact between modules or, conversely, beneficial out of phase vibration of the modules which dissipates energy. In this way, the more accurate analytical IMC models contribute to an improved understanding of the global responses of modular buildings and, hence, facilitate the analysis and design of modular structures for the multiple hazards of wind and earthquake ground motion.

Acknowledgements

First and foremost, I would like to express my deepest appreciation to my supervisors, Prof. Hong Hao and Dr Wensu Chen, for their encouragement, patience and guidance throughout my PhD journey. I would also like to extend my sincere thanks to Dr Kaiming Bi for his valuable advice and contribution to this thesis as co-author of the related publications.

I would like to thank and acknowledge the members of the Centre for Infrastructural Monitoring and Protection (CIMP) at Curtin University, including Mr Huawei Li who guided me through the development of my first ABAQUS numerical simulations, and Dr Musaad Zaheer Nazir Khan who introduced me to digital image correlation (DIC) displacement measurements. I am also grateful to final year project student Mr Forrest Tallowin for his assistance with the experiments.

I also wish to thank and acknowledge the assistance of the civil engineering laboratory technicians at Curtin University's Bentley campus, including Mr Rob Walker who fabricated the components for the experimental specimens, and Dr Arne Bredin who assisted with the load cell and digital image correlation setups.

I gratefully acknowledge the financial support received through the Australian Government Research Training Program Scholarship.

Lastly, I would like to express my gratitude to my colleagues, family and friends, for their guidance, encouragement and support.

List of published work and work prepared for publication

This thesis is assembled from a series of published journal articles and articles which are presently under review. These articles form the individual chapters as indicated below.

Chapter 2

Lacey AW, Chen W, Hao H, Bi K. Structural response of modular buildings - an overview. J Build Eng. 2018;16:45-56. https://doi.org/10.1016/j.jobe.2017.12.008

Lacey AW, Chen W, Hao H, Bi K. Review of bolted inter-module connections in modular steel buildings. J Build Eng. 2019;23:207-19. https://doi.org/10.1016/j.jobe.2019.01.035

Chapter 3

Lacey AW, Chen W, Hao H, Bi K. Effect of inter-module connection stiffness on structural response of a modular steel building subjected to wind and earthquake load. Eng Struct. 2020;213:110628. https://doi.org/10.1016/j.engstruct.2020.110628

Chapter 4

Lacey AW, Chen W, Hao H, Bi K. Experimental and numerical study of the slip factor for G350-steel bolted connections. J Constr Steel Res. 2019;158:576-90. https://doi.org/10.1016/j.jcsr.2019.04.012

Chapter 5

Lacey AW, Chen W, Hao H, Bi K, Tallowin FJ. Shear behaviour of post-tensioned inter-module connection for modular steel buildings. J Constr Steel Res. 2019;162:105707. https://doi.org/10.1016/j.jcsr.2019.105707

Chapter 6

Lacey AW, Chen W, Hao H, Bi K. New interlocking inter-module connection for modular steel buildings: Experimental and numerical studies. Eng Struct. 2019;198:109465. https://doi.org/10.1016/j.engstruct.2019.109465

Chapter 7

Lacey AW, Chen W, Hao H, Bi K. Simplified structural behaviours of post-tensioned inter-module connection for modular buildings. J Constr Steel Res. 2020;175:106347. https://doi.org/10.1016/j.jcsr.2020.106347

Chapter 8

Lacey AW, Chen W, Hao H, Bi K. New interlocking inter-module connection for modular steel buildings: Simplified structural behaviours. Eng Struct. 2021;227:111409. https://doi.org/10.1016/j.engstruct.2020.111409

Chapter 9

Lacey AW, Chen W, Hao H, Bi K. Lateral behaviour of modular steel building with simplified models of new inter-module connections. (Under review)

List of relevant additional works

The additional works relevant to this thesis but not forming part of it are listed below.

Lacey AW, Chen W, Hao H, Bi K. Numerical Study of the Structural Response to Wind Loading: Modular Building Case Study. 13th International Conference on Steel, Space and Composite Structures; 31 January – 02 February; Perth, Australia; 2018.

Lacey AW, Chen W, Hao H, Bi K. Structural Response of Modular Building Subjected to Earthquake Loading. 13th International Conference on Steel, Space and Composite Structures; 31 January – 02 February; Perth, Australia; 2018.

Lacey AW, Chen W, Hao H, Bi K. Shear Stiffness of Bolted Inter-module Connections for Modular Steel Buildings. 11th International Conference of the IFHS on Extreme Engineering; 26-28 February; Singapore; 2019.

Statement of contribution of others

The work presented in this thesis was primarily carried out by the candidate (Andrew William Lacey). The contributions of others are described as follows, while the signed statement of contribution of co-authors is attached as Appendix A.

Chapter 2

The candidate carried out the literature review and wrote the related original manuscripts which were reviewed and edited by Prof. Hong Hao, Dr Wensu Chen, and Dr Kaiming Bi.

Chapter 3

The research was formulated by the candidate who was guided by the intellectual input contributed by Prof. Hong Hao, Dr Wensu Chen, and Dr Kaiming Bi. Dr Kaiming Bi simulated the earthquake ground motion time histories and verified the related time history analysis results. The candidate carried out the numerical simulations and prepared the manuscript, which was reviewed and edited by Prof. Hong Hao, Dr Wensu Chen, and Dr Kaiming Bi, who contributed generally to the data processing, analysis and discussion of the results.

Chapter 4

The research was conceptualised by the candidate with intellectual input contributed by Prof. Hong Hao, Dr Wensu Chen, and Dr Kaiming Bi. Mr Rob Walker fabricated the components for the experimental specimens in the Civil and Mechanical Engineering Laboratory at Curtin University's Bentley campus. The candidate prepared the faying surfaces, assembled the specimens and completed the slip factor tests. Mr Forrest Tallowin assisted with the preparation and assembly of the specimens, while Dr Musaad Zaheer Nazir Khan and Dr Arne Bredin assisted with the initial setup for the digital image correlation displacement measurements. Formal analysis of the experimental data was completed by the candidate, including the digital image correlation and derivation of the force-slip curves. The numerical simulations were carried out by the candidate, while Mr Huawei Li assisted with the first numerical simulations. The candidate then proposed the load-slip model and prepared the manuscript, which was reviewed and edited by Prof. Hong Hao, Dr Wensu Chen, and Dr Kaiming Bi.

Chapter 5

Mr Forrest Tallowin proposed the post-tensioned inter-module connection and planned the quasi-static experiments with intellectual input from the candidate and Dr Wensu Chen. Mr

Rob Walker fabricated the components for the experimental specimens, which were subsequently assembled and tested by Mr Forrest Tallowin and the candidate. Formal analysis of the experimental data was completed by the candidate, including the digital image correlation, derivation of the force-slip curves, and statistical analysis of the experimental accuracy. The assembly tests were planned and completed by the candidate, with technical input on the load cell setup provided by Dr Arne Bredin. The candidate then carried out the numerical simulations, proposed the load-slip model and prepared the original manuscript, which was reviewed and edited by Prof. Hong Hao, Dr Wensu Chen, and Dr Kaiming Bi.

Chapter 6

The candidate formulated the research, developed the methodology and proposed the interlocking inter-module connection with intellectual input contributed by Prof. Hong Hao, Dr Wensu Chen, and Dr Kaiming Bi. Mr Rob Walker fabricated the components for the experimental specimens, which were assembled and tested by the candidate. The candidate then completed the formal analysis and numerical simulations, proposed the force-slip model, and prepared the manuscript, which was reviewed and edited by Prof. Hong Hao, Dr Wensu Chen, and Dr Kaiming Bi.

Chapter 7 to Chapter 8

The research method was formulated by the candidate with intellectual input contributed by Prof. Hong Hao, Dr Wensu Chen, and Dr Kaiming Bi. The numerical method was established by the candidate, while the verification of the axial and moment-rotation behaviours was developed in consultation with Dr Wensu Chen and Dr Kaiming Bi, for example. The candidate carried out the numerical simulations, formal analysis, and visualisation, and developed the simplified models including curve fitting and derivation of the analytical formulae. Finally, the candidate prepared the manuscripts, which were reviewed and edited by Prof. Hong Hao, Dr Wensu Chen, and Dr Kaiming Bi.

Chapter 9

The research method was developed by the candidate in consultation with Prof. Hong Hao, Dr Wensu Chen, and Dr Kaiming Bi. Dr Kaiming Bi simulated the earthquake ground motion time histories and verified the related time history analysis results. The candidate carried out the numerical simulations and prepared the manuscript, which was reviewed and edited by Prof. Hong Hao, Dr Wensu Chen, and Dr Kaiming Bi.

Table of Contents

Chapter 1 Introduction

1.1 Background

Modular building is a type of construction in which buildings are assembled from volumetric modules which are prefabricated offsite. Due to the favourable factory building conditions, prefabricated volumetric modular construction can reduce the construction time by 60% and the landfill waste by 70% [1], and has great potential to enhance building construction practice. Consequently, there is an established and growing interest in modular construction, particularly for taller multistorey buildings. In Australia, for example, although presently only 3% of new housing uses prefabrication [2], it is predicted that use of modular construction will increase from 3% to 10% by 2030 [1].

To enable this growth, however, there are several challenges to overcome. The independent publicly available research on the structural performance of medium- and high-rise modular buildings is limited and, consequently, in Australia, there are no specific design standards for modular buildings [3]. Moreover, the structural performance of the existing inter-module connections (IMCs), which join modules onsite and are a key difference between modular and traditional buildings, is relatively unknown. As a result, structural design of modular buildings is problematic, and there is a risk of economic loss due to overconservative structural design to compensate for the lack of knowledge, or avoidance of the new construction technique altogether. Further research is required to improve understanding of modular buildings and IMCs, and, thereby, facilitate design of these structures.

1.2 Objectives

The first objective of this thesis is to study the structural performance of column supported modular steel buildings, a type of modular building, subjected to the multiple hazards of wind loading and earthquake ground motion. For this purpose, a thorough understanding of the state-of-the-art with respect to modular building structures is to be developed. A literature review is, therefore, to be conducted on the broad subject of modular buildings. In addition, a case study is to be undertaken to characterise the performance of a relevant modular steel building, for which a six-storey building in Port Hedland is identified. A numerical model of the case study building is to be developed to assess the global building response to wind and earthquake loading and, hence, develop an understanding of the relationship between the local inter-module connection (IMC) response and the global building response.

As the IMCs are critical to the capability of modular buildings to withstand the applied loads, the existing IMCs are to be reviewed and, hence, new improved IMCs may be developed. Experimental and numerical studies are to be undertaken to establish the structural behaviours of the new IMCs. Then, simplified models should be proposed, with which the structural behaviours of the IMCs can be simplified for use in global numerical simulations. In this way, the second objective of this thesis is to contribute analytical and semi-empirical models for the structural behaviours of the IMCs, which are suitable for design purposes and may, in future works, be extended to different IMCs. Finally, the simplified IMC models are to be applied to the case study building, through which the design process can be demonstrated while the global building responses are more accurately examined.

1.3 Research outline

Following the introductory first chapter, the main body of this thesis is comprised of eight chapters, i.e., Chapter 2 to 9.

Chapter 2 presents the literature review, which is divided into two main sections. Section 2.1 presents a broad overview of the existing literature on modular building structures. This serves, firstly, to introduce the subject of modular buildings and, secondly, demonstrates the same broad appraisal undertaken by the author to establish the direction of the research presented within this thesis. Modular buildings are identified as having unique structural characteristics which may be significantly influenced by the inter-module connections (IMCs) used to connect building modules onsite. Furthermore, the design and fabrication of reliable IMCs is identified as a major challenge requiring further study. Therefore, in the second part of the literature review, i.e., Section 2.2, the focus shifts more specifically to the bolted IMCs applicable to modular steel buildings. The existing models for the structural behaviours of bolted steel connections are applied to three existing IMCs. It is demonstrated that the existing models are unable to accurately predict the structural behaviours of the existing IMCs. Hence, it is identified that, to enable development of more suitable analytical models, further study of the structural behaviours of IMCs is required, which defines the research direction in the following chapters.

Chapter 3 investigates how the local IMC behaviours can affect the global responses of modular steel buildings. A particular modular building is selected for a case study, and the building is subjected to wind and earthquake actions, while the structural behaviours of the IMCs are varied. The results further define the research direction as, among the shear, axial, and moment-rotation behaviours, the shear behaviour of the IMC is shown to have the greatest

effect on the global building responses. Hence, while Chapter 2 draws attention to the need for more accurate models of the IMC behaviours, Chapter 3 directs this attention more specifically to the shear behaviour. Chapter 4 to 6, therefore, focus on the shear behaviour.

To develop more accurate models of the shear behaviour as recommended in Chapter 2 and 3, it is essential to understand the friction/slip shear behaviour associated with the particular steel material of interest. Therefore, **Chapter 4** presents an experimental and numerical study of the friction/slip shear behaviour of slip factor test specimens constructed from grade 350 (AS/NZS 3678-350) steel. This work is undertaken for two reasons. First, it establishes the friction/slip shear behaviour of the steel material used in the following studies on the IMCs (Chapter 5 to 8) including the effect of the surface finish and bolt preload. Second, it demonstrates the accuracy of the torque-controlled bolt preload and the digital image correlation based displacement measurements which are applied in the experiments presented in Chapter 5 and 6.

Chapter 5 and **6** propose two new improved IMCs known as the post-tensioned (PT) and interlocking (IL) connection, respectively. For each new connection, experimental setups are developed to establish the friction/slip shear behaviour considering the effect of the surface finish, contact area, interlocking element, bolt preload, and hole tolerance. Numerical simulations are carried out to extend the work, and empirical models are proposed for the friction/slip shear behaviours associated with the experimental specimens.

Chapter 7 and **8** present extended numerical and analytical studies for the new PT and IL connection, respectively. The extended numerical models reflect the geometry and boundary conditions of the new IMCs within a modular structure. In this way, the extended numerical models are different to those in Chapter 5 and 6, which were based on the experimental setups. Shear forces, axial forces and bending moments are applied to the extended numerical models and the corresponding behaviours are described. Then, simplified empirical models are proposed for the shear behaviours based on the calibrated numerical results, including the initial friction/slip stage, and the subsequent bearing/yield stage. Next, simplified analytical and semi-empirical models are developed for the axial and moment-rotation behaviours, which are verified by comparison with the numerical results. Finally, the shear, axial and moment-rotation behaviours are assembled into spring models, accounting for the potential contact between the connection elements and the effect of combined actions.

Chapter 9 completes the main body of this thesis by applying the new simplified IMC models of the PT and IL connections, developed through Chapter 4 to 8, in the global numerical model of the case study building introduced in Chapter 3. The building is subjected to simulated time varying wind loads and earthquake ground motions, and the corresponding building and connection responses are described. In this way, the capabilities of the new post-tensioned and interlocking IMCs are examined, while the more accurate IMC models facilitate discussion on the corresponding global responses, and module to module interactions.

Chapter 10 summarises the main contributions of this thesis, and provides recommendations for future work.

Chapter 2 Literature review

2.1 Structural response of modular buildings – An overview[1]

2.1.1 Introduction

The literature review begins with a state-of-the-art review of modular building structures. First, recently developed structural forms and construction materials are presented as a brief introduction to modular structures. The focus is on steel framed modules with concrete and timber frame modules excluded, not for lack of importance, but for lack of recent research into the structures. Structural connections are key to the overall performance and so a detailed review of connection types is presented. Then, the structural response of modules to different hazards is considered, followed by the potential applications and future research work.

2.1.2 Module classification and developments in structural form

Modular building is a construction technique whereby building modules are prefabricated off-site. It is a type of off-site fabrication referring specifically to volumetric units which may be a structural element of a building [4-7]. Modular building, therefore, refers to the application of a variety of structural systems and building materials, rather than a single type of structure. Prefabrication by off-site manufacturing leads to a reduced overall construction schedule, improved quality, and reduced resource wastage [8-10]. The disadvantages include the lack of design guidance and relatively small structural spans due to module transport limits. The advantages of modular building outweigh the disadvantages particularly for hotel and residential applications.

Modules are classified as steel, precast concrete and timber frame modules according to the primary construction material. Steel modules are further classified as Modular Steel Building (MSB) modules [11], light steel framed modules and container modules. Their applications, advantages and disadvantages are given in Table 2.1. Load bearing steel modules are also categorised as column supported or continuously supported [12] as shown in Figure 2.1. Column supported modules have edge beams which span between corner or intermediate columns. Continuously supported modules have load bearing walls which provide continuous support [12, 13]. Three examples of steel modules are shown in Figure 2.2. The examples of precast concrete and timber framed modules are also shown in Figure 2.3.

[1] The related work in §2.1 was published in the Journal of Building Engineering:

Lacey AW, Chen W, Hao H, Bi K. Structural response of modular buildings - an overview. J Build Eng. 2018;16:45-56. https://doi.org/10.1016/j.jobe.2017.12.008

Table 2.1. Module classification

Category	Applications	Advantages	Disadvantages	Ref.
Steel – MSB module	Hotel, residential apartments	Suited to high rise buildings, high strength	Corrosion, lack of design guidance	[14-20]
Steel – Light steel framed module	Max. 10-storey, 25-storey with additional core	Lightweight	Suited to low rise buildings	[7, 8, 12, 13, 21-26]
Steel – Container module	Post-disaster housing, military operations, and residential developments	Recycle shipping containers, easy transport	Additional reinforcing required to strengthen container when openings are cut in wall	[27-30]
Precast concrete module	Hotel, prison, secure accommodation	Fire resistance, acoustic insulation, thermal performance, high mass helps meet vibration criteria, high capacity	Heavy, potential cracking at corners	[7]
Timber frame module	1- to 2-storey, education buildings, housing	Sustainable material, easy to fabricate	Poor fire resistance, durability	[7, 31]

Recent study of modular building was focused on light steel framing applied to modular buildings [12, 13, 21, 23, 24], followed by consideration of overall building design using modules [22], and then high-rise building applications [8, 25]. A broad overview of modular construction using light steel framing was given with the application of relevant British and European standards. Several types of modular construction have been presented. Many modular buildings are not exclusively modular but are hybrid structures. Modular construction is combined with a primary steel or concrete structure, for example, using a podium or skeletal structure, or a concrete core around which modules are arranged [8, 23, 25]. Column supported MSBs are well suited to medium and high-rise building applications and are popularly used in current practice. They have been developed through the research of Annan [11], Fathieh [32] and Gunawardena [33]. Annan [11] presented a summary of traditional steel building systems and appropriate analysis procedures, documented detailing requirements, reviewed floor connections and explored seismic behaviour [14-17]. Fathieh [32] contributed to the review of MSBs subject to earthquake loading [18]. Gunawardena et al. [19] subsequently extended the application of MSBs. Noting that many modular buildings are not exclusively modular, a new system was presented with strategically placed stiff modules replacing the conventional core structure [19]. Gunawardena et al. [20] refined the module design and demonstrated that

modular buildings can be self-stable for a ten-storey building subject to earthquake ground motion. The dynamic behaviour of high-rise MSBs remains to be investigated [18].

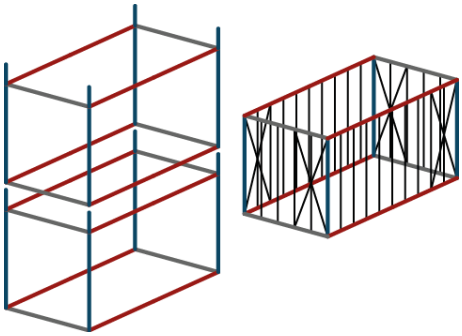

Figure 2.1. (L) Column supported modules and (R) Continuously supported modules (after Gorgolewski et al. [12])

(a) **(b)** **(c)**

Figure 2.2. (a) Modular steel building [34], (b) Light steel framed module [23], and (c) Shipping container [27]

(a) **(b)**

Figure 2.3. (a) Precast concrete modules [33] and (b) Timber frame modules [7]

2.1.3 Component materials

Prefabricated components should be as light as possible as they are transported sometimes long distances. Traditional materials of steel, concrete and timber are commonly used. The potential applications of composite sandwich structures have not been well explored [35]. Manalo et al. [36] gives an overview of fibre reinforced polymer (FRP) sandwich systems in the context of lightweight civil infrastructure. Many of the developing materials presented by Manalo et al. [36] may find application in modular buildings. To date such composite systems have been developed for application as roof, wall or floor components. Some examples of composite materials are given in Table 2.2. Use of FRP composite materials for complete modular building façades is appealing although their performance, especially with respect to

wind-borne debris impact and fire, is a developing area. In addition, the design and manufacture of reliable jointing systems is noted as a challenge which has received growing research attention [36].

Table 2.2. Composite materials with application in modular buildings

Use	Composite material	Advantages	Ref.
Wall	Rigid polyurethane foam stud frame with magnesium oxide cladding	Environment, lightweight, low cost	[35]
Floor	Glass fibre reinforced polymer (FRP) web-flange sandwich, adhesively bonded	Lightweight, strength, high serviceability stiffness, corrosion resistance, low thermal conductivity	[37, 38]
Floor	FRP-steel composite beam system	Lightweight, high strength, corrosion resistance, low thermal conductivity	[39, 40]
Floor	Glass fibre reinforced cement, polyurethane, steel laminate	Lightweight, acceptable strength, 5% damping	[41, 42]
Floor	Steel-timber composite	Lightweight, sustainable	[43-45]
Floor Roof	Cold-formed steel – timber sheet composite beam, or truss	Lightweight, efficient material use, simple fabrication, low cost, renewable and reusable materials	[46, 47]

2.1.4 Connection systems

Interconnection of frame members and modules is critical to the capability of modular buildings to withstand applied loads [48]. Despite the need for a thorough understanding, studies on the connections are limited [48]. Connections are grouped into three types: inter-module, intra-module, and module to foundation as shown in Figure 2.4. Table 2.3 provides a summary of connections for steel modules with further details given in the following sections.

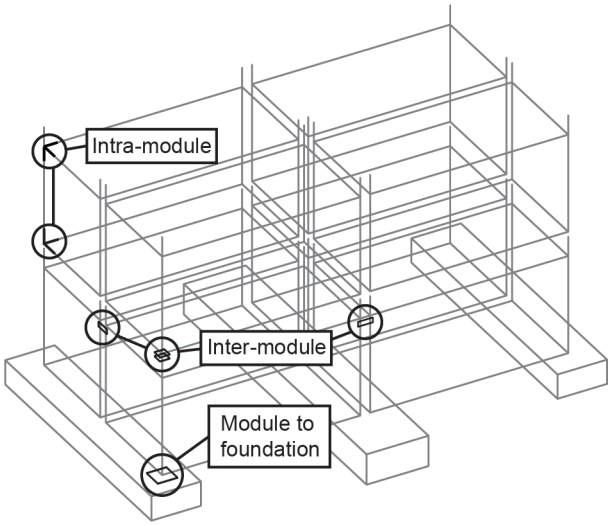

Figure 2.4. Illustration of connection types

Table 2.3. Summary of connection types

Type	Sub-Type	Advantage	Disadvantage
Inter-module	Bolted	Reduced site work; demountable	Access, slotted holes, slip, bolt tensioning
	Welded	No slip, compact, accommodate misalignment	Site work, corrosion, not demountable
	Composite (concrete-steel)	Strength, no slip, compact	Site work, not demountable
Intra-module	Bolted	Tolerance for shop assembly, deconstructable	Relatively low moment capacity, ductility and rotation capacity
	Welded	Suited to factory based construction using jig to ensure module uniformity	Does not permit rotation, steel members should be designed for hogging moments and axial forces
Module to foundation	Chain/cable/keeper plate	Low cost	Limited to low rise construction; tensioning requirements
	Site weld to base plate	Rigid connection	Additional trade on site, hot work, damage to steel corrosion protection system
	Base plate – cast in anchor bolts	Ductility	Positioning of cast in anchor bolts, tolerance in steel base plate, corrosion
	Base plate embedded in concrete	Full column strength and good ductility	Positioning of column during concrete curing, site welding

2.1.4.1 Inter-module connection

Inter-module connections (IMCs) include horizontal connections (HC) between adjacent modules in two plan directions, and vertical connection (VC) between stacked modules. It is reported that bolted connection is preferred over site welding. A gap is usually provided between the floor and ceiling beams, as shown in Figure 2.1(L), allowing for external access to IMCs and for services to pass between the beams. This suits connection between the columns, rather than between the beams. Bolted connections can be complex to accommodate connection of modules stacked in three directions while ensuring access to fasteners is provided during the install sequence. Use of long slotted holes may introduce the potential for tolerance accumulation over multiple levels, and vulnerability to slip failure in the event of large horizontal force [33]. The potential for connection slip may be controlled with the use of friction-grip or pre-tensioned bolts. VCs may incorporate a shear key or spigot [49], which assists in positioning modules and may provide structural connection where physical access is

not possible or practical. In some cases, concrete or grout is used to lock the joint in place, creating a composite concrete-steel connection. Table 2.4 presents a summary of IMCs for steel modules from the literature, and identifies the scope of the analytical, numerical and experimental investigation completed. In the latest studies, the force-displacement (F-d) and moment-rotation (M-θ) behaviours of the connection are established by detailed numerical analysis of the connection (see also §2.1.7, p.21).

Table 2.4. Existing inter-module connection types
VC: vertical connection, HC: horizontal connection, VH: vertical and horizontal connection
HSS: hollow steel section, F-d: force-displacement, M-θ: moment-rotation

Type	Illustration	Ref.	Description	Analytical / Numerical / Experimental Study
HC	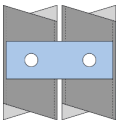	[12, 18]	Tie plate, connecting hollow or open steel section columns	-
HC	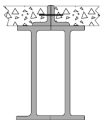	[14-17]	In-situ concrete encased bolted cleat, connecting open steel section beams	-
HC	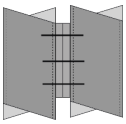	[50]	Bolted side plate, connecting HSS	Numerical – F-d and M-θ
VC	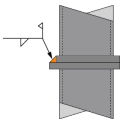	[14-17]	Site weld end plate (one side), connecting HSS	-
VC	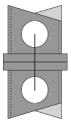	[7]	Bolted end plate, connecting HSS with access hole, or open angle section columns	-
VC	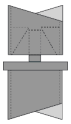	[49]	Lifting plate shear key, connecting HSS	-
VC	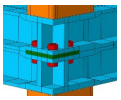	[51]	Bolted connection, connecting open steel section beams	Numerical – F-d in 1-direction (compression) and M-θ in 2-directions
VC	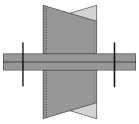	[50]	Bolted end plate (bolts on two sides), connecting HSS	Numerical – F-d and M-θ
VH	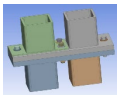	[33]	Complex bolted end plate, connecting HSS	Numerical and experimental – F-d in 1-direction (shear)

Type	Illustration	Ref.	Description	Analytical / Numerical / Experimental Study
VH	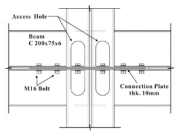	[52, 53]	Bolted connection plate, connecting HSS	Numerical – M-θ in 1-direction, cyclic loading
VH		[54]	Steel bracket welded to corner columns	Numerical and experimental – Shear and simply supported
VH	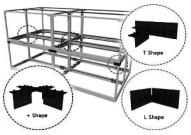	[55]	Steel bracket, bolted or welded to floor and ceiling beams	Numerical and experimental – M-θ in 1-direction, cyclic loading
VH	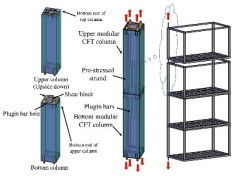	[56]	Pre-tensioned connection of columns (Composite steel-concrete)	Numerical and experimental – Simply supported, static and cyclic loading
VH	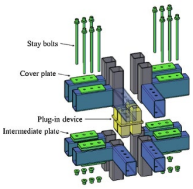	[57]	Bolted interior steel connection	Numerical and experimental – Lateral loading of beam-column assembly, static and cyclic loading
VH	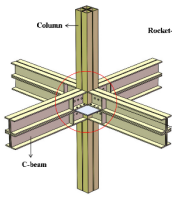	[58]	Bolted connection with rocket-shaped tenon	Analytical and numerical – Axial F-d with a focus on buckling of the column
VH	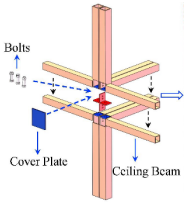	[59]	Bolted connection with welded cover plate	Experimental – Lateral loading of beam-column assembly, monotonic and cyclic loading

2.1.4.2 Intra-module connection

Intra-module connections, i.e., connections within a module, are generally representative of traditional connection details. For MSBs both welded and bolted connections are used. Considering column to beam connections, the bolted connection types include single web (or fin) plates [7, 60, 61], double angle cleats [50], and bolted end plates [61]. It is suggested that a moment resisting connection consisting of an end plate or a deep fin plate may provide lateral stiffness for low rise buildings [7]. This is unusual in that fin plate connections are often classified as simple shear connections. Fin plate connections have relatively low moment

capacity, ductility and rotation capacity [62], hence their use is suggested only for low rise (3-storey or less) buildings [7]. However, the use of such connections may make open modules susceptible to progressive collapse [62]. In this case the fin plate connection may have inadequate moment capacity, and so require strengthening. In contrast, Annan et al. [16] investigated steel floor framing with secondary beams welded directly to the main beams. This is compared with conventional steel construction which may use clip angles permitting greater rotation. The welded connections do not necessarily permit rotation such that steel members should be designed for hogging moments and axial forces which may be developed as a result [16]. Linear elastic analysis is demonstrated to be adequate for this issue and Annan et al. [16] present a process which may be adopted in design.

2.1.4.3 Module to foundation connection

Foundations may consist of in situ or precast concrete footings, bored concrete piles, augered steel piles, or some combinations. Low rise modular buildings located in areas with high lateral loading may be vulnerable to overturning and sliding failures if not adequately restrained by connection to an appropriate foundation. Building modules are commonly connected by chains, cables, keeper plates or welding to concrete or steel piles, or large mass concrete footings. Each connection type has associated disadvantages including tensioning requirements for chain and cable. In medium and high-rise construction foundations are more substantial. Base plates may be incorporated in modules and fixed to cast-in anchors, or welded on site to accessible cast-in plates. Park et al. [48] developed an embedded column connection (Figure 2.5), as an alternative to the traditional cast-in or post-fixed steel bearing plate. This connection was developed to ensure best use of the full column strength and provide good ductility. The disadvantages include the requirement for site welding between MSB columns and the end plate.

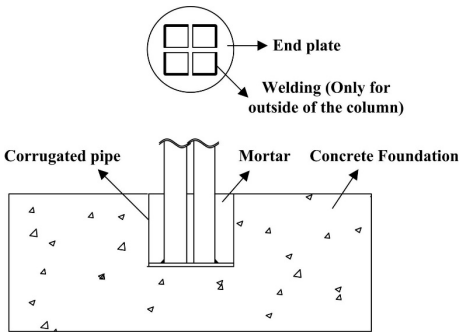

Figure 2.5. Embedded column connection [48]

2.1.5 Case study

To define the range of existing modular buildings, a list of multi-storey modular building projects has been compiled based on a review of the literature. Table 2.5 shows a selected

sample. The tallest identified prefabricated building is J57 Mini Sky City located in Changsha, China, being 57 storeys or 207.8 m tall [31]. In Australia, the tallest prefabricated building identified is La Trobe Tower, Melbourne, being 44 storeys or 133 m tall. It is in an area with relatively low wind and earthquake loading. In areas with higher lateral load requirements the maximum building height is less. For example, the tallest building within Australia's severe cyclone region is Concorde South, being 6 storeys.

Table 2.5. Selected modular building projects
* SA: student accommodation, R: residential, O: office, H: hotel

Project	Location	Storeys	Use*	Completed
Agricola College	Kalgoorlie, Australia	4	SA	2017
La Trobe Tower	Melbourne, Australia	44	R	2016
461 Dean Street	New York City, United States	32	R	2016
Coast Apartments	Rockingham, Australia	4	R	2016
J57 Mini Sky City	Changsha, China	57	R / O	2015
Concorde South	South Hedland, Australia	6	R	2014
SOHO Apartment	Darwin, Australia	29	R / H	2014
Unite Student Apartment / Hostel	Wembley, England	19	SA	2014
Port View Apartments	Port Hedland, Australia	4	R	2013
Little Hero Building	Melbourne, Australia	8	R	2010
Victoria Hall	Wolverhampton, England	25	SA	2009
Paragon Student Housing	West London, England	17	SA	2006
Royal Northern College of Music	Manchester, England	9	SA	2001

2.1.6 Hazards and structural responses

The hazards for modular buildings include transport activity, cyclone (hurricane, tornado), earthquake, explosion, progressive collapse, and fire. Hazards can be classified as natural, anthropogenic, or technological [63, 64] and the interaction can be concurrent, cascading or independent [65]. Each hazard has associated actions, or loads, for which the building structure must be designed. Different loads have different characteristics, design criteria and mitigation strategies (Table 2.6). No studies have been identified to address the method for selection of an optimal design to suit the competing requirements of different loads for modular building.

2.1.6.1 Transport and handling

Modules are designed to be lifted, with designated lift points provided on the module. They are usually lifted by a crane, although forklifts may be used in the manufacturer's yard. The

number and positioning of lift points is often determined by deflection criteria chosen to protect fragile components. Lift points are typically positioned in from each end, reducing member design actions and deformation of the chassis. General guidance on the design of lifters is available in existing documents, for example, American Standard [66-68] and DNV Offshore Standard [69]. The stiffness of a whole module is likely to be influenced by internal and external linings and manufacturers may test complete modules to establish composite stiffness. For transportation, including road, rail and sea, the loading is defined by acceleration coefficients, for example, 0.8g forward, 0.5g rearward, and 0.5g transverse during road transportation. General guidance is available in the existing documents, for example, the CTU Code [70] for cargo transport units (CTU). Transit bracing is often provided, particularly in open modules, to strengthen the structural frame and increase stiffness to help control damage to fragile components.

Table 2.6. Summary of load characteristics and design criteria

Load	Characteristics	Design Criteria
Transport & Handling	Lifting: dynamic amplification depending on module and lift arrangement; Transport: acceleration coefficients in three orthogonal directions	Stability, strength and serviceability; Deflection criteria to protect components, e.g., h/500, L/500
Wind Load	Low frequencies, ~0.01 to 2.5 Hz; Mean component and fluctuating component (gust-factor approach)	Stability, strength, serviceability (inter-storey & overall deflection, and vibration); Deflection limits for serviceability limit state, e.g., H/600 for total drift and h/500 for inter-storey drift [71]
Debris Impact	Local impact	Local penetration, opening area for internal pressure calculation [72, 73]
Earthquake	Ground motion with frequency contents in the range of 0.5 to 25 Hz; Excites fundamental, low vibration modes resulting in a global structural response	Damage criteria – displacement based, i.e., ductility ratio & inter-storey drift ratio, e.g., 1.5% inter-storey drift [74] Design criteria – life safety, collapse prevention
Blast	Short duration; local response for close-in blast, might lead to progressive collapse; For far field blast, uniformly distributed loading	Descriptive building damage level and component response
Fire	High temperature	Fire resistance level (time)

Few studies on the response of modular buildings to transport and handling have been reported. Smith et al. [75] investigated transport and handling for single storey timber framed

modules. Field testing and numerical modelling using SAP2000 were conducted and the relevant data is provided in the referenced report. It was reported that the main form of damage was cracking of internal plasterboard linings. This was caused by the lifting practices with road transport propagating cracks. It was recommended that areas for further work included the development of laboratory techniques to simulate transport under controlled conditions and the development of dampers to reduce dynamic forces.

2.1.6.2 Wind

Natural hazards such as cyclones and tornadoes encompass multiple actions including both primary wind loading, and secondary debris impact and water ingress. Wind loads are characterised by low frequencies, approximately 0.01 to 2.5 Hz, and mean and fluctuating components [76-78]. Design criteria are typically based on stability, strength and serviceability by considering inter-storey deflection, overall deflection, and vibration [79]. For example, the limits of H/600 for total building drift and h/500 for inter-storey drift [71] are specified, where H is the total building height and h is the storey height. Generally, structures are regarded as wind sensitive if the fundamental frequency is less than 1 Hz, and slenderness ratio is greater than five [72, 79, 80]. Static analysis is therefore appropriate for buildings with height less than 50 m [79], based on an empirical formula for the fundamental frequency [81, 82]. However, results presented in the literature for modular buildings suggest a value of 30 m could be more appropriate, with a frequency of approximately 1 Hz obtained numerically for a 10-storey modular building [33] (refer §2.1.6.3.3, p.18). Therefore, dynamic analysis is required for modular buildings over 30 m high. No studies are identified to address cyclonic wind loads for modular buildings.

Few studies on the response of modular structures to wind loading have been conducted. Gunawardena et al. [83] presented base shear and storey drift results for static analysis of a 10-storey modular building with wind loading applied following AS 1170.2:2011 [72] for Region A, Terrain Category 4. Three different cases of inter-connection were considered for this building: rigid connection by a rigid floor diaphragm, flexible connection by a semi-rigid diaphragm, and no connection. The results indicated the actual structural behaviour fell between that for the semi-rigid diaphragm and no diaphragm. Styles et al. [50] investigated the effect of joint rotational stiffness on the response to wind loading for an 11-storey modular building. It was reported that increasing horizontal inter-module and intra-module connection stiffness effectively reduced inter-storey drift due to wind load. Intra-module connection stiffness was shown to have a greater effect than horizontal inter-module connection stiffness. It is indicated that further studies are needed to address the factors including vertical inter-module connection stiffness and building height.

2.1.6.2.1 Wind-borne debris

Wind-borne debris impact has been observed in many strong wind events and is well documented in the existing literature [84-86]. Debris impact causes localised damage and if the envelope is penetrated may cause additional damage due to water ingress and internal pressurisation. Debris impact loading is typically specified for standard debris items, with velocity related to regional wind speed (V_R). For example, AS/NZS 1170.2 [72] specifies a 4 kg timber with 100 x 50 mm cross-section impacting at $0.4V_R$ and $0.1V_R$, and an 8 mm (2 g) steel ball impacting at $0.4V_R$ and $0.3V_R$ for the vertical and horizontal trajectory component, respectively [72]. Modular buildings are generally lightweight to facilitate transport and so may incorporate lightweight cladding materials which are vulnerable to debris impact. Recently, a systematic study of the performances of structural panels against wind-borne debris impact has been conducted experimentally by using a pneumatic cannon and numerically by using LS-DYNA [87-91] and some cost-effective engineering adaptation methods have been developed. The development of lightweight and resilient structural panel as building envelope can be incorporated into the design of modular buildings.

2.1.6.3 Earthquake

Earthquakes are characterised by ground motions with predominant frequencies in the range of 0.5 to 25 Hz, which normally excite the fundamental and low vibration modes of engineering structures and result in global structural responses [76, 77]. Extensive research works have been carried out to investigate the seismic behaviours of traditional building structures, and displacement-based damage criteria such as the ductility ratio and inter-storey drift ratio are widely used by the design guides to measure their seismic performances [77]. For example, Australian Seismic Design Code AS 1170.4 [74] specifies an inter-storey drift limit of 1.5% for the ultimate limit state. Modular buildings, due to their obvious advantages, are increasingly used in areas with high seismic hazard. Their seismic performances are, however, not adequately understood because they are a relatively new structural form. The rocking and sliding response of modules after connection damage could be the governing response modes. In such cases the conventional displacement-based criteria such as drift ratio may no longer be applicable to quantify modular building damage. Therefore, it is essential to investigate the performance of modular buildings under earthquake loadings and further propose the corresponding criteria to evaluate their seismic performances.

2.1.6.3.1 Seismic responses

Very limited studies on the seismic responses of modular structures have been conducted and these studies mainly focused on the MSB-braced frames. Annan et al. [17] conducted

experimental studies on the hysteretic behaviours of an MSB-braced frame and a regular concentrically-braced frame with similar physical characteristics. It is reported that both specimens showed stable and ductile behaviour up to very high drift ratio (3.5%). The MSB frame was more vulnerable to column bending deformation, whereas the traditional frame was vulnerable to the out of plane buckling of bracing. Annan et al. [15] further conducted incremental dynamic analysis (IDA) for 2-, 4- and 6-storey two-dimensional (2D) MSB-braced frames. It is reported that the selected MSB-braced frames exhibit a predominantly first-mode response (e.g. the mass participation factors for the 2-storey frame are 94% for the 1st mode and 5% for the 2nd mode, similarly, for the 4-storey frame, the percentages are 81% and 15% respectively, and for the 6-storey frame, the values are 77% and 17%) and limited redistribution of internal forces can result in concentration of inelasticity at the first level. Fathieh et al. [18] conducted nonlinear static pushover and IDA analyses for 2D and 3D MSB-braced 4-storey frames. It verified the concentration of inelasticity at the first level due to limited internal force redistribution and brace inelasticity, and found the 2D model overestimated the structural capacity against incipient collapse because torsional response was not accounted for in the 2D model. Gunawardena et al. [20] conducted nonlinear time history analysis for a freestanding 10-storey modular building subjected to six selected ground motions. Column hinge formation was found unavoidable in severe ground motions and column ductility was important to redistribute post yield loads. It was indicated that further studies are needed to investigate dynamic behaviours for mid- to high-rise modular buildings.

2.1.6.3.2 Over-strength and ductility

In the seismic analyses of traditional engineering structures, forces derived from an elastic response spectrum analysis are adjusted to allow for the ductility and other reserved strength. AS 1170.4 adopts a structural ductility factor (μ) and structural performance factor (S_p) as a measure of the ability to withstand inelastic displacement and other reserved strength, respectively. For the modular structures, Annan et al. [14] investigated the inelasticity of modular buildings by conducting nonlinear static pushover analyses for 2-, 4- and 6-storey 2D MSB-braced frames. The over-strength factor ($R_0=1/S_p$) and structural ductility (μ) are reported as per the National Building Code of Canada (NBCC) [92, 93]. Two methods were used to calculate the column actions due to bracing – the SRSS (Square Root of the Sum of the Squares) method [94, 95], and the DS (Direct Summation) method. The SRSS method was found to be unconservative and so the DS approach was recommended. The ductility, which is calculated as the ratio of the ultimate drift (Δ_u) to the yield displacement (Δ_y), i.e., Δ_u/Δ_y, is shown to reduce with increasing MSB frame height. The values range from 4.6 to 1.8 for 2- to 6-storey MSB-braced frames. The variation with height is reported to occur for two reasons. First, the yield displacement of braces increases with increasing frame height due to a decrease

in brace slenderness, i.e., the brace section size was not constant [14]. Second, the ultimate drift is determined by the redistribution of load after the compression brace yields [14]. The vertical inter-module connections (IMCs) affect this ability to redistribute load, and the affect increases with increasing frame height [14]. Similarly, the over-strength factor, which is calculated as the ratio of the ultimate load to the design load, is shown to reduce with increasing height [14]. The values range from 2.5 to 1.9 for 2- to 6-storey MSB-braced frames. The variation with height is again related to the ability to redistribute internal force [14]. Similar results are reported for steel moment resisting frame (SMRF) modules. Choi et al. [52] conducted nonlinear static pushover analyses for 3- and 5-storey SMRF modules with varying IMC type and stiffness, and reported over-strength factors between 2.15 and 3.76 for the 3-storey frames, and between 1.19 and 1.94 for the 5-storey frames. For each frame height, the SMRF frames with greater inter-connection stiffness had greater over-strength factor.

2.1.6.3.3 Fundamental period of modular building

The fundamental period of a modular building is an important parameter for the prediction of its seismic behaviour [96]. Many standards provide empirical formulae for the fundamental period (T_1[s]) of traditional building structures. For example, AS 1170.4 [74] gives $T_1 = 1.25 k_t h_n^{0.75}$, where h_n is the height from the base to the uppermost seismic mass in metres, and k_t is a constant depending on the structure type with a value ranging between 0.05 (for all other structures) and 0.11 (for moment-resisting steel frames). Recently, some studies have been carried out on modular buildings. Figure 2.6 shows the fundamental periods for rectangular modular buildings together with the upper and lower bounds defined in AS 1170.4. These fundamental periods are the result of numerical analysis of 2D MSB-braced frames [15], 3D MSB-braced frames [18, 33] and steel moment-resisting frame (SMRF) modules [52, 97], and experimental analysis of stacked timber frame modules [98]. It can be seen that the period values follow the trend of increasing with building height. From the limited data presented, k_t=0.05 gives a reasonable estimate for both the 2D MSB-braced frames and the timber frame modules, whereas k_t=0.075 appears more appropriate for the 3D MSB-braced frames. For the SMRF modules greater variation in the fundamental period is shown. This is the result of varying inter-module connection type and stiffness [52], and varying imposed gravity load [97]. For these SMRF modules use of k_t=0.11 to estimate the fundamental period is most accurate for the case of rigid inter-module connection. It should be mentioned that the data presented for the MSBs considers only the main structural elements and excludes the cladding elements. Cladding incorporated into modules may have a significant effect on the fundamental period due to the additional mass.

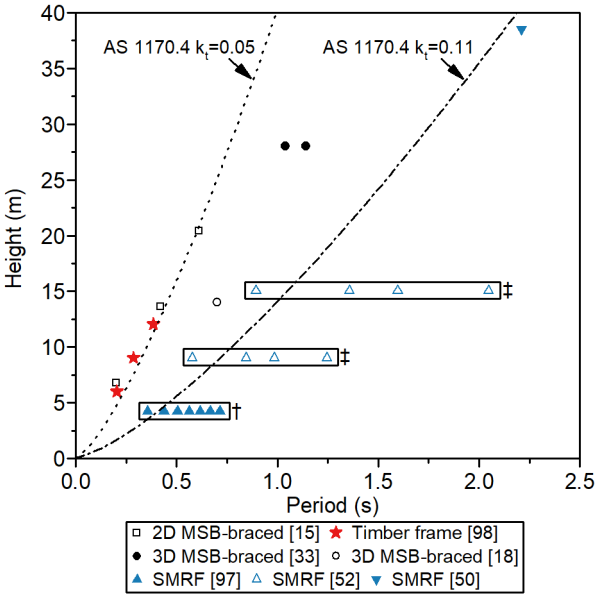

Figure 2.6. Variation of fundamental period with height for modular buildings
The existing literature includes the studies by Annan et al. [15], Gunawardena [33], Fathieh et al. [18], Shirokov et al. [97], Choi et al. [52], Styles et al. [50], and Malo et al. [98]. † indicates varying gravity load and ‡ indicates varying connection stiffness.

2.1.6.4 Blast

Blast loads can induce local and global responses. Local response, typically the result of close-in explosion, causes localised failure which might lead to progressive collapse [99]. Global response occurs for transverse load with longer exposure time [100], such as gas explosion and far field explosion. Design is typically based on descriptive building damage level, i.e., low, medium, and high, and component response. Modular buildings may be subjected to blast load from several sources including chemical / industrial / terrorist explosion. They are therefore used in industry to protect personnel [101-103] where they are referred to as blast resistant modules (BRM) or blast resistant portable buildings (BRPB) (Figure 2.7).

(a) (b) (c)

Figure 2.7. (a) One storey BRM building [101], (b) Two storey BRM building [101], and (c) Stacked BRPB complex [102]

Steel modules have a primary steel frame with walls formed by infill between roof and floor. For example, walls may consist of steel plate, cold-formed steel stud frame or sandwich panels. Typically, BRMs use 3.2 to 7.9 mm thick crimped steel plate walls fully welded to the steel frame [101]. For this type of module construction, finite element analysis is recommended to

capture failure modes, although a single degree of freedom (SDOF) approach may be adopted [101]. For general design, reference is often made to the standards including UFC 3-340-02 [104] and ASCE 41088 [99]. Hao et al. [105] provide a summary of the current practice. For steel components, response limits are given based on ductility (μ=1 to 20), support rotation (θ=1 to 12°) and side sway (height/50 to h/25) for moment-resisting frames. Overall, published qualitative studies for blast loading are limited and further studies are needed to investigate the behaviour of mid- to high-rise modular buildings.

2.1.6.5 Progressive collapse

Progressive collapse occurs when local damage from an extreme event results in overload and then failure of successive alternate load paths [106, 107]. It is a relatively rare catastrophic failure which may occur due to lack of continuity, ductility and/or redundancy [106]. The methods of design are typically categorised as indirect or direct approaches. The tie force method is an indirect approach wherein robustness is enhanced by provision of specified minimum ductility, continuity and strength [106, 107]. Direct design approaches include the alternative path method and key element design (or enhanced local resistance) [106, 107]. For modular steel buildings the tie force method may not be appropriate. This method does not consider beam rotations due to catenary action and failure may occur in low ductility connections such as standard fin plates [108]. Similarly, the key element method may not be appropriate for light steel framed modules [24]. This is because the lightweight structure may be unable to resist the relatively large design actions resulting from extreme events such as gas explosion [24].

Instead, the alternative load path approach is adopted [13, 24]. Lawson et al. [24] completed a static analysis for the loss of one corner or internal support to a light steel module, with load being transferred by shear walls back to a tying action in inter-module connections. To demonstrate the capability of the modules, tests were completed to establish the shear wall racking capacity and deflection of the module with removed supports. The required inter-module tie forces were found to be relatively low [24]. In another study, container express (CONEX) modules used for barracks were tested in Florida [109]. The modules were stacked three levels high and connected using twist locks. The work completed included simulating column removal using SAP2000, experimental column removal tests using hydraulic jacks, and finally detonation of an artillery shell at a critical location (Figure 2.8). The results confirmed progressive collapse was not an issue as per the Unified Facilities Criteria [106]. Progressive collapse studies have therefore considered only light steel framed modules and container buildings stacked three storeys high. Modular steel buildings may be vulnerable due to the use of connections with limited ductility, which is worth studying.

Figure 2.8. Expeditionary CONEX testing for progressive collapse [109]

2.1.6.6 Fire

Fire resistance is a major challenge for modular buildings. Concerns have been reported considering the use of flammable materials and the presence of a void between modules which may permit a fire to spread [110, 111]. These concerns are similar to those raised in the case of the fire at Grenfell Tower, London, UK [112]. However, studies into the fire performance of modular structures are limited. One study considered fire simulation for a container building [28] and several studies investigated the performance of developing composite materials such as fibre reinforced polymer (FRP). Composite materials have advantages which make them well suited to application in modular building. They are lightweight with high strength and stiffness and offer flexibility in shape [113-116]. However, they generally have low fire resistance and their performance as a building envelope is not well known [113, 114]. Ngo et al. [113] investigated the performance of an office building constructed from modules with glass FRP composite components forming the façade. This study provides insight into the fire performance based on numeric analysis. Nguyen et al. [114] investigated the addition of fire retardant to improve fire performance. Models were developed to predict "*fire growth index and total heat release*" for "*organoclay/glass fibre reinforced polymer (GFRP) laminates*" [114]. The performance was then considered for an office building with façade consisting of GFRP laminate on foam core. The addition of organoclay is found to prevent flash-over and horizontal flame spread. Fire performance studies are therefore mostly related to the development of FRP materials with no studies identified for modular steel buildings. In current practice, fire resistance time requirements are satisfied by providing layers of protective cladding and fire stops to control fire spread [7].

2.1.7 Current design practice and methodology

2.1.7.1 Design guidelines and theoretical analysis

General design guidance is available for light steel framed modules in the existing literature (Table 2.7). In current practice, guidance is drawn from the traditional literature. A limit state approach is adopted for design criteria considering stability, strength, and serviceability.

Building serviceability is satisfied by adherence to overall drift limits and acceleration limits for human comfort. For example, for wind loading, Mendis et al. [79] and Griffis [71] report on acceleration and drift limits. Modules should also satisfy serviceability criteria during transport and lifting. Limited guidance is available and current practice is based largely on practical experience. Serviceability during transport and lifting is mainly concerned with the potential for damage to finishes and equipment. Therefore, guidance can be found in existing literature such as Griffis [71]. For example, to control cracking of partition walls during transport and handling, limits of module height/500 and span/500 can be adopted for lateral acceleration and gravity loads. Design of MSB connections is similarly based on the traditional literature due to the lack of modular specific guidelines. For bolted connections, Gunawardena [33] and Styles et al. [50] showed structural behaviour can be established using finite element analysis based on comparison with laboratory testing. The resulting force-deformation or moment-rotation behaviours can then be incorporated into a simplified global model of the building structure. For example, Gunawardena [33] has demonstrated the use of link elements to model horizontal connections using ETABS and SAP2000.

Table 2.7. Design guidelines for modular buildings

Guideline	Application scope and notes
The Steel Construction Institute (SCI) P272 [21], SCI P302 [12], SCI P348 [22]	Architectural and general guidance on typical details for light steel framed modules
Prefab Architecture: A Guide to Modular Design and Construction [6]	General background, applications, and case studies for modular buildings
Design in Modular Construction [7]	General guidance on modular buildings with an emphasis on light steel framed modules and case studies
Code of Practice for Packing of Cargo Transport Units [70]	General guidance on transport actions for container units
Handbook for the Design of Modular Structures [117]	General guidance on design and construction aspects with an emphasis on Australian codes and standards

As for traditional structures, simplified SDOF models are available following the standard texts such as Biggs [118], Clough et al. [119], and Chopra [93]. Hao et al. [105] provided a review of current practice and its limitations for blast-resistant analysis. The limitations of SDOF models include assumptions regarding loading conditions, response mode and deflection shape [77, 105]. No theoretical analysis models developed specifically for modular buildings are identified in the literature. From low-rise construction, modular buildings are known to behave as rigid bodies, for example overturning and sliding due to wind loading [120, 121]. This understanding of modular behaviour could be extended to multi-storey stacked assemblies, adopting a rigid module, flexible inter-connection approach. Extensive

research has been reported on the rocking response of rigid structures. Hao et al. [122] provide a summary of the development up to 2011. The rocking and sliding response is known to be highly nonlinear. For example, stability depends on structure slenderness, and ground motion amplitude, frequency and duration [123]. The existing knowledge of rigid bodies could be applied to modular buildings and could form the basis of theoretical analysis for multiple hazards.

2.1.7.2 Experimental testing

Testing is typically conducted either to demonstrate compliance with performance requirements or to determine the capacity for design purposes, i.e., proof testing or prototype testing. As a new developing application, structural design of modular buildings has a greater emphasis on prototype testing, rather than reliance on standardised or pre-qualified detailing. Prototype modules may be constructed to establish overall composite stiffness including cladding, test lining response to transport and lifting actions, and to test the fit and tolerance of connection systems. Table 2.8 gives a summary of test methods for modular buildings and prefabricated components. The documentation of test methods for modular buildings is limited and standard methods are not available in some cases. For blast loading no modular specific methods are available and a summary of current practice is provided by Hao et al. [105].

Table 2.8. Test methods for modular buildings and prefabricated components

Component	Test Description	Standard Method	Example
Module	Transport and handling – field testing, measurement of wind speed/pressure, deformation & accelerations	-	[75]
Module	Overturning – wind tunnel, rigid body scale model	-	[124]
Module	In-plane shear (racking test), e.g., Figure 2.9	-	[60]
Module	Progressive collapse – general methods include laboratory simulated column removal and field testing	-	[13, 24, 109]
Module	Dynamic properties – field testing, to determine fundamental frequency, damping ratio, mode shape	-	[98]
Module frame	Cyclic seismic test – symmetric reversed-cyclic loading history	ATC-24 [125]	[17]
Panel – wall, floor, roof	In-plane shear, compressive / tensile / concentrated load, transverse flexural load (two-point or bag method)	ASTM E 564-06 [126], ASTM E 72-15 [127]	[35, 128]
Connections	Evaluation of inter-module connections, e.g. Figure 2.9	-	[33]
Module envelope	Simulated wind-borne debris impact	ASTM E1996-14a [129], ASTM E1886-13a [130]	[91]

(a) (b)

Figure 2.9. (a) Shear force load testing of connection with contactless strain measurement system [33] and (b) Racking test of complete frame [60]

2.1.7.3 Numerical simulation

Structures are typically broken down into components for piecewise analysis. Connections are modelled using finite element analysis (FEA) and the resulting behaviour is incorporated in a separate model of the frame for structural analysis. MSBs often incorporate semi-rigid connections for which the behaviour and stiffness can be established for inclusion in the global analysis [131]. FEA of connections is commonly conducted using ABAQUS [132] or ANSYS [33, 50]. For global analysis, various commercial software packages have been adopted for modular buildings, including ABAQUS [30], ANSYS [50], SAP2000 Nonlinear [16, 75], and ETABS [19]. In the specific field of earthquake engineering, RUAUMOKO 3D [20], OpenSees [18] and SeismoStruct [17] have been adopted for incremental dynamic analysis, and pushover analysis.

2.1.8 Summary

Modular building refers to the application of a variety of structural systems and building materials. Modular buildings perform differently to similar traditional structures owing to the requirements of site interconnection for modular building. Analysis, design and construction technologies of modular building are currently under further development and several key areas are identified for further study.

1. Overall module size is limited by transport capabilities and internal layouts are limited by the requirement for structural elements. Greater flexibility in internal layout could be provided by a reduction in structural member sizes, and reduction in the number of braces, shear walls and columns.

2. There remains a need for efficient lightweight systems which also address issues of robustness. At the same time, there is also a need to develop new lightweight materials for

specific application in prefabrication and modular building. The performance with respect to wind-borne debris impact and fire are developing areas.

3. Accumulated damage must be considered for portable buildings subjected to repeated and fatigue loading. In other cases where a module might be transported only once or twice in its life, damage during transport and in situ degradation are worth studying. This affects the performance for all hazard types, yet published quantitative studies are limited.

4. Connections are key to the performance of modular buildings. The design and fabrication of reliable connection systems is a major challenge. Further research is required to better define the performance of existing connection systems and limit the potential for overdesign due to limited understanding.

5. The current studies on modular buildings under earthquake are limited to 10 storeys. Further studies are needed to investigate the dynamic behaviour due to earthquake ground motion for mid- to high-rise modular buildings.

6. No studies have been identified to address dynamic wind loading, or cyclonic wind loading for modular buildings. Further studies are needed to investigate the dynamic response of modular buildings under wind loading.

7. Further studies are needed to investigate the behaviour of mid- to high-rise modular buildings subjected to blast loading. In addition, progressive collapse studies considered only light steel framed modules and container buildings. Modular steel buildings may be vulnerable due to the use of connections with limited ductility, which is worth studying.

2.2 Review of bolted inter-module connections[2]

2.2.1 Introduction

In Section 2.1, inter-module connections (IMCs) were identified as key to the structural performance of modular buildings. Research into the structural behaviours of the existing IMCs was found to be limited and further study was recommended in order to extend the knowledge. Therefore, in this section, a more focused review of bolted IMCs in modular steel buildings is undertaken. Hence, this section summarises the existing bolted IMCs and describes their structural purpose and associated design models. Methods for estimating the stiffness of bolted steel connections are identified from the literature and applied to three selected existing IMCs. In this way, the ability of the existing models to estimate the structural behaviours of the existing IMCs is evaluated.

2.2.2 Inter-module connections and their structural purpose

In this section, the inter-module connections (IMCs), which form the interface between modules, are of particular interest. The IMCs may provide vertical connectivity (VC) as illustrated in Figure 2.10(a), or horizontal connectivity (HC) as illustrated in Figure 2.10(b). Alternatively, the IMCs may provide both vertical and horizontal connectivity (VH). The term joint is used to refer to the entire segment i-j as shown in Figure 2.10(a) and (b). In this way, the inter-module joint is comprised of several beam, column and connection elements depending on the particular geometry.

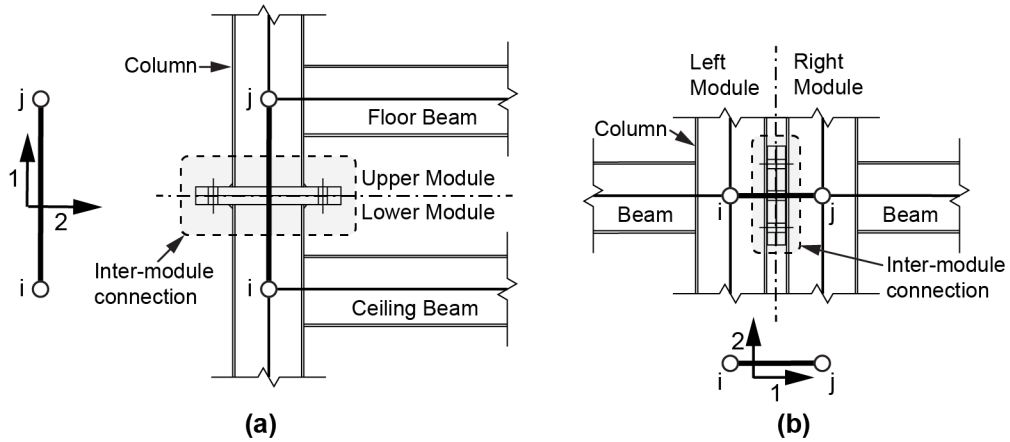

Figure 2.10. Inter-module connections providing (a) vertical connection (VC) and (b) horizontal connection (HC)

[2] The related work in §2.2 was published in the Journal of Building Engineering:

Lacey AW, Chen W, Hao H, Bi K. Review of bolted inter-module connections in modular steel buildings. J Build Eng. 2019;23:207-19. https://doi.org/10.1016/j.jobe.2019.01.035

The IMCs provide a path for load transfer and sharing between modules, and are the tying elements which allow stacked modules to effectively transfer loads to the foundation. Through load sharing the IMCs satisfy robustness requirements, preventing catastrophic progressive collapse due to local failure. In addition, individual frame member design may require lateral restraint which is provided by connection between modules. IMCs also satisfy construction and serviceability requirements. For example, IMCs may be used to pull modules together during site assembly, closing the gap between them, thereby allowing use of individual modules which are not perfectly straight or square. IMCs limit differential movement between modules which may otherwise cause damage to flashings or constitute loss of serviceability. They also limit overall building sway which might cause damage to internal linings. As shown in Figure 2.10(a), a vertical space is typically provided between the floor and ceiling beams, which allows access to the IMCs and permits services to run around and between the beams. Lawson et al. [7], for example, show a typical gap between the beams of 140 mm for corner supported modules.

Section 2.1 summarised existing connections for modular steel buildings, and the existing IMCs were summarised in Table 2.4 (p.10). It can be seen that hollow steel sections are commonly used for the module columns due to their efficiency in compression and torsion [133, 134]. Bolted connections are used for IMCs where they are preferred due to the advantages of reduced site work and demountability (Table 2.3, p.9). Disadvantages of the bolted connection include the requirements for access, tolerance by slotted holes, slip, and bolt tensioning. Considering construction requirements, the ideal IMC should be compact, easy to install on site, address tolerance requirements, and be demountable. In some cases it is also desirable that connections are reusable which may preclude the use of composite concrete-steel connections, for example.

2.2.3 Design practice and methodology

2.2.3.1 Development of inter-module joint models

For traditional steel joints relevant design models can be found in the existing standards such as those listed in Table 2.9. In the case of inter-module joints the models are still developing. The works by Annan et al. [14] consider a vertical inter-module joint which is modelled as shown in Figure 2.11. The model has rigid elements allowing for the rigidity of the beam-column joints, and a pin joint allowing for the rotation permitted by the welding on one side only. Horizontal connections are not included because the simplified two-dimensional frame does not have horizontally adjacent modules. Sultana et al. [135] investigated the use of superelastic shape memory alloy bolts in the vertical inter-module connection. The moment-rotation (M-θ) behaviour of the connection was determined based on the joint model as shown

in Figure 2.12. Rigid elements were assumed for the end plate inside the hollow section and springs were included to account for the stiffness of the external end plate and bolt.

Table 2.9. Existing standards for traditional steel connections

Standard	Application scope and notes
Eurocode 3: Design of steel structures – Part 1-8: Design of joints [136]	Joints connecting H or I sections with an emphasis on beam to column joints and column bases; Welded hollow section joints
Specification for Structural Steel Buildings, ANSI/AISC 360-16 [137]	General design of connection elements
Specification for Structural Joints Using High-Strength Bolts [138]	Specifications with an emphasis on installation requirements; Slip testing procedures
AS4100 [139]	General design of connection elements including bolts and welds

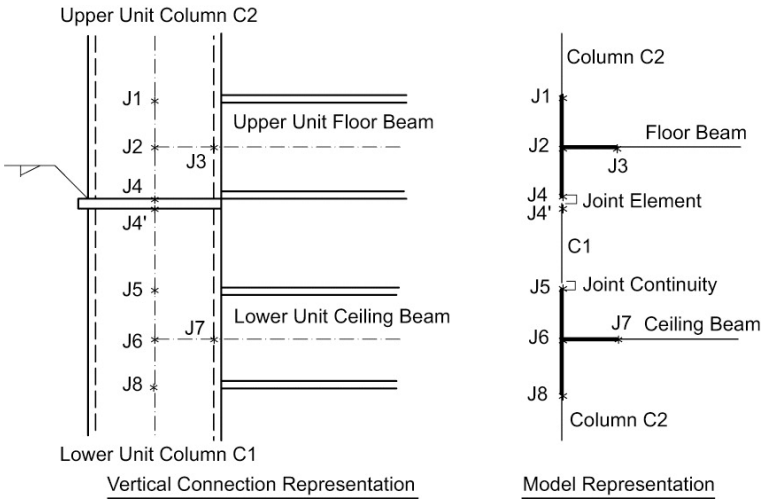

Figure 2.11. Annan et al. [14] inter-module joint model

Fathieh et al. [18] extended the work of Annan et al. [14], including both vertical and horizontal inter-module joints in a three-dimensional frame. Following Annan et al. [14], rigid elastic beam-column elements were defined considering the beam-column joint rigidity, and the short column length was included as an "inelastic force beam-column element" in the OpenSees model. Again, a pinned joint was included to permit rotation at the top of the short column section. For the horizontal joint, which was considered as a bolted steel plate, elastic behaviour was assumed by modelling the connection as an element with strength in bending and shear 30% greater than the adjacent beam section. Gunawardena [33] considered a combined horizontal and vertical connection detail. The vertical joint was modelled by beam elements with consideration of the possible locations of hinge development due to plastic yield (Figure 2.13). The horizontal joint was included as a spring which transfers lateral load between adjacent modules. The spring stiffness was determined as the shear stiffness of the

relevant inter-module connection, disregarding any potential stiffness in other directions. In this way the force-displacement (F-d) behaviour of the horizontal IMC was incorporated directly as the stiffness of the joint.

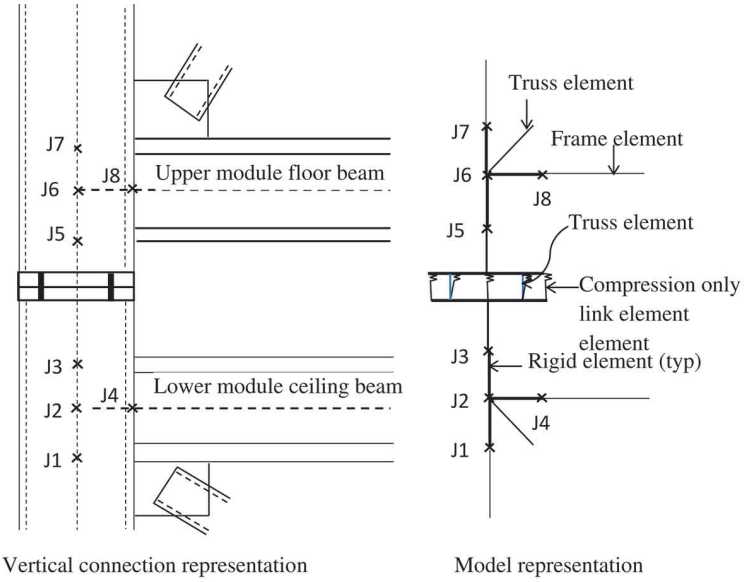

Figure 2.12. Sultana et al. [135] inter-module joint model

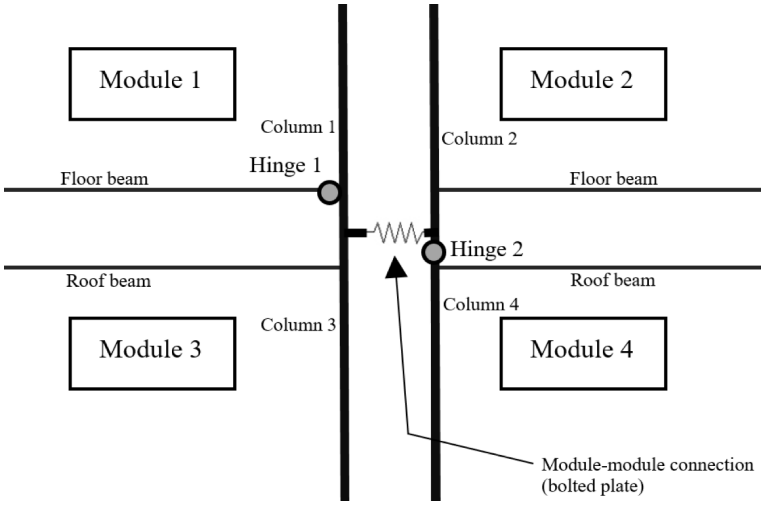

Figure 2.13. Gunawardena [33] inter-module joint model

In a subsequent work, Chua et al. [140] proposed an extended model, which was named as the translational spring model. It included a vertical link element for each column, for which axial and shear springs were input, while the moment-rotation stiffness was considered to be negligible. Similarly, the torsion-rotation stiffness was not included, and it was reported that torsion in the vertical connection (VC) was unlikely as a result of the "*volumetric nature of the modules*". Moreover, if torsion was applied to the VC, it would not affect the lateral displacement, which was the main interest in the following numerical analysis of the overall building structure. For the horizontal connection, a horizontal link element was defined which

connected the adjacent columns. Axial and shear springs were input based on the central tie plate properties, i.e., $\frac{EA}{L}$ and $\frac{GA}{L}$, while rotation was not restrained.

2.2.3.2 Experimental testing

Experiments undertaken in the previous studies are outlined in Table 2.10. Two main types of loading were considered in the literature related to modular buildings: quasi-static monotonic and cyclic. The existing experimental studies do not consider the interaction between separate horizontal connection and vertical connection, or possible contact between adjacent columns. As given in Table 2.10, several studies complete cyclic loading of full scale connections subject to lateral and axial loading. The lateral load is applied to generate a bending moment in the connection such that the moment-rotation behaviour may be recorded. The cyclic loading is undertaken to evaluate the seismic behaviour of the connection, giving information on the strength and stiffness, and the time history dependent behaviour [125]. Further information on the typical requirements for cyclic testing can be found in the American standard AISC 341-16 [141].

2.2.4 Structural behaviours of selected existing inter-module connections

Three existing inter-module connections (IMCs) were selected for detailed review, as summarised in Table 2.11. The selected IMCs (A/B/C) were taken from published works which provide details of the force-displacement (F-d) and moment-rotation (M-θ) behaviours of the IMC. These F-d and M-θ behaviours are presented and discussed in this section. Figures 2.14 and 2.17 to 2.21 replot the data presented in the referenced papers. As the boundary and loading conditions may influence the resulting behaviour, illustrations were added to the plots to show how the loads were applied in the referenced work. For the Type A connection the load application was not explicitly defined in the referenced paper and the illustrations show the interpreted load application.

In Section 2.2.5 the existing simplified models for the structural behaviours of bolted steel connections are introduced. The structural behaviours of the selected IMCs (Table 2.11) are then estimated using the simplified models. Finally, the estimated structural behaviours of the IMCs are compared with the actual behaviours introduced in this section. In this way, the following Section 2.2.5 evaluates the accuracy of the existing simplified models when they are applied to IMCs.

Table 2.10. Experimental testing

F-d: force-displacement, M-θ: moment-rotation, DIC: digital image correlation

Ref.	Experimental testing	Photos
Gunawardena [33]	F-d in 1-direction (shear) 500 kN compression load cell, load applied at a rate of 0.1 mm/min Strain measurement by non-contact DIC (ARAMIS)	
Doh et al. [54]	Steel bracket connection 90 t hydraulic jack Shear and simply supported	
Lee et al. [55]	M-θ behaviour of beam-column joint including ceiling bracket connection for cyclic loading Cyclic loading with an actuator; displacement controlled following the Korean Building Code [142] for verification of a column-beam joint	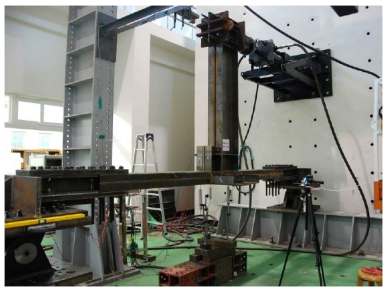
Chen et al. [57]	M-θ behaviour of beam-column joint including inter-module and intra-module connections Combined axial and lateral load; axial load 20% and 10% of column yield load Static monotonic and quasi-static cyclic loading based on JGJ 101-96 [143]	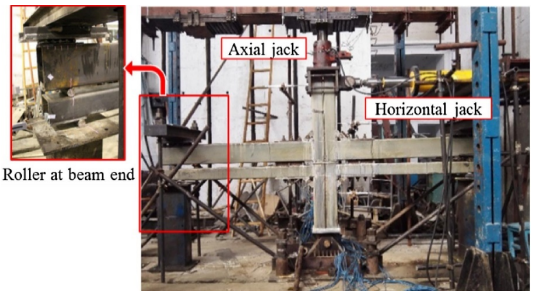
Deng et al. [59]	M-θ behaviour of beam-column joint Combined axial and lateral load; axial load 10% of column yield load Static monotonic and cyclic loading based on ATC guidelines [125]	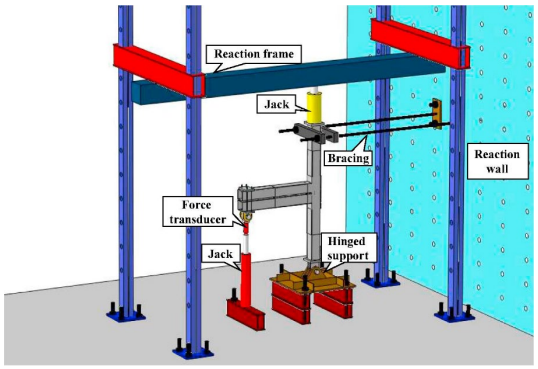

Table 2.11. Selected inter-module connections

Type	Ref.	Data	Height	Details	Illustration
A (HC)	[50]	Numerical only – Load-displacement and moment-rotation	11 storeys	300x200x6 RHS C350; M24 class 10.9	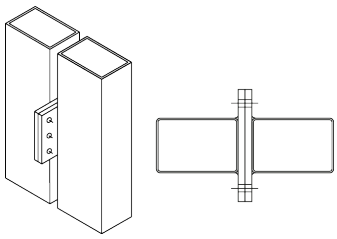
A (VC)	[50]	Numerical only – Load-displacement and moment-rotation	11 storeys	300x200x6 RHS C350; 370x410x25 G350 end plate; M24 class 10.9	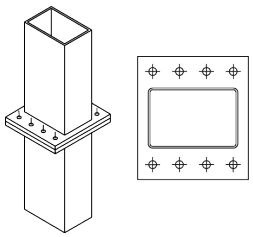
B	[33]	Numerical & experimental – Load-displacement in 1-direction (shear)	10 storeys	150x150x9 SHS C350; 25mm thick G350 plate; M12 or M16 class 8.8	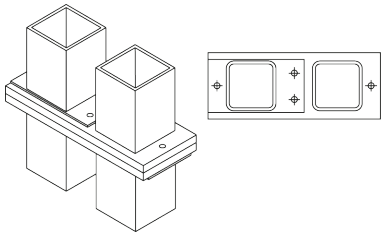
C	[57]	Numerical & experimental – Lateral loading of beam-column assembly, static and cyclic loading	4 storeys	150x150x8 SHS Q345 (315MPa yield)	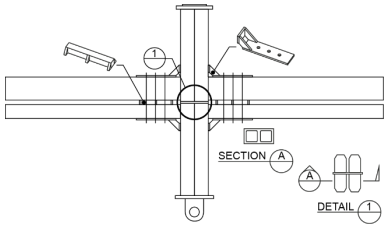

2.2.4.1 Type A (HC and VC)

The Type A connection is based on the work of Styles et al. [50] and represents a relatively simple bolted connection, with horizontal and vertical inter-module connection provided separately. In addition, the Type A connection represents the case of relatively high initial connection stiffness. The horizontal and vertical connection details are shown in Table 2.11. The horizontal connection (HC) is classified as a bolted side plate and the connection geometry is based on Section 8 of the Australian Standard AS 4100 [139]. The vertical connection (VC) is classified as a bolted end plate and the geometry is based on the Joints in Steel Construction Design Guide [144]. Styles et al. [50] present selected force-displacement (F-d) and moment-rotation (M-θ) behaviours for the connections based on numerical analysis only, citing the work of Shi et al. [145] and Luo et al. [146] for the joint modelling method. The numerical results obtained from ANSYS are validated by modelling a beam-column joint and comparing the M-θ behaviour with published experimental data [147]. SOLID48 8-node elements were

adopted and preloading of the bolts was included by PREST179 elements at the middle of the bolt shank. CONTA174 and TARGE170 elements were adopted for the contact, and welding was simulated using CPRINTF node coupling.

For the HC, Figure 2.14 shows the F-d behaviours for the X-direction (a) and Z-direction (b). For the X-direction, the connection is subjected to tension, and the resulting F-d behaviour (a) may be related to the bolt and plate bending stiffness. The failure mode is a combination of yielding of the plate and tension failure of the bolts, similar to the failure mode seen in bolted end plate joints subjected to tension, as shown in Figure 2.15. For the Z-direction, the connection is subjected to shear in combination with bending which results from the offset of the applied force (F_z) from the centre line of the connection. The F-d behaviour (b) exhibits three stages. The first stage has low stiffness due to initial slip of the connection. The second stage has increased stiffness which occurs as the bolts contact the edge of the bolt hole. This is followed by yielding and an associated reduction of the stiffness in the final stage. The failure modes include shear failure of the bolts, crushing failure of the plates and tension fracture of the plates, similar to the shear behaviour of traditional bolted connections, as shown in Figure 2.16.

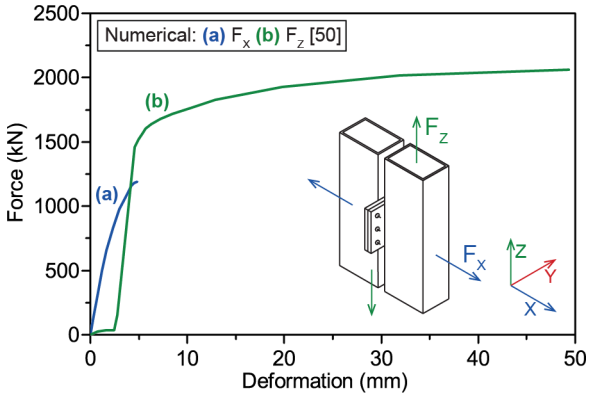

Figure 2.14. Type A (HC) – Numerical force-displacement behaviour [50]

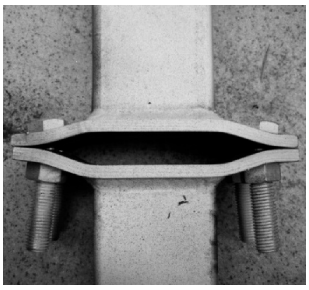

Figure 2.15. Failure mode for bolted end plate in tension [148]

Figure 2.17 gives M-θ behaviours for bending about the X-axis (a) and the Y-axis (b). The M-θ behaviours show an initial elastic stiffness, followed by a reduction in the stiffness due to yielding. For bending about the X-axis (a), the possible failure modes include shear failure of

the bolts and crushing failure of the plates. For bending about the Y-axis (b), contact between the column sections results in an increased lever arm effectively increasing the moment capacity of the connection. The failure modes include yielding of the end plate, tension failure of the bolts, and crushing or buckling of the column at the point of contact between the columns.

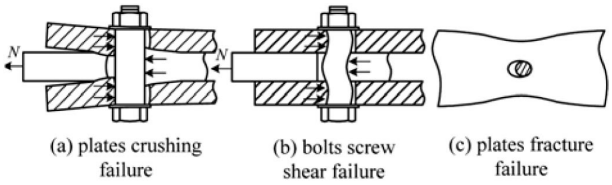

Figure 2.16. Failure modes for bolted connections subjected to shear [145]

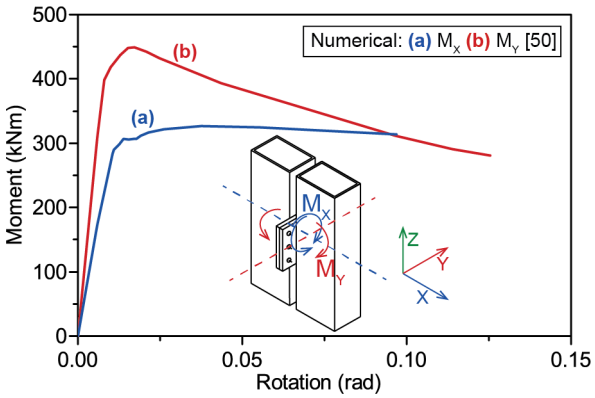

Figure 2.17. Type A (HC) – Numerical moment-rotation behaviour [50]

For the VC, only F-d behaviours are given, considering three directions as shown in Figure 2.18. For the X-direction (a) and the Y-direction (b) the connection is subjected to shear, and a two stage bilinear behaviour is shown for the F-d curve. The first stage is associated with initial slip of the bolted connection, and the second stage is associated with the increase in stiffness which occurs when the bolts contact the bolt hole edge. In comparison, a more gradual nonlinear behaviour is shown for loading in the Z-direction (c) where the connection is subjected to tension, causing bending in the plate and tension in the bolts.

2.2.4.2 Type B (VH1)

The Type B connection is based on the work of Gunawardena [33] and represents a more complex bolted end plate IMC with the horizontal and vertical connectivity provided by a single connection. In addition, Type B represents the case of relatively low initial stiffness. The F-d plot (Figure 2.19) is given based on numerical and experimental analysis and shows three clear stages. The behaviour may be simply described as tri-linear, although it should be noted that the results do not continue to failure and so may omit associated nonlinear behaviours. Three different connections were considered, and are labelled as C1, C2, and C3.

C1 used M12 bolts, whereas C2 and C3 had M16 bolts. The bolt hole sizes were 14 mm round, 18 mm round and 18x26 mm slot, respectively.

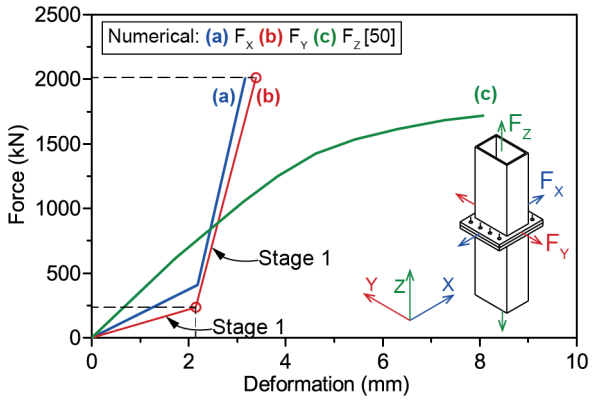

Figure 2.18. Type A (VC) – Numerical force-displacement behaviour [50]

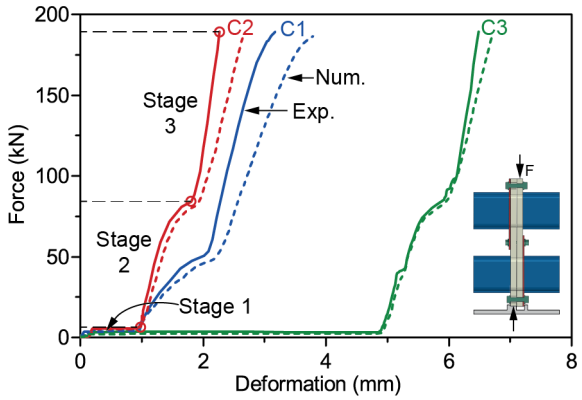

Figure 2.19. Type B (VH) – Numerical (Num.) and experimental (Exp.) force-displacement behaviour [33]

The presence of three clear stages in the F-d behaviour differs from the results of Styles et al. [50]. According to Gunawardena [33] the first stage has low stiffness and corresponds with slip continuing until half the bolt hole tolerance is taken up, and the bolt contacts the edge of the first steel plate. The second stage corresponds with combined slip and bearing of the bolts. The third stage corresponds with combined bearing and shear for all components. Looking at the F-d plot, the first stage ends at a deformation of 1 mm for C1 and C2, and 5 mm for C3, corresponding with half of the bolt hole tolerance. For each connection the first stage is shown to have very low stiffness (Figure 2.19) which may be caused by a relatively small preload in the bolts or a small friction coefficient for the faying surfaces. To simplify the experimental study, the force was applied to engage only the two main faying surfaces associated with the interface between the two thicker plates as illustrated in Figure 2.19. As shown the loading arrangement is offset by one plate thickness (25 mm), resulting in the combination of the applied shear force with a small bending moment. The numerical simulation, completed using ANSYS, was based on the experiment setup. The bolt preloads are noted to be 31.8 and 59.2

kN for the M12 and M16 bolts respectively, however limited information is presented on the numerical method.

2.2.4.3 Type C (VH5)

The Type C connection is based on the work of Chen et al. [57] and represents a complex bolted IMC with the horizontal and vertical connectivity provided by separate components within the connection. Horizontal connection is provided by a plug-in component, and vertical connection is provided by bolts through the floor and ceiling beams. The connection detail is illustrated in Table 2.11 (p.32), and further details are given by Chen et al. [57]. Experimental lateral F-d plots are presented for static monotonic loading (SC1, SC2) and quasi-static cyclic loading (QSC1-QSC4) in Figure 2.20 and Figure 2.21, respectively.

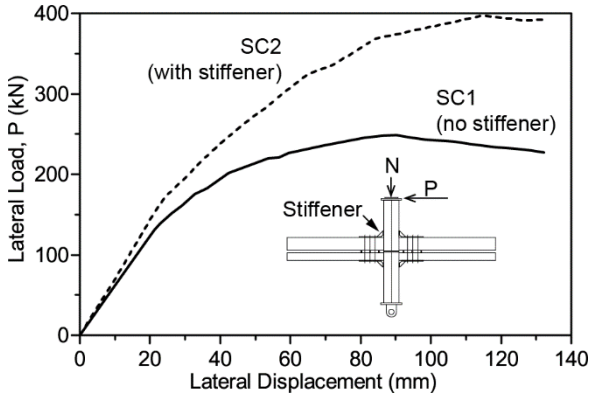

Figure 2.20. Type C – Force-displacement plot for static monotonic loading [57]

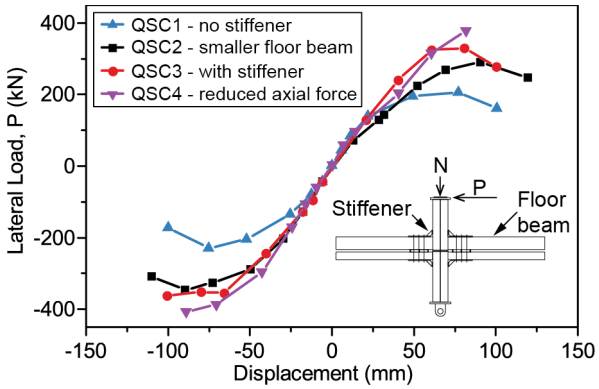

Figure 2.21. Type C – Force-displacement plot for quasi-static cyclic loading [57]

The loading includes a combination of axial and lateral loads as can be seen in the photo included in Table 2.10 (p.31). Values of 0.2 and 0.1 were adopted for the ratio of the applied axial load to the design compression strength of the column section. For the static monotonic loading, the SC1 and SC2 details differed due to the presence of the stiffeners in the case of SC2. The stiffener detail can be seen in the top right of the illustration in Table 2.11 (p.32). For the quasi-static cyclic loading, the details differed in terms of the floor beam size, inclusion

of stiffeners, and the axial force ratio. The total lateral displacement is a combination of the displacements resulting from column flexural rotation, gap opening at the joint, beam bending, and deformation of the panel zone at the module joint [57]. In the case of SC1, which does not have diagonal stiffeners, Chen et al. [57] report that the assumption of a pinned joint at the IMC is applicable. In contrast, if stiffeners are provided then greater lateral capacity is available because load is better transferred through the overall assembled joint [57]. In this case, the assumption of a pin joint would be conservative [57].

2.2.5 Estimation and comparison of structural behaviours

2.2.5.1 Shear force-displacement behaviour

For traditional bolted steel connections using high-strength bolts the shear force-displacement (F-d) behaviour can be described by a four stage model as illustrated in Figure 2.22 [145]. In the first stage (OA), the shear force is transferred by friction between the plates (Figure 2.22b). The slip load (F_{slip}), which is first reached at point A, is determined based on the relevant bolt preload and friction coefficient. Heistermann et al. [149] provide a summary of the calculation of slip load according to EN1993-1-8 [136] and the "*Specification for Structural Joints Using High-Strength Bolts*" [138]. In comparison, the Australian Standard AS 4100 [139] adopts a similar approach with the slip load of a single friction-type connection bolt given as

$$F_{slip} = V_{sf} = \mu n_{ei} N_t k_h , \tag{2.1}$$

where μ is the slip factor, n_{ei} is the number of effective interfaces, N_t is the minimum bolt installation tension, and k_h is a factor allowing for the type of hole [139].

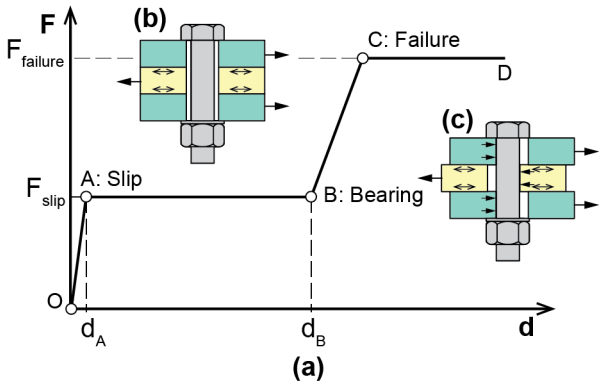

Figure 2.22. (a) Simplified four stage model of shear force-displacement of traditional bolted connections, (b) initial load transfer by friction between plates, and (c) bolt confined at B [145]

The slip factor may be established using the standard test method given in Appendix J of AS4100 [139] or alternatively the method given in Annex G of EN 1090-2 [150]. The point of slip is defined as occurring at a certain small relative displacement between the plates; 0.15 mm following EN 1090-2 or 0.13 mm following AS4100. Alternatively, if there is a sudden

slip or peak load at a smaller relative displacement this is taken as the point of slip. Therefore, the displacement at point A (d_A) is a small value less than or equal to 0.15 mm. For example, Shi et al. [145] recommend a value of 0.06 mm based on numerical analysis of a single bolt in shear.

In the second stage (AB) the friction is exceeded and the connection slips, until the bolt shank comes into contact with the plates at point B (Figure 2.22c). The displacement at point B (d_B) is typically taken as equal to the bolt hole tolerance (d_{tol}) which is defined as the difference between the bolt diameter and hole diameter. Alternatively, Shi et al. [145] suggested that d_B can be more precisely estimated as 0.925 times d_{tol}.. This is because elongation of the plate in the applied load direction is accompanied by a corresponding reduction in the width perpendicular to the applied load. As a result, the hole becomes elliptical while the bolt shank remains circular, leading to earlier contact between the bolt and the plate.

In the third stage (BC) the bolt is effectively confined and the connection stiffness is calculated allowing for each component bolt and plate stiffness. In this thesis, the method of Konkong et al. [151] is adopted. The failure point C, representing the ultimate shear capacity of the connection, is calculated based on the applicable standard, for example AS 4100 [139] or EN 1993-1-8 [136]. The factored ultimate strength is adopted for design to ensure the failure point falls below the actual F-d curve.

For inter-module connections (IMCs), Gunawardena [33] shows the initial slip stiffness may be given by

$$K_{slip} = \frac{F_{slip}}{d_{tol}}, \tag{2.2}$$

where F_{slip} is the slip resistance, and d_{tol} is the difference between the bolt diameter and hole diameter. This leads to an alternate three stage model for the shear force-displacement (F-d) behaviour of IMCs as illustrated in Figure 2.23. In this model the two stage stick-slip behaviour is replaced by a single stage (OP) with a stiffness calculated as shown in Equation (2.2).

As noted previously, the second stage (PQ) stiffness is calculated allowing for each component bolt and plate stiffness. The method of Konkong et al. [151] is adopted in this thesis. For example, considering the Type A (VC) connection the stage 2 (PQ) stiffness in the Y-direction is estimated based on the model illustrated in Figure 2.24. Figure 2.24(a) shows a section through the end plate connection, and Figure 2.24(b) shows a plan view of the end plates. For convenience of the illustration the connection is divided in half. Figure 2.24(c) shows the combined spring model. Following the Konkong et al. [151] method the overall effective stiffness is determined by assembling the relevant bolt and plate stiffness components. Twelve

component stiffness values are defined. k_1, k_3, k_4, k_6, k_7, k_9, k_{10}, and k_{12} refer to the stiffness of plate segments, and k_2, k_5, k_8, and k_{11} represent the bolt-plate interaction stiffness (Figure 2.24). The elastic modulus, shear modulus and Poisson's ratio for the plate and bolt steel materials are taken to be 200 GPa, 80 GPa and 0.3, respectively.

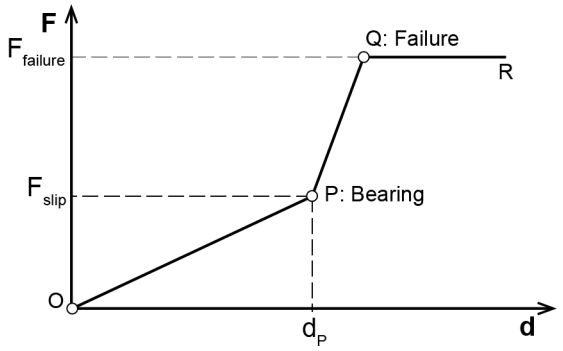

Figure 2.23. Simplified three stage model of shear force-displacement for inter-module connections

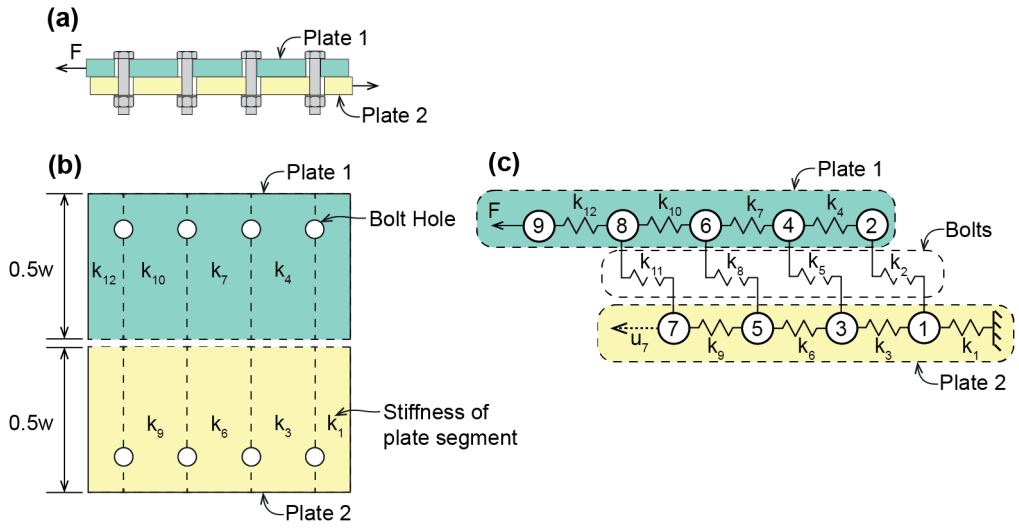

Figure 2.24. Model for the calculation of stage 2 shear stiffness of the Type A (VC) connection loaded in the Y-direction

Following the above three stage model (Figure 2.23), the stage 1 (OP) and stage 2 (PQ) stiffness values are calculated for the Type A and Type B connections as shown in Figures 2.25 to 2.27. Table 2.12 gives the stage 1 (K_{OP}) and stage 2 (K_{PQ}) calculated stiffness values and related parameters, which are defined using notation consistent with Equation (2.1). For the Type A (VC) connection the three stage simplified model matches the general profile from the numerical results. This is illustrated in Figure 2.25 which shows the model behaviour calculated in the present study (c and d) along with the numerical data reproduced from the referenced paper (a and b). For the first stage (OP), the theoretical estimate matches the numerical stiffness very well for the X-direction, but overestimates the stiffness for the Y-

direction. The numerical model is able to capture differences in load distribution through the connection which may have resulted in the different stiffness for the two directions. The effects of the load distribution on the connection stiffness are not considered by the simple theoretical model. The theoretical calculation also underestimates the displacement at point P. This occurs because the theoretical model assumes the displacement at point P is equal to the bolt tolerance, ignoring the possibility of local deformation of the plate around the bolt hole. For the second stage (PQ) the theoretical calculation again overestimates stiffness. The theoretical calculation of the second stage stiffness assumes that the load is applied at each end of the plate, as shown in Figure 2.24. In reality the shear force is applied to the plate by the column section. This results in a different distribution of the load in the actual connection, and ultimately a different overall connection stiffness. The numerical model is able to more accurately capture this behaviour. It is understood that this is the cause of the theoretical model overestimating the stage 2 stiffness.

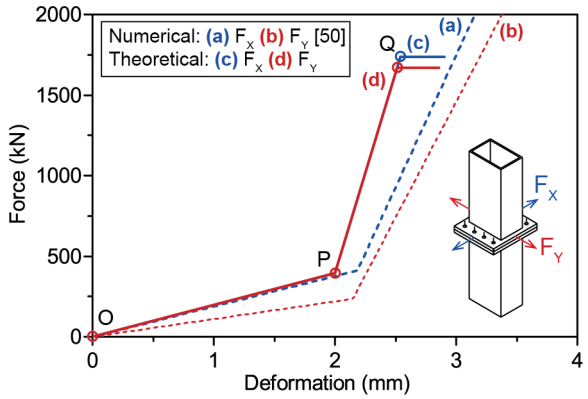

Figure 2.25. Type A (VC) – Comparison of calculated theoretical shear behaviour with numerical data [50]

Table 2.12. Parameters for calculation of theoretical shear stiffness

Type	Sub-Type	μ	n_{ei}	n_{bolts}	N_t [kN]	k_h	F_{slip} [kN]	d_{tol} [mm]	K_{OP} [x10^4 N/mm]	K_{PQ} [x10^4 N/mm]
A	HC	0.2	1	6	247.1	1	296.52	2	14.8	215
A	VC	0.2	1	8	247.1	1	395.36	2	19.8	248
B	C1	0.2	1	4	31.8	1	25.44	2	1.27	9.80
B	C2	0.2	1	4	59.2	1	47.36	2	2.37	27.6
B	C3	0.2	1	4	59.2	0.85	40.256	6	0.671	27.5

Considering the Type A (HC) connection the calculated theoretical shear stiffness (b and c) is shown in Figure 2.26 along with the numerical data reproduced from the referenced paper (a). In this case, numerical results are available for only one direction, F_z. As discussed in Section 2.2.4.1 (p.32), the numerical data (a) shows three clear stages. The first stage is associated with

initial slip of the bolted connection and is followed by an increased stiffness in the second stage as the bolts start to bear on the plate hole edges. The stiffness then reduces in the third stage due to yielding of the connection elements. The simplified theoretical calculation overestimates the stage 2 (PQ) stiffness due to the load path assumed by the theoretical model as discussed previously. For stage 1 (OP) the stiffness is also overestimated due to an overestimate of the slip load. As given in Table 2.12, the theoretical calculation of the slip load is based on a friction coefficient of 0.2 and a bolt preload of 247 kN. The preload value is given in the referenced paper [50]. The very low value of the slip load, and hence stiffness, displayed by the numerical results in comparison with the theoretical behaviour cannot be well explained by the existing theoretical model.

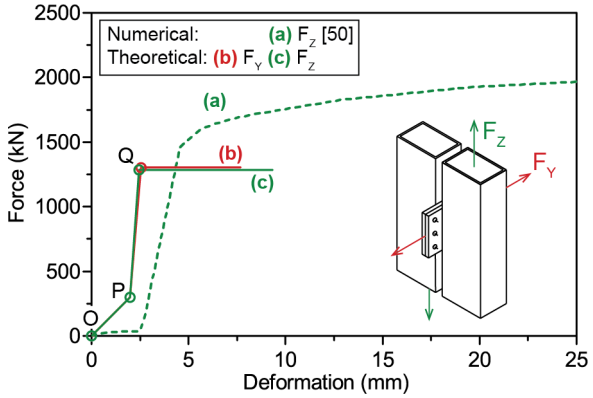

Figure 2.26. Type A (HC) – Comparison of calculated theoretical shear behaviour with numerical data [50]

In the case of connection Type B, the stage 2 shear stiffness calculated using the Konkong et al. [151] method gives a reasonable estimate when compared with the experimental and numerical results from the referenced paper (Figure 2.27). However, it is observed from Figure 2.27 that the initial stiffness cannot be calculated simply as described previously based on the estimated slip load. Instead, the plot shows low initial stiffness up to approximately (1 mm, 4 kN), (1 mm, 6.5 kN) and (5 mm, 3.5 kN) for C1, C2, and C3 respectively based on the numerical results. The slip load calculated using AS4100 does not match the numerical analysis well and the cause of the low initial stiffness is unclear. The bolt preloads were noted as 31.8 kN and 59.2 kN for the M12 and M16 bolts, respectively, with a slip factor of 0.2 assumed. Details regarding the measurement of bolt preload or slip factor for the experimental study are not provided. It remains possible that the low initial stiffness is the result of a relatively small actual bolt preload or slip factor for the faying surfaces. Overall, the simplified three stage model of shear force-displacement matches the numerical and experimental data for the selected existing connections better than the four stage model. This is because the selected connections had relatively low initial stiffness, for reasons as discussed previously.

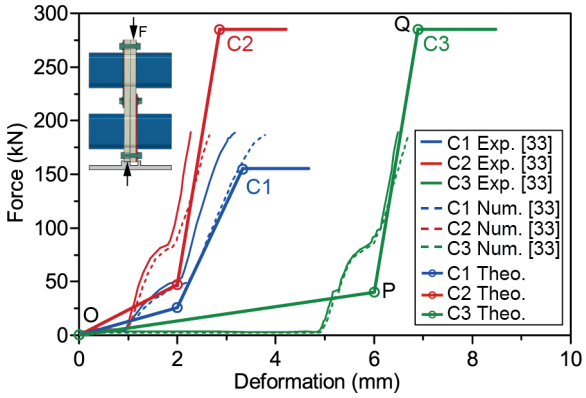

Figure 2.27. Type B – Comparison of calculated theoretical shear behaviour (Theo.) with experimental (Exp.) and numerical (Num.) data [33]

2.2.5.2 Axial force-displacement behaviour

For the ultimate tension resistance of a connection bolted on two sides, a modified T-stub method was proposed by Birkemoe et al. [152] and later recommended by Packer et al. [153] based on testing completed by Mang [154], Kato et al. [155] and Packer et al. [156] as documented by Willibald et al. [157] and Willibald [158]. An explanation can be found in *CIDECT Design Guide 3* [159, 160]. The tension stiffness can be estimated following EN 1993-1-8 [136] which gives stiffness coefficients based on elastic deformation of a T-stub model as derived by Weynand et al. [161]. The stiffness coefficients are defined such that

$$F = E.k.d \ , \tag{2.3}$$

where F is the applied force, E is the elastic modulus taken as equal to 200 GPa, k is the stiffness coefficient and d is the displacement. Stiffness coefficients are given separately for the bolts and plate, and are combined together to estimate the overall stiffness.

The end plate stiffness coefficient is given as

$$k_p = \frac{l_{eff.ini} t_p^3}{m^3} = \frac{0.9 l_{eff} t_p^3}{m^3} \ , \tag{2.4}$$

where l_{eff} is an effective length selected considering possible yield line patterns, t_p is the plate thickness, and m is the distance between the bolt centreline and the location of the uplift applied by the hollow steel section flange allowing for the weld size. The bolt stiffness coefficient is given as

$$k_b = \frac{1.6 A_s}{L_b} \ , \tag{2.5}$$

where L_b is the effective bolt length taken as the grip length plus half of the nut and bolt head height and A_s is the tensile stress area of the bolt.

However, the EN 1993-1-8 formulae are known to overestimate the stiffness when applied directly to the connection of hollow steel sections (HSS) [148]. In the case of hollow sections the load is transferred to the end plate by the welds, which results in rotation and vertical displacement of the end plate [148]. This is better considered by the Karlsen method which is based on a beam strip model for the end plate as shown in Figure 2.28 [148]. The stiffness coefficient for the end plate bending is given as

$$k_p = \frac{2\left(3a + 3m\alpha + n\alpha\right) l_{eff,ini} t_p^3}{m^2\left(3m^2\alpha + 4nm\alpha + 12am + 12an\right)}, \tag{2.6}$$

where the dimensions a, m and n are as illustrated in Figure 2.28, $l_{eff,ini}$ is the initial effective length calculated as $l_{eff,ini} = \frac{13 l_{eff}}{15}$, and α is a factor allowing for the potential local increase in stiffness of the end plate due to restraint by the HSS. The value of α is typically assumed to be 1.0 and the distance a is generally taken to be half the HSS width plus $0.8t_w$ where t_w is the weld leg length, which may be given as $\sqrt{2}t_t$ assuming an equal leg length fillet weld with throat thickness t_t [162]. Similarly, the stiffness coefficient for the bolts in tension is given as

$$k_b = \frac{4n\left(3a + 3m\alpha + n\alpha\right)}{\left(6am + 6an + 3m^2\alpha + 2n^2\alpha + 6nm\alpha\right)} \frac{A_b}{L_b}, \tag{2.7}$$

where L_b is the effective bolt length and A_b is the tensile stress area of the bolt.

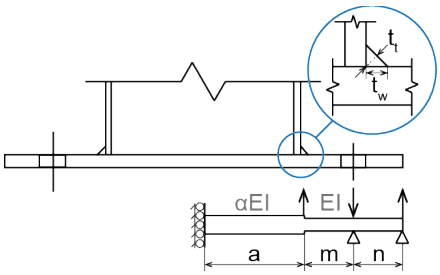

Figure 2.28. Model of half end plate strip [148]

For the Type A (VC) connection the calculated tension stiffness values are illustrated in Figure 2.29. Similarly, the calculated tension stiffness values for Type A (HC) are shown in Figure 2.30. Both figures show that the Eurocode and Karlsen formulae significantly overestimate the initial stiffness. The accuracy of the Karlsen formula has previously been demonstrated in the works by Karlsen [163] and Egeland et al. [162]. The suitability of these formulae for estimating the bolted connection stiffness is therefore not in doubt. It is understood that the estimated theoretical stiffness as illustrated in the figures is overestimated because only the stiffness of the IMC is included. Additional flexibility is introduced by the hollow section column, which should also be accounted for when calculating the overall stiffness of the inter-module joint.

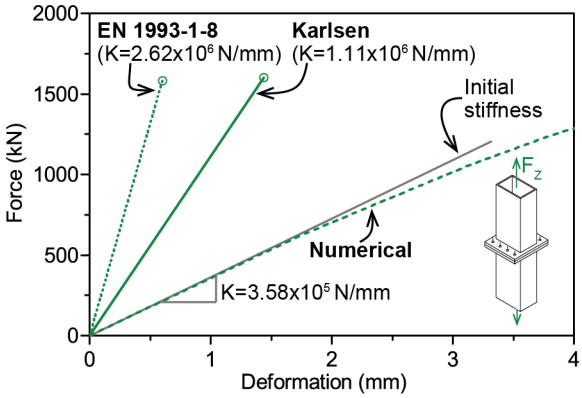

Figure 2.29. Comparison of calculated theoretical tension behaviour with numerical data for Type A (VC) [50]

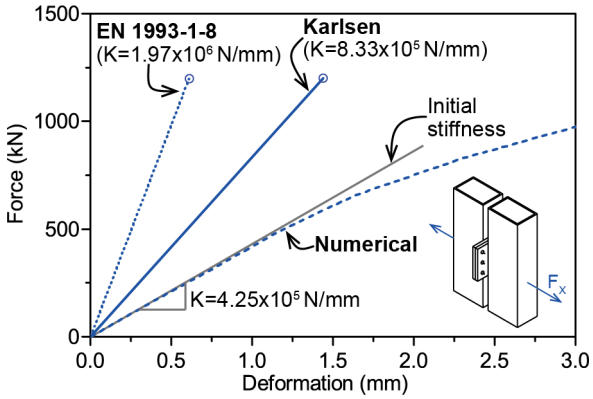

Figure 2.30. Comparison of calculated theoretical tension behaviour with numerical data for Type A (HC) [50]

The Karlsen formula can be recommended for estimating the tension stiffness of bolted end plate connections between hollow steel section columns. In this case the Karlsen formula is more suitable than the Eurocode because the end plate behaviour is more accurately modelled by the beam strip model. For inter-module joints, where the column stiffness is combined with the connection stiffness, then the theoretical calculation must be adjusted to include the column stiffness.

2.2.5.3 Moment-rotation behaviour

According to EN 1993-1-8 [136], joints may be classified as simple, continuous, or semi-continuous [136]. Simple joints do not transfer bending moments, and may be considered pinned [136]. Continuous joints are effectively rigid with full strength, such that the joint behaviour does not have a significant effect [136]. In contrast, semi-continuous joints are only semi-rigid or have partial strength such that the moment-rotation behaviour of the joint should be considered in the overall structure analysis [136]. For modular buildings, some studies report that a pin connection was used in design due to a lack of knowledge [57]. The assumption of a nominally pinned connection may not reflect the actual behaviour. The

distribution of load through the structure is affected by the joint behaviour. Design based on an incorrectly assumed joint behaviour is therefore not guaranteed to be conservative. It is therefore useful to examine the actual moment-rotation behaviour of existing joint details presented in the literature.

The moment capacity of a bolted flange plate connecting hollow steel sections (HSS) may be determined following the method given in EN 1993-1-8, as described by Steige et al. [164] for two-sided and four-sided splice connections. Alternatively, Wheeler et al. [165] present a method to calculate the moment resistance for a two-sided splice connection with two bolt rows. The stiffness may be estimated following EN 1993-1-8 and Weynand et al. [161] provide a summary of the procedure in the case of open steel sections. The general moment-rotation behaviour is typically defined either as tri-linear (Figure 2.31) or bi-linear, although any moment-rotation curve profile may be adopted provided it falls below the actual moment-rotation curve [136].

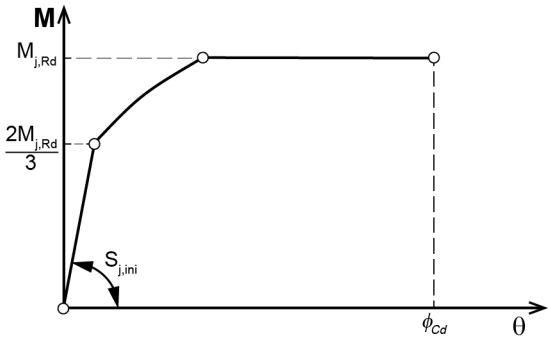

Figure 2.31. Model moment-rotation behaviour [136, 166]

Styles et al. [50] present the M-θ behaviour for the x- and y-axis rotations of the Type A (HC) connection. For the x- and y-direction rotations the connection is shown to have significant moment resistance [50], with the moment resistance of the connection exceeding that of the column section in each case. For rotation about the y-axis, the moment resistance is shown to be increased by contact between the columns below the connecting plates, which has the effect of increasing the bolt lever arm. This means that the moment capacity cannot be calculated using existing models such as EN 1993-1-8 and, further, that the length and end restraint of the column section may affect the results of numerical analysis. For rotation about the Y-axis a simple estimate of the stiffness can be obtained using EN 1993-1-8 by assuming the compression force is located at the lower plate edge. Figure 2.32 shows that a reasonable estimate of the initial stiffness is obtained in this way, however, the ultimate moment capacity is significantly underestimated in this case. The theoretical moment-rotation behaviour for rotation about the X-axis is not given due to the lack of a suitable model for torsional stiffness in the standards.

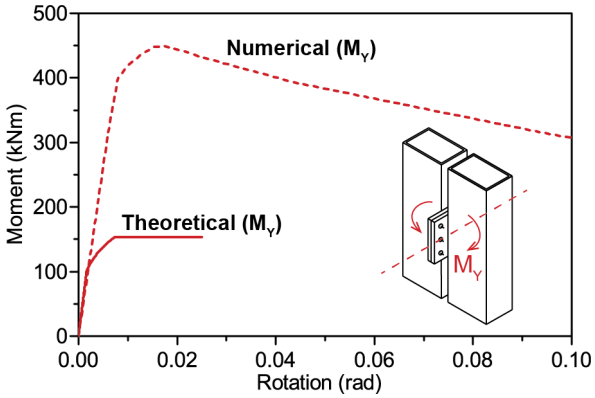

Figure 2.32. Comparison of calculated theoretical moment-rotation behaviour with numerical data for Type A (HC) [50]

Styles et al. [50] do not present data for the Type A (VC) connection. However, Sultana et al. [135] completed finite element modelling for a similar end plate splice connection and compared it with the experimental results published by Wheeler et al. [165]. The connection detail adopted a 150x150x9 SHS with four M20 high strength bolts as shown in Figure 2.33. Figure 2.34 shows the theoretical M-θ behaviour calculated by the EN 1993-1-8 formula. When compared with the numerical results it can be seen that the theoretical formula gives a reasonable estimate of the initial stiffness.

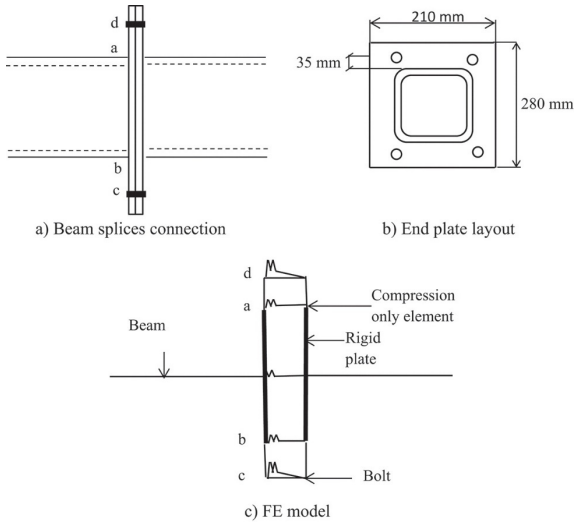

Figure 2.33. Beam splice end plate connection [135]

2.2.5.4 Combined actions and bidirectional loading

Most existing studies of IMCs are limited to a single loading action and do not consider combined actions. As noted in Section 2.2.4.3, one exception is the study by Chen et al. [57] where the lateral loading was combined with axial loading. Ratios of 0.2 and 0.1 were adopted for the ratio of the applied axial load to the design compression strength of the column section. The effect of the axial loading was not established, however, partly due to the small axial

loading adopted [57]. In this study the combined axial and lateral loading gives a combination of axial force, shear force and bending moment in the IMC. The application of axial loading to the column may affect the shear force-displacement behaviour of an end plate connection by varying the relevant normal force for the calculation of the slip load.

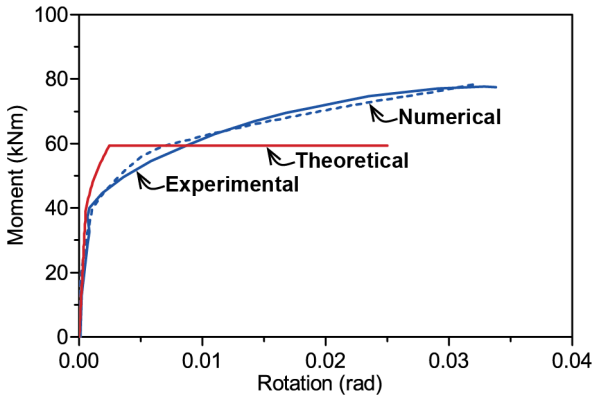

Figure 2.34. Comparison of experimental [165], numerical [135], and theoretical [136] moment-rotation behaviour

Gunawardena et al. [20] modelled a ten storey case study building, and completed the numerical analysis using the software RUAUMOKO-3D [167]. While the subject of bidirectional loading was not directly discussed an excerpt of the RUAUMOKO-3D input file is presented in an appendix to the paper [20], in which the details are given for the inter-module connection properties as modelled. It is apparent that the interaction surface between shear yield forces for the two plan directions was modelled by the equation

$$\left\{\frac{F_z^*}{F_{Y,z}^*}\right\}^{\alpha} + \left\{\frac{F_y^*}{F_{Y,y}^*}\right\}^{\alpha} = 1.0\,, \tag{2.8}$$

where F_z^* and F_y^* are the applied shear forces, $F_{Y,z}^*$ and $F_{Y,y}^*$ are the relevant shear yield forces, and $\alpha = 1$. Similarly, it is apparent that the surface between yield moments was modelled by the equation [167]

$$\left\{\frac{M_z^*}{M_{Y,z}^*}\right\}^{\beta} + \left\{\frac{M_y^*}{M_{Y,y}^*}\right\}^{\beta} = 1.0\,, \tag{2.9}$$

where M_z^* and M_y^* are the applied moments, $M_{Y,z}^*$ and $M_{Y,y}^*$ are the relevant yield moments, and $\beta = 2$ giving an elliptical failure surface. Further investigation is required to verify the validity of these formula in the case of inter-module connections.

2.2.6 Summary

This section (§2.2) presented an overview of the stiffness properties of bolted inter-module connections in modular steel buildings. The existing theoretical models were evaluated

through the detailed review of three specific connections. The main findings are summarised as follows.

1. For the shear stiffness, two different theoretical models were identified from the literature, one having four stages with relatively high initial stiffness, and the other having three stages with lesser initial stiffness. The three stage model offered the better fit, due to the relatively low initial stiffness of the selected connections, and was adopted for the theoretical calculation of stiffness. Overall, it was found that the inter-module connection shear stiffness could not be estimated accurately, especially the initial slip stiffness.

2. For the bolted end plate connection between hollow sections, the Karlsen method [148, 163] gave the better estimate of the inter-module connection tensile stiffness as compared with the formulae given in the Eurocode EN1993-1-8 . In order to calculate the effective stiffness of the joint, other structural elements such as the column section should be also considered, otherwise the stiffness may be significantly overestimated.

3. For the moment-rotation behaviour there is very limited published data specific to modular buildings. However, the initial stiffness of an end plate HSS splice connection was estimated using the existing theoretical methods [168]. It should be noted, however, that the existing theoretical formulae for strength and stiffness, such as given in EN1993-1-8, do not account for the contact between adjacent columns which may significantly affect the behaviour of the joint.

4. Most of the existing studies consider a single load action and do not consider combined actions. In cases where combined actions have been applied it is difficult to separate the response into individual components. In other cases, a single design action is assessed, although the experimental method results in a combined loading.

Finally, further research into the structural behaviour of inter-module connections is recommended to improve understanding of the structural behaviour and enable development of appropriate theoretical models. Specific consideration should be given to combined actions and the development of suitable experimental methods.

Chapter 3 Structural response of a modular steel building[1]

3.1 Introduction

In Section 2.2 it was found that the existing theoretical models were unable to estimate the structural behaviours of the inter-module connections (IMCs) accurately. In this chapter, the consequences of inaccurate IMC behaviours is examined in terms of the global building responses. That is, the primary objective of this chapter is to investigate the effect of the local IMC behaviours on the overall building response, in order to guide future development of the connection designs and associated analysis models. To achieve the primary objective, this chapter develops a numerical modelling technique in which the force-displacement (F-d) and moment-rotation (M-θ) behaviours of the IMCs are simplified using basic bi-linear and tri-linear models, respectively. A numerical model is prepared for the building previously studied by Styles et al. [50]. In this way, the application of the bi-linear and tri-linear models is demonstrated, and the limitations of these simplified models is illustrated. Despite the limitations of the simplified models, the overall behaviour of the present numerical model is verified by matching the maximum inter-storey drift with the previous study [50]. The verified numerical modelling technique is then extended to a selected six storey case study building, and the effect of the IMC stiffness is studied.

In Section 2.1, through the broad literature review, it was identified that, in Australia, despite the development of some general design guides [117], there are no specific standards for modular buildings, or the components from which they are assembled. Moreover, that there are few published studies on the structural responses of modular buildings to lateral loads. Further study was suggested, for example, on modular buildings subjected to cyclonic wind loads, and the design based on dynamic wind and earthquake loading. As a result of the lack of published studies, there is limited structural performance data for the overall behaviour of modular buildings [3], which in turn impedes the development of appropriate design standards. Therefore, the second objective of this chapter is to investigate the structural response of a selected case study building, thereby generating structural performance data which may, in combination with other studies, contribute to the development of modular building design standards.

[1] The related work in Chapter 3 was published in Engineering Structures:

Lacey AW, Chen W, Hao H, Bi K. Effect of inter-module connection stiffness on structural response of a modular steel building subjected to wind and earthquake load. Eng Struct. 2020;213:110628. https://doi.org/10.1016/j.engstruct.2020.110628

To this end, the overall building response is determined based on design analyses with increasing level of sophistication. In the case of wind loading, the overall response of the case study building is determined based on the equivalent static analysis from the Australian standard AS/NZS 1170.2 [72], compared with the time history analysis using the simulated wind load time histories as inputs. For earthquake loading, the overall response is determined based on a static analysis following the Australian standard AS 1170.4 [74], in addition to a response spectrum analysis, and time history analysis. In this way, by comparing the design methods, a more complete understanding of the structural response of the case study building is developed, while the design procedures are compared.

3.2 Simplification of the inter-module connection behaviour

To develop the numerical modelling technique, a numerical model was built following the work of Styles et al. [50]. The structure was modelled with SAP2000 [169] using beam and column elements, with nonlinear links included to model the inter-module connections (IMCs). This model was used to demonstrate the simplification of the IMC behaviour for use in the overall structural analysis. Details of the three-dimensional moment resisting frame can be found in the referenced work [50]. The YZ plane view is shown in Figure 3.1, from which it can be seen that the modules were placed either side of a central corridor, and vertical inter-module connections (VCs) connected the modules stacked in the Z-direction. The horizontal inter-module connections (HCs), which connected the modules in the X-direction, are not visible in the YZ plane view. The HCs connected adjacent module columns, with one HC provided per module column. In the Y-direction, the modules were joined by the corridor beams, and the connection between the module column and the corridor beam was assumed to be pinned in the numerical model. The individual modules were 4 x 12 x 3.5 m high, and the overall structure was formed by stacking the modules to 11 storeys high (Figure 3.1), with 300 mm vertical space between the roof purlins and the floor joists. The modules had five 300 x 200 x 6 mm rectangular hollow steel section columns on each side. The primary floor beams were 200UB25 steel sections, and the primary roof beams were 200UB22 sections. The beam-to-column connections were semi-rigid, and a moment-resisting frame was formed by the beam and column assembly.

For the horizontal inter-module connection (HC, Figure 3.2), a tri-linear model was adopted for the moment-rotation (M-θ) behaviour following EN-1993-1-8 [136]. As shown in Figure 3.3(a), this model matched the published numerical data well for rotation about the 1-axis. In the present study, the local axes are referred to as the 1-, 2-, and 3-axis, as shown in Figure 3.2. In comparison, the local axes were defined as X, Y, and Z, in the referenced paper [50]. Further, in the present study, the rotation r1 refers to rotation about the 1-axis. In contrast, in

the referenced paper [50], the rotation rx referred to the rotation causing bending in the X-direction, i.e., rotation about the Y-axis. Hence, in Figure 3.3(a), the model for rotation of the HC about the 1-axis (hc-r1) is compared with the rotation in the y-direction [50] (hc-ry), and a reasonable match is shown. In the present study, the model developed for the rotation about the 1-axis was applied for the rotations about the 2- and 3-axis. As will be shown, this simplification allowed the overall structural behaviour to be matched with the previous study [50]. However, this simplification does not capture the large moment capacity for rotation in the x-direction (hc-rx, Figure 3.3a) which was caused by contact between adjacent module columns, i.e., the simplified behaviour was conservative.

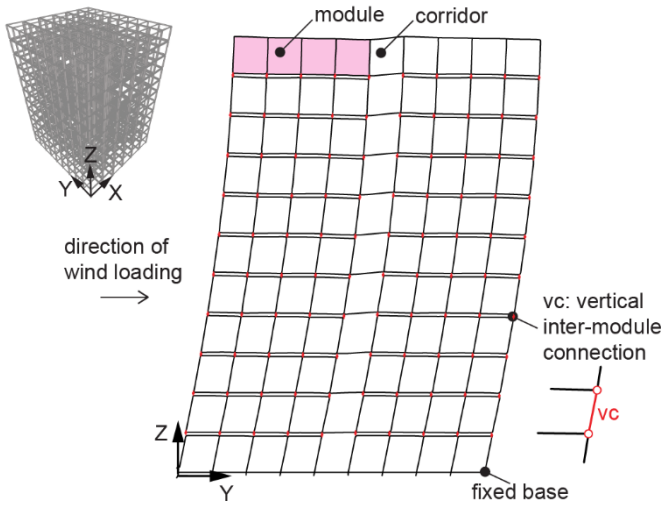

Figure 3.1. YZ plane view of moment resisting frame [50] showing lateral deformation due to wind loading

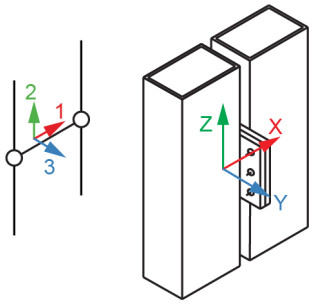

Figure 3.2. Horizontal inter-module connection (HC) adopted from Styles et al. [50]

A bi-linear model (hc-u2) was adopted for the shear F-d behaviour of the HC, as shown in Figure 3.3(b). For the published shear behaviour (hc-uz), it was observed that the overall connection behaviour was not significantly affected by the initial friction/slip stage. The bi-linear model (hc-u2) was therefore proposed as shown in Figure 3.3(b), which gave a reasonable simplified approximation of the published behaviour [50] (hc-uz). The same bi-linear model was adopted for translational shear in the 3-direction (hc-u3). Similarly, a bi-linear model was adopted for the axial behaviour, as shown in Figure 3.3(c), assuming a linear

behaviour until the factored ultimate tension capacity (ϕN_t) was reached. The bi-linear model (hc-u1) was matched to the published behaviour for axial tension (hc-ux), and a similar behaviour was assumed for axial compression.

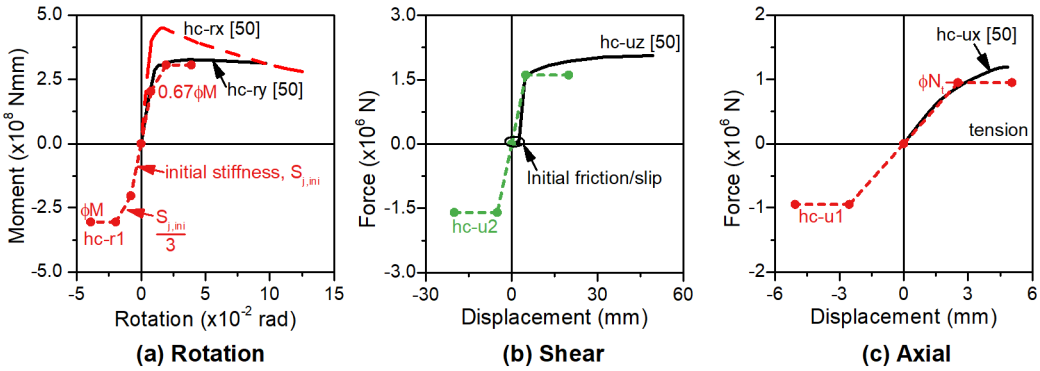

Figure 3.3. (a) Rotational, (b) translational (shear), and (c) translational (axial) simplified behaviour of the horizontal inter-module connection (HC) [50]

For the vertical inter-module connection (VC) (Figure 3.4), similar bi-linear and tri-linear behaviours were adopted for the F-d and M-θ behaviours, respectively. For the F-d behaviours (Figure 3.5(a)), the initial stiffness of the bi-linear model was selected following review of the published F-d curves [50]. The failure point was then determined by calculating the tension and shear capacities (ϕN_t and ϕV) of the connection as per the Australian standard AS 4100 [139]. For the M-θ behaviours, the tri-linear model was adopted as shown in Figure 3.5(b). In this case, there was no published data for comparison, and the initial stiffness was calculated based on a 300x200x6 RHS C350 steel column section which was 300 mm long and fixed at each end. That is, the pure bending stiffness was estimated as $\frac{EI}{L}$, where E is the elastic modulus, I is the moment of inertia, and L is the length of the column section [169]. For example, Figure 3.6 shows the axial, shear and pure bending springs in the 1-2 plane. It can be seen that the moment at j due to a unit rotation is affected by the pure bending spring and the shear spring. Hence, the pure bending stiffness was determined as

$$k_{r3} = \frac{4EI}{L} - \left(\frac{L}{2}\right)^2 \frac{12EI}{L^3} = \frac{EI}{L}, \tag{3.1}$$

where $\frac{4EI}{L}$ is the moment at j due to a unit rotation, and $\frac{12EI}{L^3}$ is the shear spring located at a distance of $\frac{L}{2}$ from j. Similarly, the torsion stiffness was estimated as $\frac{GJ}{L}$, where G is the shear modulus and J is the torsion constant of the column section. To complete the tri-linear model, the factored ultimate moment capacities (ϕM) were calculated based on the column section properties and the relevant capacity factor (ϕ) following AS 4100 [139]. Hence, the

rotational behaviours for the vertical inter-module connection were estimated based only on the column properties. The estimated rotational behaviours, therefore, were representative of a continuous module column, with a rigid inter-module connection. To verify the suitability of this simplification, the overall structural behaviour was matched with the previous study [50].

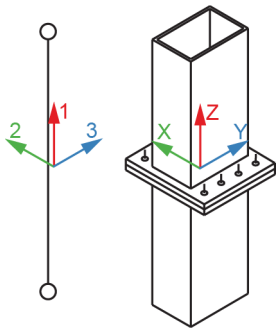

Figure 3.4. Vertical inter-module connection (VC) adopted from Styles et al. [50]

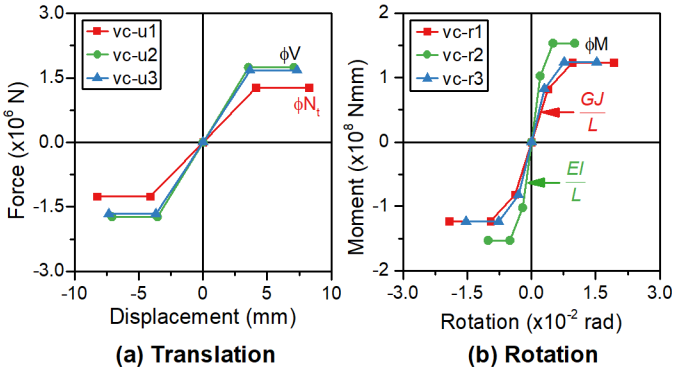

Figure 3.5. (a) Translational and (b) rotational simplified behaviour of the vertical inter-module connection (VC) [50]

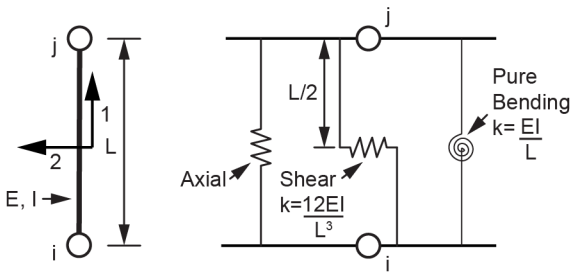

Figure 3.6. Axial, shear and bending stiffness in the 1-2 plane (adapted from [169])

To verify that the simplified models allowed a reasonable estimate of the overall structural behaviour, equivalent static wind loads were applied to the SAP2000 numerical model following the previous study [50]. The wind loads were calculated as per the Australian wind code [72], and were applied as area loads to the windward and leeward walls. The standard variation of the wind speed with height was considered, and a net pressure coefficient of 1.3

was adopted. The wind drift was assessed in the Y-direction, as shown in Figure 3.1, for comparison with the results of the previous study [50]. In the present study, the maximum inter-storey drift ratio resulting from the wind load was 0.68%. The value of 0.68% was within the range of 0.66 to 0.70% which was reported in the previous study, depending on the connection stiffness. The maximum inter-storey drift in the present study was affected by the F-d and M-θ behaviours adopted for the inter-module connections, and the intra-module connections, which were considered to be rigid in the present study. A reasonable match in the inter-storey drift value was achieved, and the simplified behaviour adopted for the inter-module connections was sufficient to capture the overall behaviour.

3.3 Numerical model of case study building

The case study building was based on a design developed for an apartment building to be located in the north west of Western Australia. It was six storeys tall, 21.15 m high, and had a layout where modules were positioned either side of a central corridor. A simplified numerical model was developed which had overall plan dimensions of 30.3 x 26.29 m including the 2.5 m wide central corridor, as shown in Figure 3.7(a). Following the numerical modelling technique developed in Section 3.2, numerical models were built using SAP2000, and frame elements were used for the structure of the module. A rigid behaviour was assumed for the intra-module connections, which consisted of fully welded hollow section frames, except for the bracing elements, which had the end moments released. The vertical (VC) and horizontal (HC) inter-module connections were included as separate nonlinear link elements, as shown in Figure 3.7(b) and (c) respectively.

The individual modules were 4.95 x 11.885 x 2.95 m high, each with a mass of 26 t. The module structure consisted of a braced steel frame with a cross bracing layout in the long module dimension, and a chevron layout in the short dimension, as shown in Figure 3.7(d). The modules had five 150 mm square hollow steel section columns on each side, and the structure of a level 1 module is shown in Figure 3.8. For the level 1 modules, the mass of the structural elements included in the numerical model was approximately 10 t. To allow for the mass of the non-structural components, additional joint loads were included in the numerical model based on the tributary area, as shown in Figure 3.8. For the foundations, each level 1 module was restrained at each of the four main columns. Following the work of Annan [11] and Fathieh [32], the vertical and horizontal translations were restrained, however, rotations were permitted.

The structure of the corridor consisted of 150C24 joists at 450 mm centres. The joists were connected to the short edge beam of the module, and spanned between the modules. Figure

3.9 shows a typical detail for the connection of the corridor joists to the module beam. In comparison with the welded connections for the module frame, the corridor joist connection detail was considered to permit greater rotation. Hence, the corridor joist connections were pinned in the numerical model, i.e., moments were released at each end of the joist. An area load of 0.5 kPa was added to account for the additional mass of the 24 mm thick compressed fibre cement corridor flooring. The roof consisted of 70x70x3 SHS stubs which were connected to the top of the upper modules, and supported C20a steel channels which spanned in the long module dimension. Purlins, which spanned between the steel channel beams, were not included in the structural model. An area load of 0.15 kPa was added to the roof to account for the additional mass of the purlins and the roof sheeting.

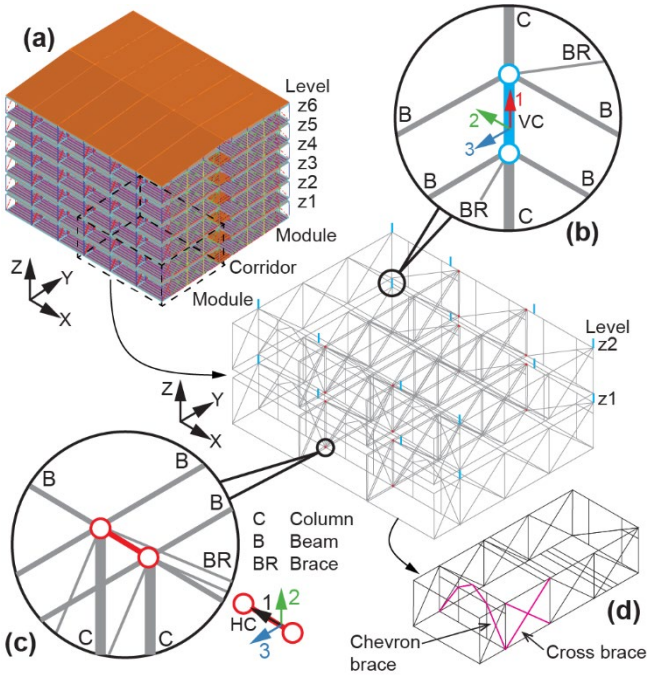

Figure 3.7. Case study building showing (a) overall numerical model, (b) vertical inter-module connection (VC), (c) horizontal inter-module connection (HC), and (d) individual module structure

The case study building presented in this chapter is a simplified version of the actual building design. The full proprietary details of the original design are withheld, and the analysis and corresponding discussions relate to the simplified building. This simplification does not, however, diminish the relevance of the results. The corridor layout adopted is a commonly used arrangement of the modules and practical examples include the apartment building in the Jinghai District of Tianjin Ziya circular economy park [170], and the student residence at Bond Street, Bristol [8]. Column supported braced steel modules are a common type of module construction (§2.1.2, p.5), which may also include container-like modules consisting of a steel frame and corrugated plate walls which are modelled by equivalent cross braces in the

structural analysis [171]. As will be shown in the following sections 3.3.1 to 3.3.3, the inter-module connection stiffness properties were derived from typical bolted connection details, which were similar to the connection details for the case study building, thereby ensuring the relevance.

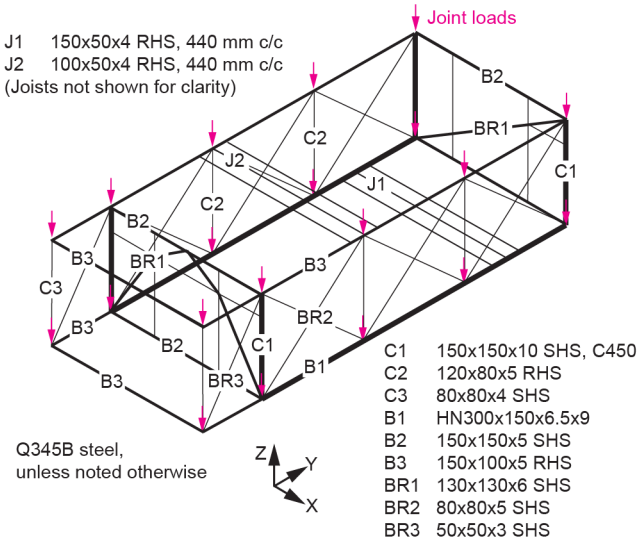

Figure 3.8. Individual module structure showing additional joint loads

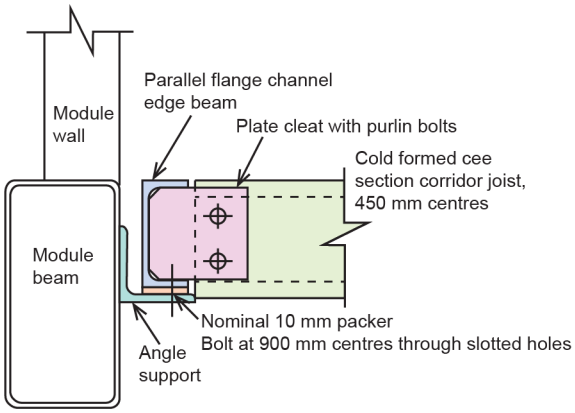

Figure 3.9. Typical detail showing connection of a corridor joist to a module beam

3.3.1 Initial stiffness

In the first simulation, the VC initial spring stiffness was calculated assuming the connection consisted of a prismatic beam (150x150x5 SHS) which was 575 mm long and fixed at each end. The 575 mm length refers to the vertical distance between the centreline of the roof beam, and that of the corresponding floor beam above. The resulting stiffness values and the corresponding equations are listed in Table 3.1. The 150x150x5 SHS had a cross-sectional area (A) of 2810 mm^2, a moment of inertia (I) of $9.70x10^6$ mm^4, a torsion constant (J) of $15.6x10^6$ mm^4 and an elastic modulus (E) and shear modulus (G) of $2x10^5$ MPa and $0.8x10^5$ MPa, respectively. Hence, the initial stiffness values adopted for the vertical inter-module

connection (IMC) were representative of a continuous module column, with a rigid IMC. This initial estimate of the stiffness was considered to be sufficient for the primary objective of the present study, which was to investigate the influence of the IMC stiffness on the overall building response. Hence, following the first simulation, the stiffness values were varied as described in Section 3.3.3. The secondary objective was to investigate the structural responses of a case study building. In this respect it should be acknowledged that the initial benchmark analyses represent the case of a rigid vertical IMC. The effect of the IMC stiffness on the overall structural behaviour is discussed in Section 3.6.4 (p.70).

Table 3.1. Initial stiffness of vertical inter-module connection (VC) in the numerical model of the benchmark case study building

Link DoF	Description	Equation	Value
u1	Axial	$EA \cdot L^{-1}$	9.8×10^5 N.mm^{-1}
u2	Shear	$12EI \cdot L^{-3}$	1.2×10^5 N.mm^{-1}
u3	Shear	$12EI \cdot L^{-3}$	1.2×10^5 N.mm^{-1}
r1	Torsion	$GJ \cdot L^{-1}$	2.2×10^9 N.mm.rad^{-1}
r2	Bending	$EI \cdot L^{-1}$	3.4×10^9 N.mm.rad^{-1}
r3	Bending	$EI \cdot L^{-1}$	3.4×10^9 N.mm.rad^{-1}

The HC was a bolted connection similar to that in the work of Styles et al. [50]. Styles et al. [50] did not report the M-θ behaviour for rotation about the 2-axis, and the M-θ behaviour for rotation about the 3-axis was complicated by the contact between the adjacent columns. Therefore, an order of magnitude estimate of the initial spring stiffness was made based on the work of Styles et al. [50], and the same initial stiffness was adopted for r1, r2, and r3. This differs from the rotational stiffness for the VC, for which the initial stiffness was estimated based on the column section as shown in Table 3.1.

Table 3.2. Initial stiffness of horizontal inter-module connection (HC) in the numerical model of the benchmark case study building

Link DoF	Description	Value
u1	Axial	3.0×10^6 N.mm^{-1}
u2	Shear	5.4×10^6 N.mm^{-1}
u3	Shear	5.4×10^6 N.mm^{-1}
r1	Torsion	2.0×10^{10} N.mm.rad^{-1}
r2	Bending	2.0×10^{10} N.mm.rad^{-1}
r3	Bending	2.0×10^{10} N.mm.rad^{-1}

For the translational stiffness of the HC, the order of magnitude estimates were improved by applying the formula for the shear and tension stiffness of a bolted connection as presented by Gunawardena [33]. For example, the shear stiffness of the bolts was calculated as [33]

$$k_{bolt,shear} = \frac{GA}{L}, \tag{3.2}$$

where G is the shear modulus for the bolt material, A is the tensile stress area for the bolt, and L is the grip length which was taken as the combined thickness of the clamped plates. The resulting stiffness values are given in Table 3.2.

3.3.2 F-d and M-θ curves

For the nonlinear elastic analyses, multi-linear elastic relationships were defined for the nonlinear link elements in the SAP2000 model. For the VC, the ultimate capacities of the 150x150x5 SHS C450 section were determined following the Australian standard AS4100 [139]. Following Section 3.2, bi-linear and tri-linear relationships were adopted for the F-d and M-θ behaviours, respectively. For the F-d behaviours, the bi-linear behaviour had a constant initial stiffness until the factored ultimate capacity of the section was reached, as shown in Figure 3.10(a). For the rotational behaviours, the tri-linear behaviour was assembled following EN1993-1-8 [136]. The initial stiffness was maintained until the applied moment reached two thirds of the factored moment capacity. The stiffness was then reduced by a stiffness modification factor equal to 3. The stiffness was again held constant until the factored ultimate capacity was reached, as shown in Figure 3.10(b). The F-d and M-θ curves for the HCs were similarly constructed, as shown in Figure 3.10(c) and (d).

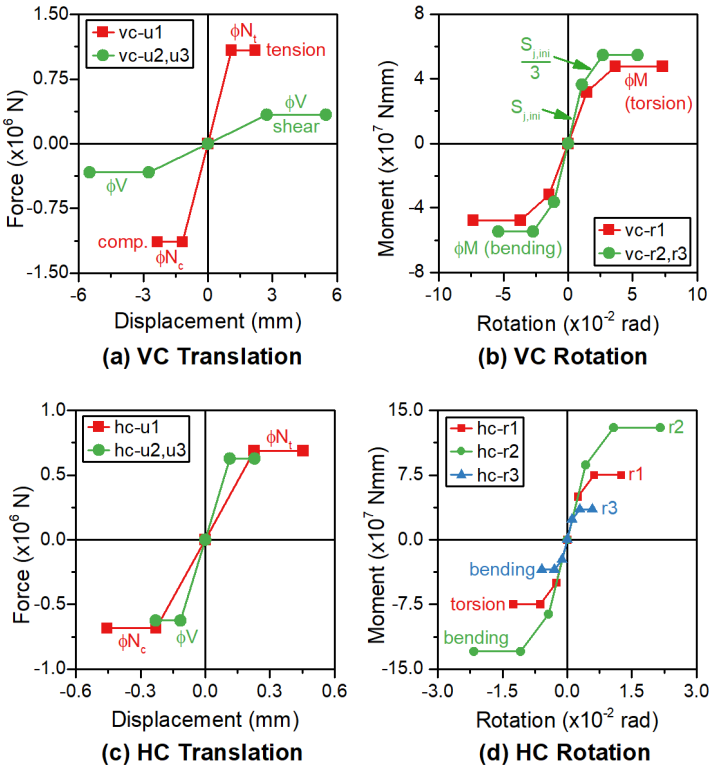

Figure 3.10. F-d and M-θ curves for the vertical (VC) and horizontal (HC) inter-module connections in the benchmark case study building analysis

3.3.3 Varying stiffness

The initial inter-module connection stiffness was varied in the numerical simulations to investigate the effect on the overall response of the case study building. The range of values considered are summarised in Table 3.3. For each initial stiffness, a corresponding F-d or M-θ curve was generated as described in Section 3.3.2. For example, Figure 3.11(a) shows the reducing initial stiffness in the 2-axis direction for the vertical inter-module connection (vc-u2). The benchmark (C6B) is labelled, which refers to the initial numerical model with the first estimate of the inter-module connection stiffness for the six storey case study building. The stiffness was then varied as shown. Figure 3.11(b) shows the corresponding change in the F-d behaviour with the reduced initial stiffness. Similarly, Figure 3.11(c) shows the change in the M-θ behaviour as the initial M-θ stiffness for vc-r2 was reduced to zero, to model the case of a pinned connection (C6E).

Table 3.3. Initial inter-module connection stiffness values for the case study building
Shaded cells highlight series of different stiffness values.

Ref	Vertical Connection (vc)				Horizontal Connection (hc)		
	u1 (N/mm)	u2, u3 (N/mm)	r1 (Nmm/rad)	r2, r3 (Nmm/rad)	u1 (N/mm)	u2, u3 (N/mm)	r1, r2, r3 (Nmm/rad)
C6A	1E20	1E20	1E20	1E20	3.0E6	5.4E6	2.0E10
C6B	9.8E5	1.2E5	2.2E9	3.4E9	3.0E6	5.4E6	2.0E10
C6J	9.8E5	1.2E5	2.2E9	1.7E9	3.0E6	5.4E6	2.0E10
C6C	9.8E5	1.2E5	2.2E9	0	3.0E6	5.4E6	2.0E10
C6D	9.8E5	6.1E4	2.2E9	0	3.0E6	5.4E6	2.0E10
C6E	9.8E5	3.1E4	2.2E9	0	3.0E6	5.4E6	2.0E10
C6G	9.8E5	1.5E4	2.2E9	0	3.0E6	5.4E6	2.0E10
C6H	9.8E5	7.5E3	2.2E9	0	3.0E6	5.4E6	2.0E10
C6I	9.8E5	3.8E3	2.2E9	0	3.0E6	5.4E6	2.0E10
C6F	9.8E5	1.0E3	2.2E9	0	3.0E6	5.4E6	2.0E10
C6M	9.8E5	1.2E5	2.2E9	3.4E9	3.0E6	5.4E6	1.0E20
C6N	9.8E5	1.2E5	2.2E9	3.4E9	3.0E6	5.4E6	1.0E9
C6O	9.8E5	1.2E5	2.2E9	3.4E9	3.0E6	5.4E6	1.0E6
C6P	9.8E5	1.2E5	2.2E9	3.4E9	3.0E6	5.4E6	0
C6Q	9.8E5	1.2E5	2.2E9	3.4E9	1.5E6	2.7E6	0
C6R	9.8E5	1.2E5	2.2E9	3.4E9	7.5E5	1.4E6	0
C6S	9.8E5	1.2E5	2.2E9	3.4E9	3.8E5	6.8E5	0
C6T	9.8E5	1.2E5	2.2E9	3.4E9	1.9E5	3.4E5	0
C6U	9.8E5	1.2E5	2.2E9	3.4E9	4.7E4	8.5E4	0
C6V	9.8E5	1.2E5	2.2E9	3.4E9	1.2E4	2.1E4	0

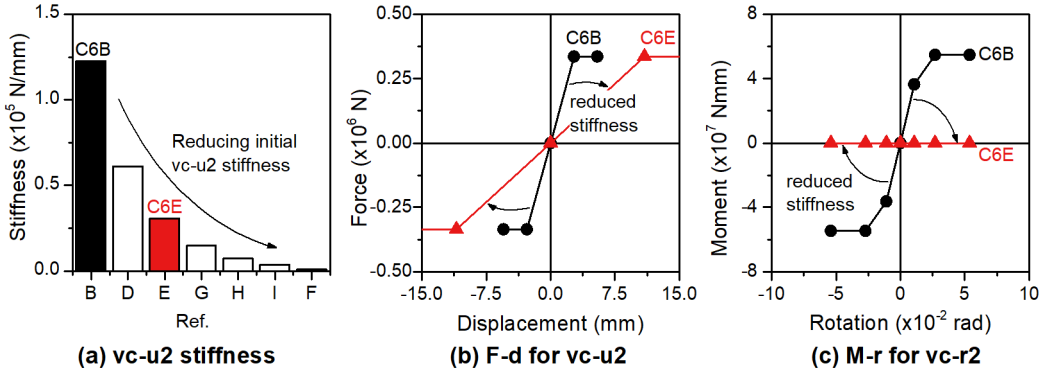

Figure 3.11. Varying stiffness of the vertical inter-module connection (VC): (a) Reducing initial stiffness in the 2-axis direction, (b) Corresponding change in F-d behaviour, and (c) Change in M-θ behaviour

C6B is the initial benchmark numerical model and C6E refers to the model with pinned connections.

3.3.4 Damping ratio

The damping ratio for the fundamental natural frequency of a steel building can be estimated by the empirical formula [172]

$$\zeta_1 = \frac{0.52}{H} + 320\frac{x_H}{H} + 0.0023\,, \tag{3.3}$$

where H is the building height, x_H is the tip displacement, and $\frac{x_H}{H} \le 2\times10^{-5}$ is the tip drift ratio. Overall recommended and standard damping values were given in tabular form by Tamura [82]. For example, in the case of steel buildings with the height less than 30 m, the standard values for the damping ratio, ζ_1, are 2.5% for habitability and 3% for the safety limit state in the elastic range. The damping properties can be estimated by full scale non-destructive testing. For example, Malo et al. [98] reported the dynamic properties of a 2x2 stack of prefabricated residential modules. The height of the modules was approximately 3 m, giving a total height of 6 m. The estimated damping percentage for the transverse mode associated with sway in the long module dimension was 3.2% based on the experimental modal analysis protocol, and 3.9% based on the system identification protocol [98]. It was, therefore, considered reasonable to adopt the standard damping ratio [82] of 3% for the safety limit state, and a constant modal damping of 3% was assumed for the wind time history analysis using SAP2000. For the earthquake response spectrum and time history analyses, however, a constant modal damping of 5% was adopted for consistency with the design standard [74].

3.4 Definition and analysis of wind action

The equivalent static wind load was determined using the Australian standard AS/NZS 1170.2 [72]. The building was to be located near the coast in the north west of Western Australia, a site location which has high design wind loads due to the occurrence of cyclones in the area.

For the ultimate limit state (ULS), the mean regional wind speed was determined as V_{1000}=93.5 m/s, based on the classification as Importance Level 3, Region D, and Terrain Category 2. For the serviceability limit state (SLS), the return period was taken to be 25 years, which gave a regional wind speed of V_{25}=53 m/s. The six storey case study building was divided into six height segments z1 to z6, and the design wind pressures were calculated following the standard [72], with equivalent joint loads applied in the numerical model based on the tributary area. The Deaves and Harris model [173] was adopted to define the mean wind speed profile; therefore, the wind pressures for z1 to z6 increased with height.

For comparison with the equivalent static wind load, the numerical analysis was also completed using simulated time varying wind loads. The fluctuating component of the wind velocity was simulated following the method of Amirinia et al. [174]. Turbulence spectra and spatial coherence were defined in the frequency domain, and the time histories were generated using an inverse Fourier transform. The fluctuating component of the wind velocity, $u_i(t)$, was combined with the mean component, $\overline{u}_i$, to give the total wind velocity, $U_i(t)$, as

$$U_i(t) = \overline{u}_i + u_i(t) . \tag{3.4}$$

The time varying nodal drag force, $F_i(t)$, was then defined as

$$F_i(t) = 0.5 C_D \rho A_i U_i^2(t) , \tag{3.5}$$

where A_i is the surface area, $\rho = 1.2$ kg/m^3 is the air density, and $C_D = 1.3$ is the drag coefficient. That is, the forces were calculated based on the total wind velocity and the relevant tributary area.

Wind data recorded for tropical cyclones show some differences in the turbulence spectra for cyclonic wind, in comparison with non-cyclonic wind [174]. The case study building was located in an area subjected to cyclonic wind; therefore, a cyclonic wind turbulence spectrum was required to simulate the wind velocity. Two different models were identified in the literature for the cyclonic turbulence spectrum. Hence, in the present study, a comparison is made between the results for each of cyclonic turbulence spectra, and a third spectrum, which was introduced to reflect neutral (non-cyclonic) conditions. First, the Kaimal et al. [175] spectrum was adopted for neutral conditions, which defined the power spectrum of the longitudinal wind velocity fluctuation as [176]

$$\frac{nS_{uu}(n)}{u_*^2} = \frac{200f}{(1+50f)^{\frac{5}{3}}} , \tag{3.6}$$

where n is the frequency, and $f = \frac{nz}{\overline{u}(z)}$ depending on the mean velocity, $\overline{u}(z)$, which varies

with height, z. Next, the Yu et al. [177] spectrum was used, which defines the spectrum for hurricanes at 10 m over land as

$$\frac{nS_{uu}}{u_*^2} = \frac{-0.9999f^2 + 3.112f + 1.159\times10^{-4}}{f^3 + 18.64f^2 + 1.188f + 3.35\times10^{-3}}. \tag{3.7}$$

The resulting spectrum shows higher energy at lower frequencies, in comparison to the spectrum for neutral conditions (Equation (3.6)). Finally, the Li et al. [178] spectrum was used, which has higher energy at higher frequencies, and defines the spectrum for the typhoon back eye-wall region as

$$\frac{nS_{uu}(n)}{\sigma_u^2} = \frac{16.66f}{1.72 + 237.24f^{5/3}}, \tag{3.8}$$

where σ_u is the standard deviation of the longitudinal fluctuating wind velocity. The correlation between the fluctuating wind at different points was considered in the vertical Z-direction, and the spatial coherence function was defined as [174]

$$\gamma_{ij}(n) = \exp\left[-\alpha\left(\frac{\Delta z}{z_m}\right)^c \sqrt{\left(\frac{n\Delta z}{\bar{u}_m}\right)^2 + (\beta\Delta z)^2}\right], \tag{3.9}$$

where i and j are two points along the building height separated by a distance Δz, $z_m = 0.5(z_i + z_j)$, $\bar{u}_m = 0.5(\bar{u}_i + \bar{u}_j)$, and $\alpha = 10$ [179] and $\beta = c = 0$ [174].

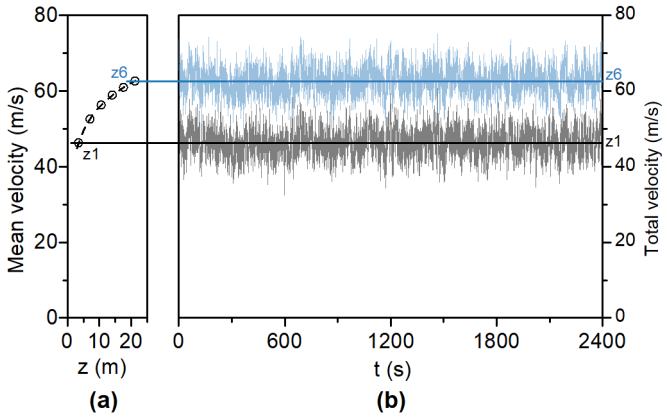

Figure 3.12. (a) Mean velocity profile, and (b) longitudinal wind velocity simulated based on the Kaimal et al. [175] spectrum

The simulated fluctuating wind loads were well matched to the associated models for the turbulence spectrum and spatial coherence. For example, Figure 3.12(a) shows the mean velocity profile, and Figure 3.12(b) shows the fluctuating longitudinal wind velocity for z1 and z6, which was simulated based on the Kaimal et al. [175] turbulence spectrum. Figure 3.13 shows the power spectral densities for the simulated wind velocities based on the turbulence spectra, in comparison with the associated models. The simulated values match the

associated models well. Figure 3.14 shows the coherency loss between segments z1 and z2 for the wind simulated based on the Kaimal et al. [175] spectrum, and demonstrates a good match with the model (Equation (3.9)).

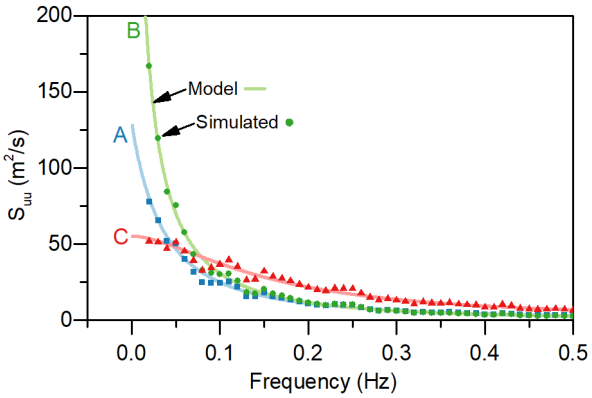

Figure 3.13. Power spectral densities for simulated wind velocities

A, B and C refer to the Kaimal et al. [175], Yu et al. [177], and Li et al. [178] spectra, respectively. S_{uu} is the spectral density of the longitudinal wind velocity.

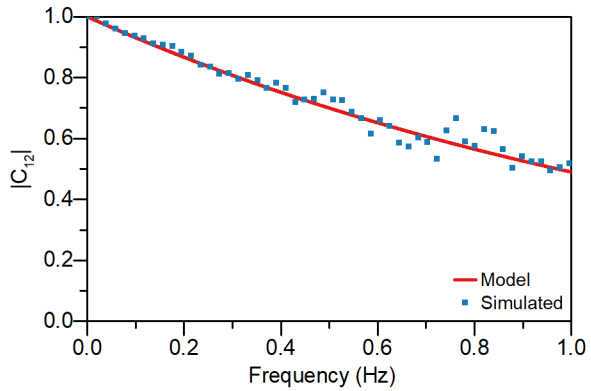

Figure 3.14. Coherency loss between z1 and z2 for wind simulated based on the Kaimal et al. [175] spectrum

3.5 Definition and analysis of earthquake action

The design earthquake actions were determined using the Australian standard AS 1170.4 [74]. The Australian standard is divided into three earthquake design categories, known as EDCI, EDCII, and EDCIII. EDCI, which applies to structures less than or equal to 12 m high with low seismic hazard, permits the earthquake lateral force to be estimated as 10% of the seismic weight. In contrast, EDCII allows an equivalent static analysis, and EDCIII specifies a dynamic analysis which may consist of a response spectrum analysis, or time history analysis with ground motions simulated based on the design response spectrum. While EDCII was applicable to the case study building, requiring at least an equivalent static analysis, numerical analyses were completed using three methods to allow comparison. First, the earthquake action was simplified to a horizontal equivalent static force based on the design spectrum given in

the standard [74]. Second, a response spectrum analysis was completed wherein the response to the standard design spectrum [74] was estimated by modal superposition in the SAP2000 numerical model. Finally, a time history analysis was undertaken based on simulated ground motion time histories.

Based on the nominal site location of the case study building, the earthquake hazard factor (Z) was 0.12, indicating a relatively low seismic hazard, and the sub-soil class was Ce, indicating a shallow soil site [180]. The acceleration time histories were simulated using the spectral representation method [181], based on the standard design spectrum [74], and had a duration of 40.95 s with a 0.01 s time interval. That is, the power spectral density was derived to match the target acceleration response spectrum. The target acceleration response spectrum was determined based on a probability factor of k_p=1.3, as applicable for an annual probability of exceedance of 1/1000. Ground motion time histories were then generated based on the estimated power spectral density. Twenty time histories were simulated for each of the two plan directions. For example, Figure 3.15 shows the twenty simulated acceleration time histories for the first plan direction, with the first time history (a1) highlighted.

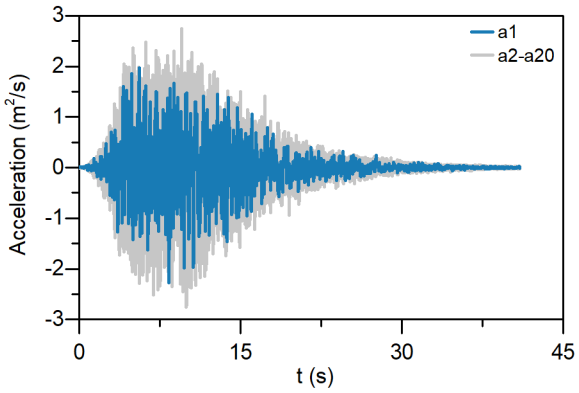

Figure 3.15. Twenty simulated acceleration time histories with the first time history (a1) highlighted

Figure 3.16 shows the response spectral acceleration for the first acceleration time history, which was simulated based on the model curve [74]. The simulated values are shown to match the target response spectrum well. Each time history analysis was implemented in SAP2000 as a *Nonlinear Modal Time-History Analysis* [169]. Therefore, due to the selected analysis method, the only nonlinearity considered was that of the nonlinear links which modelled the F-d and M-θ behaviours of the inter-module connections.

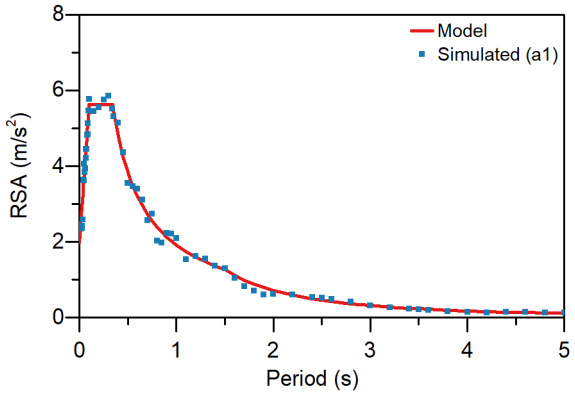

Figure 3.16. Response spectral acceleration (RSA) for the first acceleration time history (a1) simulated based on the model [74]

3.6 Overall structural response of case study building

3.6.1 Response to wind action and effect of turbulence spectra

The design criteria for modular buildings subjected to wind loading are related to the stability, strength and the serviceability, which is related to the inter-storey deflection, the overall deflection and the vibration (§2.1.6.2, p.15). Considering the total and the inter-storey drift, the typical limits are H/600 and h/500, respectively, where H refers to the overall height of the building, and h refers to the height of a storey. For the total drift, the benchmark case study building had maximum drift in the Y-direction of 32.7 and 10.5 mm for the ultimate and serviceability equivalent static wind loads, respectively. These results, which were obtained from equivalent static analyses (ESA) using the SAP2000 numerical model, were generally consistent with the time history analyses (THA), which gave 30.8, 31.9, and 33.1 mm, and 10.5, 10.7, and 11.4 mm, for the ultimate and serviceability wind loads based on the Kaimal et al. [175], Yu et al. [177], and Li et al. [178] turbulence spectra, respectively. As shown in Figure 3.17(a), which presents the drift in the Y-direction at a nominal time increment, the total drift was made up of drifts occurring in the module and in the IMCs. It can be seen that a significant portion of the drift occurred in the IMCs, thereby confirming that both the IMC stiffness and the module stiffness influence the overall drift. It should be acknowledged that the assumption of a relatively stiff module can result in a more significant contribution of the IMCs to the overall drift. Hence, if the module stiffness is reduced, a greater portion of the overall drift may occur in the module rather than the IMCs.

For the inter-storey drift ratio (IDR), the maximum value occurred at the third level, i.e., between the second and third storey. This is shown in Figure 3.17(b) which presents the maximum IDR resulting from the THA based on wind simulated according to the Kaimal et al. [175], Yu et al. [177], and Li et al. [178] turbulence spectra. It can be seen that the Li et al. [178] turbulence spectrum gave the largest IDR, and the specific maximum values were

0.170%, 0.177%, and 0.184% for the Kaimal et al. [175], Yu et al. [177], and Li et al. [178] turbulence spectra, respectively, considering the ultimate limit state. For the serviceability limit state, a lesser wind speed applied, and the maximum values were 0.067%, 0.068%, and 0.071%, respectively. Similar to the total drift, the ESA gave a reasonable estimate of the IDR, indicating a maximum value of 0.062% for the serviceability limit state.

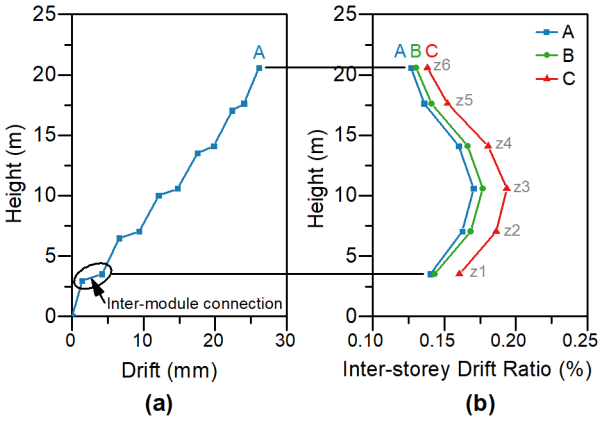

Figure 3.17. (a) Drift at nominal time increment and (b) maximum inter-storey drift ratio
A, B and C refer to the time histories simulated based on the Kaimal et al. [175], Yu et al. [177], and Li et al. [178] spectra, respectively.

Figure 3.18 shows the displacement power spectral density (PSD) which was calculated based on the displacement at the top of the case study building. The figure shows the background component of the response, which was caused by wind gusts with frequency less than the fundamental frequency of the building [76]. Similarly, the resonant response, which was associated with the first natural frequency of 1.4 Hz, can be seen in the figure. To explain the different magnitude of the response for the three turbulence spectra, Figure 3.19 shows the normalised power spectral density for the simulated wind. The x- and y-axes correspond with the form of the turbulence spectra given in equations (3.6) and (3.7), i.e., the y-axis shows $\frac{nS_{uu}(n)}{u_*^2}$ and the x-axis shows $\frac{nz}{\bar{u}(z)}$. The Li et al. [178] turbulence spectrum gave the largest response in Figure 3.18 because this spectrum had its peak closest to the first natural frequency for the building, i.e., the resonant peak in Figure 3.19 is located at a normalised frequency equal to $\frac{1.4Hz \times 20.575m}{62.68m/s} = 0.46$. If the aerodynamic admittance function, which was neglected in the present study, was included then a reduced resonant response would be expected. However, by neglecting the aerodynamic admittance function in the present study, the differing resonant response due to the turbulence spectra could be illustrated by comparing the displacement PSD, as in Figure 3.18.

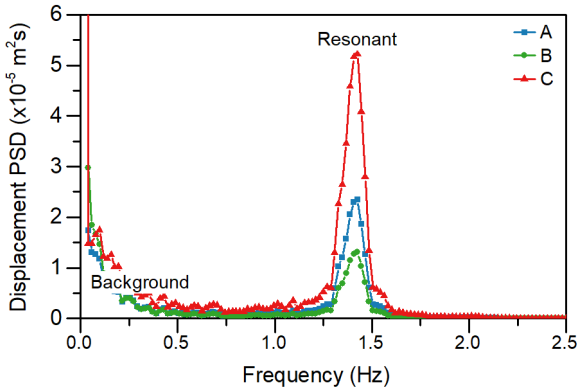

Figure 3.18. Spectra of top storey displacement

A, B and C refer to the time histories simulated based on the Kaimal et al. [175], Yu et al. [177], and Li et al. [178] spectra, respectively.

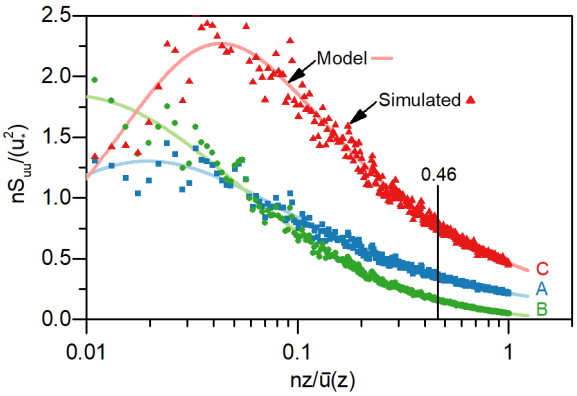

Figure 3.19. Normalised power spectral densities

A, B and C refer to the time histories simulated based on the Kaimal et al. [175], Yu et al. [177], and Li et al. [178] spectra, respectively.

3.6.2 Response to earthquake action

The maximum inter-storey drift ratio (IDR) from the response spectrum analysis was 0.262% and it occurred at the second level. In comparison, the mean time history response showed a maximum of 0.265% at the third level, i.e., 1% more than the response spectrum value. Overall, the response spectrum analysis gave a reasonable estimate of the average time history response, as shown in Figure 3.20, where the mean time history response (Mean TH) can be seen in comparison with the response spectrum analysis (RSA) result. The maximum IDR limit of 0.265% was substantially less than the drift limit of 1.5% (§2.1.6.3, p.16), suggesting the design for wind loading was the more critical criterion for the case study building. For the overall drift, the maximum in the Y-direction from the time history analysis was 53 mm. In comparison, the response spectrum analysis gave a maximum of 47 mm. For the X-direction, the maximum from the time history analyses was 44 mm, and the maximum from the response spectrum analysis was 36 mm.

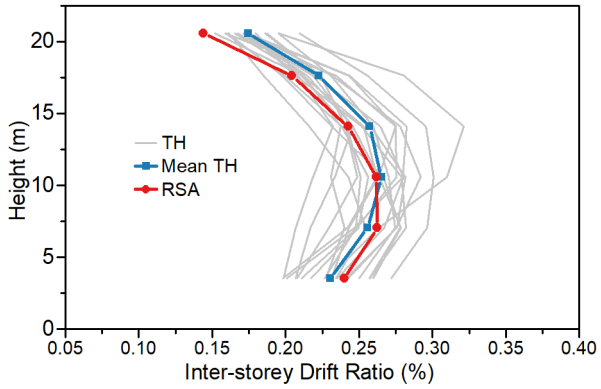

Figure 3.20. Maximum inter-storey drift ratio in the Y-direction for the time history (TH) and response spectrum analyses (RSA)

The case study building had a height which was less than 25 m, which allowed the earthquake performance to be demonstrated by a static analysis according to AS 1170.4 [74]. Following this standard, the horizontal equivalent static shear force was calculated using the equation

$$V = \left[\frac{k_p Z C_h(T_1) S_p}{\mu}\right] W_t, \tag{3.10}$$

where k_p is the probability factor (1.3), Z is the earthquake hazard factor (0.12), C_h is the spectral shape factor depending on the fundamental period (T_1), S_p is the structural performance factor, μ is the structural ductility factor, and W_t is the seismic weight of the structure. The fundamental period was estimated according to AS 1170.4 which gave the fundamental period (T_1) as

$$T_1 = 1.25 k_t h_n^{0.75}, \tag{3.11}$$

where k_t is a factor depending on the structure type, and h_n is the height to the uppermost seismic mass. The factor k_t was taken to be 0.05 as applicable for "*all other structures*", giving a fundamental period of 0.6164 s. The site soil class was assumed to be *Ce* indicating a *shallow soil site*. The *structural performance* (S_p) and *ductility factor* (μ) were selected based on the standard descriptive categories. The most appropriate category was "*Steel structures – Other steel structures not defined above*", which gave μ=2 and S_p=0.77. For comparison, from the existing literature, one study obtained μ=1.8 and S_p=0.526 ($1/S_p$=1.9) for a 6-storey MSB-braced frame [14] (§2.1.6.3.2, p.17). Hence, the ratio S_p/μ was approximately 0.292 for the 6-storey modular braced frame modular in the previous study. In comparison, the design standard [74] indicated a ratio of S_p/μ=0.38, based on which we would expect Equation (3.10) to overestimate the base shear force for the case study building by approximately 30%. Nevertheless, the base shear force was calculated to be 2,582 kN for the case study building using Equation (3.10).

For comparison, the base shear force was determined from the design response spectrum analysis as 2,241 kN for the earthquake in the Y-direction (Y+0.3X). Assuming the response spectrum analysis gave the more accurate value, the equivalent static value overestimated the shear force by 15%. However, it was observed that the fundamental period of the structure differed from that estimated by Equation (3.11). Based on eigenvector analysis of the numerical model, the fundamental period was estimated to be 0.6711 s when the seismic weight was taken as equal to the self-weight, and 0.7121 s if the seismic weight included 30% of the imposed floor and roof actions. The equivalent static base shear calculated by Equation (3.10) based on the more accurate fundamental period of 0.7121 s was approximately 2,235 kN, which closely matched the value of 2,241 kN from the response spectrum analysis. Hence, it can be seen that the difference between the equivalent static and the response spectrum analysis shear forces was caused primarily by the difference in the fundamental period. With the correct fundamental period, the horizontal equivalent static shear force was 0.3% less than the response spectrum analysis value, which in turn was 0.8% less than the maximum time history value.

3.6.3 Natural period of vibration and its effect on the structure analysis

As shown in the Section 3.6.2, the fundamental period is used in simplified analyses to predict the structural response. In the case of modular buildings the variation of the fundamental period with height is not well established (§2.1.6.3.3, p.18). To investigate the variation of the fundamental period with height, the height of the case study building was varied from six to two storeys, and the fundamental period was estimated by eigenvector analysis of the numerical model. The results for the case study building are shown in Figure 3.21, along with the data from the existing literature. Three existing models are also shown, including H/42 [81, 82] and $0.0625H^{0.75}$ which applies to braced steel frames, and $0.1375H^{0.75}$ which applies to moment-resisting steel frames [74]. It can be seen that the variation with height for the case study building was generally consistent with the previous studies of modular buildings composed from braced steel frames. H/42 is shown to provide a lower bound estimate, however, the accuracy reduces with increasing height. In comparison, $0.0625H^{0.75}$ is shown to overestimate the period for the case study building with heights less than 17 m, and underestimate the period for heights greater than 17 m, depending on the inter-module connection stiffness. For the modular structures composed from moment-resisting steel frames, $0.1375H^{0.75}$ is shown to give a reasonable estimate, depending on the IMC stiffness.

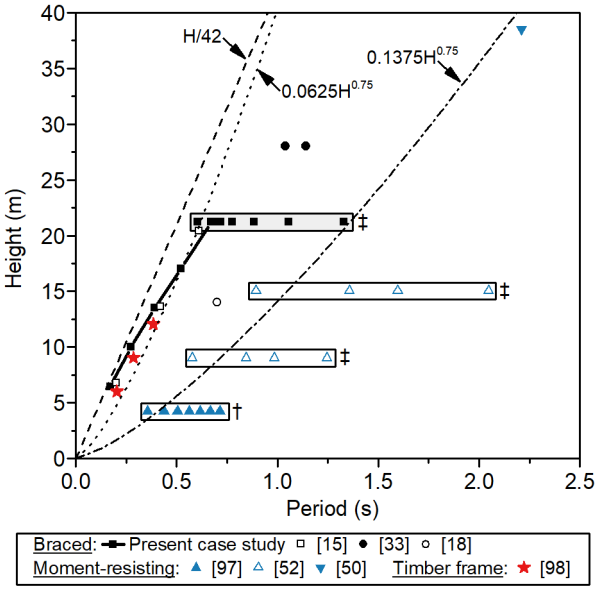

Figure 3.21. Fundamental periods for the case study building compared with data from the existing literature

The existing literature includes the studies by Annan et al. [15], Gunawardena [33], Fathieh et al. [18], Shirokov et al. [97], Choi et al. [52], Styles et al. [50], and Malo et al. [98]. H is the building height, † indicates varying gravity load, and ‡ indicates varying connection stiffness.

3.6.4 Effect of the inter-module connections

As discussed in Section 3.3.3 (p.59), the initial IMC stiffness was varied in the numerical simulations to investigate the effect on the overall response of the case study building. The translational stiffness of vertical inter-module connection (VC) in the along load direction had the greatest effect on the overall building performance. For example, increasing the translational stiffness of the VC reduced the fundamental period (Figure 3.22) and the maximum inter-storey drift ratio due to the serviceability wind load (Figure 3.23). In the case of earthquake loading, increasing the VC translational stiffness resulted in a reduced IDR (Figure 3.24), but increased the base shear force (Figure 3.25). A higher VC translational stiffness may be provided by increasing the column section size, increasing the number of bolts, or by increasing the bolt size and, hence, preload. In this way the results follow the expected behaviour in that increasing the steel section sizes may reduce the overall deflection and fundamental period and, hence, result in a stiffer building that attracts a higher base shear force.

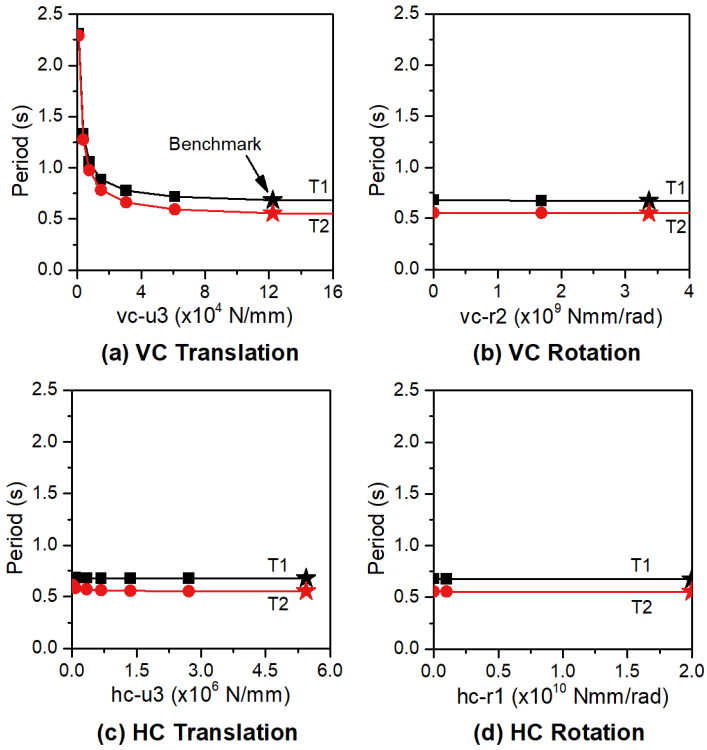

Figure 3.22. Effect of inter-module connection stiffness on the first two natural frequencies (T1 and T2)

★ indicates the result for the benchmark case study building.

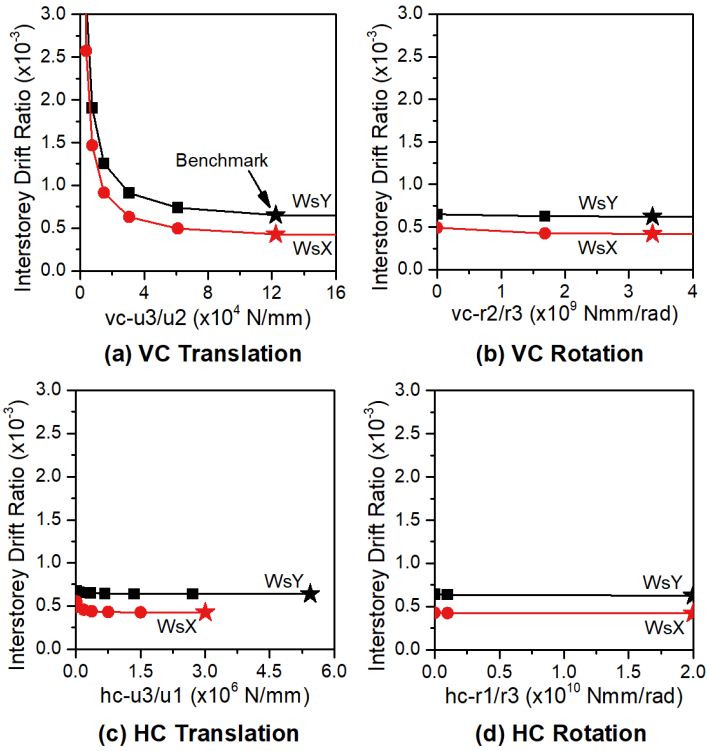

Figure 3.23. Effect of inter-module connection stiffness on the inter-storey drift ratio for the serviceability wind

WsX and WsY refer to wind in the X- and Y-direction, respectively.

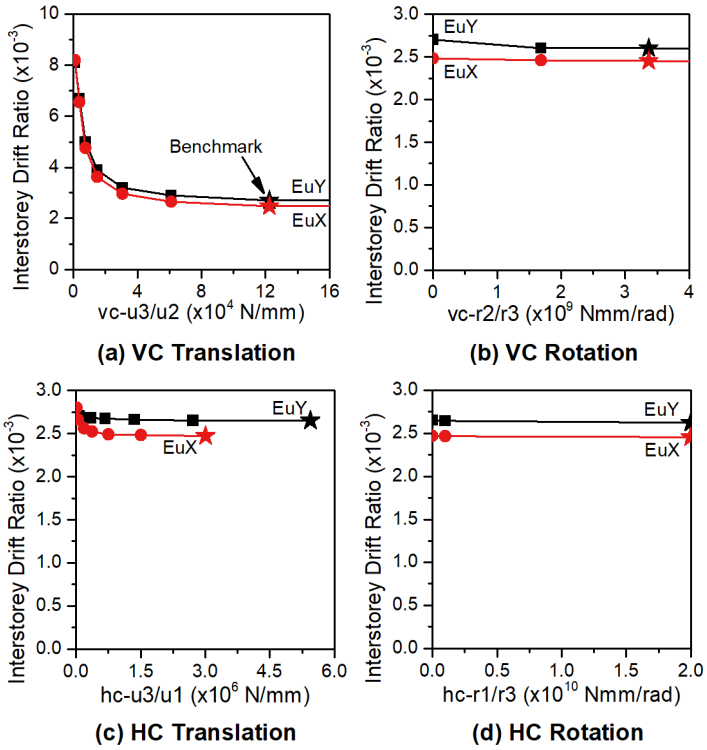

Figure 3.24. Effect of inter-module connection stiffness on the inter-storey drift ratio for the ultimate limit state earthquake

EuX and EuY refer to earthquake in the X- and Y-direction, respectively.

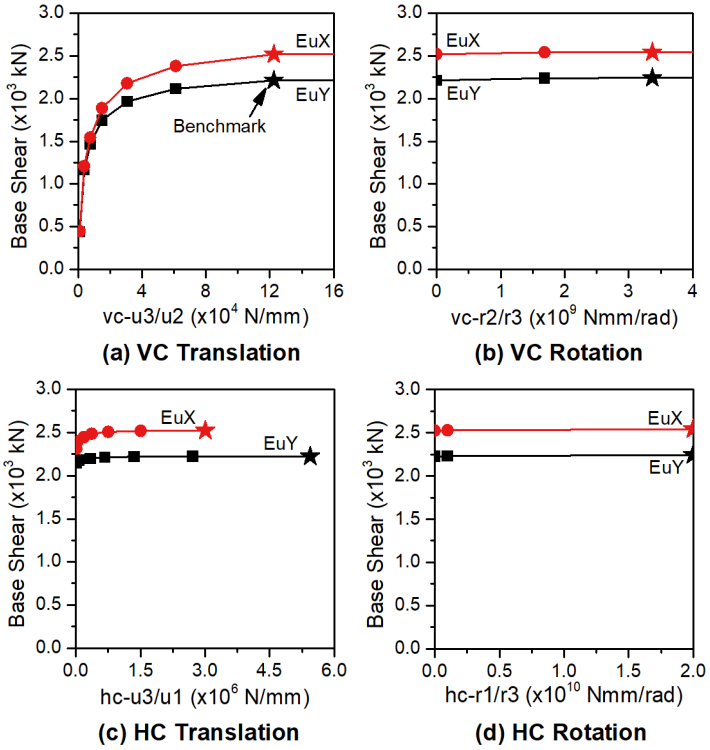

Figure 3.25. Effect of inter-module connection stiffness on the base shear force for the ultimate limit state earthquake

EuX and EuY refer to earthquake in the X- and Y-direction, respectively.

More importantly, however, the results show that the translational stiffness was relatively more important than the rotational stiffness of the vertical inter-module connection (VC). For example, Figure 3.22 shows that varying the rotational stiffness vc-r2, while the remaining stiffnesses were maintained at the benchmark values, had little effect on the fundamental period. The translational stiffness had greater effect than the rotational stiffness because the modules were rigid in comparison with the inter-module connections. Reducing the rotational stiffness of the VCs, for example, resulted in a small increase in the displacement due to the additional rotation. However, the load was transferred to the modules which were able to resist the additional design actions due to the stiffness and strength built into them to accommodate transport actions. This is a typical feature of modular building, which requires modules to be designed for loads induced when they are lifted by a crane and transported to the site [1]. In the present numerical studies, the modules were stiff due to the use of rigid intra-module connections, and due to the bracing incorporated in the modules.

Due to the relative importance of the translational stiffness of the VC, it is particularly important to have an accurate model for the translational force-displacement behaviour. Although in the previous sections the simplified translational (shear) behaviour allowed a match in the maximum inter-storey drift, it is clear from the results of this chapter that neglecting the initial friction/slip stage of the connection may not be appropriate in all cases. The friction/slip stage, which effectively lowers the initial stiffness, should be included in the shear F-d model, and an improved model is required to ensure this joint behaviour is accurately captured.

3.6.5 Comparison with moment resisting frame modular building

For the Styles et al. [50] 11 storey moment-resisting frame building, the critical parameter for the serviceability wind load assessment was the inter-storey drift, rather than the total building drift. In the present study of a six storey braced frame building, the total deflection limit was approximately 36 mm (H/600) and the inter-storey drift limit was 5.9 mm (h/500) indicating an inter-storey drift ratio limit of 0.2%. The maximum serviceability wind drift for the benchmark case study building was approximately 11 mm, and the maximum inter-storey drift ratio was approximately 0.07%. Therefore, consistent with the previous study [50], the maximum inter-storey drift was the more critical parameter for the serviceability wind load assessment in the present study, i.e., $\frac{0.07\%}{0.2\%} = 0.35 > \frac{11mm}{36mm} = 0.31$. In the previous study [50], the maximum inter-storey drift due to serviceability wind loading occurred between levels 3 and 4 for the 11 storey building. In comparison, in the present study of a six storey building,

the maximum inter-storey drift occurred at the third level, i.e., between the second and third floor level as shown in Figure 3.17(b).

In the previous study [50], the intra-module connection stiffness was reported to have the greatest role in the overall resistance to lateral loads, i.e., greater than the inter-module connection (IMC) stiffness. However, the previous study [50] considered only the horizontal IMC stiffness, and did not account for the effect of the vertical IMC stiffness. In comparison, in the present study, both the horizontal and vertical IMC stiffnesses were considered. For the present study, as shown in Figure 3.17(a), it is clear that the drift due to wind loading was composed of drifts due to the deformation of the module and the deformation of the IMC. It is, therefore, clear that the overall resistance to lateral loads was influenced by the stiffness of the vertical IMC and also by the stiffness of the module, and, hence, by the intra-module connection stiffness. The present study indicates that the vertical IMC stiffness has a significant role in the overall resistance to lateral loads.

3.7 Summary

This chapter demonstrated the application of a numerical method wherein the translational and rotational behaviours of the inter-module connection were simplified, and then incorporated in the overall numerical model. The numerical technique was able to predict the overall structural response to lateral loads, which was verified by comparison with a selected previous study. The main findings are summarised as follows.

1. The inter-module connection influenced the overall response to lateral loads. In particular, the translational stiffness of the vertical inter-module connections in the along load direction was shown to have the greatest effect, while the rotational stiffness had relatively little effect.

2. Due to the relative importance, it is recommended that a more accurate model is developed for the shear behaviour of inter-module connections. While the simplified bi-linear model was suitable for the study in this chapter, a more accurate model which considers the friction/slip behaviour would allow more precise modelling of the overall building response to lateral loading, as the connection shear stiffness can significantly affect the building response.

3. For the six storey braced frame case study building, the equivalent static analyses for wind and earthquake loading generally gave a good estimate of the overall building behaviour in comparison with the two more accurate methods of response spectrum and time history analysis.

4. Following the analysis of the base shear due to earthquake ground motion, it was found that the existing empirical formula for the fundamental period of braced steel frame buildings may not be applicable in the case of modular buildings. It is suggested that the fundamental period should be established directly from the numerical model in preference to the existing empirical formula.

Chapter 4 Shear behaviour of traditional bolted steel connections[1]

4.1 Introduction

As shown in Chapter 3, the shear stiffness of the inter-module connections (IMCs) can significantly affect the global response of modular buildings. However, as identified in Section 2.2, the existing model for the shear behaviour of IMCs (Figure 2.23, p.39) cannot accurately estimate the behaviour obtained from experimental and numerical studies, especially the initial slip stiffness. Therefore, further study of the friction/slip shear behaviour is required to enable development of a more precise model. This study begins with the friction/slip shear behaviour of traditional bolted steel connections which, once established, can form the basis of the development of further models for different connection types, such as IMCs.

For the traditional bolted steel connections, a simplified four stage model typically represents the shear behaviour (Figure 2.22, p.37). In this model, the first part (OA) is the friction stage, in which friction between the steel plates resists the applied shear force. Most standards adopt a friction model in which the friction resistance is calculated as the product of a friction coefficient and applied normal force. The friction coefficient, known as the slip factor (SF), is determined experimentally based on a standard test method such as that given in Annex G of EN 1090-2 [150]. The existing shear F-d model (Figure 2.22, p.37) assigns an arbitrary stiffness based on the slip load and an assumed slip displacement (d_A), which is typically taken as 0.15 mm for the standard slip factor test specimen [182]. However, the F-d behaviour during OA is not necessarily linear as shown by recent studies of the slip factor for steel [149, 182-185]. Different F-d behaviours are observed depending on the connection geometry, materials, nature of the loading and the environmental conditions. In order to develop accurate models of the initial slip behaviour of bolted steel connections, further study of the F-d behaviour in the standard test is required.

Numerous studies have investigated the slip factor of typical structural steel materials. For example, the Australian Steel Institute *Connection Design Guide 1* [186] gives a summary of slip factors based on the work of Kulak et al. [187]. In this review, a natural steel surface is defined as a surface with loose mill scale and dirt removed by wire brushing, and any grease removed by a solvent. Considering all the test data available for ASTM A7, A36 and A440

[1] The related work in Chapter 4 was published in the Journal of Constructional Steel Research:

Lacey AW, Chen W, Hao H, Bi K. Experimental and numerical study of the slip factor for G350-steel bolted connections. J Constr Steel Res. 2019;158:576-90. https://doi.org/10.1016/j.jcsr.2019.04.012

structural steels, in addition to Fe37 and Fe52 steel tested in Europe, an average slip factor of 0.33, and a standard deviation of 0.07, is reported based on 327 tests [187]. Blast cleaning of the faying surface is reported to increase the slip factor in comparison with the natural clean mill scale surface, and an average slip factor of 0.51 (standard deviation 0.09) is reported based on 186 tests of ASTM A7, A36, and Fe37 steel. Cruz et al. [183] and Heistermann et al. [149] report a slip factor of 0.47 and 0.50 for S275 mild steel depending on the type of shot used to obtain the sand blasted surface finish. Annan et al. [188] report an average slip coefficient of 0.53 for the blast cleaned surfaces of CAN/CSA G40.21 350AT category 3 steel. However, the data for Australian specification steel materials, which may differ in terms of the requirements for chemical composition and mechanical properties, is lacking. In addition, the shear behaviour of bolted joints made from the Australian steel material is also not well understood. Investigation of the F-d behaviour for the standard slip factor test assembly is therefore required in order to develop an appropriate model for the material.

Therefore, this chapter presents an investigation into the shear force-displacement behaviour of AS/NZS 3678-350 [189] steel, a commonly used Australian specification steel. Experimental study is conducted following the method given in Annex G of EN 1090-2 [150], based on which the short term slip factor of the steel surface is established depending on the surface condition. Digital image correlation (DIC) is adopted to overcome issues related to the displacement measurement location. Torque controlled preloading of the bolts is adopted for the experimental testing by following Australian standard AS/NZS 1252.1 [190]. In addition, numerical analysis is conducted and the numerical models are calibrated based on the slip factor test results. Empirical formulae are then proposed for the prediction of the initial slip behaviour.

4.2 Standard test method and surface finish

The slip factor for the steel-steel faying surface may be established using the standard test method given in Appendix J of AS4100 [139], or alternatively the method given in Annex G of EN 1090-2 [150]. From a literature review, EN 1090-2 is the more commonly referenced standard and so is adopted for this study. For instance, Cruz et al. [183], Heistermann et al. [149] and Stranghöner et al. [182] adopt this method. However, despite its common use, some details of this test method are unclear, which may lead to inconsistency of the application among different researchers [182]. The unclear details include the locations at which slip deformation should be measured and the loading rate.

4.2.1 Location of displacement measurement

Slip is typically measured between adjacent points on the inner plate and the cover plate. This is measured at each end, and on both sides. Ideally this requires eight displacement transducers, although some previous studies used only four transducers. The layout of displacement transducers in some previous studies are illustrated in Figure 4.1. Some studies recorded measurements at the cover plate edge, as shown in Figure 4.1(a), (b) and (d), whereas other studies recorded measurements at the centre of the bolt group, as shown in Figure 4.1(c). Stranghöner et al. [182] reported that a stiffer load slip response was obtained if the slip was measured at the centre of the bolt groups, compared with measurement at the plate ends, due to the elongation of plates being included in the latter measurements. The differing load slip stiffness becomes relevant if the slip load is defined with reference to the slip deformation.

4.2.2 Rate of loading

EN 1090-2 defines normal speed tests as those with overall duration of ten to fifteen minutes. Stranghöner et al. [182] investigated the effect of test duration on the measured slip factor. The duration was shown to have only a minor effect on the measured slip factor. In comparison, Appendix J of AS4100 specifies a rate of loading of 0.5 kN/s or less, which may be directly applied to the universal testing machine using load control. A loading rate of 0.4 kN/s was therefore adopted in the present experimental program.

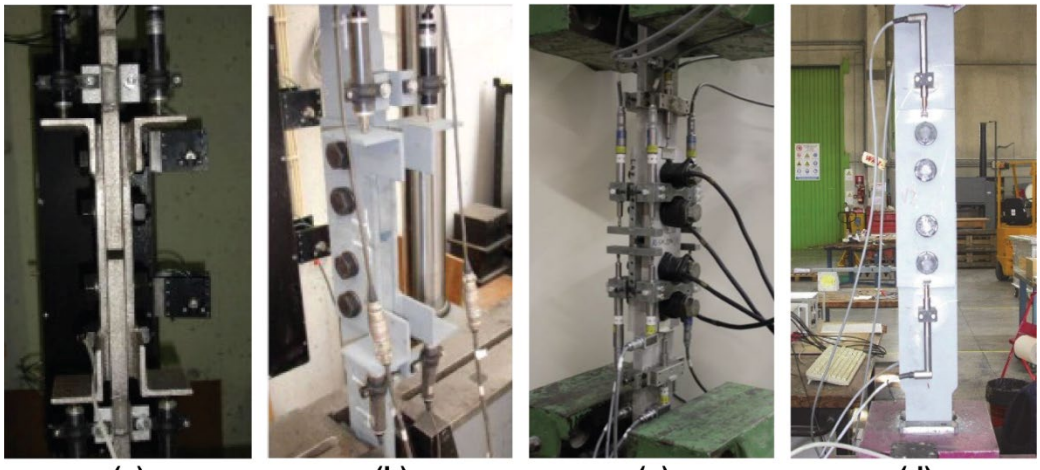

Figure 4.1. Layout of displacement transducers in previous studies, (a) [183], (b) [149], (c) [184], and (d) [185]

4.2.3 Effect of contact pressure

Increasing the contact pressure was reported to result in a decrease in the friction coefficient for steel-steel surfaces [149], following an exponential relationship [191]. Stranghöner et al. [182] reported a slight increase in the static slip factor for decreasing preload, for surface

finishes of alkali-zinc silicate (ASI), spray metallized with zinc (Zn-SM) and combined alkali-zinc silicate and spray metallized with zinc (ASI-Zn-SM). The tribological phenomena which cause the relationship between contact pressure and friction coefficient are not understood completely [149], but may be explained by surface asperities being flattened by the applied contact pressure [187].

4.2.4 Method of bolt tensioning

The Australian Standard AS4100 permits either the "*part-turn method of tensioning*", or "*tensioning by use of direct-tension indication device*" [139], although other methods are not excluded [192]. With the 2016 revision, AS/NZS 1252.1 provides the details of the torque-tension relationship for use in tightening bolt assemblies with the general relationship

$$M_{r,i} = k_m d F_{p,C} \,, \tag{4.1}$$

where $M_{r,i}$ is the torque applied to the nut, k_m is a factor based on the k-class, d is the nominal bolt diameter and $F_{p,C}$ is the minimum specified bolt preload. The k-class is chosen based on the tightening method, with class k2 required for the torque tightening method. The k_m factor is determined by the assembly test as documented in Appendix D of AS/NZS 1252.1:2016 [190].

While torque controlled tightening of bolts is a part of normal practice in Europe and America, the method is historically not common in Australia due to a lack of confidence [192]. With the revision of AS/NZS 1252.1 it is expected that this will change as the reliability of the available bolt assemblies improves over time [192]. This study, therefore, adopts the torque tightening method in order to investigate the accuracy which may be obtained using this method to control the preload.

4.2.5 Steel surface finish

Steel surface finishes are typically specified with reference to Australian standard *AS 1627 Metal finishing – Preparation and pretreatment of surfaces*. AS 1627 Part 4 [193] covers abrasive blast cleaning of steel. The standard is oriented towards the cleaning of steel prior to the application of corrosion protection coatings. Four blast cleaning classes are defined as *Sa 1*, *Sa 2*, *Sa 2.5*, and *Sa 3*, in order of increasing cleanliness. *Sa 1* refers to light blast cleaning in which only the loose mill scale are removed [193, 194]. *Sa 3* refers to a visually clean surface which has all of the visible mill scale removed leaving behind a uniformly coloured surface [194].

AS 1627.4 Appendix B refers to pictorial surface preparation standards given in AS 1627.9 [195]. AS 1627.9 in turn refers to ISO 8501-1 [196]. ISO 8501-1 gives photos of representative

surfaces for the preparation grades (Sa 1 through Sa 3), and rust grades (A through D). Figure 4.2(a) presents an example page from ISO 8501-1 showing rust grades A and B, and Figure 4.2(b) presents an example page showing representative photographs for sand blasted steel surfaces. Following these standards, the blast cleaning class is determined by visually comparing the prepared steel surface with the representative photographs, as illustrated in Figure 4.2(b).

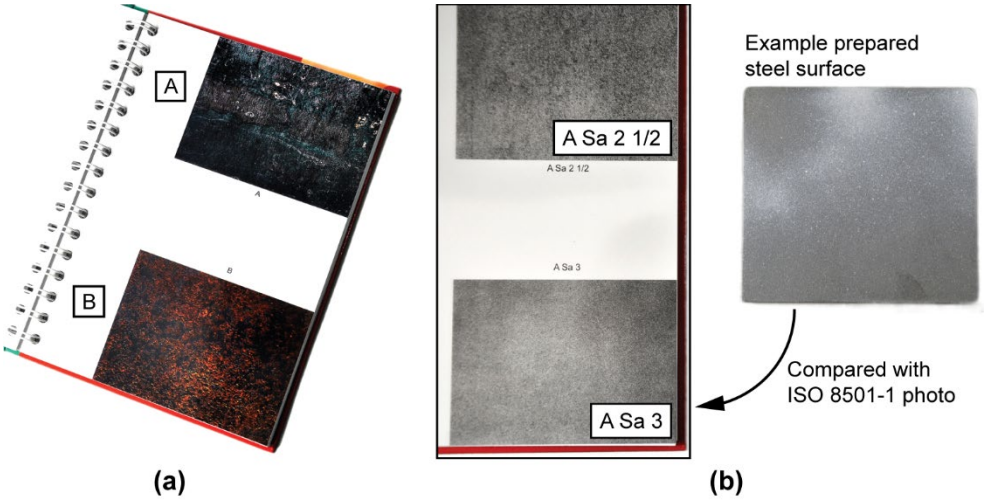

Figure 4.2. (a) Page from ISO 8501-1 showing rust grades A and B, (b) Prepared steel surface shown alongside ISO 8501-1 representative photos

4.3 Experimental program

4.3.1 Test specimens

Fifteen standard test specimens, labelled SF1 through SF15, were adopted using M16 EN 14399-3 [197] k2 HR property class 8.8 bolts. As shown in Table 4.1, five specimens were tested for each surface finish in order to obtain the average behaviour. The width of the inner plate was tapered at the end, as shown in Figure 4.3, to suit the available universal testing machine (Shimadzu AGS-300kNX). The inner plates were 16 mm thick and 50 mm wide at the end, with two 18 mm diameter holes. They were cut from the same material to give approximately equal thickness. The outer plates were 8 mm thick and 80 mm wide, with two 18 mm diameter holes to match the inner plates.

Table 4.1. Slip factor test specimens

Specimen	Surface finish
SF1-SF5	Clean mill scale (Sa 0)
SF6-SF10	Sa 1
SF11-SF15	Sa 3

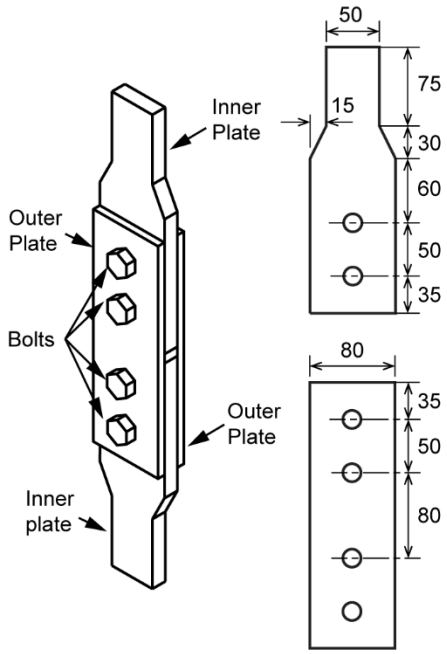

Figure 4.3. Illustration of test assembly

4.3.2 Surface preparation

The surfaces of test specimens SF1 to SF5 were maintained in the clean mill scale condition. The surfaces of the remaining specimens were sand blasted using a Fiora Machinery Model B sand blaster, with an industry standard 80 mesh size. Specimens SF6 to SF10, and SF 11 to SF15 had the surfaces blasted to a Sa 1 and Sa 3 grade finish respectively. Figure 4.4 shows photographic examples of the surface finishes. For convenience in the following sections the clean mill scale surface finish is referred to as Sa 0.

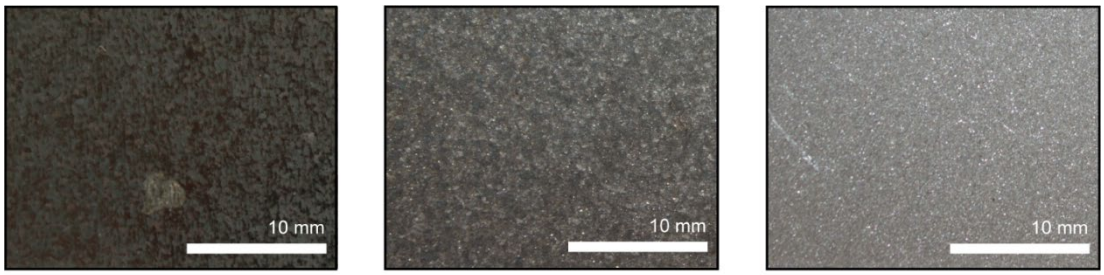

Figure 4.4. Photos showing example of (a) clean mill scale Sa 0, (b) Sa 1, and (c) Sa 3 surface finish

4.3.3 Specimen assembly

The plates were bolted together and the bolts tensioned before testing. Figure 4.5 shows an example test specimen prior to assembly (a) and after assembly (b). In order to ensure that the initial resistance was due only to friction, the bolts were positioned and aligned to give the maximum slip tolerance as shown in Figure 4.5(c). The bolts were tensioned using a torque

wrench. A two stage process was adopted involving initial tightening to $0.75M_r$ followed by final tightening to $1.10M_r$, where M_r is the torque required to give the specified preload of 95 kN. The torque (M_r) was calculated using Equation (4.1) based on the manufacturer supplied k-value (0.136). The assembled specimen was tested as soon as possible after tensioning to minimise the loss of preload with time.

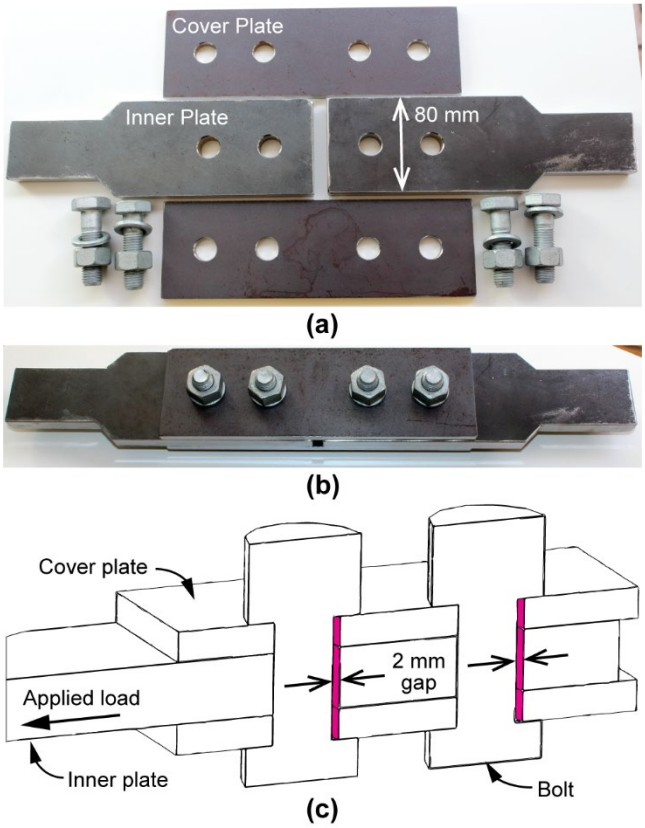

Figure 4.5. Slip factor test specimen (a) prior to assembly, (b) after assembly, and (c) illustration showing bolt hole tolerance

4.3.4 Digital image correlation method

Specimens were loaded using a Shimadzu AGS-300kNX universal testing machine (UTM) as shown in Figure 4.6. The load was applied at a slow rate of 0.4 kN/s, which was selected to give an overall test duration of 10 to 15 minutes per specimen. Prior to testing, a speckle pattern was applied to the specimen surface using spray paint, as shown in Figure 4.7. A camera was used to record a video of the front side of the specimen during the test. The recorded videos were converted to a series of images, based on which digital image correlation (DIC) was performed to determine the vertical displacement. The slip was then calculated as the difference in vertical displacement between adjacent points on the inner and cover plates at the centre bolt group location, as shown in Figure 4.7 for slip at the top of the connection. For slip at the bottom, similar points were selected at the lower centre bolt group level. The slip was taken as the average of the relative vertical displacement between points P1 and P3, and

points P2 and P3. For the DIC analysis the ncorr program was adopted [198]. The DIC technique can be verified against actual readings from strain gauges as proven in the studies by Yuan et al. [199, 200].

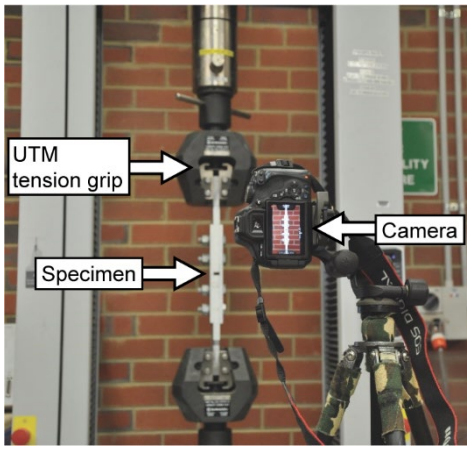

Figure 4.6. Slip factor test setup

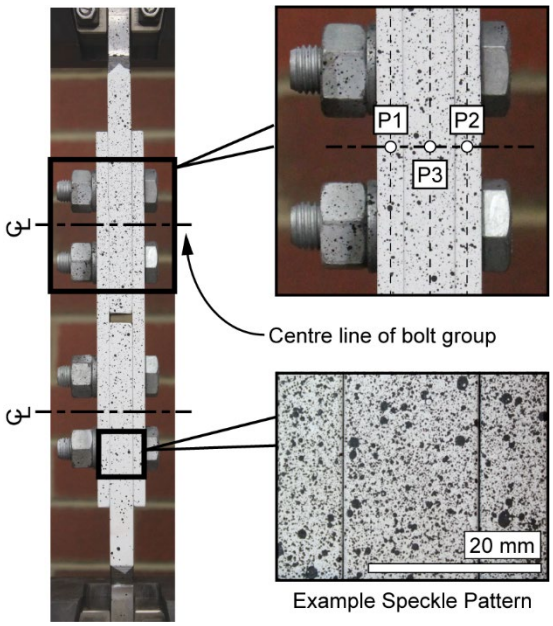

Figure 4.7. Example speckle pattern and points used for slip calculation at the top of the specimen

4.3.5 Results and analysis

Figure 4.8(a) shows the force and overall displacement recorded by the UTM. Sa 0, or clean mill scale finish specimens, are shown to have lower slip load than the Sa 1 and Sa 3 finish specimens. Sa 1 finish specimens are shown to have a similar slip load to the Sa 3 finish specimens. The Sa 0 specimen plots generally show slip at both the top and bottom end of the specimen. This is illustrated for the first specimen, SF1, in Figure 4.8(b). For SF1, slip occurred at the bottom, followed by slip at the top of the specimen. For the other specimens,

some slipped at the bottom first, whereas others slipped at the top first, depending which end of the specimen had the lower slip resistance. However, it is not possible to determine the timing of the slip at each end based only on the overall displacement. Therefore, in addition to displacement measurements recorded by the UTM, displacements were determined using DIC. The main output from the DIC is vertical displacements on the visible edges of the specimen for each recorded image, i.e., each time increment. For example, this is illustrated in Figure 4.9, which shows the vertical displacement of SF1 immediately prior to slip (a), after slip at the bottom (b), and after slip at the top (c).

The slip at each end of the specimen was calculated based on the mean displacements on both sides of the specimen at the centre of each bolt group. The relevant points at the top of the specimen are illustrated in Figure 4.7. Figure 4.10(a) shows two exemplary shear load-slip (F-d) curves which were obtained for the specimen SF5, which slipped at the bottom (SF5b) and then at the top (SF5t). The curves demonstrate the general behaviour which was observed for all the specimens. As load was applied to the specimen the slip between the plates slowly increased due to minor relative displacement between the plates. As slip occurred the specimen increased in length and the testing machine was unable to maintain the applied force. A drop in force was therefore observed following major slip. After the drop in force, the load gradually increased again with several minor slips until the initial 2 mm bolt hole tolerance (Figure 4.5(c)) was taken up and the plate came into contact with the bolt shank. At this stage the bolt was bearing on the plates as shown in Figure 4.10(a). In the present study the main focus is the initial stage of the F-d curve. Figure 4.10(b) shows a closer view of the F-d curves for specimen SF5, with the maximum slip for the x-axis set as 0.3 mm to display the initial F-d behaviour. In this initial stage the displacements were very small, and noise from the DIC is clearly observed in Figure 4.10(b).

The F-d curves for all of the clean mill scale Sa 0 specimens are shown in Figure 4.11(a). Similarly, Figure 4.11(b) and (c) show the curves for the Sa 1 and Sa 3 sand blasted specimens. respectively. In each case the mean behaviour is shown, which was determined by calculating the average force across all the similar specimens for selected slip values. For the clean mill scale Sa 0 specimens, some specimens showed a single major slip, whereas other specimens showed several small slips prior to the major slip. As illustrated in Figure 4.10(c), SF5t shows the first behaviour with a single major slip, and SF1t shows the second behaviour with several small slips prior to the major slip. The cause of the two different behaviours is discussed in Section 4.4.2 (p.93).

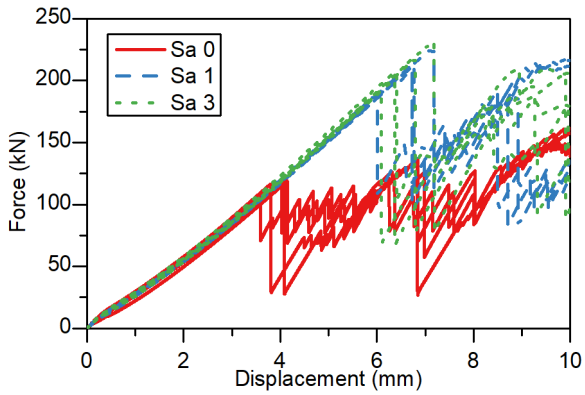

(a) All specimens

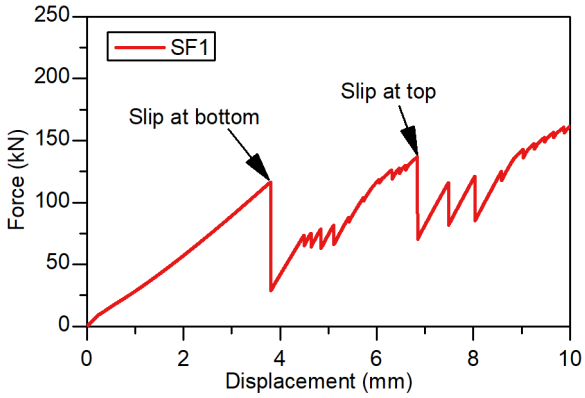

(b) SF1

Figure 4.8. UTM force-displacement plot for (a) all specimens, and (b) SF1

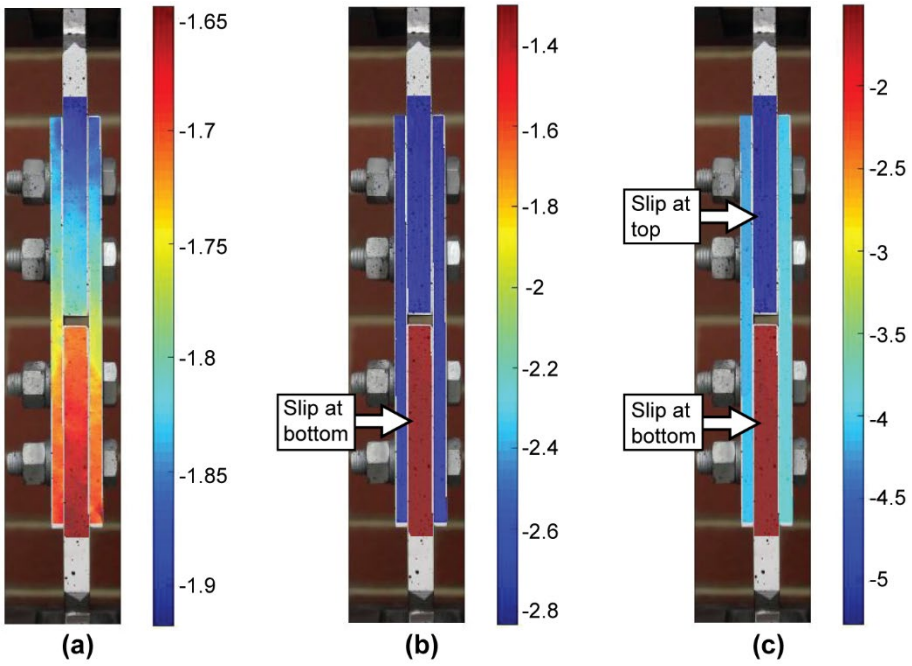

Figure 4.9. Vertical displacement (mm) of SF1 (a) immediately prior to slip, (b) after slip at bottom, and (c) after slip at top

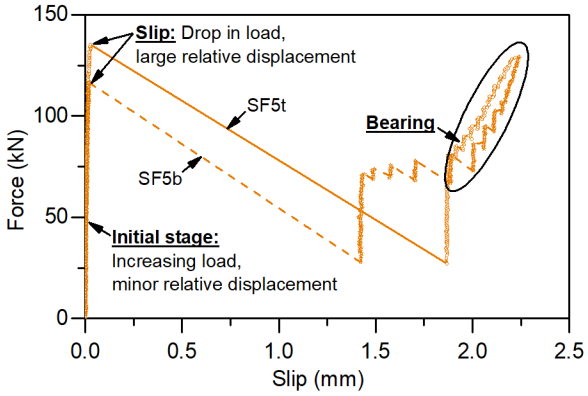

(a) SF5

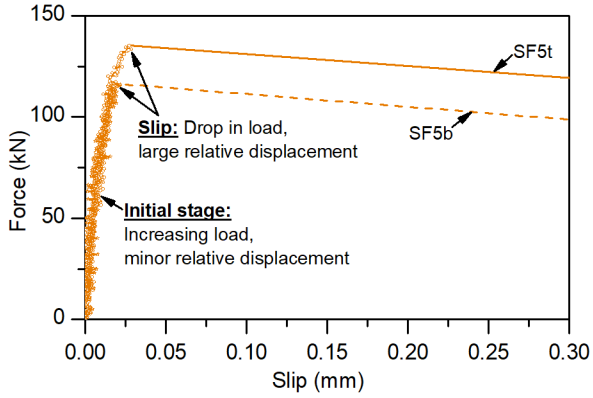

(b) SF5

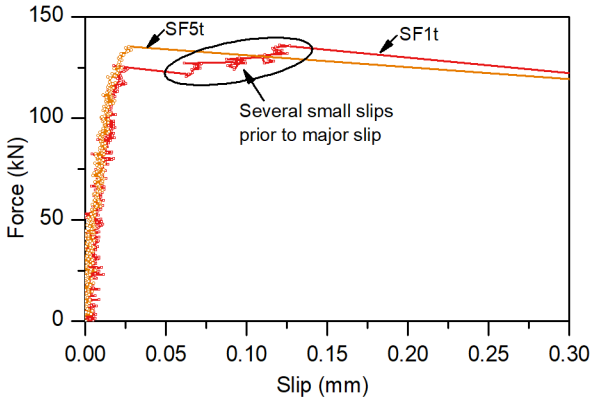

(c) SF1t and SF5t

Figure 4.10. Force-slip plot for SF5 (a & b) and SF1t & SF5t (c)

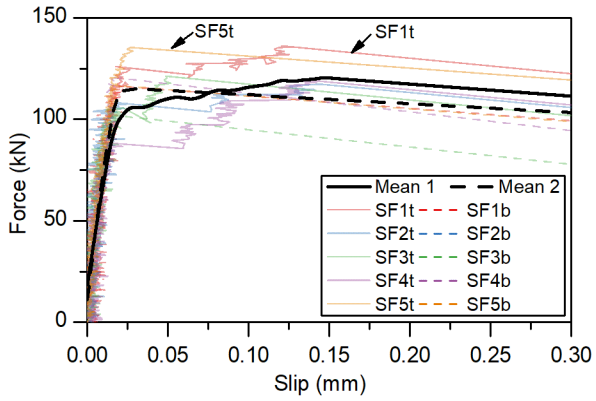

(a) Clean mill scale (Sa 0)

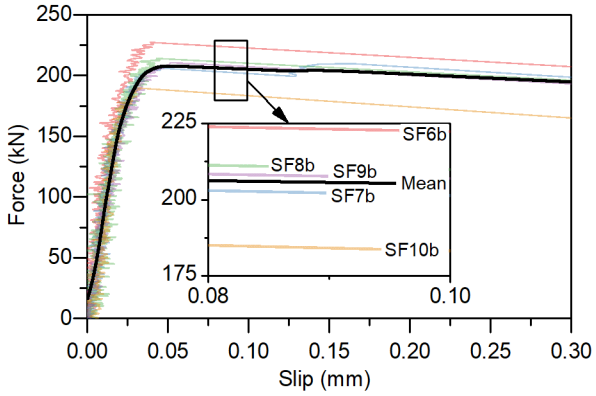

(b) Sand blasted (Sa 1)

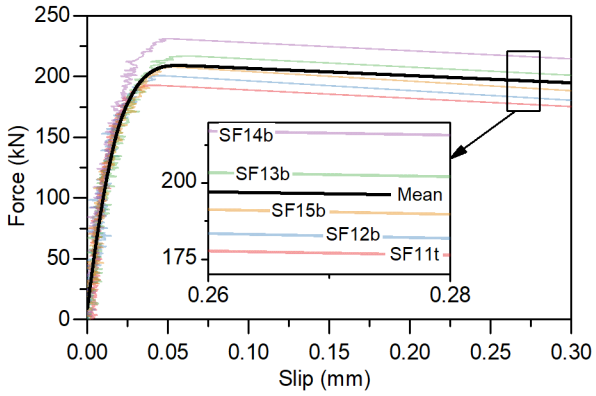

(c) Sand blasted (Sa 3)

Figure 4.11. Force-slip plot for clean mill scale (Sa 0) specimens (a), and Sa 1 (b) and Sa 3 (c) sand blasted specimens

Finally, the slip load was determined based on the force-slip curve. In all cases the slip load was taken as the peak force prior to slip. The individual, mean and standard deviation of the slip factors were determined using the following formulae [150]:

$$\mu_i = \frac{F_{si}}{4F_{p,C}}, \tag{4.2}$$

$$\mu_m = \frac{\sum \mu_i}{n}, \text{ and} \tag{4.3}$$

$$s_\mu = \sqrt{\frac{\sum (\mu_i - \mu_m)^2}{n-1}}, \tag{4.4}$$

where F_{si} is the individual slip load, $F_{p,C}$ is the bolt tension, and n is the number of slip load values obtained from the test specimens. For design purposes, the characteristic slip factor is calculated based on the 5% fractile with 75% confidence level. Assuming ten values are obtained, the characteristic slip factor may be determined as [150]

$$\mu_k = \mu_m - 2.05 s_\mu . \tag{4.5}$$

Table 4.2 shows the individual test results, and Table 4.3 shows the mean and standard deviation of the slip load, and the mean, standard deviation and characteristic slip factor for each of the surface finishes. A slip load was not recorded for SF2b because the bottom of specimen SF2 did not slip during the experiment, due to an unusually high slip resistance. The results show that the bolt preload can be well controlled using the torque method, as confirmed by the relatively low standard deviation obtained for the slip load. Standard deviations of 8.99 kN, 13.5 kN and 15.1 kN were obtained for the clean mill scale (Sa 0), Sa 1 and Sa 3 specimens, respectively. This corresponds to 7.5%, 6.4% and 7.2% of the mean slip load respectively, and incorporates variations in the steel surface, bolt preload, and associated measurement errors.

After testing the specimens were disassembled and photos were taken to record the condition of the faying surfaces. For example, Figure 4.12(a) shows the surfaces for SF1, a clean mill scale specimen (Sa 0), and Figure 4.12(b) shows the surfaces for SF12, a Sa 3 sand blasted specimen. Wear of the surfaces is shown to be limited to the local area around each bolt hole. Figure 4.13(a) to (d) show a closer view of the relevant area around the bolt holes, illustrating the range of damage observed. For the clean mill scale surfaces (Sa 0), some specimens exhibited damage to the mill scale layer, and mill scale fragments were observed around the exposed steel substrate, as shown in Figure 4.13(a) and (b). In other cases, there was no damage to the mill scale layer but a slightly shiny surface was observed for the surface Sa 0,

as shown in Figure 4.13(c). Figure 4.13(d) illustrates the typical damage observed for the sand blasted specimens (Sa 3). A shiny smoothed surface can be seen around the bolt holes.

Table 4.2. Summary of individual test results

Ref.	Surface finish	Slip load, F_{si} (kN)	Slip factor, μ_i
SF1b	Clean mill scale	116.5	0.3065
SF1t	(Sa 0)	127.3	0.3350
SF2t		117.5	0.3093
SF3b		101.8	0.2680
SF3t		121.1	0.3187
SF4t		119.5	0.3145
SF4b		120.4	0.3168
SF5b		116.7	0.3071
SF5t		135.3	0.3560
SF6b	Sa 1	227.2	0.5980
SF7b		206.0	0.5422
SF8b		213.8	0.5627
SF9b		210.9	0.5549
SF10b		190.0	0.4999
SF11t	Sa 3	192.5	0.5067
SF12b		200.9	0.5286
SF13b		217.0	0.5709
SF14t		231.7	0.6097
SF15t		207.8	0.5467

Table 4.3. Mean slip load and slip factor depending on the surface finish

Surface finish	Mean slip load, F_{sm} (kN)	Standard deviation, s_{Fs} (kN)	Mean slip factor, μ_m	Standard deviation, s_μ	Characteristic slip factor, μ_k
Sa 0	119.6	8.985	0.3146	0.02365	0.27
Sa 1	209.6	13.50	0.5516	0.03553	0.50
Sa 3	210.0	15.10	0.5525	0.03975	0.50

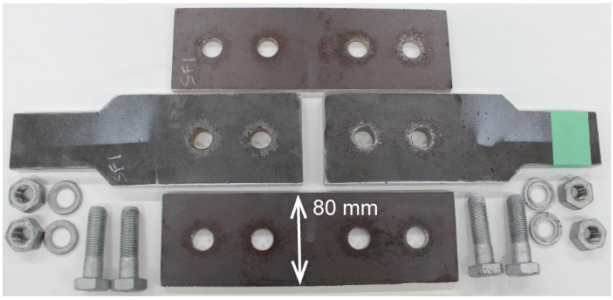

(a) SF1 Clean mill scale (Sa 0)

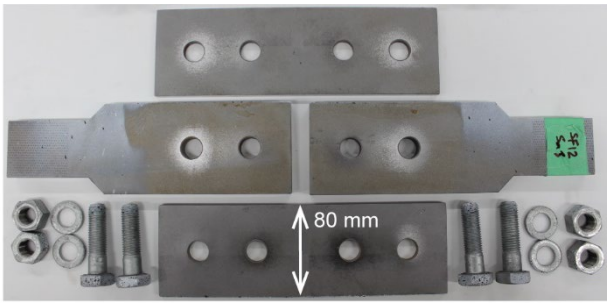

(b) SF12 Sand blasted (Sa 3)

Figure 4.12. Condition of faying surface after testing

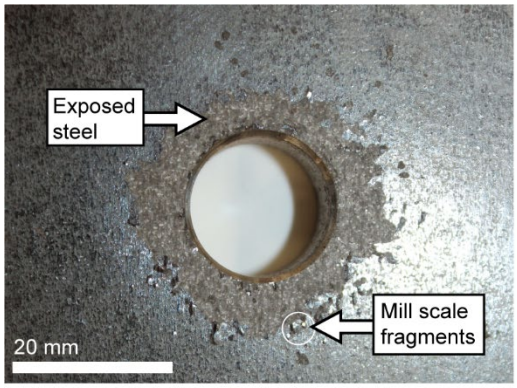

(a) Sa 0

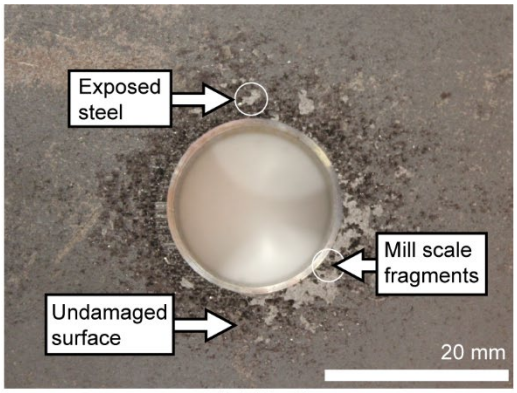

(b) Sa 0

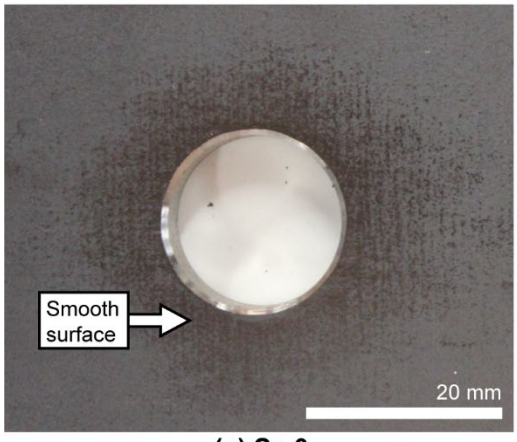

(c) Sa 0

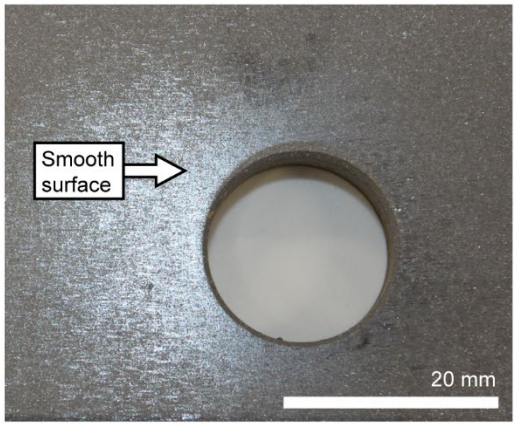

(d) Sa 3

Figure 4.13. (a) Clean mill scale (Sa 0) surface with fully exposed steel around bolts, (b) Sa 0 with partially exposed steel, (c) Sa 0 without mill scale damage, and (d) sand blasted surface (Sa 3) with smoothed surface around bolts

4.4 Discussion and evaluation of experimental results

4.4.1 Slip factor for AS/NZS 3678-350

For the clean mill scale surface a mean slip factor of 0.31 was obtained with a standard deviation of 0.02. The characteristic slip factor for design was calculated as 0.27 based on the 5% fractile with 75% confidence level. This is marginally less than the average slip factor of 0.33, standard deviation 0.07, reported by Kulak et al. [187] for ASTM A7, A36, A440, Fe37 and Fe52 steels in the clean mill scale condition. Compared with these steels, AS/NZS 3678-350 differs in terms of the yield stress and chemical composition. For example, the Australian grade 350 has a minimum yield stress of 320 to 360 MPa depending on the thickness, and a maximum carbon content of 0.22 %. In comparison, A36 steel has a minimum yield point of 250 MPa and a maximum carbon content of 0.26 %.

For the sand blasted surface finish a mean slip factor of 0.55 was obtained for the Sa 1 and Sa 3 grades, with standard deviations of 0.036 and 0.040 respectively. The characteristic slip factor was calculated as 0.50 based on the 5% fractile with 75% confidence level. There was not a significant difference between the mean slip factor for the Sa 1 and Sa 3 grades. The mean slip factor of 0.55 is greater than the value of 0.51 (standard deviation 0.09) for blast cleaned A7, A36, and Fe37 steels reported by Kulak et al. [187]. However, the mean slip factor of 0.55 is consistent with the value of 0.558 reported by Cruz et al. [183] for sand blasted S275 steel. A greater difference is observed comparing the characteristic values, with 0.50 obtained in the present study and 0.476 reported by Cruz et al. [183]. The study by Cruz et al. [183] had a greater standard deviation which explains the difference in the characteristic values.

According to the related standards, EN 1090-2 indicates a slip factor of 0.50 for blast cleaned surfaces, 0.30 for surfaces with loose rust removed by wire brushing, and 0.20 for surfaces as rolled [150]. In comparison, the *Specification for Structural Joints Using High-Strength Bolts* [138] indicates a slip factor of 0.33 for uncoated clean mill scale surfaces, and 0.50 for uncoated blast cleaned surfaces. Based on the results of this study use of a standard value of 0.30 for the clean mill scale surface would be unconservative. It should be noted that the characteristic value obtained (0.27) is dependent on the specific conditions of the test specimens, including the mill scale thickness and composition. If not identified by project specific slip factor tests, the overall safety of the design may have been ensured by the partial safety factor (1.25 [150]) or capacity factor (0.8 [139]) applied in the calculation of the slip load. For the sand blasted surface the characteristic value of the slip factor from the current study matches the standard value of 0.50.

4.4.2 Load slip behaviour and effect of surface condition

The experimental results may be explained in the context of the adhesion theory of friction, as summarised by Loo et al. [201] and Khoo et al. [202]. Figure 4.14 shows a conceptual illustration of contacting mill scale surfaces. The surface consists of a series of high points which are known as asperities. While two contacting plates appear to have a large contact area, the real contact area is much smaller. The contact is limited to selected areas known as junctions, depending on the topography.

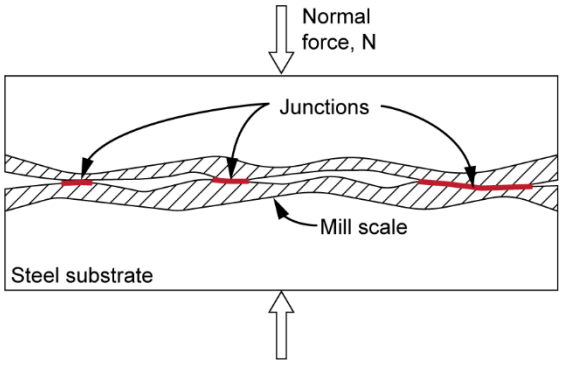

Figure 4.14. Conceptual illustration of contacting mill scale surfaces

The resistance to tangential relative movement is known as friction, and it depends on the applied normal force and the coefficient of friction [202]. The friction resistance is made up of two components, namely adhesion and deformation. The adhesion component is caused by inter-atomic attractions which develop between the contacting surfaces [202]. The deformation component is caused by plastic deformation of interlocking asperities as the surfaces slide over one another.

Oxide layers, such as mill scale, provide separation between the underlying steel surfaces, thereby reducing the adhesion which can develop [201]. However, as the surfaces start to slide over one another the oxide layer may be damaged exposing the underlying steel material. Junctions can then be formed between the exposed steel surfaces, resulting in an increased friction resistance. The real contact area is increased resulting in an increase in the friction resistance. In specimens where the mill scale layer was damaged (e.g. Figure 4.13(a,b)), the F-d curve shows an increase in the friction resistance after the initial slip (e.g. SF1t in Figure 4.11(c)). In comparison, specimens with no damage to the mill scale layer (e.g. Figure 4.13(c)) showed a sudden slip with no subsequent increase in the friction resistance (e.g. SF5t in Figure 4.11(c)). The surfaces with no damage to the mill scale layer showed little wear, other than a slightly shiny appearance around the bolts, which may be attributed to a smoothing of the surface at these locations. It may be concluded that the mill scale surfaces have a lower slip

factor due to the relatively smooth surface, in addition to the reduced adhesion resulting from the oxide layer separation.

For rough surfaces, the asperities may interlock and the friction resistance is increased by the requirement that asperities move over, or through, one another [201]. For the sand blasted specimens, the worn surfaces appeared to be shiny. This suggests that, at the contacting areas, the process of sliding had flattened the asperities, leaving behind a smoother surface which presents as a shiny surface. The increased friction resistance for the sand blasted surfaces may, therefore, be attributed to the deformation component of friction, wherein the asperities deform plastically as the surfaces slide.

In the case of the clean mill scale (Sa 0) surface, two different force-slip behaviours were observed, as explained previously. For the sand blasted surfaces, however, the force-slip behaviour was consistent across all of the specimens. The variation in the behaviour for the Sa 0 surface may be attributed to the mill scale layer which varies in several aspects, including thickness, strength and adhesion to the underlying substrate. In comparison, the sand blasted surfaces were more uniform due to the controlled sand blasting process.

4.4.3 Evaluation of digital image correlation method

By using DIC, full field displacements were obtained on the visible face of the specimen. This allowed the selection of any points for the calculation of relative displacement during post-processing. In comparison, linear variable differential transformers (LVDTs) are more limited, recording displacements only for specific points. The experimental force slip plots, for example Figure 4.11, show noise in the DIC data which originates from several sources including notably the camera sensor in combination with the external lighting. However, the DIC data clearly displays the force slip behaviour even at small slip values in mm. This force-slip behaviour was compared with the numerical simulations, to which a good match is obtained by inputting the relevant friction coefficient, as will be shown in the following Section 4.5.

4.5 Numerical simulation

Numerical simulations are conducted to ensure the load-slip (F-d) behaviour was accurately captured by the experimental program, and to investigate the parameters which affect the F-d behaviour. A numerical model is developed using ABAQUS, and it is illustrated in Figure 4.15. Following the experiments, the gap between the bolt shank and the adjacent plate is set as 1.9 mm in the numerical analysis. This provides an initial separation of 0.1 mm between the surfaces. Following the analysis of the experiment results, the slip is determined as the

relative displacement between the inner and outer plates at the centre of the bolt group as shown in Figure 4.16. The displacement of the outer plate is taken as an average value such that the slip is given by

$$slip = \delta_{P3} - 0.5\left(\delta_{P1} + \delta_{P2}\right), \tag{4.6}$$

where δ_{P1}, δ_{P2}, and δ_{P3}, are the displacement in the z-direction at the points P1, P2, and P3, respectively.

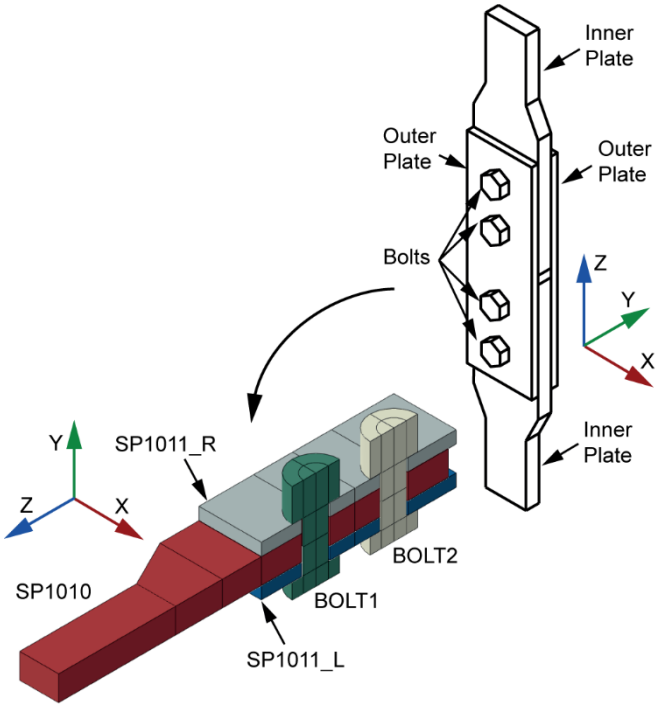

Figure 4.15. Illustration of ABAQUS numerical model

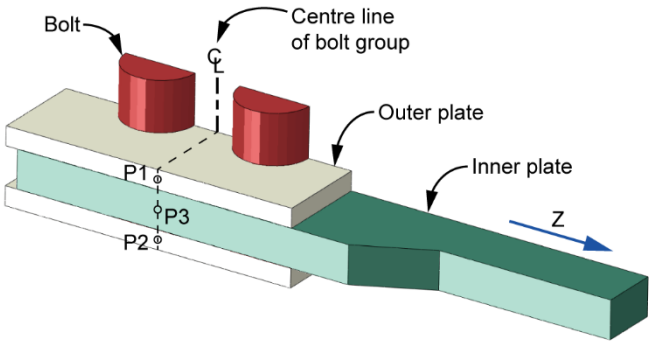

Figure 4.16. Location of displacement measurements for the calculation of slip in the numerical model

4.5.1 Material properties

A quad-linear profile was used for the steel stress strain properties based on the work of Yun et al. [203]. Following AS4100 [139] the elastic modulus was taken to be 200 GPa and the Poisson's ratio as 0.25. The relevant material parameters are given in Table 4.4.

Table 4.4. Summary of material properties

Description	Standard	Minimum yield stress (MPa)	Minimum tensile strength (MPa)	Minimum elongation (%)
Bluescope Xlerplate, 8mm thick	AS/NZS 3678-350	360	450	20
Bluescope Xlerplate, 16mm thick	AS/NZS 3678-350	350	450	20
Hobson M16x2.0Px60,8.8,HR Bolts	AS/NZS 1252	660	800	12

4.5.2 Interaction and contact property

Krolo et al. [204] outlines guidelines for modelling preloaded bolts in structural connections. The bolt preload technique was adopted with three main analysis steps. An artificial boundary condition, shown in Figure 4.17, which prevents translation of the bolt mid-section in all three directions, was applied for the first step. In the second step, the bolt load was created using the *Apply force* method, and the contact interactions were applied. The bolt surface was defined as the master surface for the bolt to plate contact pairs, as shown in Figure 4.18. An interaction property was defined for the plate to plate contact areas which had *Penalty friction* for the tangential behaviour and *Hard Contact* with the *Augmented Lagrange* enforcement method for the normal behaviour. The elastic slip was explicitly defined as 10^{-3} mm for the tangential behaviour, based on the study by Husson [205]. Similarly, for the bolt head to plate contact areas an interaction property was defined with *Penalty friction* and *Hard Contact*. The bolt shank to plate contact interaction was taken to be frictionless with *Hard Contact*. In the third step, the tension force was applied to the plate surface as shown in Figure 4.17.

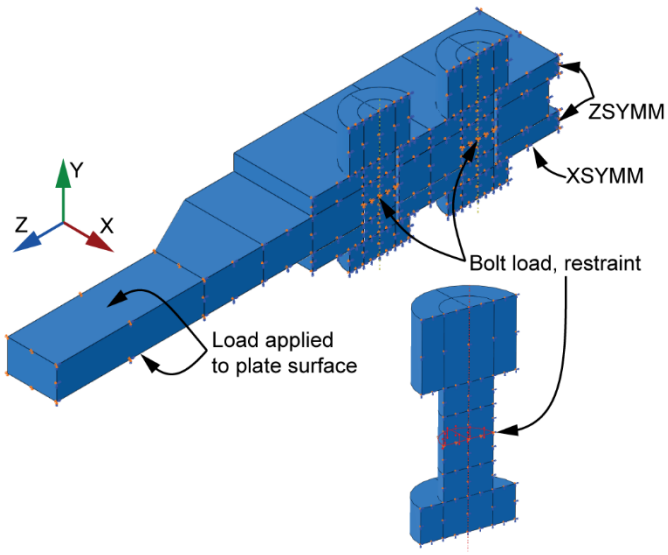

Figure 4.17. Load and boundary conditions for numerical model

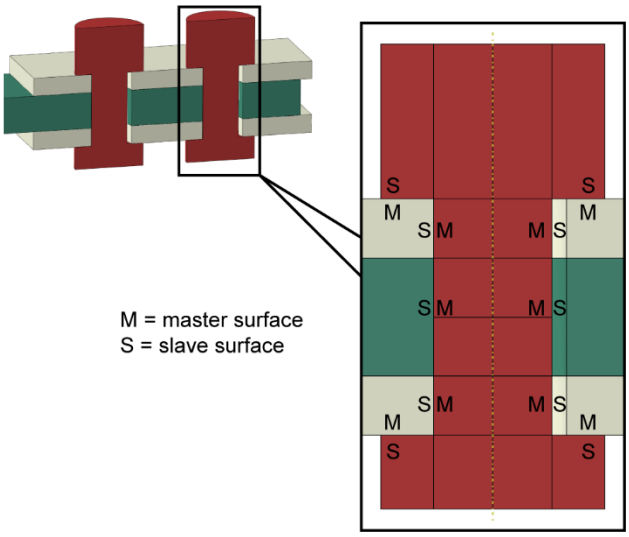

Figure 4.18. Master/slave assignments for bolt-plate contact in numerical model

4.5.3 Mesh convergence

First order 8-node linear brick, reduced integration elements with hourglass control, known as C3D8R [206], are adopted. The effect of the mesh size on the resulting force-slip behaviour is investigated by preparing numerical models with nominal mesh sizes of 4, 2, and 1 mm as shown in Figure 4.19. A friction coefficient of 0.31 is used based on the clean mill scale surface finish. The resulting force-slip (F-d) behaviour is shown in Figure 4.20. A nominal mesh size of 2 mm is found to be fine enough, with the F-d curve indistinguishable between the 2 and 1 mm mesh sizes. A mesh size of 2 mm is therefore adopted for the numerical analysis with a friction coefficient of 0.55.

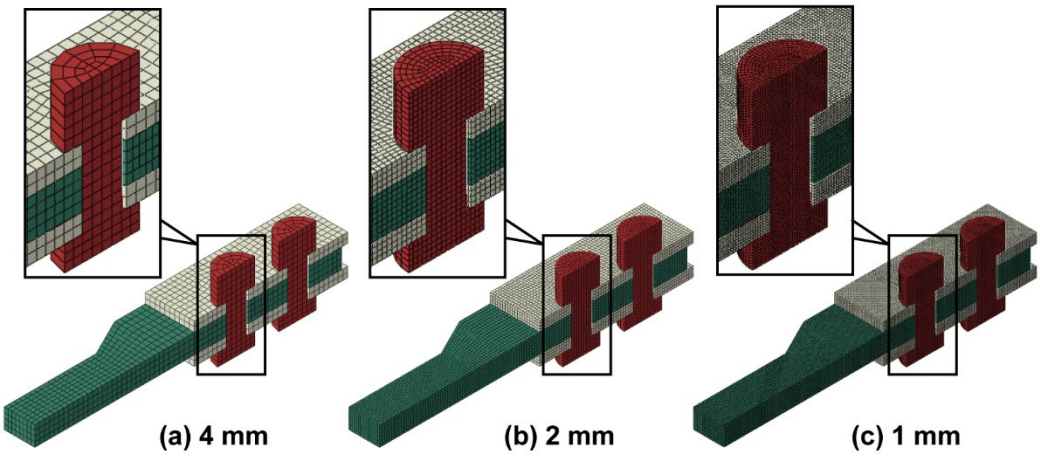

Figure 4.19. Nominal mesh sizes of (a) 4, (b) 2, and (c) 1 mm

4.5.4 Numerical calibration

Figure 4.21(a) shows a comparison between the numerical result (i) and the mean experimental results (ii and iii) for the plain mill scale surface finish. Similarly, Figure 4.21(b) shows a comparison between the numerical result (i) and the mean experimental result (ii) for the Sa 3

sand blasted surface finish. A good match is observed between the numerical and the mean experimental results. As explained previously, the experimental results show a drop in force following major slip as the testing machine was unable to maintain the force applied. This is not observed in the numerical simulation where the force does not drop due to a change in length of the specimen. It should also be noted that the present numerical model cannot capture multiple small slips as was observed for some of the clean mill scale specimens.

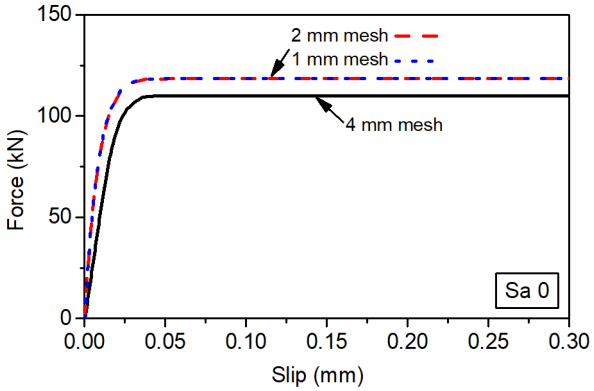

Figure 4.20. Numerical force-slip curves for different mesh sizes

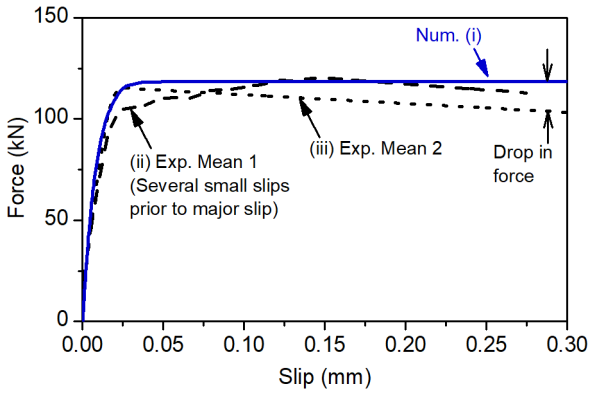

(a) Clean mill scale (Sa 0)

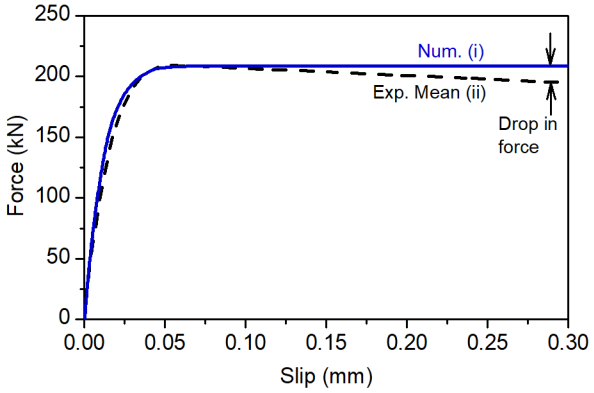

(b) Sand blasted (Sa 3)

Figure 4.21. Comparison between numerical and mean experimental data for (a) Sa 0, and (b) Sa 3 surface finish

4.6 Load-slip models and parametric study

4.6.1 Location of displacement measurement

In the preceding sections the slip is calculated based on displacement measurements taken at the centre of the respective bolt group. However, several previous studies take measurements at the end of the outer plates. In the present study, full field displacements are available due to the use of digital image correlation. A good match is obtained between the numerical and experimental results for measurements at the plate end (PE) location, for example as shown in Figure 4.22(a) for the Sa 3 specimens.

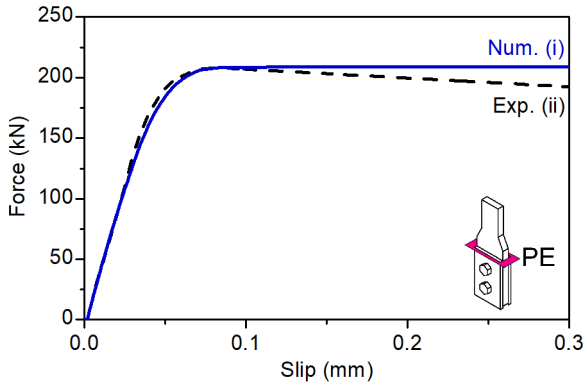

(a) Sand blasted (Sa 3) at plate ends (PE)

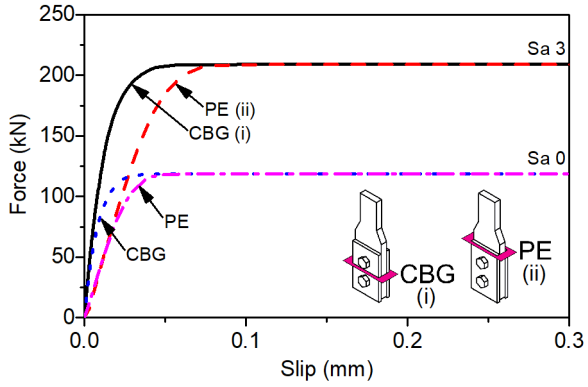

(b) Centre bolt group (CBG) and plate ends (PE)

Figure 4.22. (a) Comparison between numerical and experimental data for mean Sa 3 response at plate ends (PE), (b) Comparison between PE and centre bolt group (CBG) measurement locations based on numerical data

Figure 4.22(b) shows a comparison between the force-slip behaviour measured at the centre bolt group (CBG) (i) and PE (ii) locations based on the numerical simulations. A less stiff response was recorded at the PE location due to the additional plate elongation in the measurements at this location. While the load-slip response varies, the additional relative displacement measured at the PE location had no effect on the slip load in the present study. In the case of the Sa 3 specimens, for example, the CBG response shows major slip at 0.05

mm. In comparison, the PE response shows major slip at approximately 0.08 mm relative displacement. The peak load was unchanged and still occurred prior to the standard limit of 0.15 mm so the same slip load was recorded. Since measurement at the plate ends only affects the initial stiffness, its effect could be generalised because the displacement of the plate under uniaxial tensile load can be straightforwardly calculated.

4.6.2 Proposed load-slip model

Based on the calibrated numerical results, the initial force-slip behaviour at the centre bolt group location can be approximated by an exponential function of the form

$$F(d) = A\left[1 - \exp\left(\frac{-d}{B}\right)\right], \tag{4.7}$$

where d is the slip (mm), F is the applied load (kN), and A and B are parameters. This function passes through the origin and then increases to become asymptotic to the value of A which is the upper limit. The parameter B controls the rate of increase towards the upper limit.

Figure 4.23 shows the proposed model for the Sa 0 and Sa 3 specimens in comparison with the existing model [145]. The y-axis shows the normalised load (F/F_{sm}) which is the applied shear force divided by the slip resistance. Compared to the existing model [145], the proposed exponential model provides a more accurate representation of the initial slip stiffness, which may be desirable for the design of slip-critical connections.

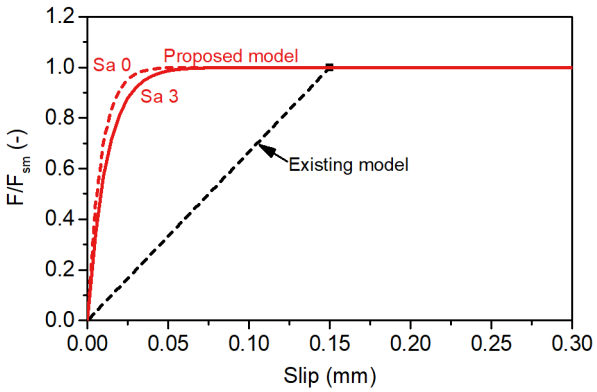

Figure 4.23. Comparison of proposed and existing model [145]

Figure 4.24(a) shows a good match between the fitted curves and the numerical data for the CBG measurement position. The fit to the numerical data provides a reasonable fit to the experimental data and may be preferred for design purposes when the reduction in load following slip is not relevant. For example, Figure 4.24(b) applies to the Sa 3 sand blasted specimens and shows the exponential fit to the numerical data along with the experimental data.

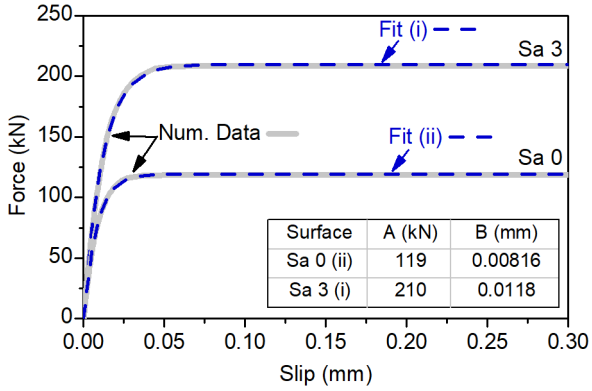

(a) Sa 0 & Sa 3 (CBG)

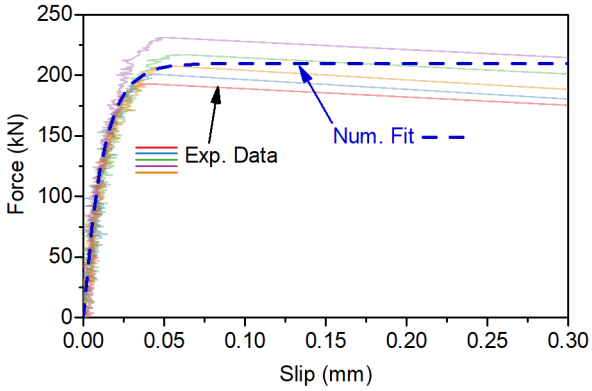

(b) Sa 3 (CBG)

Figure 4.24. (a) Exponential fit to numerical data, and (b) Sa 3 exponential fit compared with experimental data

4.6.3 Slip factor and bolt preload

The slip factor and preload are varied in the numerical model to investigate the effect on the parameters A and B in the proposed model. For each numerical simulation the proposed exponential model is fitted to the resulting force-slip curve. Figure 4.25 shows the variation of A with the slip factor (a) and bolt preload (b). Similarly, Figure 4.26 shows the variation of B. The parameters A and B depend on the slip factor and the preload. Fitting a curve to the numerical data, the parameter A may be estimated as

$$A(\mu, N_t) \approx 3.99 \mu N_t \,, \tag{4.8}$$

where μ is the slip factor, and N_t (kN) is the bolt preload. It is apparent that Equation (4.8) closely resembles the existing empirical formula for the slip resistance of a bolted steel connection [187]. Therefore, A may be more accurately given as

$$A(\mu, N_t) = n_s n_b \mu N_t \,, \tag{4.9}$$

where n_s is the number of slip planes, and n_b is the number of bolts. Similarly, the parameter B may be estimated as

$$B(\mu, N_t) \approx \frac{N_t}{9.407 \times 10^3 \, kN/mm} + 1.377 \times 10^{-2} \, mm.\mu - 6.416 \times 10^{-3} \, mm \, . \tag{4.10}$$

The empirical formula for A and B, i.e., equations (4.9) and (4.10), provide a reasonable fit to the numerical data as shown in Figure 4.25 and Figure 4.26.

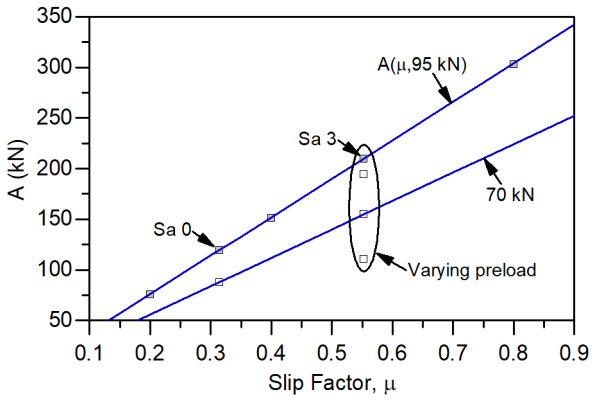

(a) Slip Factor

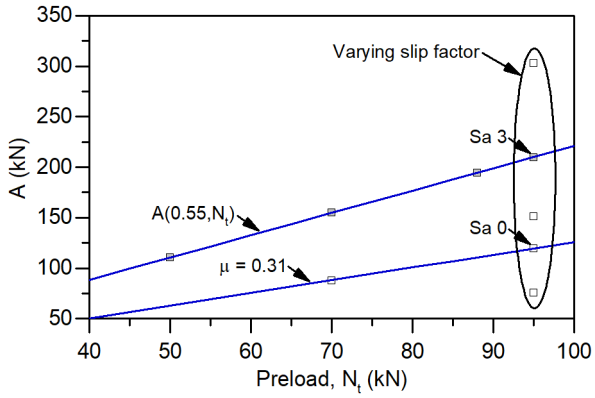

(b) Preload

Figure 4.25. Variation of A with slip factor (a) and preload (b)

4.6.4 Application of proposed model

Three experimental force-slip curves are selected from the literature to demonstrate the application of the proposed model to other materials [149, 182, 184]. Table 4.5 presents a summary of the relevant parameters for the selected force-slip (F-d) data. The F-d curves apply to S275 [149], S355 [182] and 1.4404 stainless steel [184]. Figure 4.27 shows the proposed model (Equation (4.7)) fitted to the selected data. A good fit is shown for the S355 and 1.4404 stainless steel materials. For the S275 material the proposed model (Equation (4.7)) does not fit the data as well. This may be due to the use of the plate end (PE) measurement location in the referenced study [149], whereas the proposed exponential model was developed for the centre bolt group (CBG) location.

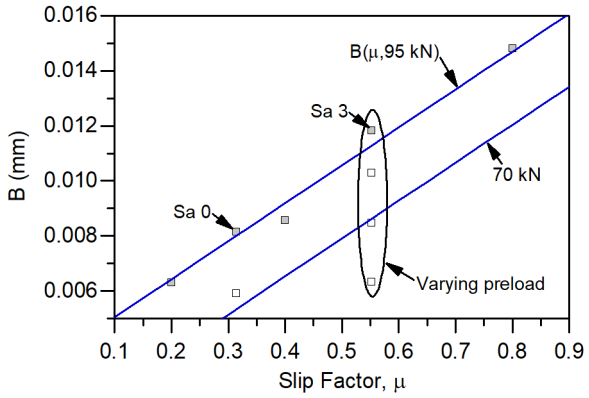

(a) Slip Factor

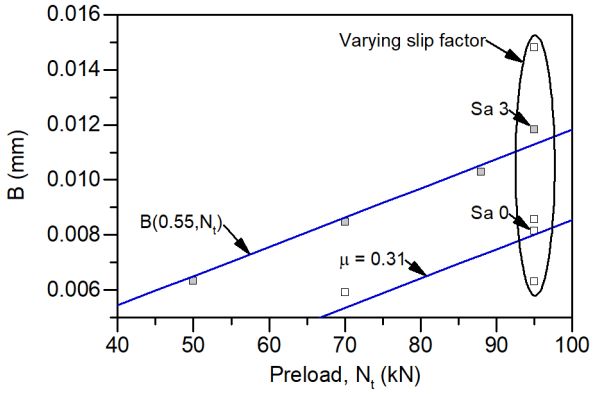

(b) Preload

Figure 4.26. Variation of B with slip factor (a) and preload (b)

Table 4.5. Summary of parameters for selected load-slip data
PE – plate edge, CBG – centre bolt group

Ref.	Steel material	Surface finish	Slip factor	Bolt size / preload (kN)	Location	Proposed model (Equation (4.7)) fit		Proposed empirical formula	
						A (kN)	B (mm)	A (kN)	B (mm)
[149]	S275	Sa 2.5	0.558	M20 / 170	PE	452	0.0888	379	0.0193
[182]	S355J2C+N	Sa 2.5	0.81	M20 / 172	CBG	568.5	0.0410	557	0.0230
[184]	Stainless steel, 1.4404	Grit blasted	0.55	M16 / 88	CBG	188	0.0176	194	0.0105

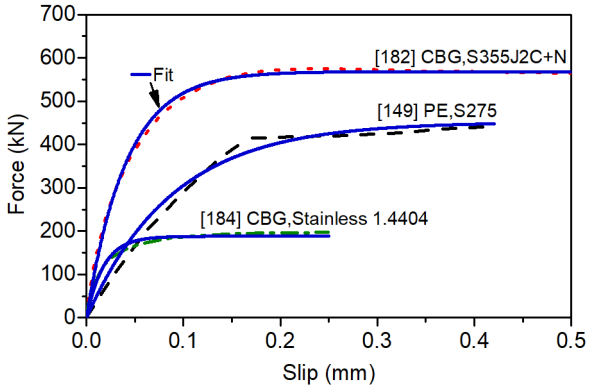

Figure 4.27. Proposed model fitted to data from the literature

Table 4.5 shows the parameters *A* and *B* which result from fitting the proposed exponential model (Equation (4.7)) to the selected data. For comparison, the parameters are calculated using the proposed empirical formula, i.e., equations (4.9) and (4.10). The empirical formula for *A* (Equation (4.9)) matches the CBG curve fit values well. However, if the PE measurement location is used then the value of *A* is underestimated. This occurs because elongation of the inner plate is incorporated in the slip measured at the plate end location. Due to the 0.15 mm slip limit specified in the standard [150], the PE measurement location resulted in an underestimate of the slip resistance in the referenced study [149]. Therefore, although Equation (4.9) (p.101) provides a good estimate of the slip resistance and, hence, parameter *A*, it is only applicable for the CBG location. In comparison, the proposed empirical formula for parameter *B* (Equation (4.10), p.102) does not match the curve fit values. This may be due to the different materials which exhibit different initial F-d behaviours. For design purposes, the value of *B* may be obtained through experiments, as was done in the present study for the G350 steel material.

4.7 Summary

The shear load-slip behaviour of AS/NZS 3678-350 steel (G350) material was investigated in this study by conducting experiments and numerical simulations. The test results were discussed and explained in terms of the adhesion theory of friction. The main findings are summarised as follows.

1. The characteristic slip factors for the AS/NZS 3678-350 (G350) steel material are 0.27 and 0.50 for the clean mill scale (Sa 0) and Sa 3 sand blasted surfaces, respectively. This matches the standard value of 0.50 well for the sand blasted surface, however, the standard value of 0.30 for the clean mill scale surface overestimates the slip factor by 11 % based on the specimens in the present study. The slip factor was shown to be insensitive to the

surface finish, where the degree of sand blasting, i.e., Sa 1 and Sa 3, is defined by visual assessment to the ISO 8501-1 standard.

2. The bolt preload can be reasonably controlled using the torque method, as confirmed by the relatively low standard deviation obtained. The use of digital image correlation to determine slip displacements was demonstrated to be effective and is recommended for use in slip factor testing.

3. The existing model [145] gives a conservative prediction of the initial slip stiffness. A more accurate empirical model is proposed for the load-slip behaviour of the standard slip factor test specimen [150], depending on the surface condition. The exponential empirical model provides a good fit to the data with slip measured at the centre of the bolt group (CBG).

4. The proposed model can be applied in the development of slip critical connections. For example, the model may be applied to inter-module connections in modular steel buildings, for which adequate site assembly tolerances are required while limiting slip displacement. In this application an accurate model for the initial slip is important because the large number of connections can result in large cumulative displacement over the building height.

Chapter 5 New post-tensioned (PT) connection: Experimental and numerical studies[1]

5.1 Introduction

In Chapter 2 it was identified that the design and construction of reliable inter-module connections is a major challenge. Therefore, in this chapter, a new post-tensioned (PT) inter-module connection is developed and investigated. The connection permits vertical connection between modules without the requirement for external access. While the proposed connection may offer improvements in terms of constructability, the structural performance in shear remains to be demonstrated. The main objective of this chapter is, therefore, to investigate the structural performance of the proposed connection. An experimental study is conducted to establish the shear force displacement behaviour by applying quasi-static monotonic loading. The initial portion of the load-slip behaviour is focused on in order to enable the development of a suitable model for the initial slip stiffness. Numerical analysis is completed and the model is calibrated based on the experiments. The main parameters influencing the slip behaviour, including the bolt preload, slip factor and contact area, are investigated. Following the parametric study based on the numerical simulations, an empirical model is proposed for the initial shear load slip behaviour of the proposed connection.

5.2 Proposed post-tensioned (PT) connection

The proposed connection consists of a shear key combined with a post tensioned tie rod which is located inside of the hollow steel sections (HSS) that form the module columns. The conceptual detail is illustrated in Figure 5.1. The shear key component is made up of an upper and lower square hollow section, each of which is shop welded to a plate (P1). The plate P1 has a central hole to allow a threaded rod to pass through. An access opening is provided in the module columns, and a plate P2 is shop welded within each of the columns as shown. During site assembly, the shear key component is placed in the lower module column, and the lower module is lifted and installed in its final location within the overall structure. Then, the upper module is lifted and placed on top of the lower module with the shear key serving to locate the upper module in position as it is lowered by the crane. Once the upper module is

[1] The related work in Chapter 5 was published in the Journal of Constructional Steel Research:

Lacey AW, Chen W, Hao H, Bi K, Tallowin FJ. Shear behaviour of post-tensioned inter-module connection for modular steel buildings. J Constr Steel Res. 2019;162:105707. https://doi.org/10.1016/j.jcsr.2019.105707

placed, the opening in the HSS column wall allows the tie rod to be installed and tensioned from inside the modules.

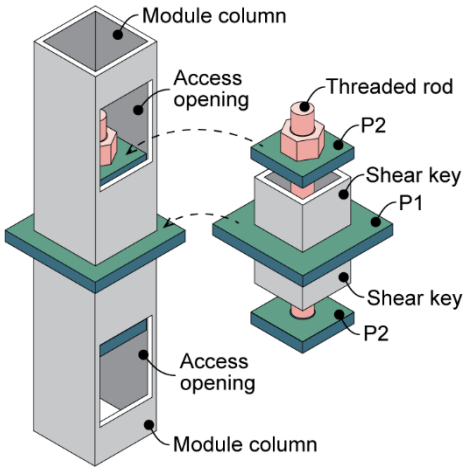

Figure 5.1. Proposed post-tensioned (PT) inter-module connection

The proposed connection offers a simple detail which may be considered visually appealing because the majority of the connection components are hidden from external view. The access opening provided in the column wall allows the tie rod to be installed from inside the module such that the requirement for working at heights during site installation is reduced. If disassembly of the structure is considered, the module may be simply relocated after the tie rod component is removed.

Regarding the potential disadvantages, the present detail allows for only vertical connection between modules. A detail which provides horizontal connection could be devised, however, this is beyond the scope of the present study. The detail has potentially awkward shop welding details where the plate is welded inside of the hollow section. The welding process was found to be reasonable for the column size adopted in the following experimental study (75 mm). The use of a single tie rod may require a large diameter rod which may be difficult to tension. To allow for tensioning of the tie rod during site installation, access openings are required in the internal finishes of the module and in the steel column wall. Care should be taken in the selection of the opening size to permit access to tension the rod, and ensure the strength of the column is not compromised.

Inter-module connections with access holes may be classified as semi-rigid connections, allowing a stable cyclic frame response with large deformation capacity [53]. However, the reduction in the loading capacities of the steel hollow section column must be considered in design. The opening shape may be refined to limit stress concentrations and suit the tensioning procedure. In addition, cover plates may be provided to enhance the visual appearance, protect

the connection components from the elements, and strengthen the column as required. It should be noted that the access openings may be eliminated completely if the tensioning rod extends the full building height with the use of couplers, as in the work of Zheng et al. [207]. However, this would require external access during site assembly and the protruding tie rods may pose a safety issue. Overall, the proposed connection offers significant advantages, which outweigh the disadvantages.

5.3 Experimental study

5.3.1 Method and specimens

To investigate the behaviour of the proposed connection, an experimental program was performed at Curtin University. Six connection specimens were prepared with varying surface finish, torque controlled threaded rod preload and contact surface area as shown in Table 5.1.

Table 5.1. List of connection specimens and associated parameters

Specimen	Surface Finish	μ_m	Torque (Nm)	Preload (kN)	Contact Surface Area
NSB-150	Clean mill scale	0.31	150	45	Standard (1530 mm^2)
NSB-250	Clean mill scale	0.31	250	81	Standard (1530 mm^2)
Sa3-150	Sa3 sand blast	0.55	150	45	Standard (1530 mm^2)
Sa3-250	Sa3 sand blast	0.55	250	81	Standard (1530 mm^2)
Sa3-150-IA	Sa3 sand blast	0.55	150	45	Increased (3474 mm^2)
Sa3-250-IA	Sa3 sand blast	0.55	250	81	Increased (3474 mm^2)

The specimens were prepared to be loaded in compression using a Shimadzu 300kN universal testing machine (UTM), as shown in Figure 5.2. Each specimen consisted of an inner part and two outer parts. As shown in Figure 5.3(b) the inner part had a central plate (P1) with an inner SHS welded on either side. The inner SHS had an outer width of 59 mm and was fabricated from 6 mm thick plate, and P1 was fabricated from 8 mm thick plate with a central 24 mm diameter hole through which the M20 threaded rod passed. As shown in Figure 5.3(a), each outer part had a plate (P2) with a 75x75x6 SHS welded on one side. P2 was fabricated from 12 mm thick plate and had a 24 mm diameter hole through which the M20 threaded rod passed. The P2 plates were welded externally to the 75x75x6 SHS. This allowed an easier external fillet weld between P2 and the 75x75x6 SHS for the experimental specimens, without significantly affecting the shear behaviour. Prior to loading, the inner and outer parts were assembled by inserting the M20 threaded rod through, and tensioned by tightening the M20 nut on one end. One at a time, the specimens were placed into the UTM with the two outer SHSs supported on the lower compression plate via two steel bearings, and load applied by the top compression plate to the central plate P1. A maximum load of 200 kN was applied,

starting from zero and increasing at a rate of 0.15 kN/s. A nominal 4 mm gap was provided between the inner and outer SHSs such that the applied load was initially resisted by friction between the outer SHSs and the central plate P1.

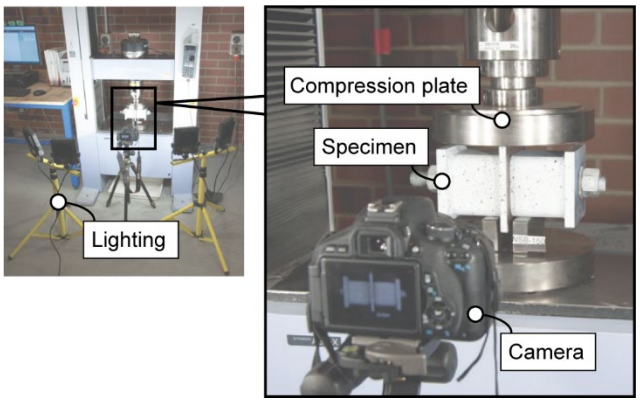

Figure 5.2. Setup for experimental testing

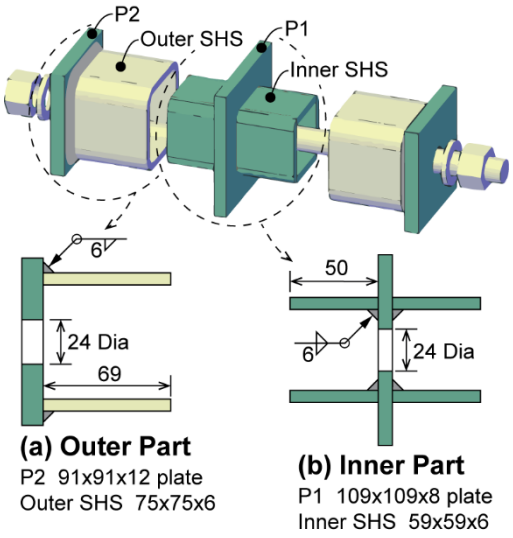

Figure 5.3. Illustration of standard specimen assembly showing (a) outer part and (b) inner part
All dimensions in mm.

All the specimens used the same steel materials, namely 75x75x6 C350 hollow steel sections, grade 350 hot rolled plates, and property class 8.8 threaded rods. 6 mm fillet welds were adopted generally as shown in Figure 5.3 and Figure 5.4, and the minimum nominal tensile strength of the weld metal was specified as 430 MPa. The contact surface area was increased by welding 6 mm thick plate around the outside of the outer SHSs as shown in Figure 5.4. This increased the apparent contact area from 1530 mm^2 for the 75x75x6 SHS to 3474 mm^2 for the SHS plus plate section.

Before testing the specimens were assembled and the tie rods were tensioned using a torque wrench (Figure 5.5a). During tensioning, the specimen was clamped with acrylic shims to ensure the correct positioning of the inner hollow section (Figure 5.5). The inner hollow section was positioned to give the maximum gap of 4 mm between the inner and outer hollow sections nearer the lower compression plate of the UTM (Figure 5.5c). This ensured that the connection was operating in friction mode at the start of the test.

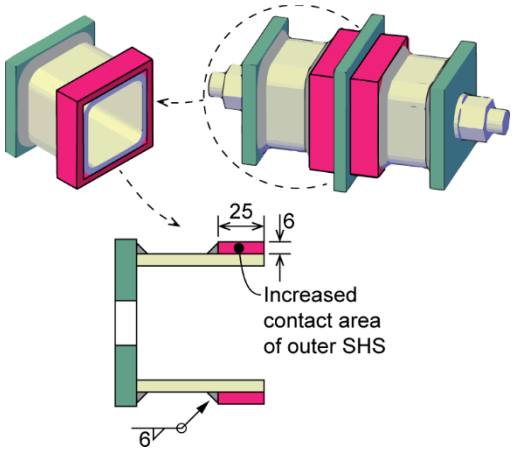

Figure 5.4. Illustration of specimen assembly with increased contact area
All dimensions in mm.

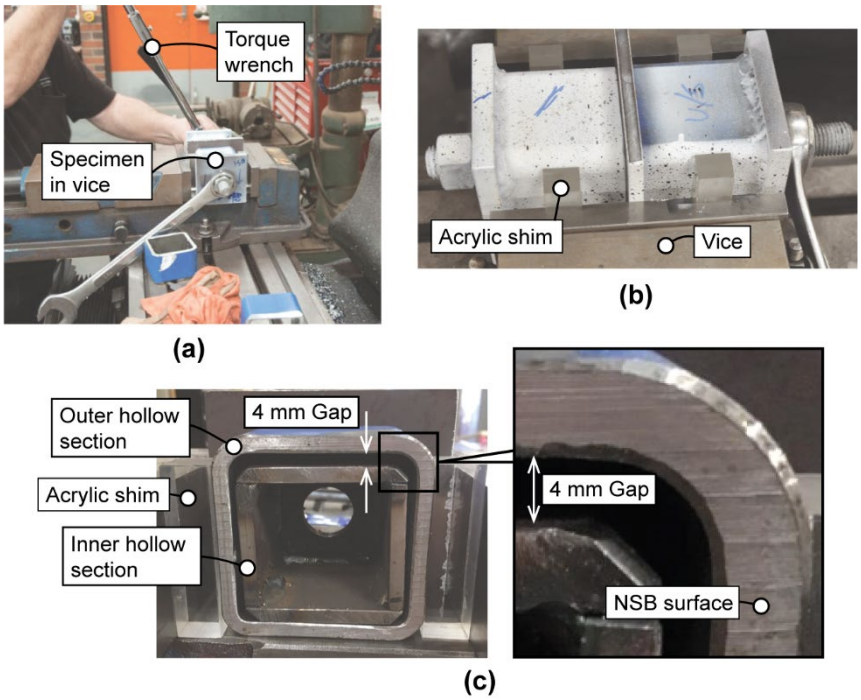

Figure 5.5. Assembly of test specimens

5.3.2 Slip factor

Slip factor testing was conducted in Chapter 4 following the method given in Annex G of EN 1090-2 [150]. Fifteen specimens were tested with three different surface finishes – clean mill scale, and sand blasted grade Sa1 and Sa 3 to Australian standard *AS 1627.4* [193]. The clean mill scale surface specimens gave a mean slip factor of 0.3146 with a standard deviation of 0.024. The Sa 3 sand blasted specimens gave a mean slip factor of 0.5525 with a standard deviation of 0.040. Further details on the slip factor testing are provided in Chapter 4.

5.3.3 Torque controlled preloading

Assembly tests were completed to determine the relationship between the torque applied to the nut and the resulting preload in the threaded rod. A custom 200 kN barrel load cell was used to measure the load in the threaded rod. Prior to the assembly test, the load cell was calibrated using a Shimadzu AGS-300kNX universal testing machine (UTM). The load cell was placed in the UTM and a compression load applied. The load cell signal was recorded for selected force values. The resulting linear fit was used to determine the force measured by the load cell based on the output signal. The linear fit was then checked by loading from 0 to 200 kN at a rate of 1 kN/s using the UTM. Figure 5.6 plots the UTM force against the 200 kN barrel load cell force, showing a reasonable match between the two. For example, Figure 5.7 shows the percentage error calculated relative to the UTM measurement, which was designated Class AA to AS 2193 [208] indicating a maximum error of ± 0.5 %. As shown, the percentage error inherent in the linear fit was approximately 16 % for a force of 45 kN, and 3.3 % for a force of 81 kN. In the following assembly tests, the forces measured with the barrel load cell were corrected for the known percentage error, such that only the repeatability error remained.

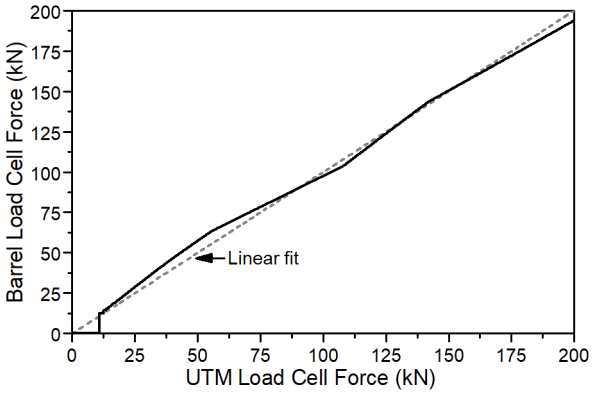

Figure 5.6. Plot of force measured by custom barrel load cell against force measured by universal testing machine (UTM) load cell

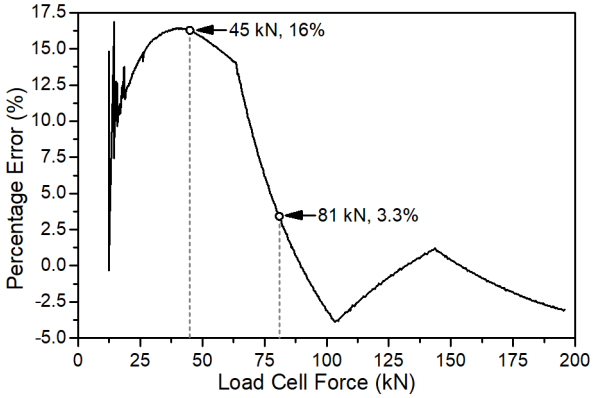

Figure 5.7. Percentage error in custom barrel load cell force calculated with respect to the UTM load cell force

The setup for the assembly test is illustrated in Figure 5.8. A length of M20 threaded rod was held in a vice by the lower nuts. Rotation of the rod was restricted using two nuts tightened against one another. Additional tests were completed in which the lower nut was welded to the threaded rod to ensure rotation of the rod was not permitted. The custom load cell was positioned in between the lower and upper nuts. During the test the upper nut was tightened using a click type torque wrench (Sidchrome ½" drive, 30-270 Nm). The rod force and nut rotation were recorded for each applied torque value. Figure 5.9 shows an example of the variation of the rod force with time. The applied torque values are labelled at the relevant times.

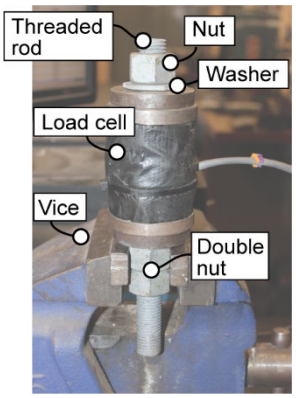

Figure 5.8. Setup for threaded rod assembly test using custom load cell

Figure 5.10 shows the average rod force plotted against the applied torque. An initial torque of 40 Nm was applied to snug tighten the nut. A peak rod force was reached as the nut was tightened, after which the rod force slightly decayed. Figure 5.10 plots the sustained rod force, which is the force approximately sixty seconds after the torque was applied. The sustained value gives an indication of the rod force applicable in the following connection shear tests. Considering a torque of 250 Nm the mean rod load was 81 kN with a standard deviation of 2.7 kN. For a torque of 150 Nm the mean rod load was 45 kN with a standard deviation of 2.3 kN.

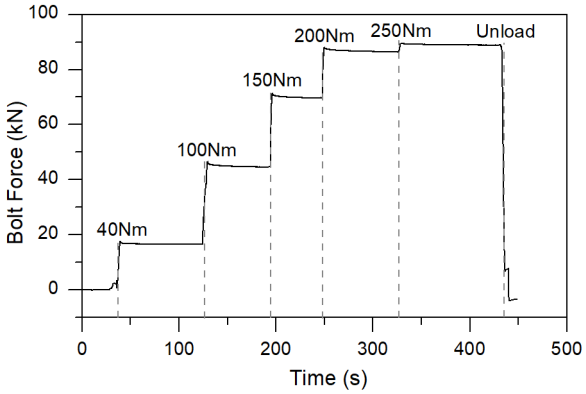

Figure 5.9. Example plot of load cell measured rod force against time

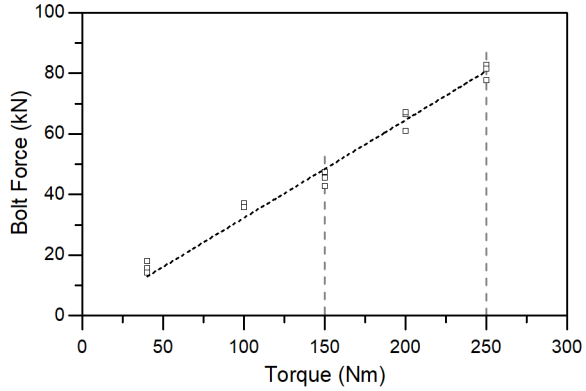

Figure 5.10. Plot of rod force against torque

5.3.4 Results and analysis

Vertical displacements were calculated based on the images recorded throughout the test. The Matlab program, ncorr [198, 209], was adopted for the digital image correlation (DIC) used to evaluate the displacements. The accuracy of the DIC method has been verified with reference to strain gauge measurements in the works by Yuan et al. [199, 200, 210]. As an example, Figure 5.11 shows the vertical displacements obtained for specimen NSB-150 at the nominated time increment. For each time increment the vertical displacements were extracted at the points P1 to P3 as illustrated in Figure 5.11. The displacements at points P1 and P3 were averaged and subtracted from the displacement at point P2 to obtain the relative displacement, which is referred to as the slip. This was repeated for each time increment to produce the force-slip plot for each specimen as shown in Figure 5.13 and Figure 5.14.

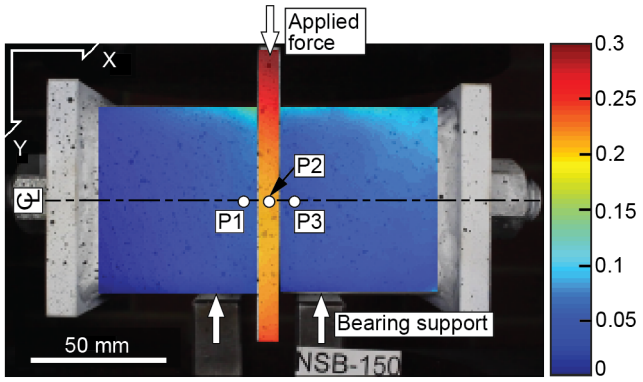

Figure 5.11. NSB-150 vertical displacement (mm) at t=295s (46 kN) showing location of displacement measurements for calculation of slip

For the standard slip factor test given in Annex G of EN 1090-2 [150], the slip load is typically taken to occur at a slip displacement of 0.15 mm (iii), unless there is an earlier peak (i) or sudden slip (ii), as illustrated in Figure 5.12. Following a similar approach, the slip load was determined for each specimen based on the experimental force-slip curves. In Figure 5.13 and Figure 5.14 a star symbol (☆) is used to denote the location of the slip load on the force-slip curve, and the method used to identify the location is noted. For example, Figure 5.13(a) shows the slip load for NSB-150 was identified by the change in the slope of the force-slip curve, in addition to review of the DIC displacements, which was also used for the specimens shown in Figure 5.13(b, c) and Figure 5.14(a, b). In comparison, Figure 5.13(d) shows the slip load for Sa3-250 was identified as the peak value in the force-slip curve. Figure 5.13(d) also shows a low initial slope of the force-slip curve for Sa3-250 which was caused by rotation of the specimen, and is discussed further in Section 5.5. For each specimen the slip load represents the point at which there was a sudden change in the slope of the experimental force-slip curve. Table 5.2 gives a summary of the slip load and the corresponding relative displacement when the slip occurred.

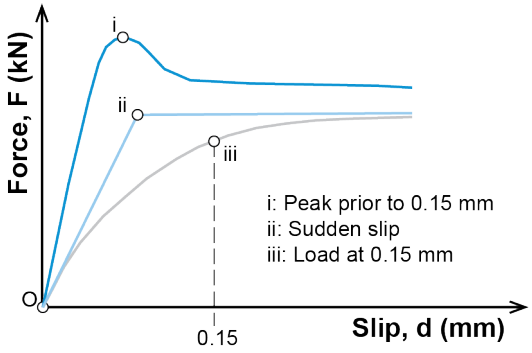

Figure 5.12. Force-slip behaviours in slip factor test
Adapted from [138, 182].

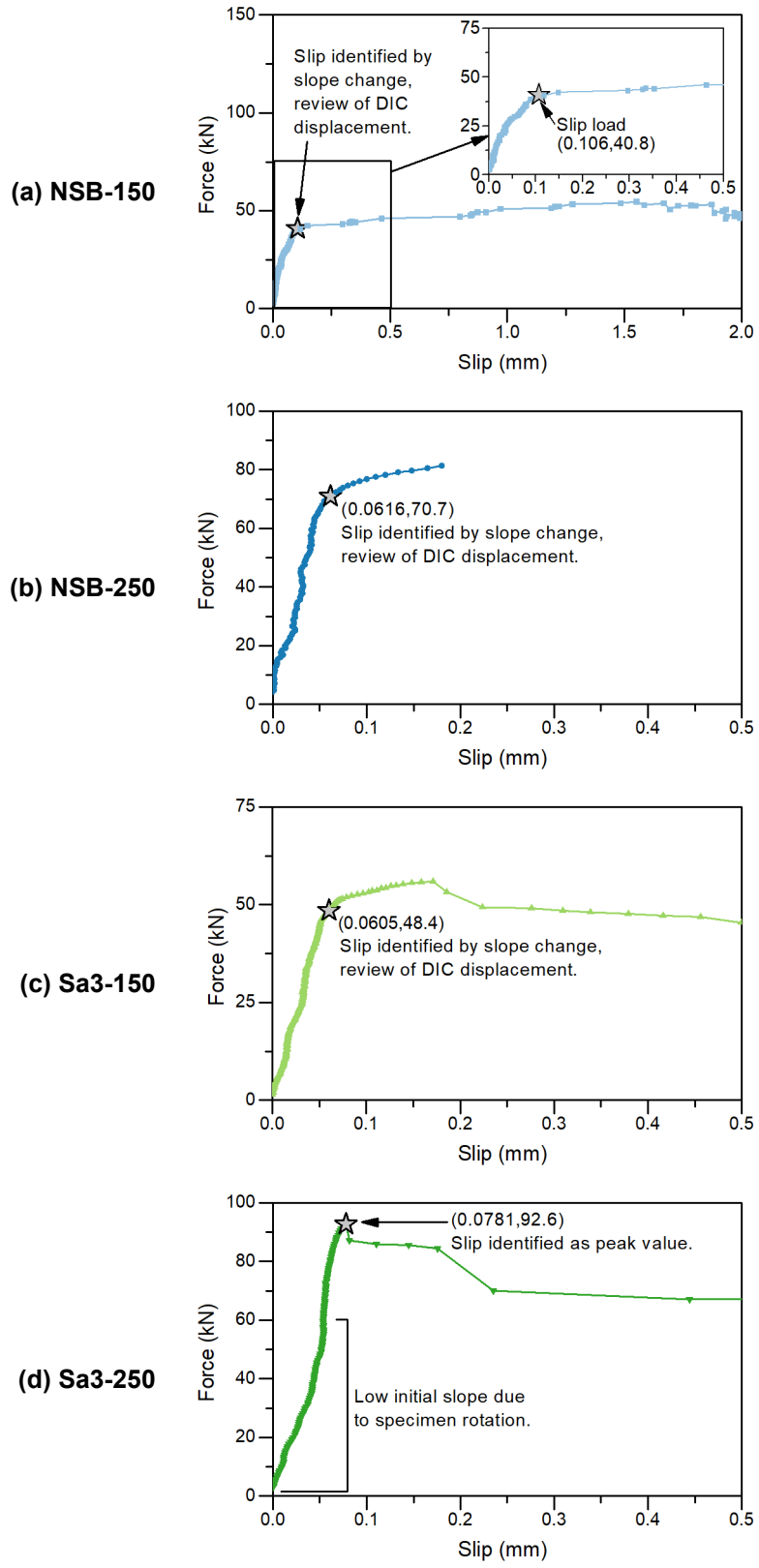

Figure 5.13. Experimental force-slip plots showing slip load (☆)

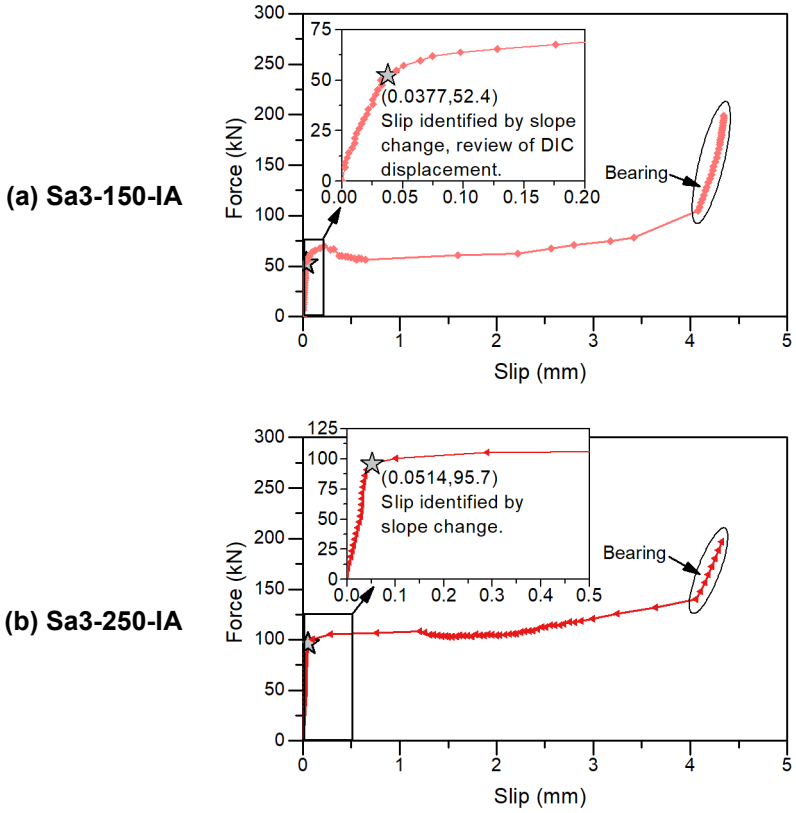

Figure 5.14. Experimental force-slip plots showing slip load (☆)

Table 5.2. Experimental slip load and corresponding relative displacements

Specimen	Slip Load (kN)	Slip (mm)
NSB-150	40.8	0.106
NSB-250	70.7	0.0616
Sa3-150	48.4	0.0605
Sa3-250	92.6	0.0781
Sa3-150-IA	52.4	0.0377
Sa3-250-IA	95.7	0.0514

Comparing the slip loads between the specimens, the following observations were made with respect to the effect of the bolt preload, contact area, and surface finish. Increasing the preload from 45 to 81 kN increased the slip load from 40.8 to 70.7 kN (73%) for the plain surface finish (NSB), 48.4 to 92.6 kN (91%) for the Sa 3 finish, and 52.4 to 95.7 kN (83%) for the Sa 3 finish with increased surface area. Increasing the apparent contact area from 1530 to 3474 mm^2 increased the slip load from 48.4 to 52.4 kN (8.2%) for Sa3-150, and 92.6 to 95.7 kN (3.4%) for Sa3-250. The Sa 3 surface finish gave a slip load that was increased from 40.8 to 48.4 kN (19%) for the 45 kN preload, and 70.7 to 92.6 kN (31%) for the 81 kN preload, compared to the clean mill scale surface. The results showed that the slip load was significantly

affected by the preload and the surface finish. In contrast, the apparent contact area had a relatively small effect on the slip load. Discussion on the cause of these observations is provided in Section 5.4.3 (p.121).

After testing, the specimens were disassembled to examine the faying surfaces. For the central plate P1, wear was identified as the shiny smoothed areas in the shape of the contacting outer SHS. This is shown in Figure 5.15 for the NSB-250 (b), Sa3-250 (d) and Sa3-250-IA (f) specimens. For the NSB specimens, the clean mill scale layer was not damaged (Figure 5.15b). For the specimens with increased contact area, e.g., Sa3-250-IA, deformation of the outer SHS could be seen in the smoothed surface left on the central plate P1, as shown in Figure 5.15(f). For the outer SHS, wear was mostly observed at the top, where load was applied to the central plate by the testing machine compression plate. Similar to the central plate, the wear generally presented as shiny smoothed areas. Fine tracks were observed on the surface of the outer SHS for some specimens, which appeared to have been ploughed by the high points at the interface. Ploughed tracks are evident in Figure 5.15(a) and (c) for the NSB-250 and Sa3-250 specimens, respectively.

5.4 Discussion and evaluation of experimental results

5.4.1 Accuracy

The preload was controlled using the torque tightening method, wherein the preload was related to the torque applied to the nut by a torque wrench. This method of preloading is commonly used internationally [192]. In Australia, however, use of this method is less common because of uncertainty in the reliability of the method when applied to locally available materials [192]. An indication of the expected accuracy can be found in the standard texts. For example, the *Machinery's Handbook* [211] gives an indicative accuracy of ± 25 % for the torque method. As shown in Section 5.3.3 (p.112), for the 250 Nm applied torque, the mean preload was 81 kN with a standard deviation of 2.7 kN, which gave a 95 % confidence interval of 81 kN ± 3.8 %. For the 150 Nm torque, the 95 % confidence interval was 45 kN ± 5.8 %. Overall, in the present study, an accuracy of ± 5.8 % was achieved using the torque method for preloading of the threaded rod. In comparison with the suggested accuracy of ± 25 % for the torque method [211], the achieved accuracy of ± 5.8 % demonstrates good control of the preload during the experiments.

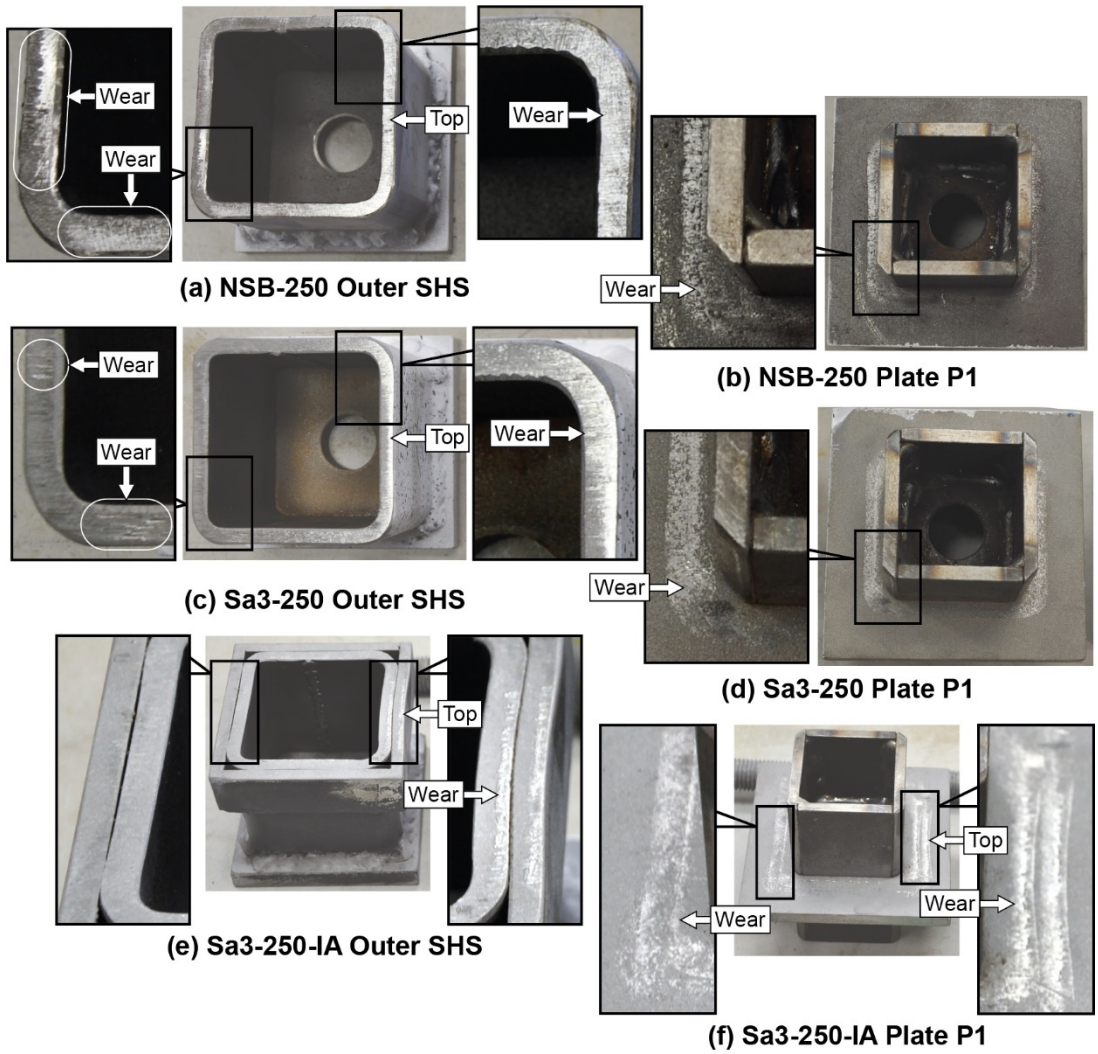

Figure 5.15. Photos of faying surfaces after testing

In Chapter 4, slip factor testing was completed to establish the slip factor for the G350 steel plate interfaces. The mean slip factor for the clean mill scale surface was 0.3146, and the standard deviation was 0.02365, based on nine measurements of the slip load (Table 4.3, p.90). The 95% confidence interval for the mean slip factor can be given as [212]

$$\mu_m - 1.96\frac{s}{\sqrt{n}} < \mu < \mu_m + 1.96\frac{s}{\sqrt{n}}, \tag{5.1}$$

where μ_m is the mean slip factor from the nine samples, s is the sample standard deviation, and n is the number of samples. Following Equation (5.1) the 95% confidence interval for the clean mill scale surface can be given as 0.31 ± 0.015, or 0.31 ± 4.9% expressed as a percentage of the mean. Similarly, the 95% confidence interval for the Sa 3 sand blasted surfaces can be given as 0.55 ± 5.6 %.

The variation of the slip factor was due mainly to variation of the bolt preload and the surface profile. For further analysis it is desirable to estimate the proportion of the slip factor variation

which was due only to the surface profile. This requires an estimate of the variation of the bolt preload. The bolt preload for the slip factor tests was torque controlled based on a manufacturer supplied k-factor (Equation (4.1)). The mean k-factor for the M16 bolts used for the slip factor tests (§4.3.3, p.82) was 0.136, and the coefficient of variation was 0.044, based on five assembly tests completed by the manufacturer in accordance with EN 14399-2 [213]. The standard deviation was therefore 0.0060, and the 95% confidence interval was ± 3.9% of the mean. This gives an indication of the uncertainty of the preload in the slip factor tests. Given that the slip factor was calculated as a ratio between the slip load and preload, the variation due to the surface profile for the clean mill scale specimens can be estimated using the confidence intervals as [214]

$$\sqrt{(0.049)^2 - (0.039)^2} = \pm 3.0\%, \tag{5.2}$$

where 0.049 represents the confidence interval for the slip factor, and 0.039 represents the confidence interval for the preload. Similarly, for the Sa 3 sand blasted specimens, the variation due to the surface profile can be estimated as

$$\sqrt{(0.056)^2 - (0.039)^2} = \pm 4.0\%. \tag{5.3}$$

Finally, the uncertainty in the slip load for the post-tensioned connection specimens can be estimated by combining the variation of the rod preload with the variation of the surface profile. Hence, the maximum uncertainty was estimated as

$$\sqrt{(0.058)^2 + (0.040)^2} = \pm 7.0\%, \tag{5.4}$$

where 0.058 represents the confidence interval for the rod preload resulting from the 150 Nm torque and 0.040 represents the confidence interval for the sand blasted surface slip factor. Similarly, for the specimen with a clean mill scale surface and 81 kN preload, i.e., NSB-250, the variation of the slip load was estimated as

$$\sqrt{(0.038)^2 + (0.030)^2} = \pm 4.8\%. \tag{5.5}$$

This uncertainty should be considered when evaluating the effect of the investigated parameters of preload, slip factor and contact area in the following sections.

5.4.2 Load-slip behaviour

The load-slip curves given in Figure 5.13 (p.116) and Figure 5.14 (p.117) generally show a consistent behaviour. As the load was applied, the slip gradually increased as a result of small relative displacements between the central plate and the outer SHS. The applied load slowly increased at a rate of 0.15 kN/s until the friction resistance was exceeded and there was a large

slip. After this major slip a peak and corresponding reduction in force can be seen in the load-slip curve which can be attributed to the difference between the static and kinetic friction coefficient for the faying surfaces. The slip then continued to increase with little change in the force until the bolt hole tolerance of approximately 4 mm was reached. For the increased area specimens, the load-slip behaviour was recorded into the bearing phase. At approximately 4 mm, the inner SHS came into contact with the outer SHS causing a sudden increase in the load-slip stiffness. The tests were stopped in this bearing phase.

Initially, load applied to the specimen was resisted by friction between the central plate and the outer SHSs. As the applied load was increased, some rotation of the outer SHSs was permitted, due to the offset of the lower bearings (see Figure 5.16). This had the effect of increasing the normal force at the top of the specimen, and reducing it at the bottom of the specimen. Given that friction resistance increases with increasing normal force, the upper faying surfaces resisted a greater portion of the applied load, resulting in more wear in this area.

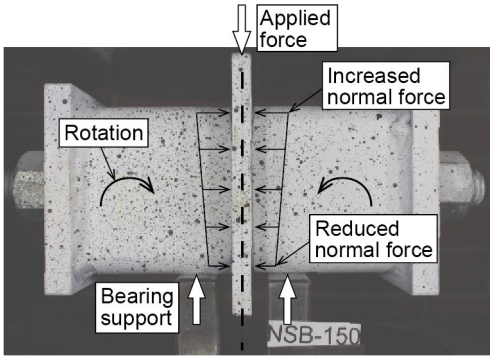

Figure 5.16. Illustration of normal force variation due to offset bearing support

5.4.3 Slip Load

Clean mill scale surfaces generally have a lower slip factor which is the result of a smooth surface in combination with reduced adhesion caused by the separation of the steel substrates [201, 202]. In comparison, sand blasted surfaces generally have a higher slip factor, which is caused by sharper asperities which can interlock, providing greater resistance to tangential movement [201]. These general statements are supported by the results of the present study, where the slip load for the sand blasted surface was increased for each of the sand blasted specimens, compared with the clean mill scale specimens, as shown in Figure 5.17(a). Considering the effect of the bolt preload directly, the results showed that increasing the preload significantly increased the slip load for each of the specimens as shown in Figure 5.17(b). Increasing the apparent contact area also increased the resulting slip load as shown in Figure 5.17(c). Increasing the contact pressure reduces the effective slip factor due to

flattening of the surface asperities [149, 187]. Increasing the contact area effectively reduced the contact pressure in the experiments thereby increasing the slip factor and, hence, the slip load. However, the increase in the slip load was relatively small. The 8.2 % increase in the slip load for the Sa3-150 specimen is not significant considering the accuracy discussed in Section 5.4.1 (p.118).

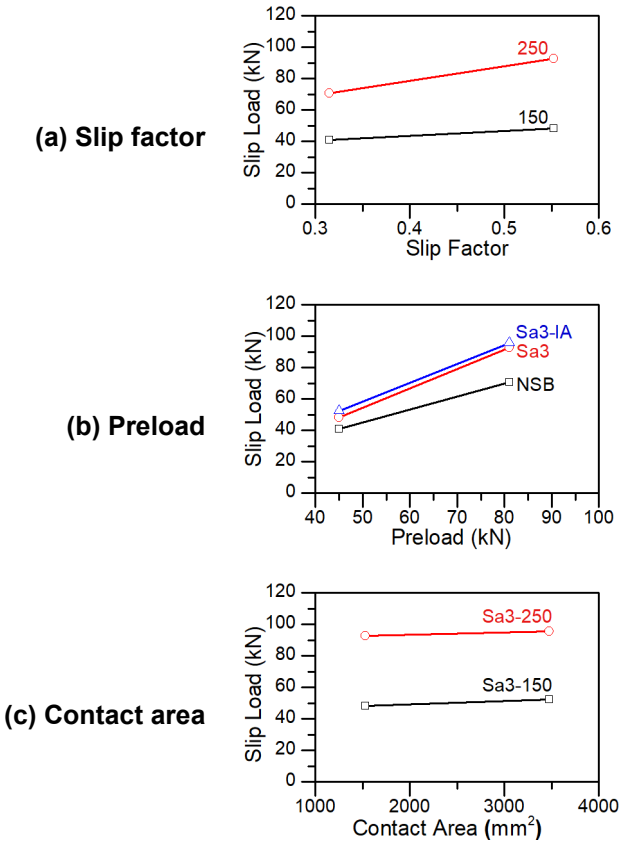

Figure 5.17. Effect of slip factor (a), preload (b) and contact area (c) on the experimental slip load

5.5 Numerical simulation

Numerical simulations were completed to extend the results of the experimental program. A finite element model was developed using ABAQUS. Two geometries were defined, one for the standard specimen (Figure 5.18a), and the other for the specimen with increased contact area (Figure 5.18b). As shown in Figure 5.18, one quarter of the geometry was defined due to the symmetry about the XY and ZY planes. In the numerical simulations, the slip was calculated as the relative displacement between the central plate P1 and the outer hollow section, in the same way as for the experimental analysis (§5.3.4, p.114).

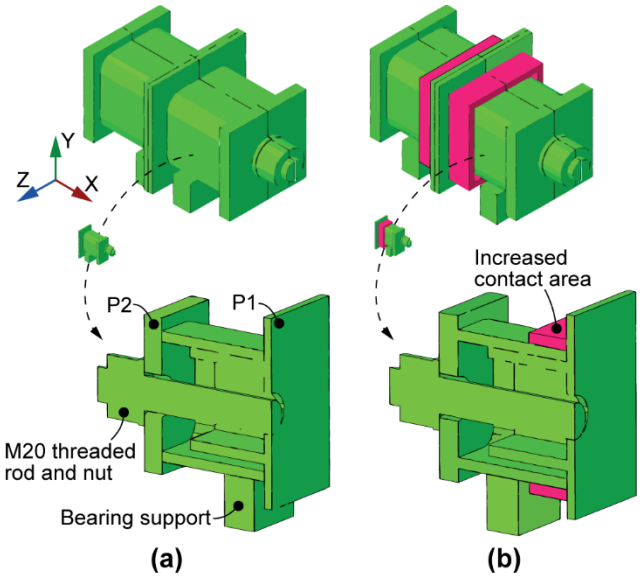

Figure 5.18. Numerical model for (a) standard specimen and (b) increased contact area specimen

5.5.1 Material properties

The stress strain properties for the steel materials were defined based on the quad-linear profile proposed by Yun et al. [203]. The elastic modulus and Poisson's ratio were defined as 200 GPa and 0.25 respectively [139]. The associated material properties are shown in Table 5.3.

Table 5.3. Material properties

Description	Steel grade	Thickness [mm]	Minimum yield stress (MPa)	Minimum tensile strength (MPa)	Minimum elongation (%)
Orrcon Steel hollow section, AS/NZS 1163	C350L0	6	350	430	12
Bearing support, AS/NZS 3679.1	300	≤50	300	440	22
Bluescope Xlerplate, AS/NZS 3678	350	≤12	360	450	20
Hobson Precision Sampsonrod M20 threaded rod	Class 8.8		660	800	12

5.5.2 Interaction and contact

The numerical analysis consisted of three steps. The contact interactions were applied in the first step. The penalty friction formulation was adopted for the tangential behaviour in the ABAQUS numerical model. *Hard Contact* with the *Penalty* enforcement method was adopted for the normal behaviour. In the second step, the bolt load was defined using the applied force

method. In the third step, the bolt length was fixed, and the shear force was applied to the central plate surface as shown in Figure 5.19.

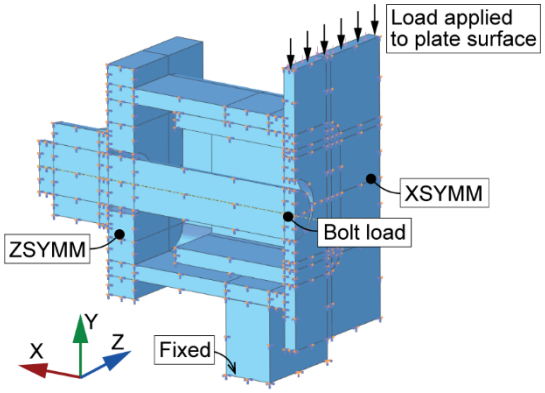

Figure 5.19. Loading and boundary conditions

The penalty method, which was adopted for the tangential behaviour, allows relative motion between the surfaces prior to slip [206]. The maximum slip permitted when the surfaces should be sticking is known as the elastic slip (γ_{crit}). This is shown in Figure 5.20 which presents the frictional shear stress plotted against the relative displacement, or total slip, between the surfaces. Two parameters are required to define the friction behaviour. First, the friction coefficient is required to define the critical shear stress at which the surfaces will slide, which is given as

$$\tau_{crit} = \mu p \,, \tag{5.6}$$

where μ is the friction coefficient and p is the contact pressure. Following Equation (5.6), τ_{crit} depends on the contact pressure, the distribution of which may depend on the geometry and relative material strengths in a nonlinear model. Second, the elastic slip is required to define the maximum slip in the sticking phase. The elastic slip is analogous to the minor relative displacement between surfaces due to local displacement of the surface profile. The elastic slip therefore depends on the surface profile and the material strength. As shown in Figure 5.20 the stiffness in the sticking stage is given as

$$k_{s,i} = \frac{\tau_{crit}}{\gamma_{crit}} \,. \tag{5.7}$$

Since the critical shear stress depends on the contact pressure, the stiffness varies throughout the analysis [215]. The elastic slip (γ_{crit}) values for the contact between P1 and the outer SHS in the present numerical model were determined by comparison with the experimental results, which is described in the following numerical calibration (§5.5.4). For the contact between the bearing support and the outer SHS the friction coefficient was set as 0.3, and the elastic slip was taken generally as 0.001 mm [205]. The lower friction coefficient reflected the smoother

surface of the bearing which was in contact with the painted surface of the outer SHS. For contact between the galvanised bolt, which was integrally modelled with the nut and washer, and the plate P2, the friction coefficient was set as 0.05 [216]. In the case of contact between the bolt shank and the plates P1 and P2, the tangential behaviour was taken to be frictionless [204].

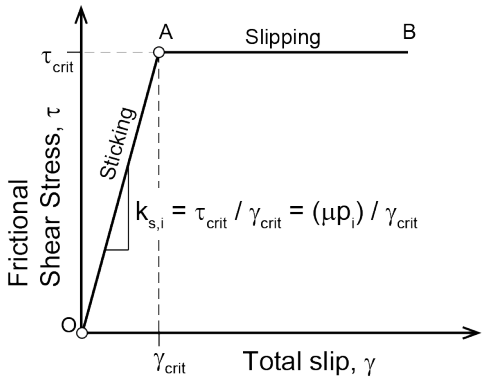

Figure 5.20. Plot of frictional shear stress against total slip [206]

5.5.3 Mesh convergence

The mesh consisted of first order 8-node linear brick elements. The mesh convergence was investigated by conducting simulations with nominal mesh sizes of 8, 4, and 2 mm for the specimen Sa3-150-IA (Figure 4.19). As shown in Figure 4.20 the overall shape of the load-slip curve was not sensitive to the mesh size. Three clear stages are shown, including the initial stage prior to slip, the slip stage, and the post-slip increase in stiffness due to bearing between the steel parts. Focussing on the initial stage (Figure 4.20a) the 4 mm mesh size gave a sufficiently accurate load-slip curve for the transition into the slip stage. For the bearing stage (Figure 4.20b) the smaller mesh sizes provided a better representation of the curved shape of the bolt and inner hollow section giving a more accurate point of contact between the curved elements. Again, the nominal 4 mm mesh size was found to be sufficient.

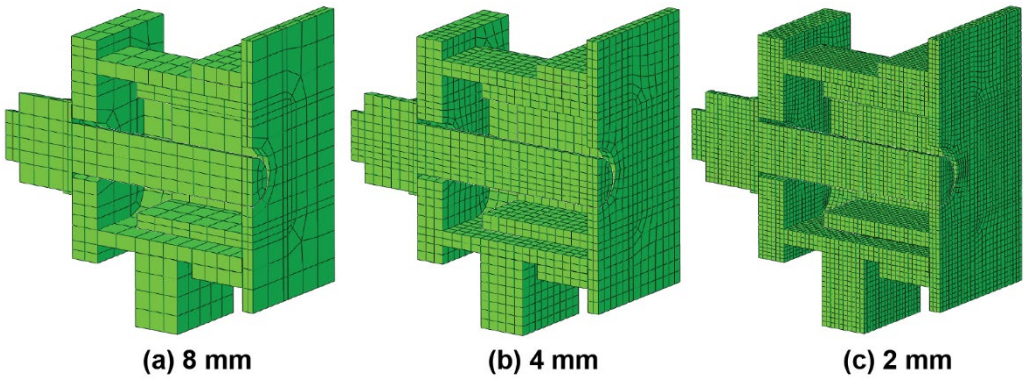

Figure 5.21. Mesh sizes of (a) 8, (b) 4, and (c) 2 mm

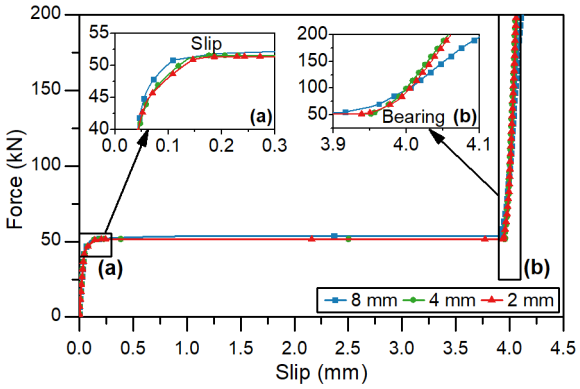

Figure 5.22. Numerical load-slip curves for varying mesh size

5.5.4 Numerical calibration

To calibrate the numerical model, the friction coefficient and elastic slip were input based on the experimental results. For the NSB specimens the slip factor test result (0.3146) was not directly applicable due to the difference in the faying surface condition for the connection specimens in comparison with the slip factor test specimens. In the slip factor tests the natural steel surfaces formed the faying surfaces, as shown in Figure 5.23(b). For the connections, the sliding interfaces were made up of a natural plate surface and the cut surface of a square hollow section, as shown in Figure 5.23(a). While the plate surface was similar to the surface in the slip factor tests, the cut surface of the hollow section was different. During fabrication the hollow sections were cut and the surface was prepared with a milling machine as required. This produced a surface free of mill scale, and with a repeated pattern of ridges as shown in Figure 5.5(c) (p.111). The lack of mill scale and the rougher patterned surface profile resulted in a higher effective friction coefficient for the NSB connection specimens. The friction coefficient for the NSB specimens was more accurately estimated as 0.5 based on the experimental data. The friction coefficient of 0.5 gave a good match between the numerical and experimental results for both cases under different preloads, as shown in Figure 5.24(a). For the Sa3 and Sa3-IA specimens, however, the sand blasting process gave a more uniform controlled surface which was consistent with the slip factor testing. The friction coefficient was, therefore, input as 0.5525 based on the slip factor tests (Table 4.3, p.90), resulting in a good match to the experimental results as shown in Figure 5.24(b,c).

The elastic slip values were determined by iteration, adjusting the elastic slip in the numerical model and matching the resulting initial stiffness of the force-slip curve with the experimental result. The elastic slip for the two NSB specimens was 0.05 mm which gave a good match to the initial stiffness from the experiments as shown in Figure 5.24(a). The elastic slip for the four sand blasted specimens was 0.045 mm. The initial stiffness was matched reasonably well

to the experimental results as shown in Figure 5.24(b,c). However, the initial stiffness from the experiments varied between the specimens. Although care was taken in the fabrication and assembly, the specimens were not identical. Instead, the fabrication and assembly tolerance varied across the specimens, resulting in a subtle variation in the resulting force-slip behaviour. For example, the central plate may have been slightly rotated in plane relative to the applied load, either due to misalignment of the outer hollow sections (Figure 5.25a) or due to the angle of the cut surface of the hollow section (Figure 5.25b). This would have resulted in an unequal distribution of load between the faying surfaces giving a lower initial slip load and hence load-slip stiffness. For example, Figure 5.24(b) shows a low initial slope for the Sa3-250 experimental force-slip curve which is not well matched to the numerical result. At a later stage of the curve, however, the slope increases as the specimen firmly contacts the two bearings and the slope is closer to the numerical result. Similarly, the central plate may have been rotated out of plane (Figure 5.25c) affecting the vertical displacements and, hence, load-slip behaviour recorded. In the final calibration the numerical result gave a slightly larger initial stiffness for the Sa3 specimens, and a slightly smaller stiffness for the Sa3-IA specimens, compared with the experimental results. Overall, a reasonable match was achieved for the four sand blasted specimens using an elastic slip of 0.045 mm. However, the calibration process highlights the sensitivity of the inter-module connection to the alignment. It is, therefore, suggested that biaxial shear be considered in future works to resolve this aspect of the behaviour.

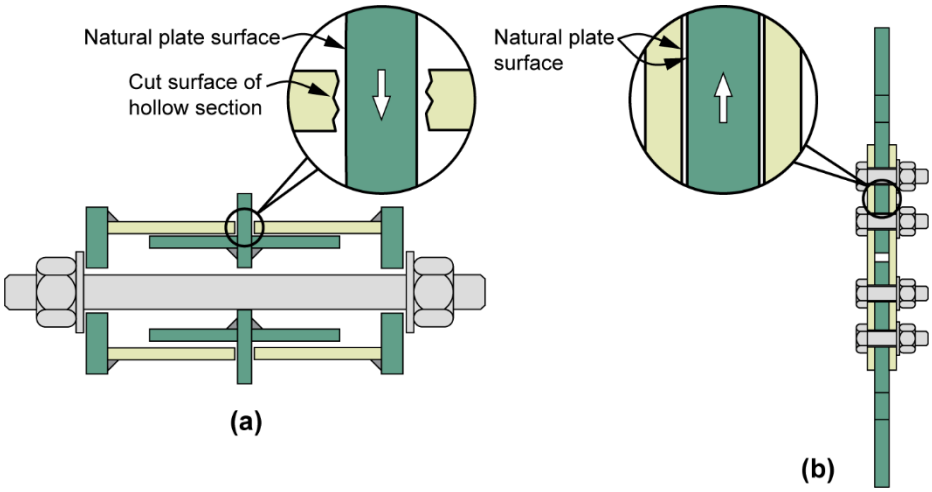

Figure 5.23. Illustration of faying surfaces in (a) connection specimens and (b) slip factor test specimens

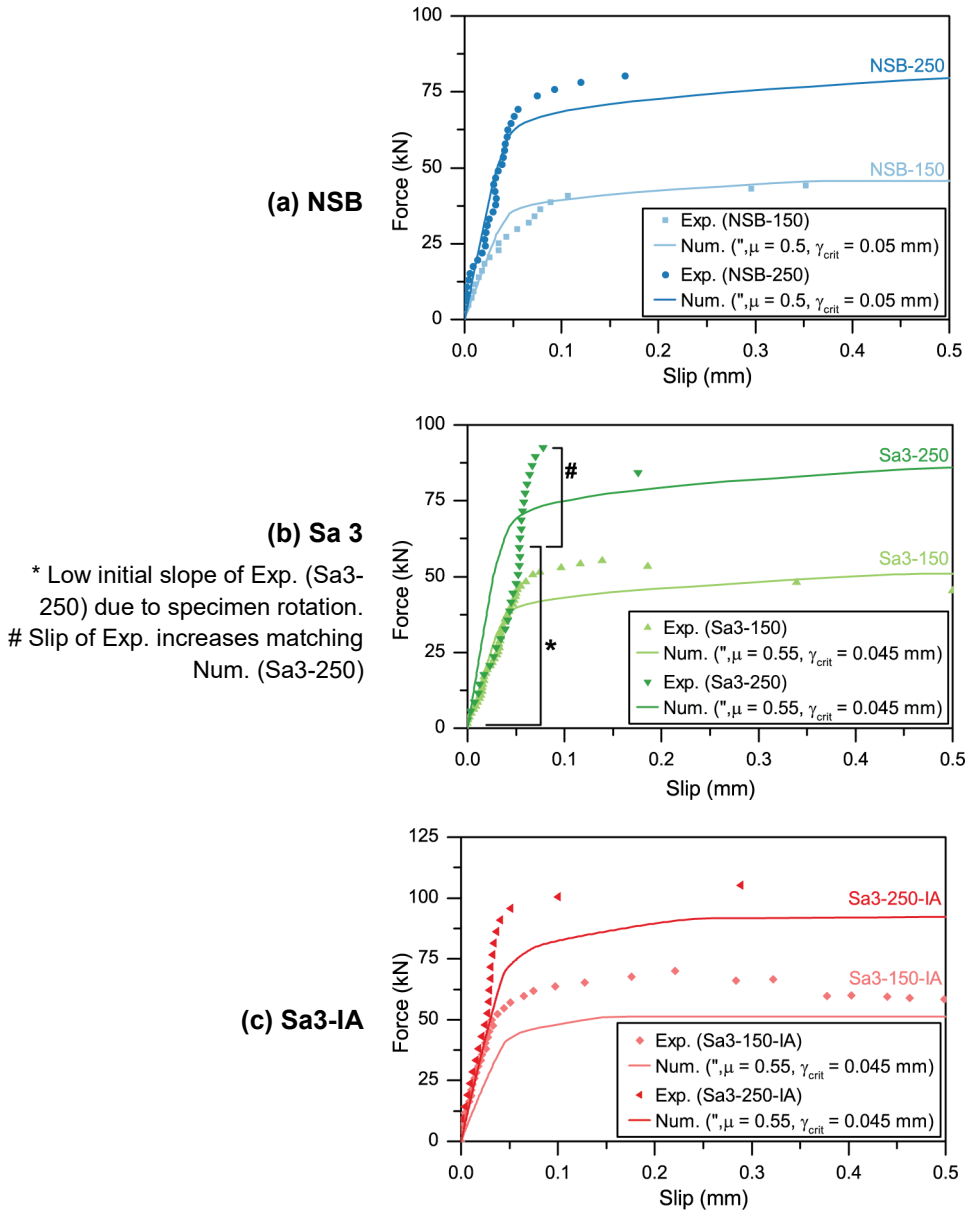

Figure 5.24. Comparison between numerical and experimental force-slip curves

The smaller elastic slip for the sand blasted specimens gave a larger initial force-slip stiffness which may be explained by the difference in the surface profile. For rougher sand blasted surfaces, interlock of the asperities may restrain local displacement until the applied force is sufficient to force the asperities over or through each other leading to slip. However, the difference in the elastic slip for the NSB (0.05 mm) and Sa3 (0.045 mm) specimens was relatively small. For engineering design purposes it may be sufficient to adopt the larger elastic slip (0.05 mm) which corresponds with the smaller initial stiffness.

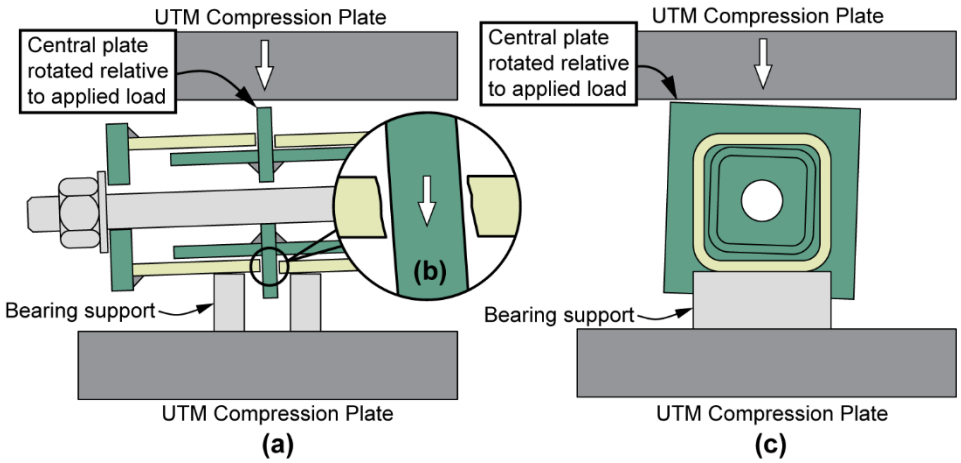

Figure 5.25. Illustration of possible specimen variation due to fabrication and assembly tolerances

5.6 Theoretical verification and proposed load-slip model

5.6.1 Prediction of slip load according to existing standards

The slip resistance of a friction-type connection, assuming equal preload in all of the bolts, is calculated as [187]

$$F_{slip} = \mu n_s n_b N_t, \tag{5.8}$$

where μ is the slip factor, n_s and n_b are the number of slip planes and bolts respectively, and N_t is the bolt preload. This general formula for the slip resistance is adopted by the existing standards, for example AS4100 [139]. Using this formula the slip resistance can be calculated for each of the specimens as shown in Table 5.4. The percentage error is given which is the error in the estimated slip load in comparison with the experimental slip load. The existing empirical formula (Equation (5.8)) gives a good estimate of the slip resistance for the sand blasted (Sa 3) specimens. The greatest percentage difference between the experimental and estimated slip load for the sand blasted specimens is -6.5 %, which is less than the estimated uncertainty in the experimental slip load which is ± 8.6 % as shown in Section 5.4.1 (p.118). For the plain mill scale specimens, i.e., NSB-150 and NSB-250, the estimated slip resistance is substantially less than the experimental value. This is explained by the difference in the faying surface condition for the connection specimens, in comparison with the slip factor test specimens as explained in Section 5.5.4 (p.126).

Table 5.4. Experimental and estimated slip resistance

Specimen	Experimental Slip Load, $F_{slip,exp}$ (kN)	μ_m	N_t (kN)	Estimated slip load $F_{slip,est}$ (kN)	$\frac{\left(F_{slip,est}-F_{slip,exp}\right)}{F_{slip,exp}}$ (%)
NSB-150	40.8	0.3146	45	28.3	-30.7
NSB-250	70.7	0.3146	81	51.0	-28.0
Sa3-150	48.4	0.5525	45	49.7	2.71
Sa3-250	92.6	0.5525	81	89.5	-3.36
Sa3-150-IA	52.4	0.5525	45	49.7	-5.11
Sa3-250-IA	95.7	0.5525	81	89.5	-6.52

5.6.2 Comparison with existing connections

To demonstrate the improvement in initial stiffness offered by the proposed connection, two existing inter-module connections were selected for comparison. The two selected studies reported the force-slip behaviour of the inter-module connection allowing direct comparison with the results of the present study. The first selected connection was previously presented by Styles et al. [50]. It consisted of a 300x200x6 RHS C350 column with 370x410x25 mm G350 end plates, and a total of eight M24 class 10.9 structural bolts, as shown in Figure 5.26(a). The relevant preload of 247 kN was considered in the ANSYS numerical simulation using PREST179 elements which were located in the middle of the bolt shank. The second selected connection was previously presented by Gunawardena [33]. It consisted of 150x150x9 SHS C350 columns, 25 mm thick G350 end plates, and M12 or M16 class 8.8 structural bolts, as shown in Figure 5.26(b). Three different connection geometries were considered. One connection had M12 bolts with 14 mm round holes (TG1), another had M16 bolts with 18 mm round holes (TG2), and the other had M16 bolts with 18x26 mm slotted holes (TG3). The bolt preloads for the M12 and M16 bolts were 31.8 and 59.2 kN, respectively.

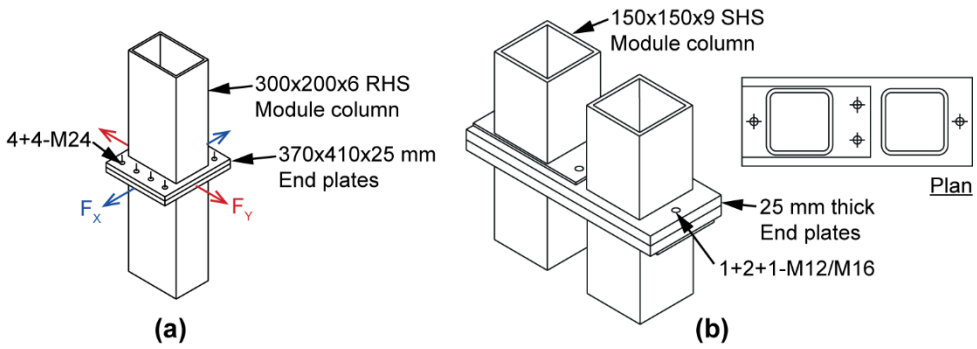

Figure 5.26. Illustration of existing inter-module connections from the work of (a) Styles et al. [50] and (b) Gunawardena [33]

Figure 5.27 plots the experimental results from the present study against the results for the two selected inter-module connections from the previous studies [33, 50]. Figure 5.27(a) compares the present results with the numerical results published by Styles et al. [50]. Figure 5.27(b) compares the present results with the experimental results from the previous study by Gunawardena [33]. On the y-axis the force is normalised by dividing by the slip resistance which is estimated based on Equation (5.8). Slip at a normalised force less than one therefore indicates a relatively low slip resistance. The plots show that the proposed PT connection has greater initial load-slip stiffness than either of the existing IMCs.

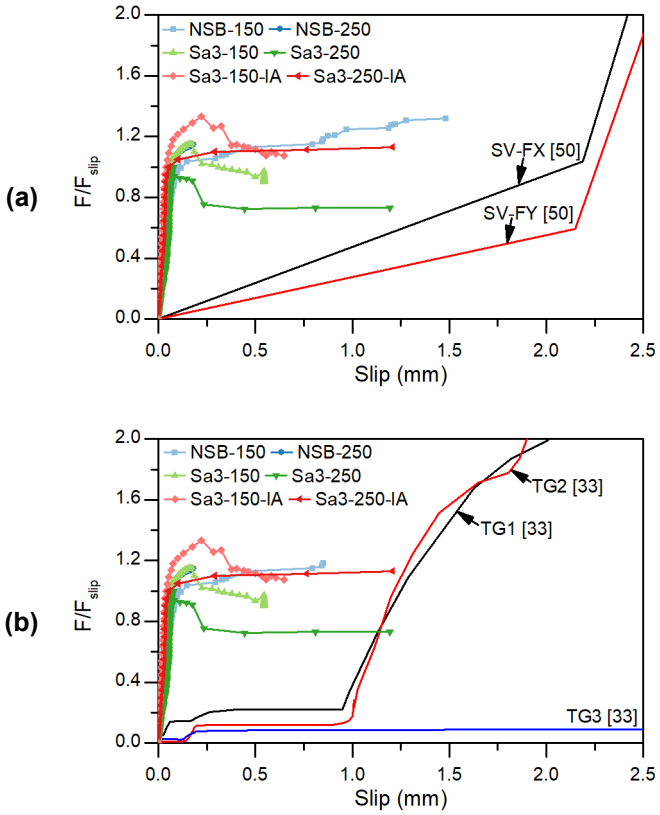

Figure 5.27. Comparison of the present experimental results with data for the existing inter-module connections presented by (a) Styles et al. [50] and (b) Gunawardena [33]

5.6.3 Load slip model

Based on the experimental and numerical results, a shear load-slip model is proposed for the new inter-module connection as shown in Figure 5.28. The proposed model differs from the existing model (Figure 2.23, p.39) in the first stage (OP). In the proposed model the initial load-slip behaviour is modelled by the exponential function

$$F(d) = A\left[1 - \exp\left(\frac{-d}{B}\right)\right], \tag{5.9}$$

where F (kN) is the applied load, d (mm) is the slip, and A (kN) and B (mm) are parameters.

This exponential function is chosen to match the experimental behaviour, and better represents the initial load-slip stiffness than the linear behaviour assumed in the existing model (Figure 2.23, p.39). Equation (5.9) applies generally in the initial friction/slip stage, i.e., $0 \leq d \leq d_P$ where d_P is the bolt hole tolerance, and the parameters A and B, which control the slip resistance and initial stiffness, may be calibrated based on experiments. It should be noted, however, that Equation (5.9) is a simplified model which is not able to capture the effect of all factors affecting the force-slip curve. For example, if the faying surfaces are damaged as they slide over one another there may be a corresponding increase in the friction coefficient, resulting in an increase in the slip resistance which is not captured by Equation (5.9). The second and third stages, i.e., PQ and QR are the same as in the existing model (Figure 2.23, p.39). PQ represents the bearing stage in which the stiffness can be calculated based on the combined shear and bending stiffness of the outer and inner hollow sections. Q is the failure point which represents the ultimate shear strength of the connection and may be estimated based on the existing design standards considering the typical failure modes. The failure modes include, for example, shear yield of the weld between the inner SHS and the central plate, combined bending and shear of the inner and outer SHS, and local bearing failure of the outer and inner SHS.

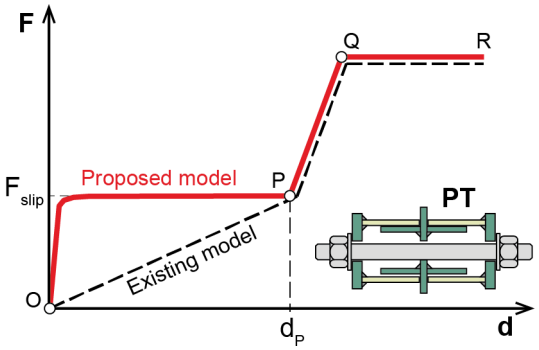

Figure 5.28. Proposed shear force-slip model

To demonstrate the application of the proposed model, the exponential function (Equation (5.9)) is fitted to the experimental data. Figure 5.29 shows the resulting curves fitted to the experimental data for the NSB (a), Sa3 (b) and Sa3-IA (c) specimens. Figure 5.29(d) shows the fitted curves for all of the specimens, to allow direct comparison. Figure 5.29 generally shows a good fit to the experimental data. For the sand blasted specimen Sa3-250, the fitted curve does not match the experimental data well. This is due to the variation in the load-slip stiffness caused by the fabrication tolerance as discussed in Section 5.5.4 (p.126).

(a) NSB

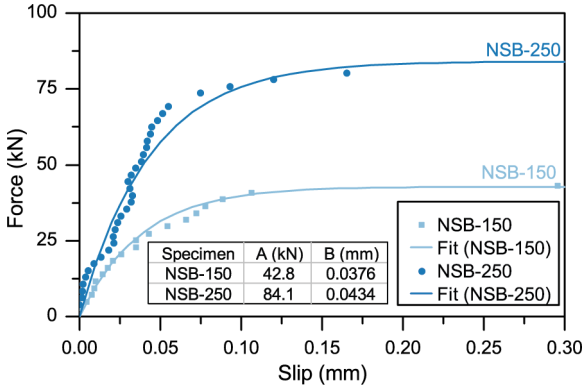

(b) Sa3

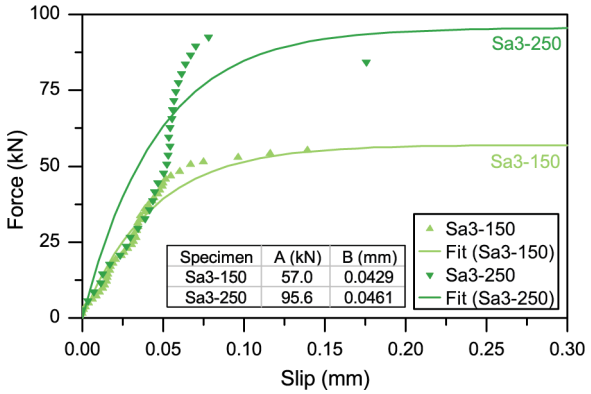

(c) Sa3-IA

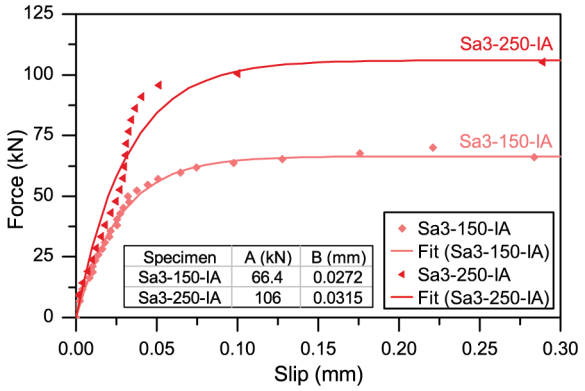

(d) All Specimens

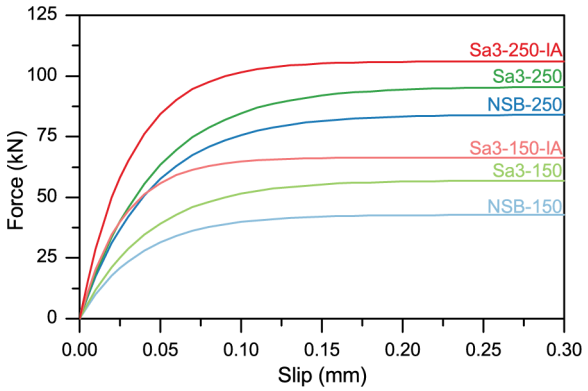

Figure 5.29. Exponential fit to experimental data for (a) NSB, (b) Sa3, (c) Sa3-IA, and (d) all of the specimens

5.6.4 Effect of slip factor and bolt preload

To investigate the effect on the initial load-slip behaviour, the slip factor and preload were varied in the numerical model for the standard connection geometry (Figure 5.3, p.110). The slip factor was varied from 0.2 to 0.6, and the preload from 50 to 145 kN. The elastic slip was set as 0.05 mm following the numerical calibration (§5.5.4, p.126). The proposed exponential function (Equation (5.9)) was fitted to each numerical load-slip curve giving the parameters A and B. A was found to depend on the slip factor and preload. A curve was fitted to the A values which showed that A may be estimated as

$$A(\mu, N_t) \approx 1.97 \mu N_t , \tag{5.10}$$

where N_t (kN) is the preload and μ is the slip factor. This can be recognised as the standard equation for the slip resistance of friction-type connections (Equation (5.8), p.129). In this case there was one bolt and two slip planes such that A may be more accurately estimated as

$$A(\mu, N_t) = F_{slip} = \mu n_s n_b N_t = 2\mu N_t . \tag{5.11}$$

Figure 5.30 applies this empirical formula (Equation (5.11)) and shows a linear relationship for the selected preload and slip factor values. The numerical data used for the curve fit is also shown.

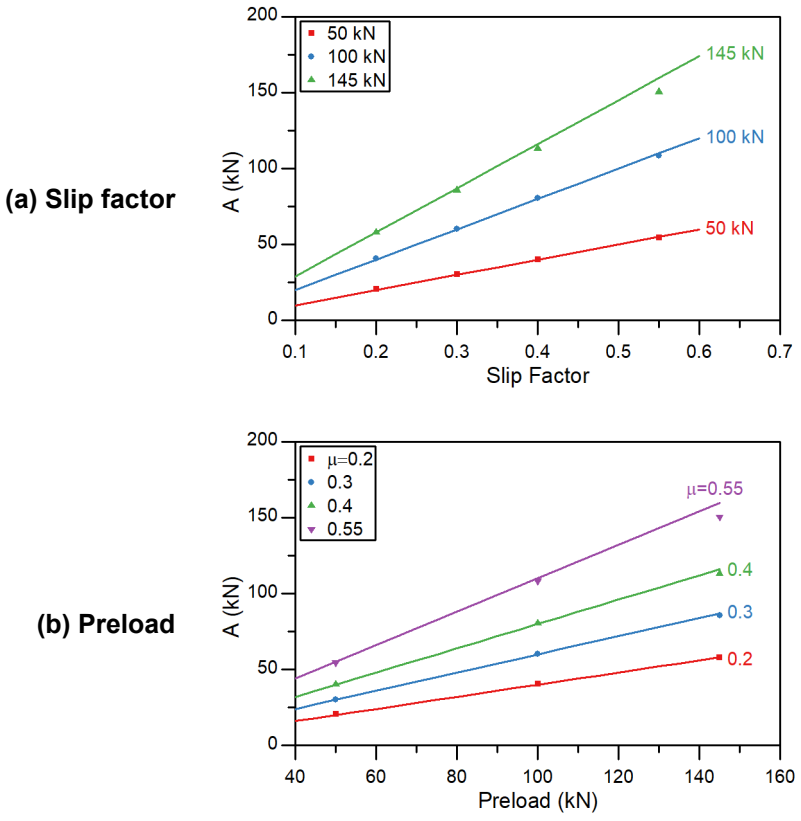

Figure 5.30. Variation of parameter A with (a) slip factor and (b) preload

Figure 5.31 presents the variation of B with the slip factor (a) and the bolt preload (b). The parameter B is shown to be approximately constant. The value of B from the numerical analyses ranged from 0.035 to 0.039 mm. For engineering design purposes, a value of 0.04 mm can be recommended for B.

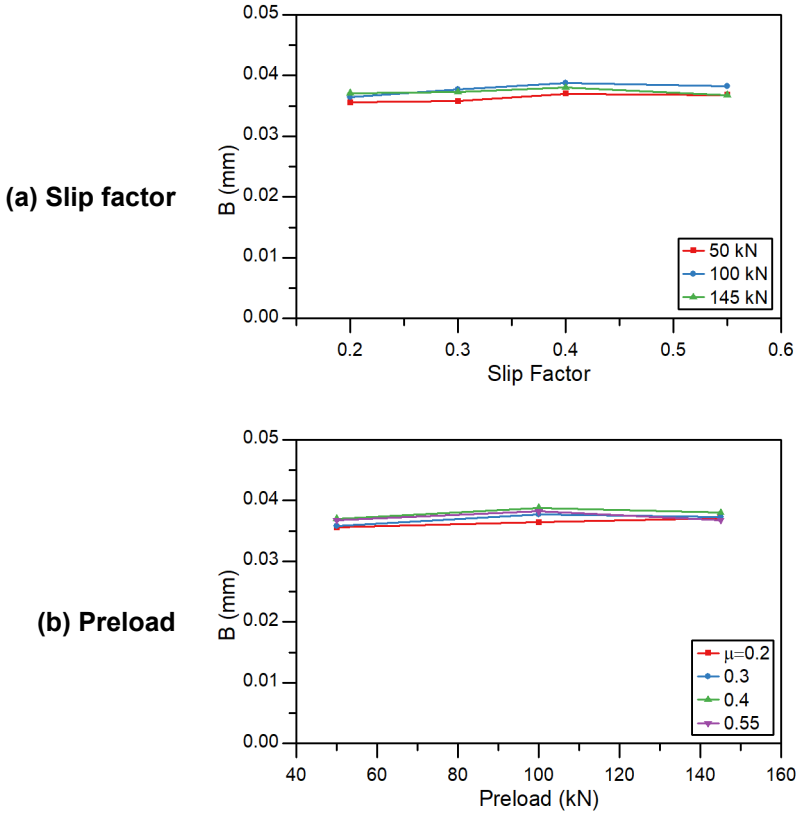

Figure 5.31. Variation of parameter B with (a) slip factor and (b) preload

5.7 Summary

A new post-tensioned (PT) vertical inter-module connection (IMC) for modular steel buildings was proposed in this chapter. Experimental and numerical investigation of the initial shear load-slip behaviour was conducted. The test results were discussed and an empirical model was proposed. The main findings are summarised as follows.

1. For the proposed PT connection, the slip load can be effectively controlled by varying the bolt preload and faying surface slip factor. Sand blasting the faying surfaces increased the slip factor, which gave a greater slip resistance. Increasing the bolt preload significantly increased the slip load. Increasing the contact area resulted in a small increase in the slip load, which was not significant given the accuracy of the slip load measured in the experiments.

2. The proposed PT connection has greater initial load-slip stiffness than the existing inter-module connections presented by Styles et al. [50] and Gunawardena [33].

3. A new exponential model is proposed for the initial load-slip behaviour of the PT connection. The model is better suited to IMCs which exhibit high initial shear stiffness, such as the PT connection. The model has two parameters, i.e., A and B, which can be obtained through experiments, or estimated for design purposes. The first parameter, A, defines the slip load, and can be estimated using the empirical formula for slip resistance. The second parameter, B, controls the initial load-slip stiffness, and a value of 0.04 mm is suggested for design purposes.

Chapter 6 New interlocking (IL) connection: Experimental and numerical studies[1]

6.1 Introduction

This chapter introduces a novel interlocking (IL) inter-module connection (IMC). The proposed IMC combines structural bolts with interlocking elements to improve the constructability and shear force-slip behaviour. An experimental study is conducted to establish the shear behaviour. A method and setup are developed, and in-plane displacements are recorded throughout the experiments using digital image correlation (DIC). The bolt tightening torque is defined to control the bolt preload with reference to the manufacturer supplied k-factor. Parametric studies are conducted considering the effects of the interlocking elements, bolt preload, and bolt hole tolerance on the shear behaviour. Finally, an improved model is proposed for the shear force-displacement behaviour of the proposed IL connection.

6.2 Proposed interlocking (IL) connection

An interlocking connection detail is envisaged which combines structural bolts with interlocking elements. The pre-tensioned bolts provide the initial shear stiffness and the slip resistance can be demonstrated based on the preload and slip factor. After the initial slip, the connection transitions to a bearing type where the bolts and the interlocking components contribute to the shear resistance. The interlocking components assist with correct positioning of the module during site installation and provide safety during construction, prior to installation and tensioning of the bolts. The tolerance may be adjusted to suit the anticipated accuracy in site positioning of the modules, and the desired interplay of the connection elements in the shear slip sequence.

More specifically, the interlocking connection proposed in this chapter is shown in Figure 6.1. The features of the proposed connection, which was developed for modular buildings with steel columns, include: horizontal connection by plate P2, vertical connection by structural bolts (the grey bolts in the figure), and locating pins for site assembly and improved shear stiffness. The locating pins are inserted through and welded to the underside of plate P1. The P1/locating pin assemblies are then welded to the top end of the lower columns during shop fabrication of the lower modules. After placement of the lower modules on site, the plate P2

[1] The related work in Chapter 6 was published in Engineering Structures:

Lacey AW, Chen W, Hao H, Bi K. New interlocking inter-module connection for modular steel buildings: Experimental and numerical studies. Eng Struct. 2019;198:109465. https://doi.org/10.1016/j.engstruct.2019.109465

is placed on top of the P1 plates, with the locating pins extending through P2. The upper modules are then placed on top, with the locating pins extending through the P3 plates, which were shop welded to the bottom end of the upper module columns. Structural bolts are then inserted through the combined thickness of the plates P1, P2, and P3. The proposed connection offers a simplification of detailing with the ability to provide connection between up to eight modules, i.e., four lower and four upper modules. The site installation is relatively easy, as is the end of life deconstruction. Safety during construction is considered and improved by the interlocking component, i.e., the locating pin. Considering the disadvantages, the detail requires site installation of the P2 plates, and site installation and tensioning of the bolts. The latter may require external access which may interfere with the building finishes, which is another disadvantage. However, the potential advantages are expected to compensate for the disadvantages.

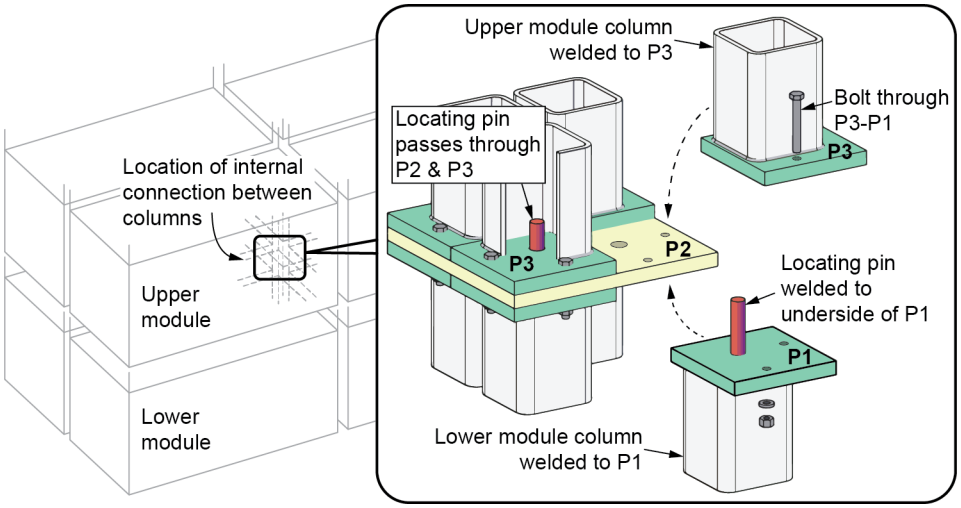

Figure 6.1. Proposed interlocking inter-module connection

6.3 Experimental study

6.3.1 Method and specimens

An experimental study was completed to investigate the shear force-slip (F-d) behaviour of the proposed connection. Six specimens were fabricated with different bolt preload, bolt hole tolerance, and presence or absence of locating pins, as shown in Table 6.1. There were three main specimen types: A, B, and C. The geometry for the A specimens is shown in Figure 6.2 which includes a cut away view showing the otherwise hidden components. The plates are labelled SP14t, SP14b, SP16, SP15t, and SP15b for convenience in the following discussions. These labels follow the fabrication drawings where SP referred to single parts, and t and b referred to the top and bottom of the assembled specimen (Figure 6.2). The A specimens had a standard bolt hole tolerance of 2 mm, i.e., a 14 mm diameter hole, as specified for M12 bolts

in the Australian standard AS 4100 [139]. The 12 mm diameter locating pins had a corresponding 16 mm diameter hole. This gave a tolerance of 4 mm for the locating pins which ensured that the bolts would bear on the plates at the same time as the plates contacted the locating pins. During assembly the specimens were aligned to allow the maximum slip displacement during the test, thereby ensuring the initial shear resistance was due to friction between the plates. The B specimens were fabricated without locating pins but were otherwise the same as the A specimens. The C specimens had slotted holes with a diameter of 14 mm and a length of 22 mm, as illustrated in Figure 6.3. Slotted holes were included to investigate the effect on the F-d behaviour. The slotted hole was expected to give a reduced slip resistance and greater slip displacement in comparison with the standard hole tolerance.

Table 6.1. Test matrix.

Specimen	A1	A2	B1	B2	C1	C2
Bolt preload (kN)	50	35	50	35	50	35
Hole tolerance	Standard	Standard	Standard	Standard	Slotted	Slotted
Locating pin	Y	Y	N	N	Y	Y

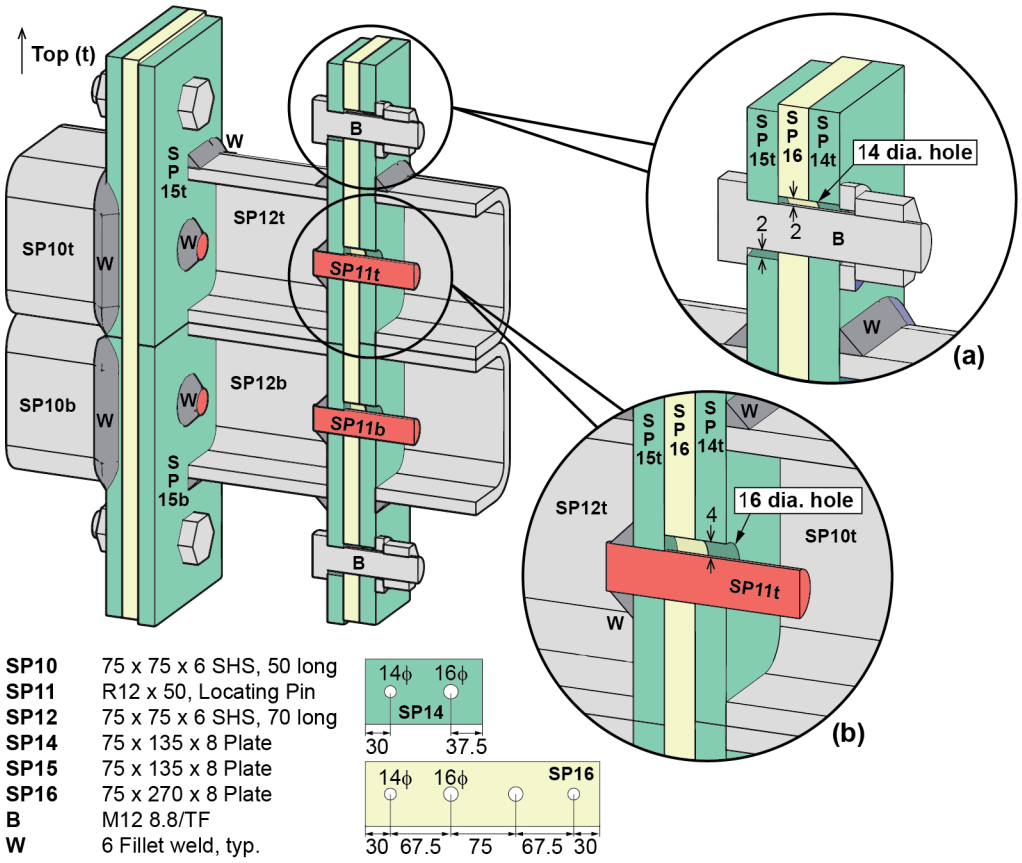

Figure 6.2. Illustration of specimen A showing (a) bolt hole and (b) locating pin details
All dimensions in mm.

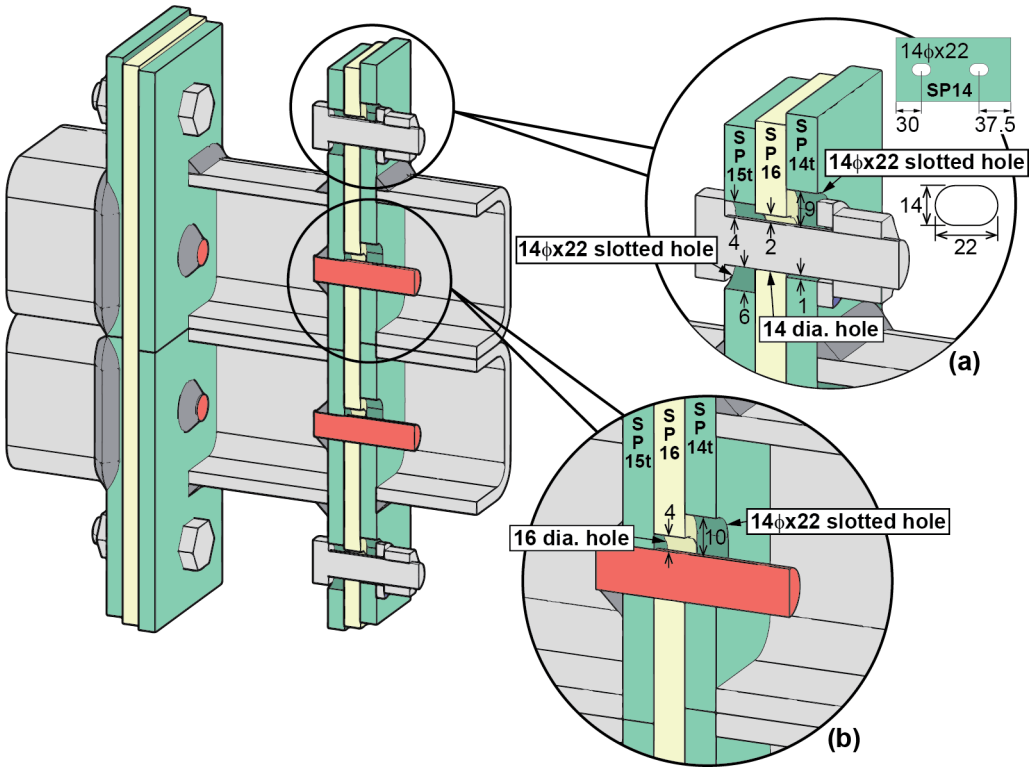

Figure 6.3. Illustration of specimen C showing (a) bolt hole and (b) locating pin details
All dimensions in mm.

Each specimen consisted of a simplified two-column connection detail which was duplicated to give a balanced loading arrangement. The loading arrangement is illustrated in Figure 6.4 and the actual setup is shown in Figure 6.5. The connection was tested in shear using a compression load from a Shimadzu AGS-300kNX universal testing machine (UTM). Load was applied to the specimen by the top compression plate at a rate of 0.1 kN/s, starting from zero and increasing to a maximum of 250 kN. The load was transferred from the top compression plate to the upper hollow section columns by two upper bearings, which provided clearance around the bolts (Figure 6.4a). Similarly, at the bottom, the load was transferred from the specimen through the lower bearing to the lower compression plate. For the upper bearings there was a nominal gap of 7 mm between the bearing and the adjacent end plate, allowing for the weld between the plate and hollow section (Figure 6.4b). The lower bearing was located approximately centrally, giving a nominal gap of 5mm (Figure 6.4c). A chamfer was provided to the lower bearing edge to ensure adequate clearance between the bearing and the weld (Figure 6.4c).

Prior to testing the specimens were assembled and the bolts were tensioned using a torque wrench. The torque (M_r) required to give the specified preload (N_t) was calculated based on the general relationship given in AS/NZS 1252.1 [190], i.e., Equation (4.1) which was presented in Section 4.2.4 (p.80). From the manufacturer supplied test certificate, the mean k-factor (k_m) was 0.119, and the corresponding coefficient of variation was 0.042 based on five

assembly tests. The five tests were performed by the manufacturer in accordance with EN 14399-2 [213].

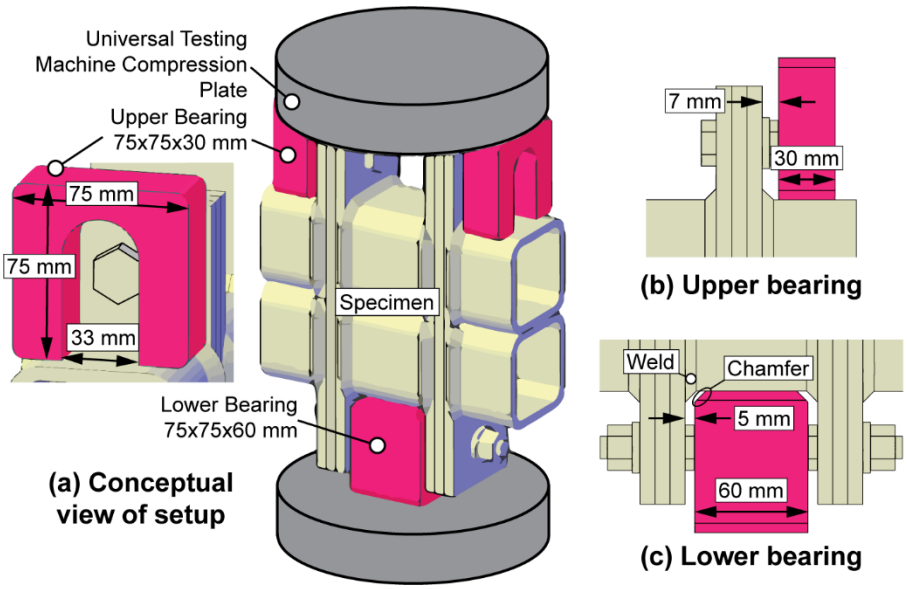

Figure 6.4. (a) Conceptual view of experimental setup showing (b) Upper and (c) Lower bearing details

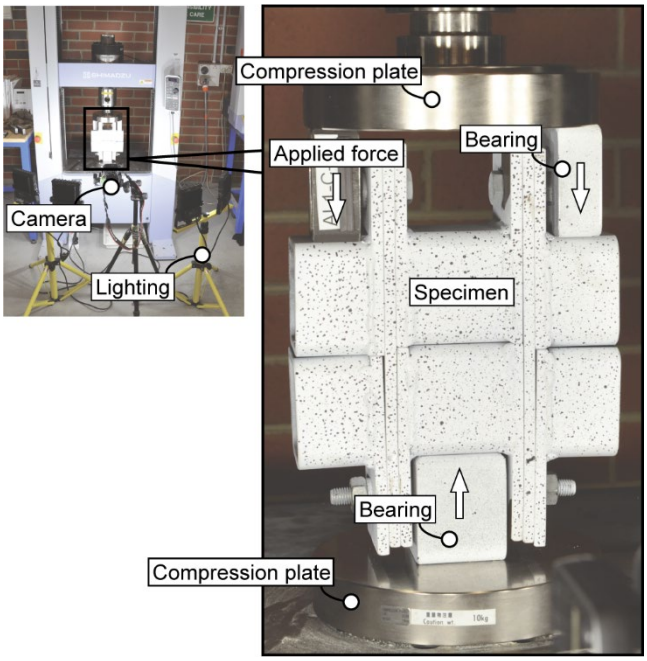

Figure 6.5. Photo of experimental setup

A summary of the materials used for the specimens is given in Table 6.2. The faying surfaces of the steel plates were maintained in the clean mill scale condition. The slip factor was 0.31 as determined by slip factor testing in accordance with Annex G of EN 1090-2 [150]. Chapter 4 provides details on the slip factor testing and associated analysis. The M12 bolts were hot dip galvanised, giving a clean mill scale / galvanised interface between the plates and bolts.

The bearings had a smooth machined surface which was in contact with the factory painted finish of the hollow sections.

Table 6.2. Material properties for the interlocking (IL) connection specimens

Description (Parts, refer Figure 6.2, p.139)	Grade	Cross-section dimensions (mm)	Min. yield stress (MPa)	Min. tensile strength (MPa)	Min. elongation (%)
Hollow section, AS/NZS 1163 (SP10, SP12)	C350L0	75x75x6	350	430	12
Square bar, AS/NZS 3679.1 (Bearings)	300	75x75	290	440	22
Round bar (SP11)	300	R12	375	530	34
Plate, AS/NZS 3678 (SP14, SP15, SP16)	G350	75x8	360	450	20
M12x1.75Px50,8.8, HR Bolts AS/NZS 1252 (B)	Class 8.8	-	640	800	12

6.3.2 Results and analysis

A speckle pattern was applied to the front surface of each specimen and digital image correlation (DIC) was undertaken to determine the vertical displacements following the established method [200, 210]. For example, Figure 6.6 and Figure 6.7 show the vertical displacement contour of A1 at two selected time increments. For each time increment the vertical displacements (mm) were determined at selected points as shown. Points 1 to 4 were located along the lower column centreline, and the slip was calculated as the average difference in vertical displacement between the points 1 and 2, and 3 and 4. That is, the slip at the lower columns (d_{lower}) was calculated as

$$d_{lower} = 0.5\left[\left(\delta_1 - \delta_2\right) + \left(\delta_4 - \delta_3\right)\right], \tag{6.1}$$

where δ_i is the vertical displacement at point i. Similarly, points 5 to 8 were located along the upper column centreline, and the slip at the upper columns was calculated as

$$d_{upper} = 0.5\left[\left(\delta_5 - \delta_6\right) + \left(\delta_8 - \delta_7\right)\right] . \tag{6.2}$$

The force obtained from the UTM was then plotted against the slip determined from the DIC. For example, the resulting F-d curves for A1 are shown in Figure 6.8. Although reasonable care was taken in the fabrication and assembly, variation in the part dimensions and straightness resulted in some gaps between the connection elements prior to loading. Due to the gap between SP15t and SP15b (Figure 6.8a), the initial slip for the lower column centreline

was resisted by friction at the SP15b / SP16 interfaces. Therefore, only the preload of the two lower bolts contributed to the initial slip resistance resulting in a lower initial slip resistance. The full connection slip resistance, to which the preload of all four of the bolts contributed, was not reached until after the initial gaps were closed.

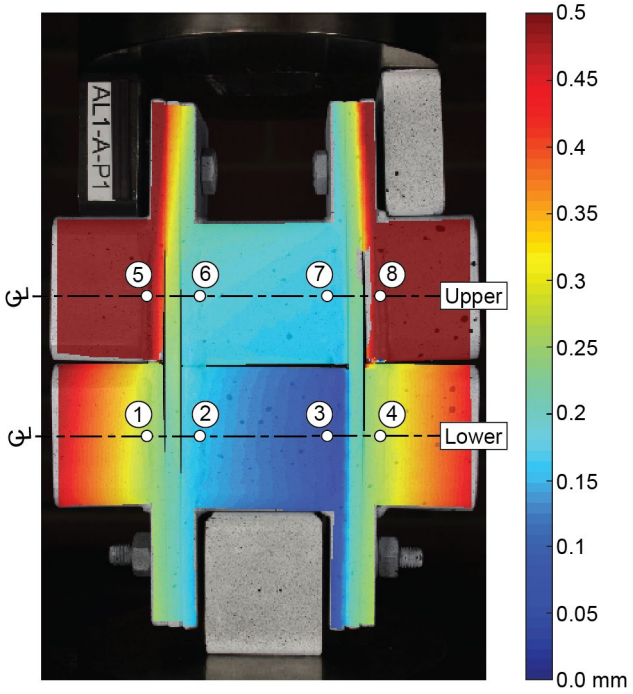

Figure 6.6. Vertical displacement contour (mm) of A1 for an applied force of 46.2 kN

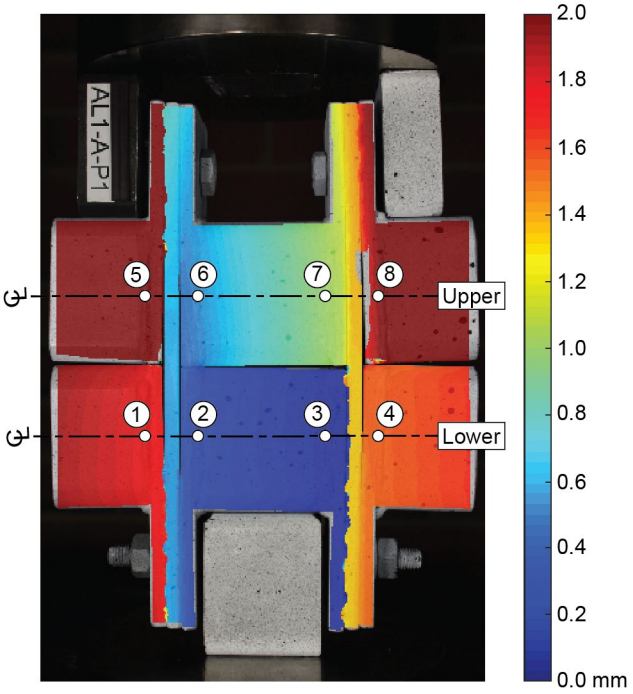

Figure 6.7. Vertical displacement contour (mm) of A1 for an applied force of 93.8 kN

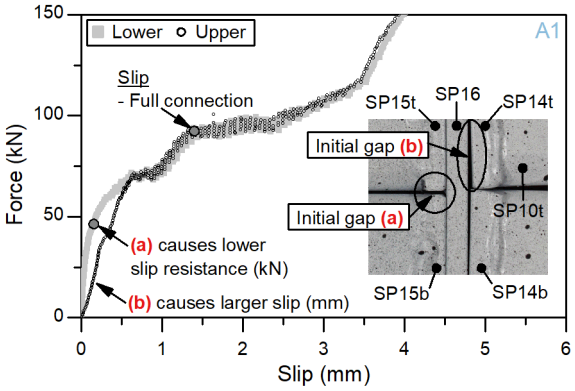

Figure 6.8. Force-slip plot for A1 showing slip at the lower and upper column centrelines

For the upper column centreline, the F-d curve was affected by the initial gap between SP14t and SP16 (Figure 6.8b). The gap (b) was present in the specimens due to the fabrication process, during which the plate SP14 was welded to column SP10. The plate was welded on three sides and the heat from the process resulted in a small curvature in plate SP14. As a result, when the specimen was assembled, there was a gap between SP14t and SP16. This initial gap (b) allowed the SP14t / SP10t assembly to rotate as the load was applied. The rotation increased the vertical displacement at points 5 and 8 (Figure 6.7), and therefore increased the slip (mm), which was calculated following Equation (6.2), prior to the initial slip resistance (kN). The slip at the lower column centreline was less affected by the plate curvature. Therefore, to reduce the effect of the SP14 plate curvature, the slip for the remaining specimens was calculated from the lower column centreline only. The resulting F-d curves are shown in Figure 6.9 and Figure 6.10.

Each of the specimens had initial gaps between the connection elements, although the size of the gaps varied. As a result, the F-d curves in Figure 6.9 and Figure 6.10 generally exhibit a lower initial slip resistance for which only two of the four preloaded interfaces were effective. The position of the initial slip points were determined as the first significant change in slope of the F-d curve. Once the initial gaps were closed, the full connection slip resistance was reached as all four of the preloaded interfaces contributed to the friction resistance. The position of the full connection slip points were similarly determined by examining the slope of the F-d curve. For A2, the initial gaps were small and the lower initial slip resistance was not apparent by visual inspection of the F-d curve (Figure 6.9b). Therefore, only the full connection slip resistance was determined for A2. The slip resistances are summarised in Table 6.3.

For A2 and B2 the point at which the bolts started to slide was clearly identifiable as a small increase in the slip resistance at approximately 2 mm slip, as shown in Figure 6.9(b) and Figure

6.10(b), respectively. To explain how the bolts could slide, Figure 6.11 illustrates a possible slip sequence focussing on one of the top bolts as shown in Figure 6.11(a). In the illustrated sequence, the connection slips at the SP15t/SP16 and SP16/SP14t interfaces until SP14t comes into contact with the bolt shank, as shown in Figure 6.11(b). SP16, SP14t and the bolt then slide together until the bolt shank comes into contact with SP15t, as shown in Figure 6.11(c).

Table 6.3. Summary of experimental slip resistance

Specimen	A1	A2	B1	B2	C1	C2
a. Full connection slip resistance (kN)	93.8	68.6	97.8	70.2	105	60.2
b. Initial slip resistance (kN)	46.2	-	48.2	31.8	51.3	30.2
b / a	0.49	-	0.49	0.45	0.49	0.50

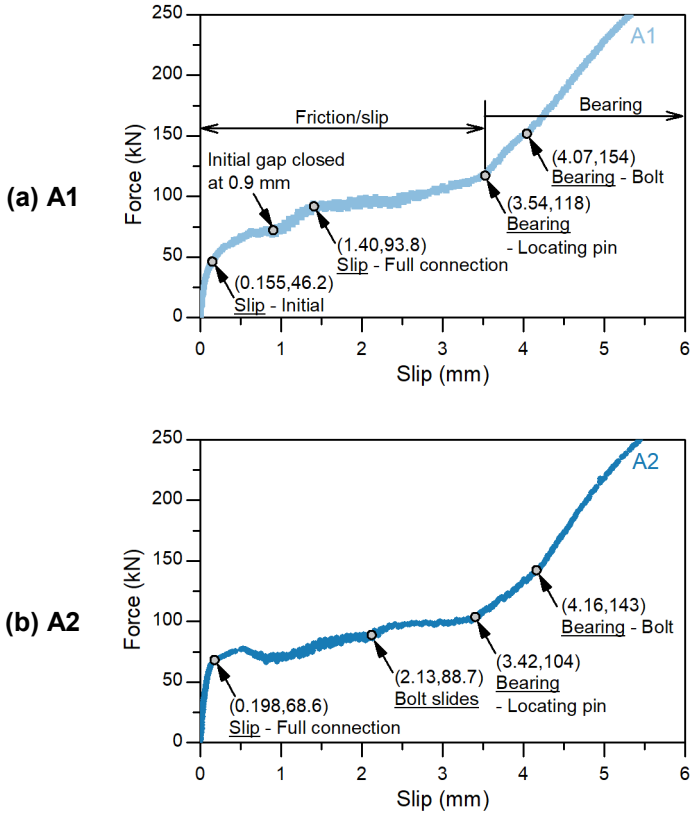

Figure 6.9. Experimental force-slip plots for (a) A1 and (b) A2

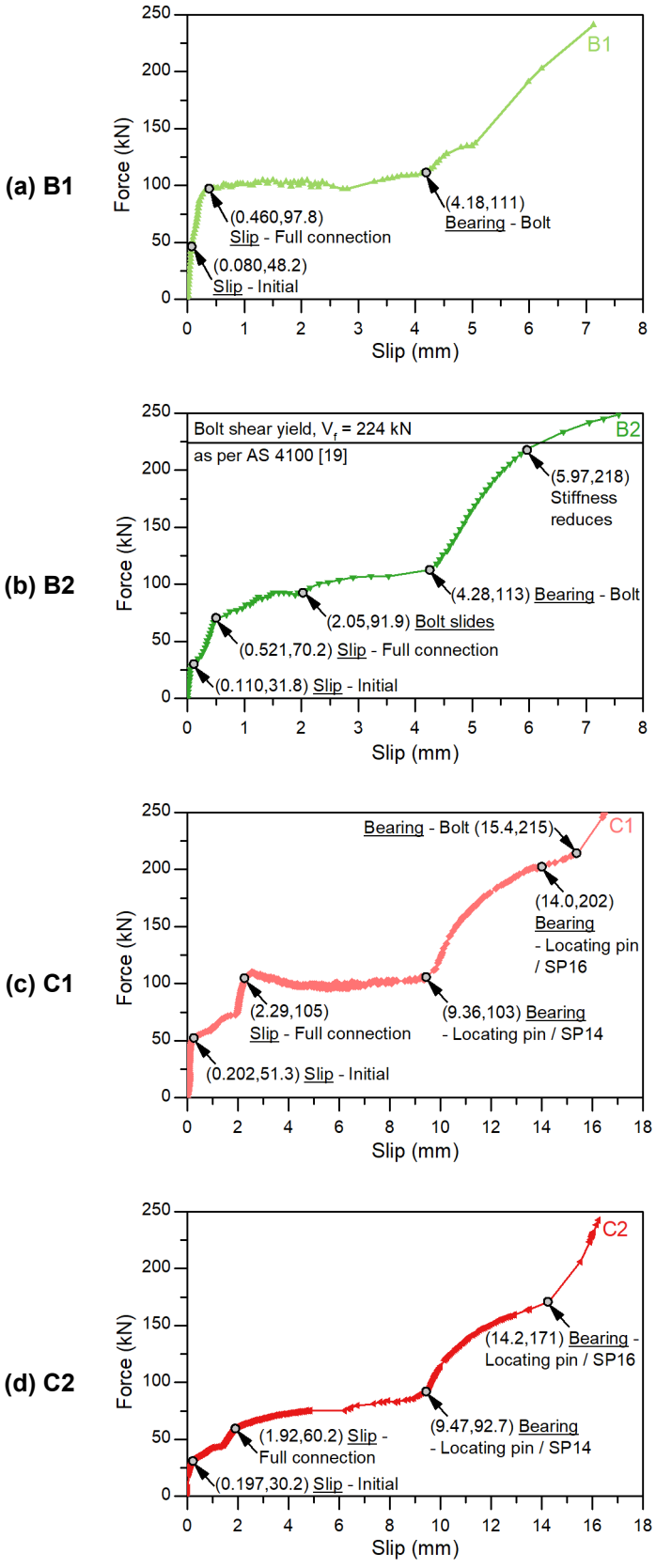

Figure 6.10. Experimental force-slip plots for (a) B1, (b) B2, (c) C1, and (d) C2

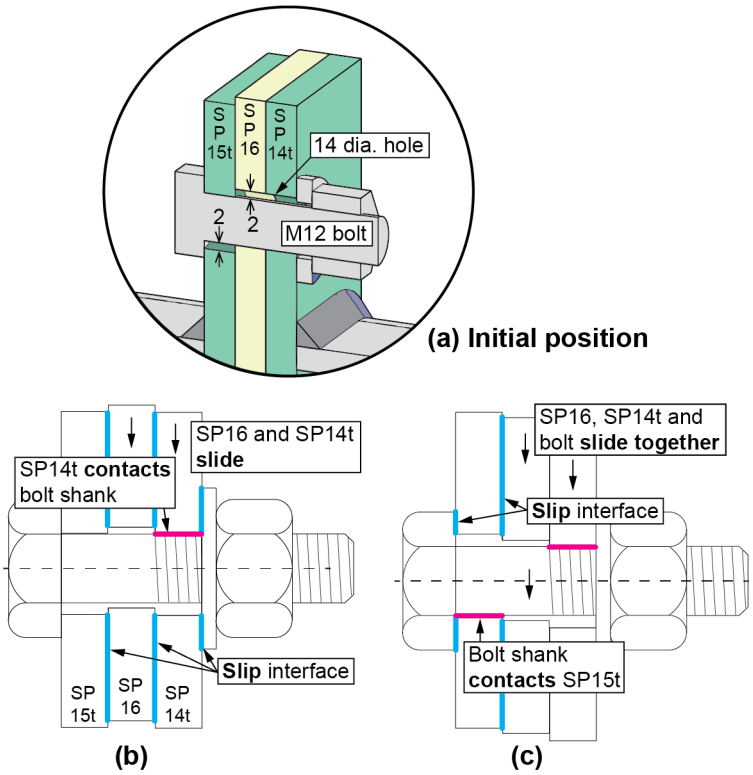

Figure 6.11. Illustration of possible slip sequence in the experiments

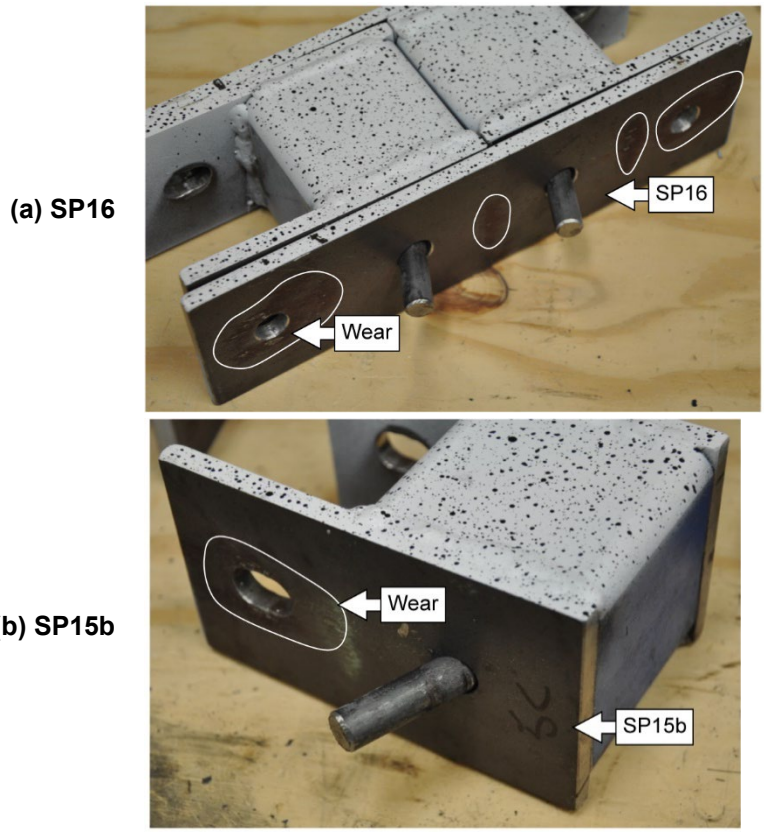

Figure 6.12. Post-test faying surfaces of C2 for (a) SP16 and (b) SP15b

Once the tests were completed the specimens were disassembled to examine the faying surfaces and performance of the locating pins. Plastic deformation of the locating pins was observed for the A and C specimens, as shown in Figure 6.12 for C2. In all the specimens, wear of the plate was observed around the bolt hole and at the upper SHS flange as shown in Figure 6.12(a). The wear of the plates at the upper SHS flange location was caused by the rotation of the outer hollow sections, i.e., SP10t, due to the bending induced by the offset loading. Damage of the mill scale layer around the bolt holes was observed for some specimens as shown in Figure 6.13 for C2 and Figure 6.14 for B2. This explains the increasing slip resistance observed for some specimens, for example B2 (Figure 6.10b). As the surfaces slid over one another, the mill scale layer was damaged exposing the underlying steel surface and so increasing the friction resistance.

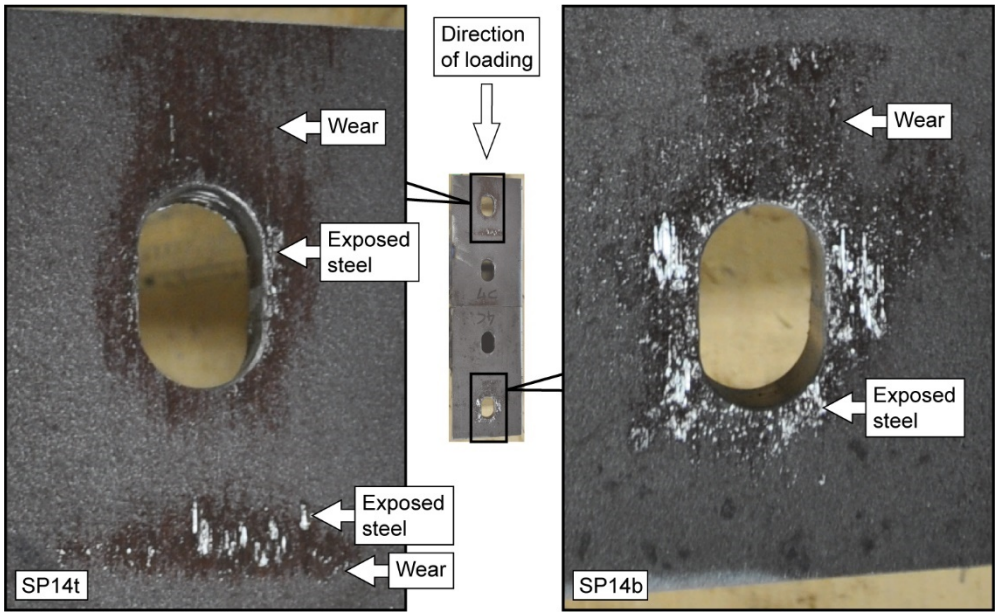

Figure 6.13. Post-test faying surfaces of C2-SP14t and SP14b showing wear around slotted holes

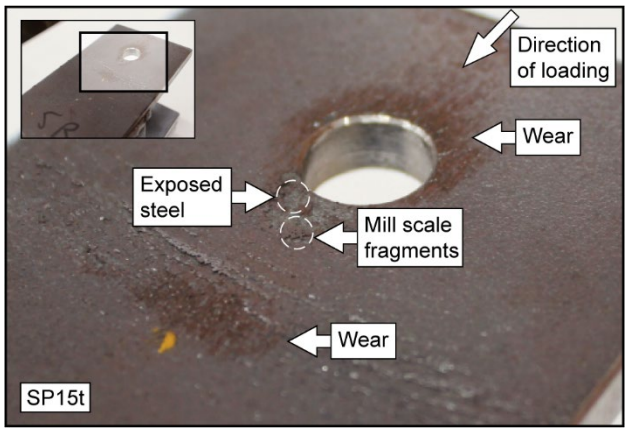

Figure 6.14. Post-test faying surface of B2-SP15t showing wear around standard round holes

6.4 Discussion and evaluation of experimental results

6.4.1 Accuracy of the slip load

In Section 5.4.1 (p.118), the variation of the slip factor due to the surface profile was estimated as ± 3.0% based on the clean mill scale slip factor tests (Chapter 4). For the M12 bolts used in the present inter-module connection tests, the mean k-factor was 0.119, and the coefficient of variation was 0.042, based on five assembly tests completed by the manufacturer in accordance with EN 14399-2 [213]. The 95% confidence interval for the preload in the connection tests is therefore ± 3.7% of the mean (Equation (5.1), p.119). Combining the variation of the preload with that of the surface profile, the uncertainty of the inter-module connection slip load is estimated as

$$\sqrt{(0.037)^2 + (0.030)^2} = \pm 4.8\% \tag{6.3}$$

where 0.037 represents the confidence interval for the preload, and 0.030 represents the confidence interval for the slip factor.

6.4.2 Behaviour of locating pins and bolts

The locating pins had little influence on the F-d behaviour in the initial friction/slip stage (Figure 6.9a, p.145). This was because the locating pins were not engaged until after the initial slip which allowed the plates to slide into contact with the locating pins. As a result, the slip resistance for the type A and B specimens is expected to be the same, except for variation in the surface profile and bolt preload. Therefore, the slip resistance for A1 and B1, and A2 and B2 may be averaged, giving 95.8 kN and 69.4 kN for the 50 kN and 35 kN preload, respectively.

The locating pins reduced the slip displacement in the bearing stage. The presence of the locating pins in combination with the bolts increased the shear resistance. Therefore, while the B specimens showed an increase in slip approaching shear yield of the bolts, this was not observed for the A specimens. For example, the force-slip stiffness for B2 (Figure 6.10d) starts to reduce once the load approaches approximately 218 kN. This corresponds well with the estimated shear yield capacity of the four M12 bolts with threads excluded from the shear plane (224 kN) as per AS4100 [139]. For B1 (Figure 6.10c) the reduction in stiffness is not shown as clearly. This is because the DIC process resulted in less accurate measurements of the slip due to a relatively poorer quality of the speckle pattern on this specimen. Several inaccurate data points were excluded from Figure 6.10(c). In contrast, the A specimens did not show a significant reduction in stiffness before the maximum force of 250 kN was reached, as shown in Figure 6.10(a, b), because the shear resistance was increased by the locating pins.

Figure 6.15 shows a bolt from B1 after testing. The bolts had one interface with threads excluded, i.e., SP15/SP16 and one interface with threads included, i.e., SP16/SP14. Deformation of the bolt is visible at the SP15/SP16 interface and at the SP16/SP14 interface. B1 slipped at the SP16/SP14 interface first causing SP14 to contact the bolt shank before SP16. This resulted in a bending action in the bolt as the shear load was applied by SP14 and resisted SP15 which was offset by the thickness of SP16 (8 mm). The photo (Figure 6.15) shows that the bolt was approaching, but had not yet exceeded, the shear yield capacity. This confirms that the bolts in the B specimens were carrying most of the applied shear force. That is, after slip, the applied shear force was resisted by the bolts, rather than friction between the plates.

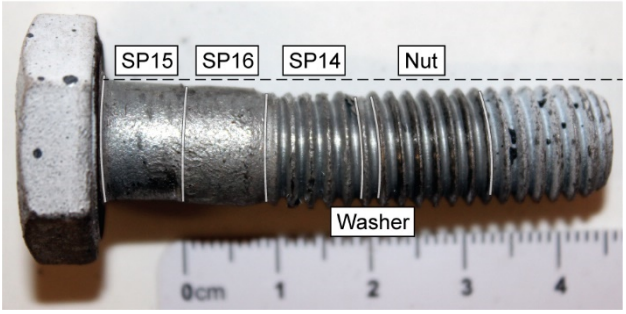

Figure 6.15. Photo of post-test bolt from B1

In comparison there was less visible deformation of the bolts in the A specimens after testing due to the presence of the locating pins. Deformation of the locating pins was observed as shown in Figure 6.16 for A2. Local bearing of the locating pin can be seen due to contact from SP14. Bending of the locating pin was caused by the bending action generated due to the load applied by SP14 being offset from SP15 by the thickness of SP16 (8 mm). The yielding of the locating pins occurred because the locating pins were engaged before the bolts, as shown in Figure 6.10(a, b). After the locating pins were deformed the bolts were engaged and the applied shear force was shared between the bolts and locating pins. A similar behaviour was observed for the C specimens, except that a larger deformation of the locating pins occurred as a result of the increased hole tolerance, as shown in Figure 6.12 for C2. The slip sequence for the C specimens is discussed further in Section 6.5.3

The slip at the transition into the bearing stage differed between the A and B specimens. For the A specimens (Figure 6.10a, b), the plates came into contact with the locating pins at an average slip of 3.48 mm. Then, at an average slip of 4.12 mm, the bolt was also in bearing. For the B specimens (Figure 6.10c, d) the bearing stage started when the plates came into contact with the bolts at an average slip of 4.23 mm. Thus, for the A and B specimens, the bolts were in bearing at an average slip of 4.17 mm and the locating pins were in bearing at a slip of 3.48 mm. The difference may be explained by the bolts having on average a slightly

smaller diameter than the locating pins. In addition, local deformation of the thread on the bolt shank may have contributed to the larger slip for the bolts.

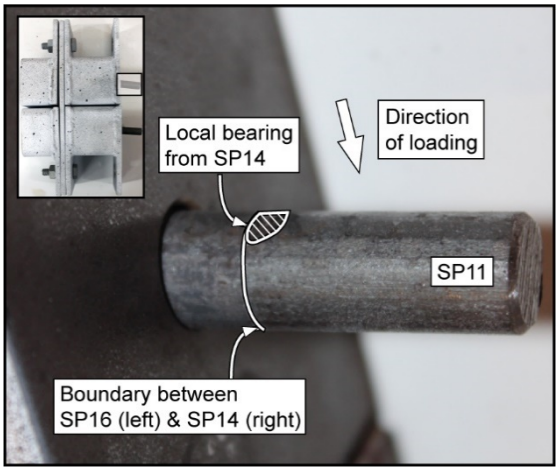

Figure 6.16. Photo of post-test locating pin from A2

6.4.3 Effect of bolt preload

The bolt preload influenced the F-d behaviour in the friction/slip stage (Figure 6.10a), with the slip resistance being greater for the higher preload. Average slip resistances of 95.8 kN and 69.4 kN were recorded for preloads of 50 kN and 35 kN respectively. The slip resistance was approximately proportional to the preload, i.e., $\frac{95.8kN}{50kN} = 1.92$ and $\frac{69.4kN}{35kN} = 1.98$. The ratio of the slip resistance to the bolt preload was slightly higher for the smaller preload of 35 kN, suggesting the slip factor was slightly greater. Although increasing the preload increased the slip resistance, the slip factor decreased slightly due to the increased preload. The decrease in the slip factor can be explained by a relatively greater flattening of the surface asperities in response to the increased contact pressure. If, for example, 0.31 is accepted as the slip factor for the 50 kN preload, then a slip factor of 0.32 may apply for the 35 kN preload. However, the difference in the slip factor was small and may equally be explained by variation in the surface profile or bolt preload. Therefore, the effect of the preload on the slip factor was neglected and the slip factor was taken to be a constant value of 0.31 based on the slip factor testing.

6.4.4 Hole tolerance

Comparing Figure 6.10(a, b) with Figure 6.10(e, f) (p.146), it can be seen that the slotted holes for the C specimens increased the slip displacement which occurred after the slip resistance was exceeded. Considering the effect on the slip resistance, the use of slotted holes was expected to increase the contact pressure which would have the effect of flattening the surface asperities and so reduce the slip resistance [149, 187]. This was observed for the 35 kN preload

for which the slip load reduced from 69.4 kN to 60.2 kN, i.e., 13%. Conversely, for the 50 kN preload the slip load increased from 95.8 kN to 105 kN, i.e., 9.6%. This difference in behaviour may be explained by the surface mill scale layer. For example, for the smaller preload of 35 kN the increase in the contact pressure due to the slotted holes may flatten the surface asperities leading to a reduced slip resistance. However, the larger preload starts with higher contact pressure, and the additional contact pressure due to the slotted hole may be enough to damage the mill scale layer exposing the underlying steel thereby increasing the slip resistance. This explanation is supported by the photos of the post-test faying surfaces which show the specimens with slotted holes (Figure 6.13, p.148) had more severe damage to the mill scale layer than the specimens with standard hole tolerance (Figure 6.14, p.148).

6.4.5 Fabrication and assembly tolerance

The initial slip resistance of the specimens was reduced due to initial gaps between the connection elements. For engineering design purposes, the reduction in performance which may be expected due to typical fabrication and assembly tolerances should be considered. Table 6.3 shows the initial slip resistance (b), the full connection slip resistance (a), and the ratio between the two (b/a). As a result of the initial gap (Figure 6.8a), only two of the four bolt preloads contributed to the initial slip resistance. Therefore the initial slip resistance was approximately half that of the full connection slip resistance, to which all four of the bolt preloads contributed. This sensitivity to the fabrication and assembly tolerance should be considered when designing the inter-module connections. Although the connection design may not feature a horizontal gap between the columns, it may be appropriate to consider a small gap to ensure the assumed behaviour is conservative. In the experiments the largest initial gap was approximately 0.9 mm for the A and B specimens which had standard round holes (Figure 6.9a), and 1.9 mm for the C specimens which had slotted holes (Figure 6.10c).

6.4.6 Comparison with existing connections

To evaluate the shear behaviour of the proposed interlocking connection, a comparison may be made with the shear behaviour of the existing inter-module connections (IMCs). Two IMCs were selected for comparison, as introduced in Section 5.6.2 (p.130). The first selected connection was studied by Styles et al. [50], who completed numerical simulations to establish the shear F-d curve. The IMC joined two 300x200x6 RHS columns vertically by using 370x410x25 mm end plates with two rows of four M24 property class 10.9 bolts. In comparison, the interlocking IMC specimens joined 75x75x6 SHS columns using 8 mm thick plate with two tensioned M12 property class 8.8 bolts and two R12 locating pins. The resulting F-d curves for the previous connection are shown in Figure 6.17(a) labelled as SV-FX and SV-FY for loading in the x- and y-direction, respectively. In this figure, the x-axis shows the slip

divided by the hole tolerance. The hole tolerance is defined as the approximate slip displacement after which the shear force is transferred by bearing rather than friction. For example, the hole tolerance was 4 mm for the A and B specimens, and 10 mm for the C specimens. For the connection presented by Styles et al. [50] the hole tolerance was 2 mm. The y-axis shows the applied force divided by the actual slip resistance of the full connection, i.e., a value of 1 on the y-axis corresponds to the actual slip resistance.

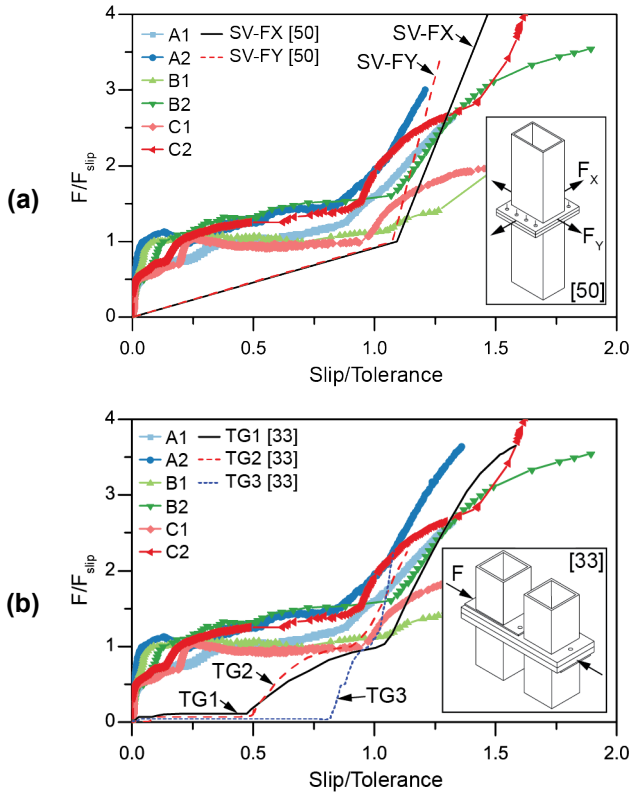

Figure 6.17. F-d curves for IL connection compared with existing inter-module connections studied by (a) Styles et al. [50] and (b) Gunawardena [33]
F/F_{slip} = applied force / slip resistance, Slip/Tolerance = displacement at slip / hole tolerance

The second selected connection was studied by Gunawardena [33], who completed experiments and numerical simulations to establish the shear F-d curve. This existing IMC detail was also a bolted end plate as shown schematically in Figure 6.17(b). It had 150x150x9 SHS columns with 25 mm thick end plates. Gunawardena [33] considered three variations of the connection. The first, labelled as TG1, had four M12 property class 8.8 bolts with standard 14 mm round bolt holes. The second, TG2, had four M16 bolts with corresponding 18 mm holes. The third, TG3, also had M16 bolts, but with slotted holes which were 18 mm wide and 26 mm long. The hole tolerance was 2 mm for TG1 and TG2, and 6 mm for TG3. The main difference between the second selected connection and the interlocking IMC specimens was the use of the locating pins for the interlocking connection, and the simplification of the stacked plate arrangement. The resulting experimental F-d curves for the previous connection

are shown in Figure 6.17(b) labelled as TG1, TG2, and TG3. It can be seen in Figure 6.17(a, b) that the proposed interlocking connection specimens gave an improved initial shear F-d stiffness in comparison with the selected existing IMC details.

6.5 Numerical simulation

Numerical simulations were conducted to support the experimental program and allow further parametric study. A finite element model of each experimental specimen was developed using ABAQUS version 6.14 [206]. Taking advantage of the symmetry, only one quarter of the specimen was modelled, for example, as shown in Figure 6.18(a) for specimen A. Symmetry boundary conditions were defined in ABAQUS for the x-direction (XSYMM) and z-direction (ZSYMM), as shown in Figure 6.18(b). A multilinear profile was adopted for the stress strain curve of the steel materials, using the quad linear profile based on regression analysis by Yun et al. [203]. The elastic modulus was set as 200 GPa and the Poisson's ratio as 0.25 following AS4100 [139]. The yield and ultimate strengths were determined based on the relevant material specification, as shown in Table 6.2 (p.142).

6.5.1 Interaction and contact property

For the plate interfaces, i.e., SP15/SP16/SP14 an interaction property was defined in ABAQUS using *Penalty friction* for the tangential behaviour. Following the slip factor tests the friction coefficient was set as 0.3146 (Table 4.3, p.90), and the elastic slip was set as 0.001 mm [205]. The normal behaviour was defined as *Hard Contact* with penalty enforcement. Interaction properties were similarly defined for the other contact areas. The friction coefficient between the bolt head and plate was taken as 0.05 [216]. The bolt shank to plate contact was taken to be frictionless [204]. Three steps were defined for the analysis. The contact interactions were established in the first step. Then, the bolt load was defined in the second step using the *applied force* method in ABAQUS. The bolt length was subsequently fixed, and the compression force was applied to the upper bearings in the third step, as shown in Figure 6.18(b). The bottom of the lower bearing was fixed, and the top of the upper bearing was limited to translation in the y-direction. These boundary conditions reflected the experiments in which restraint was provided by the universal testing machine compression plates (Figure 6.4, p.141), with friction developed at the interface between the compression plates and the bearings.

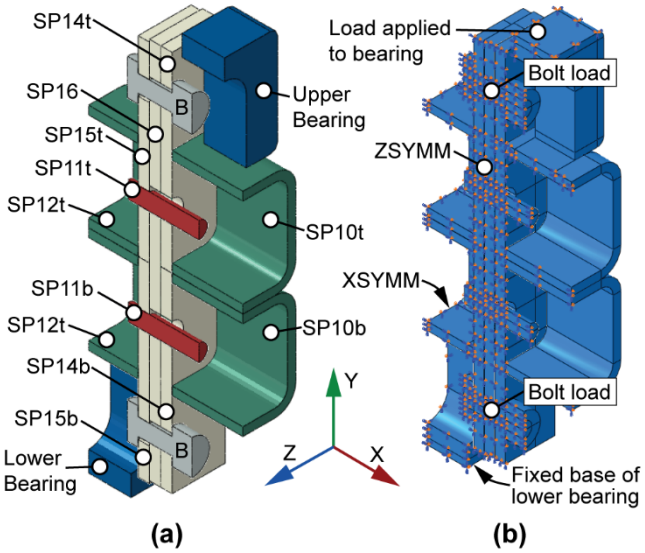

Figure 6.18. (a) ABAQUS numerical model for specimen A, and (b) Typical loading and boundary conditions

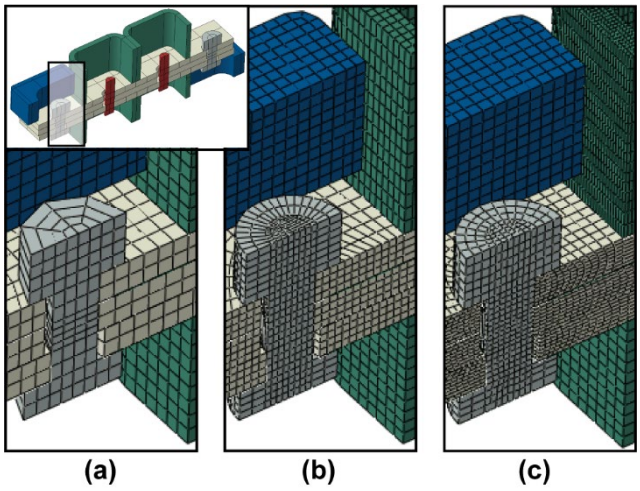

Figure 6.19. ABAQUS numerical model for specimen A showing nominal mesh sizes (a) 4, (b) 2, and (c) 1 mm

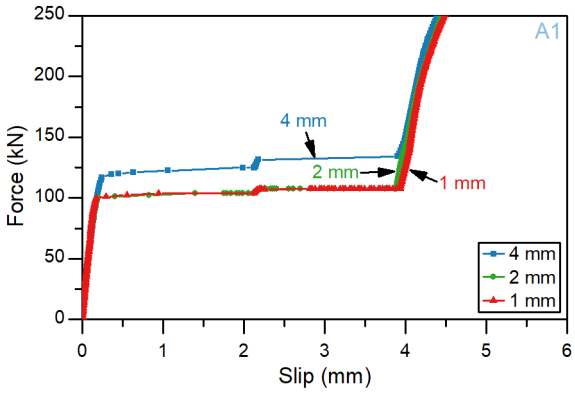

Figure 6.20. Numerical force-slip behaviour of A1 for mesh sizes 4, 2, and 1 mm

6.5.2 Mesh convergence

First order 8-node linear brick, reduced integration elements were used for the mesh. To ensure the mesh element size was sufficiently small the model was analysed with increasingly smaller mesh size and the resulting F-d behaviour compared. First, a coarse 4 mm mesh size was used as shown in Figure 6.19(a). This was followed by a general 3 mm mesh with the areas of interest refined to 2 mm (Figure 6.19b), and finally with the area of interest refined to 1 mm (Figure 6.19c). The resulting F-d behaviours are shown in Figure 6.20. A nominal mesh size of 2 mm is shown to be fine enough, with little difference in the resulting F-d plot compared with the finer 1 mm mesh. It should be noted that the gap between the locating pin and adjacent plate was set as 3.9 mm in the numerical simulation. This provided an initial separation of 0.1 mm which was beneficial for the initial convergence.

6.5.3 Numerical calibration

Figure 6.21 shows the numerical results as compared with the experimental F-d curves. In the experiments the effective friction coefficient for the steel plates varied throughout the specimen. The interface with the lower friction coefficient slipped first, followed by the next lowest in sequence. In comparison, in the numerical simulations, the same friction coefficient was adopted for all the steel plate interfaces, based on the slip factor tests. As a result, the slip sequence in the numerical simulations does not necessarily match that from the experiments.

For example, for B1 the initial slip in the experiment was at the SP14/SP16 interfaces. However, the sliding interface was constantly changing throughout the slip stage in the experiment. In contrast, in the numerical simulation the SP14/SP16 interface slipped followed by the SP16/SP15 interface in turn. As a result, the slip stage for the numerical F-d curve is effectively a horizontal line, with an increase in the force at a slip of 2 mm as SP14 contacted the bolt shank causing the bolt to start sliding. Other than the different F-d curve in the friction/slip stage, this difference in slip sequence can change the loading conditions for the bolts in the bearing stage. For example, with load applied by the SP14 plate and resisted by the SP15 plate there is an 8 mm offset which results in additional bending in the bolt (Figure 6.15). The additional bending deformation is one reason for the low stiffness in the bearing stage for the experimental result in comparison with the numerical result. Further, in the experiments, additional deformation was permitted by the deformation of the bolt threads and the rotation of the bolt shank relative to the nut. The bolt threads were not included in the numerical model, and the nut was combined with the bolt shank effectively preventing rotation. The numerical stiffness is, therefore, greater than the experimental stiffness.

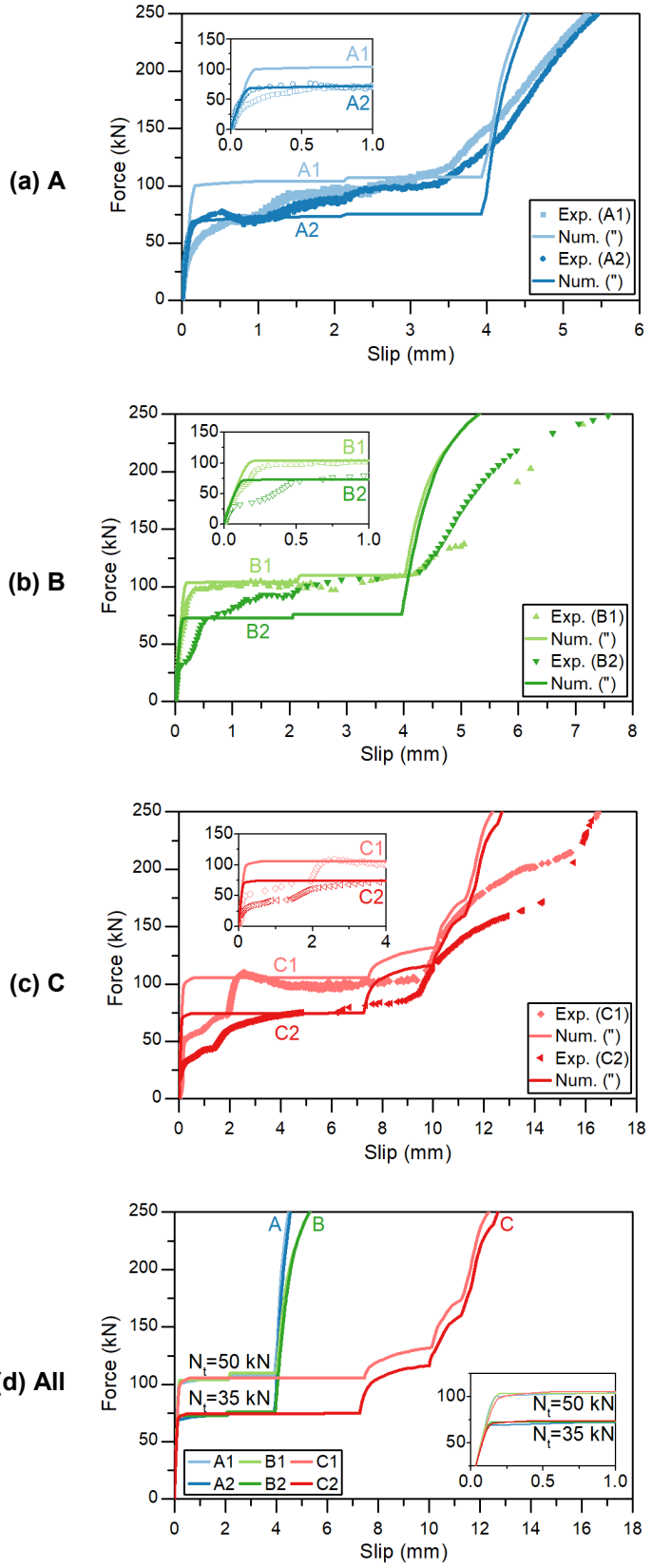

Figure 6.21. Comparison between numerical and experimental F-d curves for the (a) A, (b) B, and (c) C specimens, and (d) numerical F-d curves for all the specimens

Similarly, for C1 the slip sequence in the numerical simulation differed from the experimental result. In the experiment the slip occurred at the SP14/SP16 and SP15/SP16 interfaces. With photos at 2 s intervals, and a loading rate of 0.1 kN/s, it appeared as though the slip occurred at the SP14/SP16 and SP15/SP16 interfaces simultaneously. This slip continued until SP14 contacted the locating pin. The locating pin then deformed along with slip between the plates, until SP16 contacted the locating pin, increasing the F-d stiffness. Soon after, the total slip was enough to engage the bolts in bearing. In the numerical simulation, however, the SP14/SP16 interface slipped first. After a slip of 7 mm, SP14 and SP16 started to slide along with the bolt. The slip occurred at the SP16/SP15 interface until SP16 contacted the locating pin. Then, bending of the locating pins occurred, but the bolts did not come into bearing. These two different slip sequences explain the difference in the experimental and numerical F-d curves for the C specimens shown in Figure 6.21(c).

To match the numerical to the experimental result, the friction coefficient may be varied in the numerical simulations to ensure the slip sequence is consistent. However, a more meaningful calibration may be achieved by simply matching the initial stiffness of the force-slip curves. Disregarding the low initial slip resistances due to gaps, the numerical slip resistance gives a good match to the experimental slip resistance as shown in Table 6.4, considering the experimental uncertainty (§6.4.1, p.149). For C2 the slip resistance was overestimated by 16% based on the numerical simulation, compared with the experimental result. This is consistent with the 13% reduction in the slip resistance due to the slotted holes increasing the contact pressure and flattening the surface asperities (§6.4.4, p.151) considering the experimental uncertainty (§6.4.1, p.149).

Table 6.4. Comparison between experimental and numerical slip resistance

Specimen	A1	A2	B1	B2	C1	C2
Experimental slip resistance, $F_{slip,exp}$ (kN)	93.8	68.6	97.8	70.2	105.0	60.2
Numerical slip resistance, $F_{slip,num}$ (kN)	99.9	68.9	102.0	72.2	98.9	70.0
Error $\left(F_{slip,num} - F_{slip,\exp}\right) / F_{slip,\exp}$ (%)	6.5	0.4	4.3	2.8	-5.8	16.0

6.6 Proposed load-slip model

6.6.1 OP: Friction/slip

Following the numerical and experimental results, a model is proposed for the shear force-slip behaviour of the new interlocking inter-module connection as illustrated in Figure 6.22. The proposed model differs from the existing model for inter-module connections (Figure 2.23,

p.39) in the friction stage OP. Whereas the existing model assumes a linear behaviour, in the proposed model the initial force-slip behaviour is given by the exponential function

$$F(d) = \alpha\left[1 - \exp\left(\frac{-d}{\beta}\right)\right], \tag{6.4}$$

where F is the shear force (kN), d is the slip of the connection (mm) and α and β are parameters which define the upper limit and initial stiffness, respectively. The exponential function represents the initial stiffness more accurately than the linear behaviour assumed in the existing model.

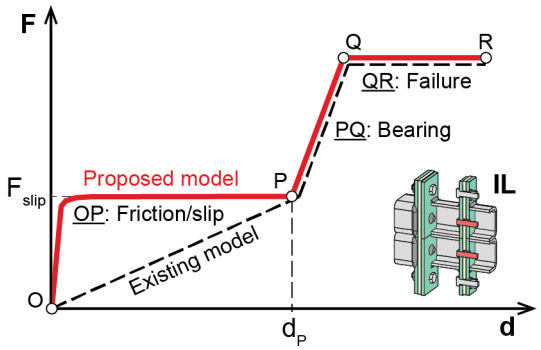

Figure 6.22. Proposed load-slip model

Equation (6.4) was fitted to the calibrated numerical results for the experimental specimens resulting in a good fit as shown in Figure 6.23 for the A (a), B (b) and C (c) specimens. The exponential model does not capture the increase in the force at a slip of 2 mm as the bolt starts sliding, resulting in a slightly conservative F-d behaviour which can be seen in Figure 6.23(a, b). Figure 6.23(d) shows the exponential fit for all the specimens together to allow comparison. As shown, there is little difference in the slip resistance provided by the specimens A, B, and C, other than due to the differing preload. It should be noted, however, that the slip factor was not varied for the numerical simulations. For engineering design, the slip resistance should be reduced where slotted holes are adopted to account for the possible reduction in the slip factor, as discussed in Section 6.4.4 (p.151). A reduction factor of 0.87 is appropriate based on the present experimental results. This is consistent with the existing design standard AS4100 [139] which specifies a reduction factor of 0.85 for short slotted holes such as those used in specimen C.

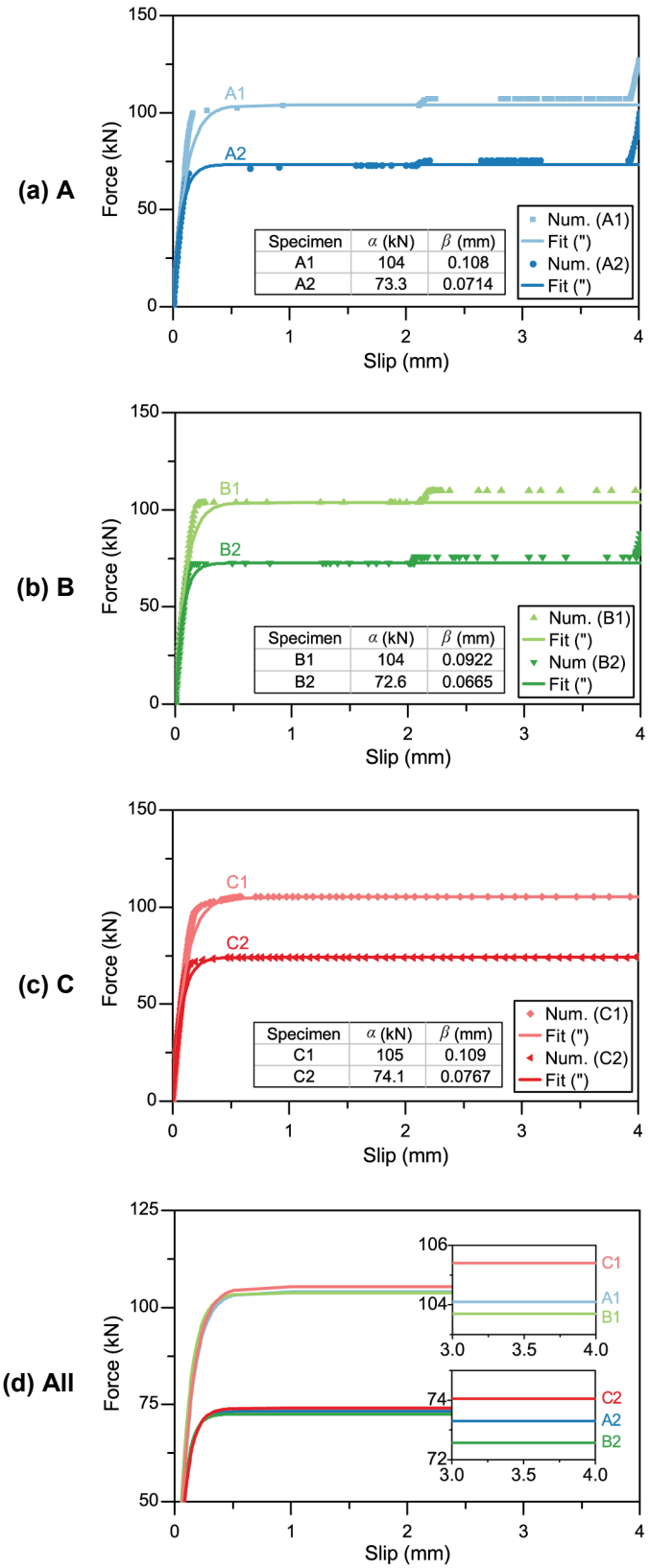

Figure 6.23. Exponential fit to numerical data for (a) A, (b) B, (c) C, and (d) all the specimens

Following the curve fit for each specimen, the resulting α and β values were examined. The parameter α was not significantly affected by the presence of the locating pins, or by the bolt hole tolerance. α was affected by the slip factor and bolt preload, with a larger preload giving a greater value for α, such that α may be estimated as

$$\alpha(\mu, N_t) \approx 6.64 \mu N_t \,, \tag{6.5}$$

where μ is the slip factor and N_t is the preload (kN). It should be noted that Equation (6.5) applies to the full specimen which incorporated two connections, one on each side. For a single connection with two bolts the value of α should be halved. Similarly, the parameter β was not significantly affected by the locating pins or the bolt hole tolerance, but the slip factor and preload did have an effect which may be estimated as

$$\beta(\mu, N_t) \approx \frac{N_t}{473 kN/mm} + 0.149 mm.\mu - 0.0657 mm \,. \tag{6.6}$$

6.6.2 PQ: Bearing

The slip displacement at the transition to the bearing stage, i.e., d_P in Figure 6.22, may be taken as the effective bolt hole tolerance. As discussed in Section 6.4.2 (p.149), the bearing stage may begin at a slightly smaller or larger slip displacement depending on the geometry. However, the difference in slip displacement is relatively small, and the bolt hole tolerance gives a reasonable estimate of the average behaviour. The stiffness in the bearing stage can be estimated following the method of Konkong et al. [151] as outlined in Section 2.2 (p.26). As shown in Figure 6.24(a), the use of three plates can result in an offset bearing arrangement for the bolts, causing a reduction in the effective stiffness for the bolts, which must be accounted for in design. The effective stiffness for the locating pins may be estimated by following a similar approach using a cantilever beam model as shown in Figure 6.24(b).

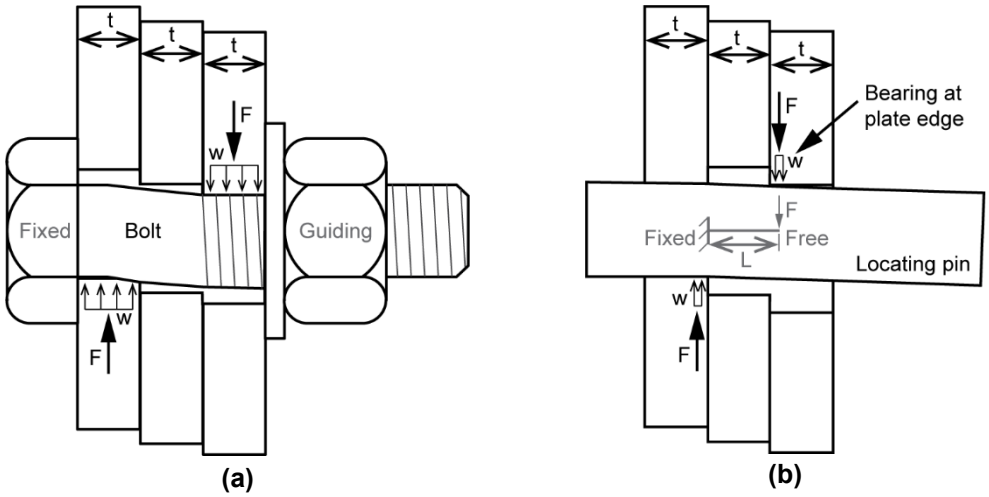

Figure 6.24. Illustration of (a) bolt bending and (b) locating pin bending due to offset shear loading

6.6.3 QR: Failure

Following the existing model (Figure 2.23, p.39) the failure load can be estimated by summing the shear capacities of the bolts and interlocking elements as appropriate. The slip displacement at the transition to the failure stage can then be calculated based on the estimated failure load, and the bearing stiffness in the previous stage PQ. Consideration should be given to the combination of bending and shear, as illustrated in Figure 6.24(a) and (b). The combined bending and shear actions may be considered by the equation [202]

$$\frac{M^*}{M}+\frac{V^*}{V}\leq 1\,, \tag{6.7}$$

where M^* and V^* are the applied moment and shear force, and M and V are the plastic moment and shear yield capacity, respectively.

6.7 Summary

A new interlocking inter-module connection was proposed for modular steel buildings. The shear force-slip (F-d) behaviour was investigated by experimental tests and numerical simulations. The main findings are summarised as follows.

1. The proposed interlocking inter-module connection offers a simplification of detailing with the ability to connect eight modules. The slip resistance of the inter-module connection depends primarily on the slip factor and bolt preload, while the locating pins provide additional shear resistance after the initial slip. The hole tolerance had a small effect on the slip resistance, and the experimental results support the use of a reduction factor of 0.85 for short slotted holes in comparison with standard round holes.

2. The proposed interlocking inter-module connection offers an improved initial shear F-d stiffness in comparison with the selected existing inter-module connection details [33, 50].

3. An empirical model was proposed for the shear force-slip behaviour based on the calibrated numerical results. The model is made up of three stages: friction/slip, bearing, and failure. For the friction/slip stage, an exponential formula was proposed which accurately represents the initial stiffness. For the bearing and failure stages, linear functions may be adopted, similar to the existing force-slip model for inter-module connections (Figure 2.23, p.39).

Chapter 7 Simplified models for the post-tensioned (PT) connection[1]

7.1 Introduction

In Chapter 5 a new post-tensioned (PT) inter-module connection (IMC) was introduced, and an empirical model was proposed for the shear behaviour of the experimental specimens. While the axial and moment-rotation (M-θ) behaviours may be relatively less significant than the shear behaviour (Chapter 3), simplified models are still required to define the performance of the connection. Therefore, this chapter investigates the axial force-displacement and M-θ behaviours of the PT connection. A numerical model is developed for the post-tensioned IMC. It is calibrated based on the experimental shear behaviour from Chapter 5, and the simplified empirical model for the shear behaviour is refined and extended to the bearing/yield stage. The numerical model is then further extended to the axial and M-θ behaviours. The numerical results are compared with the simplified analytical behaviours, which are derived in this chapter. In addition, the numerical results are compared with the experimental behaviours of selected existing IMCs. The differences are explained by the variation in the connection geometry and loading conditions, and the similarities are found to build confidence in the present numerical results.

7.2 Post-tensioned (PT) connection

The post-tensioned inter-module connection, which was introduced in Chapter 5 (Figure 5.1, p.108), is composed of a threaded rod and a hollow steel section shear key. During the site installation, which is described in Section 5.2 (p.107), the threaded rod is inserted and tensioned from within the module, via access openings. The access opening is located in the wall of the column, below the ceiling beam and above the floor beam. In Chapter 5, for example, it was shown as a rectangular opening (Figure 5.1), nominally 125 mm wide and 175 mm high, for a 150 mm square hollow section column.

In modular steel buildings the inter-module joint (IMJ) is made up of beam, column and connection elements (§2.2). The beam and column elements may be included as frame elements in the global model. Therefore, in the following sections, the stiffness of the inter-module connection (IMC) was established excluding the stiffness of the column. That is, the

[1] The related work in Chapter 7 was published in the Journal of Constructional Steel Research:

Lacey AW, Chen W, Hao H, Bi K. Simplified structural behaviours of post-tensioned inter-module connection for modular buildings. J Constr Steel Res. 2020;175:106347. https://doi.org/10.1016/j.jcsr.2020.106347

IMC was defined as shown in Figure 7.1. Hence, the IMC stiffness was defined with respect to the length **bc**, and the column lengths **ab** and **cd** must be included in the global model which applies the simplified models derived in this study. With this definition, the access opening is located away from the IMC. Hence, while the access opening may reduce the column section capacities, it does not necessarily have a significant effect on the stiffness of the IMC. Therefore, the access opening was not included in the following numerical simulations, and the column section capacities must be considered in the global model.

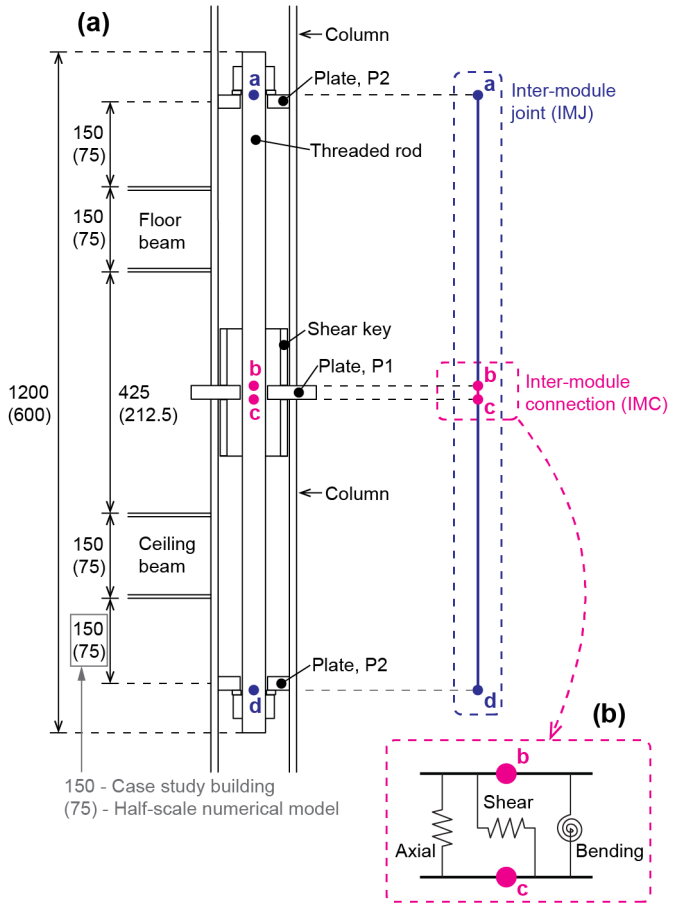

Figure 7.1. Post-tensioned inter-module connection
Adapted from Chapter 5. All dimensions in mm.

7.3 Numerical simulation

7.3.1 Geometry

A finite element model was developed in ABAQUS [206], and the geometry was based on the previous case study (Chapter 3). For the case study building, the columns and beams were 150 mm square hollow sections (SHS), and there was a clear vertical distance of 425 mm between the ceiling and floor beams (see Figure 7.1). In the present chapter, the centreline of plate P2 was located 150 mm above the floor beam, and 150 mm below the ceiling beam, i.e., there was a vertical distance of 1025 mm between the middle of the two P2 plates. The threaded rod

was therefore nominally 1200 mm long, allowing for the nut and washer thicknesses. A half-scale numerical model was adopted, as shown in Figure 7.2, such that the threaded rod was nominally 600 mm long, and the columns were 75 mm square hollow sections. By using a half-scale model, the numerical shear behaviour could be calibrated by comparison with the experimental results from Chapter 5.

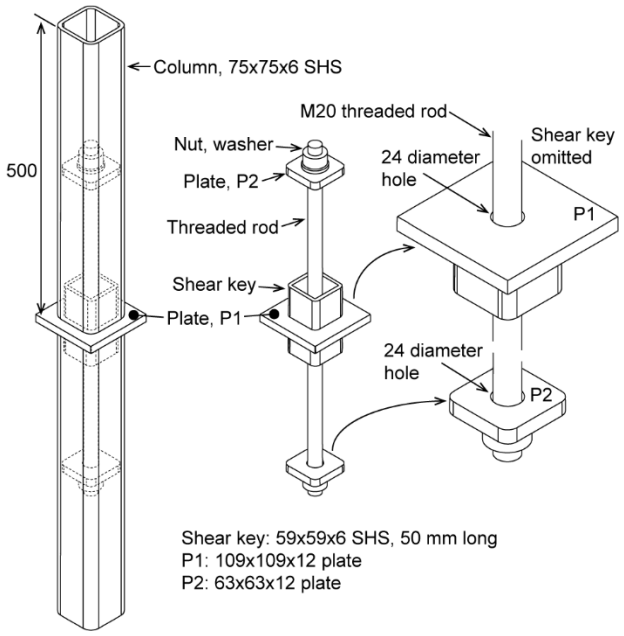

Figure 7.2. Numerical model
All dimensions in mm.

The wall thicknesses for the 150 and 75 mm columns were 10 mm and 6 mm, respectively. For the numerical model, the 6 mm thickness was selected to match the specimens in the previous experiments (Chapter 5). In the previous experiments, the 6 mm thickness was adopted to match the 6 mm fillet welds (Figure 5.3, p.110), and to ensure the columns had adequate bearing capacity. In the following sections, the axial force-displacement and moment-rotation behaviours are derived analytically, accounting for the thickness of the column. For the shear force-displacement behaviour, the column thickness may affect the simplified empirical model, which is discussed further in Section 7.4.2 (p.172).

7.3.2 Materials

The materials adopted in this chapter, i.e., the type, thickness and grade of the steel, were based on the previous experiments which are presented in Chapter 5. The plates P1 and P2 were 12 mm thick grade 350 hot rolled steel, the shear key was assembled from 6 mm thick grade 350 plates, and the column section was 75x75x6 SHS C350. A quad-linear model [203] was adopted for the stress-strain curves of the steel. The elastic modulus was defined as 200 GPa, Poisson's ratio was defined as 0.25, and the yield and tensile strengths were adopted as shown

in Table 5.3 (p.123). For the grade 350 plate sections, i.e., P1, P2, and the shear key, the yield strength was 360 MPa as indicated in AS/NZS 3678 [189] for plate thicknesses less than or equal to 12 mm.

7.3.3 Contact interactions and constraints

Hard contact and penalty friction were adopted for the normal and tangential behaviour, respectively. The friction coefficient (μ) and elastic slip (γ_{crit}) were input for the column-plate interfaces based on the calibration with the experimental data. The values are summarised in Table 5.1. A contact property was defined for the rod-plate interfaces, and μ and γ_{crit} were 0.05 and 0.001 mm, respectively (Chapter 5). Similarly, a contact property was defined for the shear key-column interfaces, and μ and γ_{crit} were 0.3 and 0.001 mm, respectively. The shear key was tied to the central plate, to reflect the welded detail in the previous experiments (Chapter 5). Similarly, P2 was tied to the column.

7.3.4 Loading and boundary conditions

The bolt load was defined in the first step using the applied force method. Then, the shear, axial, or bending moment was applied as required. As shown in Figure 7.3, the shear force was applied to the column webs at the bottom of the upper column, while the upper surface of the lower column was restrained. For the axial behaviour, the axial load was applied to the upper column at the top surface of P2, while the lower column was restrained, as shown in Figure 7.4. For the moment-rotation behaviour, the moment was applied to top of the upper column relative to the reference point (RP), while the lower column was restrained, as shown in Figure 7.5.

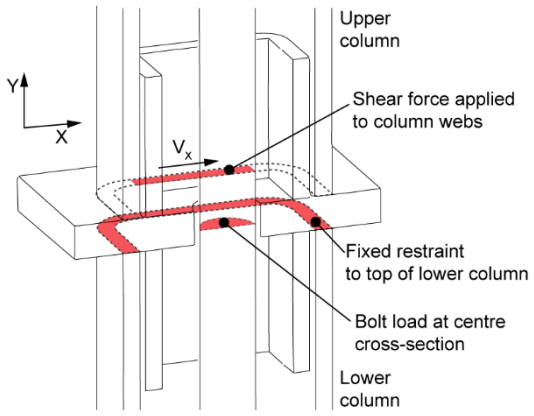

Figure 7.3. Loading and boundary conditions for shear behaviour

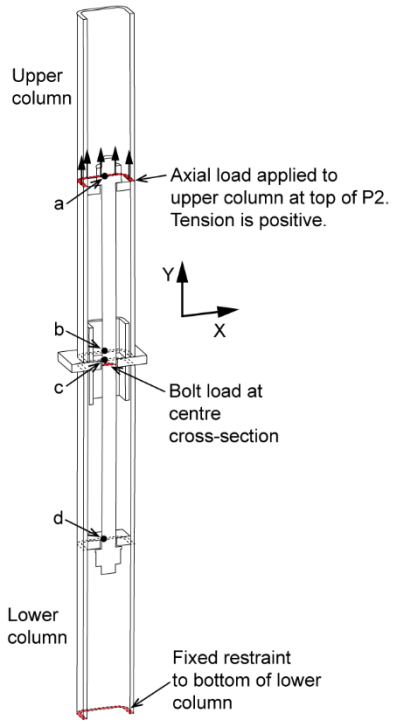

Figure 7.4. Loading and boundary conditions for axial behaviour

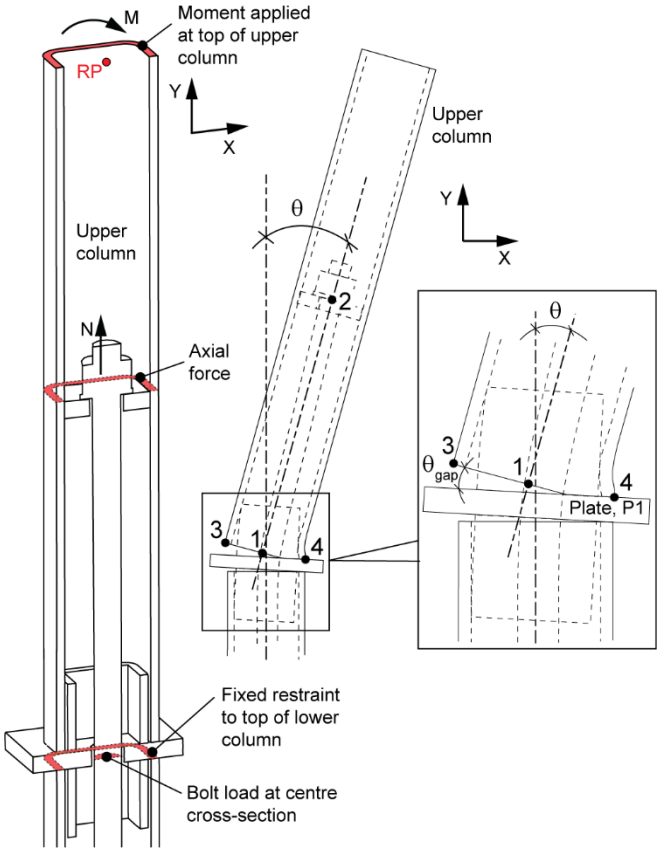

Figure 7.5. Loading and boundary conditions for moment-rotation behaviour

7.3.5 Mesh convergence

First order 8-node linear brick elements were used for the mesh. For each loading type, i.e., shear, axial and moment, the influence of the mesh size was investigated by incrementally halving the size and observing the effect. For example, the moment-rotation (M-θ) behaviour was determined for three nominal mesh sizes of 4, 2, and 1 mm. The nominal 2 mm mesh was found to be sufficient, with little difference between the behaviour for the 2 and 1 mm meshes. However, the nominal 2 mm mesh overestimated the initial stiffness associated with yielding of the column. Hence, a nominal mesh size of 2 mm was adopted, however, the size was reduced to 1 mm at the base of the column where the yielding occurred. Through a similar procedure, a nominal mesh size of 4 mm was sufficient for the shear and axial behaviours. Therefore, the nominal 4 mm mesh was adopted for the pure shear and axial behaviours. For consistency, the refined 2 mm mesh was adopted for the combined actions, such as axial loading combined with bending.

7.3.6 Model calibration

The present numerical shear behaviour was compared with the experimental results from Chapter 5. Numerical models were prepared based on the experimental specimens. As shown in Table 5.1 (p.109), the specimens were labelled NSB-150, NSB-250, Sa3-150, and Sa3-250, which refers to the different surface finish and preload. NSB indicates a clean mill scale surface for the column-plate interface, and Sa3 indicates a Sa 3 class sand blasted surface finish [193]. 150 and 250 refer to the torque (Nm) applied to the nut, which was related to preloads of 45 and 81 kN, respectively (Chapter 5). The slip factor (μ), and elastic slip (γ_{crit}) were input for the tangential contact behaviour to ensure the numerical shear behaviour matched the experimental results.

In the previous experiments (Chapter 5) there were two slip planes, because the load was applied to the central plate while the columns were restrained (Figure 5.2, p.110). In comparison, in the present numerical model, there was only a single slip plane, because the load was applied to the upper column, while the lower column was restrained. Therefore, the slip resistance in the present numerical simulations was half that of the experimental specimens. Hence, to match the experimental behaviour, the present numerical force was multiplied by two.

As shown in Figure 7.6, the numerical behaviour was matched to the experimental behaviour. To quantify the agreement, percentage errors were calculated for the initial stiffness and the slip load, assuming the experimental value was the most accurate, i.e., $\frac{V_{slip,num} - V_{slip,\exp}}{V_{slip,\exp}}$.

Comparing the initial stiffness, the experimental behaviour for Sa3-250 shows a relatively low initial stiffness (Figure 7.6a). This was caused by misalignment of the specimen during the experiment (Chapter 5), and, hence, it is not replicated in the numerical result. Otherwise, the largest percentage error was 1.8% for NSB-250. Apart from experimental error, the main reason for this difference was the different boundary conditions. In this chapter, the top of the lower column was fixed, such that the restraint was located 12 mm from the slip plane. In comparison, in the experiments (Chapter 5), the restraint was provided by a bearing support which was located up to 30 mm from the slip plane. This resulted in a slightly different distribution of the contact pressure, and hence a slightly different value for the initial stiffness.

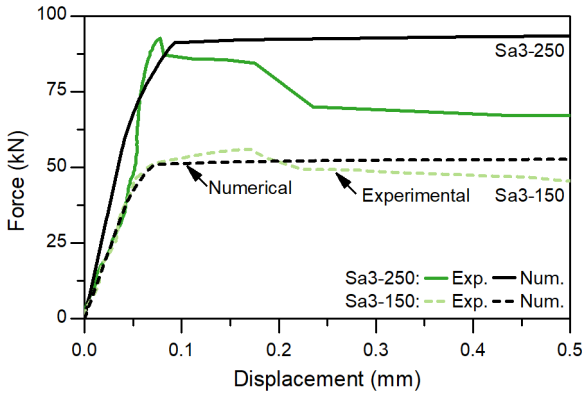

(a) Sa3

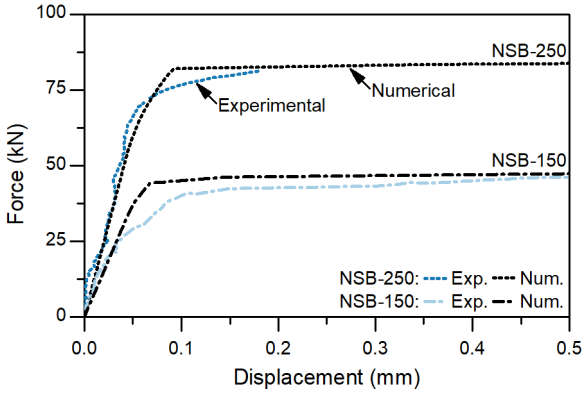

(b) NSB

Figure 7.6. Comparison between numerical and experimental shear behaviour for (a) Sa3 and (b) NSB specimens

In all of the specimens, the numerical behaviour shows a more sudden transition into the slip stage, in comparison to the experimental behaviour, due to the different boundary conditions. For the NSB specimens (Figure 7.6b), the less severe friction behaviour in the experiments gave low slip loads, while the more severe numerical behaviour gave high slip loads, resulting in a large maximum percentage error of 16% for NSB-250. For the Sa3 specimens, the interlocking angular surface asperities of the sandblasted surfaces caused a severe friction

behaviour, which caused a reduction in the applied force following slip, but was more consistent with the numerical behaviour prior to slip. The largest percentage error in the slip load was 5.3% for Sa3-150, which was caused by variation of the surface finish and bolt preload in the experiment.

7.4 Shear force-displacement behaviour

7.4.1 Numerical results

7.4.1.1 Shear force (V)

Figure 7.7 shows the numerical shear force-displacement curves, in which the friction/slip and bearing/yield stages are clearly visible. In the friction/slip stage, the displacement increased slowly until the friction resistance was exceeded at point 1. The friction resistance was generated around the column perimeter, while the shear force was applied to the column webs (Figure 7.3, p.166), causing local deformation of the column flange (Figure 7.8b). As the friction resistance was exceeded there was a corresponding lateral displacement, and the upper column moved across, coming into contact with the shear key at point 2 (Figure 7.8a). The shear key was located centrally within the column, and there was initially a clear distance of 2 mm either side. Therefore, point 2 was located at a displacement of 2 mm. Due to the local deformation of the column flange, the contact area between the upper column and the shear key at point 2 was reduced (Figure 7.8b). Then, since there was still a clear distance of 2 mm between the shear key and the lower column, the lateral displacement continued, and the upper column and shear key assembly moved across together, relative to the lower column, until the key contacted the lower column at point 3 (Figure 7.8a). Hence, point 3 was located at a displacement of 4 mm. The bearing/yield stage started after point 3, when the shear key was confined by the columns resulting in a significant increase in the stiffness. Eventually, at point 4, the shear force was sufficient to cause yielding of the upper column, resulting in a gradual reduction in the stiffness.

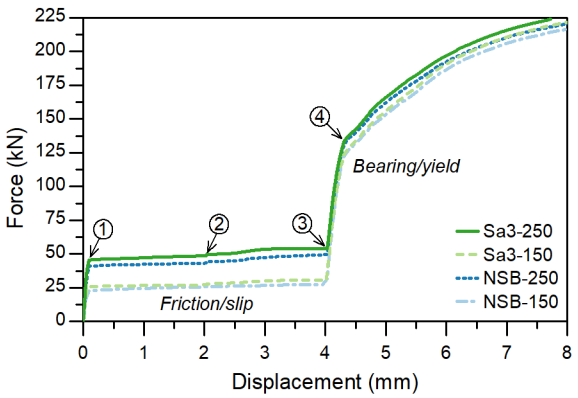

Figure 7.7. Numerical shear force-displacement curves

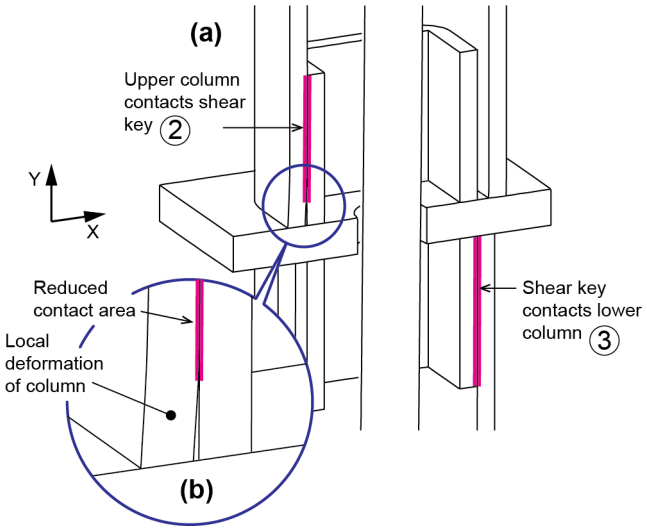

Figure 7.8. Numerical model showing key stages of the shear behaviour

7.4.1.2 Axial – shear force interaction (N+V)

To determine the effect on the shear behaviour, an axial force (N) was applied to the upper column, after which the shear force was applied, and incrementally increased to the maximum value. The axial forces considered included 0.5Nt, 0.1Nc, and 0.2Nc, where Nt was the ultimate tension capacity of the M20 rod, and Nc was the ultimate compression capacity of the column section. An axial load of 0.1 to 0.2Nc was considered as a typical value for modular buildings (§2.2.5.4, p.46). The resulting shear force-displacement curves (Figure 7.9) show that the axial compression force increased the slip resistance and shear yield capacity. Similarly, axial tension reduced the slip resistance and shear yield capacity.

7.4.1.3 Moment – shear force interaction (M+V)

To determine the effect on the shear force-displacement behaviour, a bending moment (M) was applied to the upper column at the same time as the shear force was applied. Following the cantilevering column arrangement of the numerical model, it was envisaged that a lateral load applied at the top of the column would generate a corresponding combination of shear and bending at the bottom of the column, and that the moment to shear ratio would depend on the column length. Hence, three cases were considered: M/V=1 m, M/V=0.5 m, and M/V=0.25 m. The resulting force-displacement behaviours are shown in Figure 7.10, along with the pure shear behaviour for comparison. Although small lateral displacements were recorded for the combined moment and shear load cases, they were associated with column rotation, and shear slip of the connection did not occur. The negative slope shown for the combined load cases was caused by local yielding of the column flange at the location where the lateral displacement was measured.

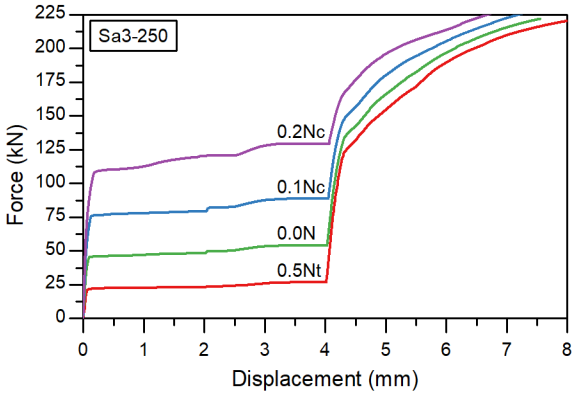

Figure 7.9. Numerical shear behaviour for varying axial load

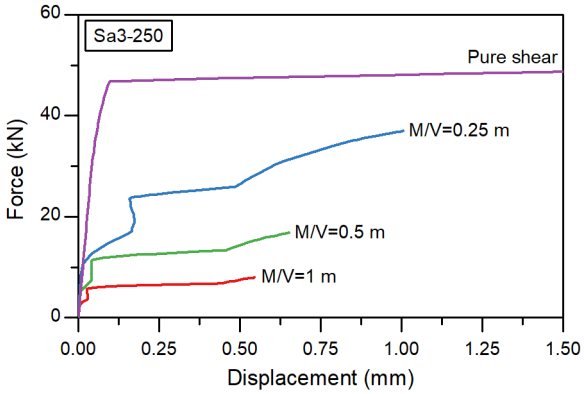

Figure 7.10. Numerical shear behaviour for varying moment

7.4.2 Simplified empirical model

7.4.2.1 Friction/slip (OP)

In Chapter 5, an exponential function was proposed for the shear force-displacement behaviour of the experimental specimens in the initial friction/slip stage as Equation (5.9) (p.131). In the present chapter the model for the friction/slip stage is refined, and the model for the following bearing/yield stage is developed. The simplified model proposed is shown in Figure 7.11. An improved function is proposed for the initial friction/slip behaviour as

$$V(x) = V_{slip}\left\{1-\exp\left[\frac{-\left(K_{OP,i}-K_{OP,p}\right)x}{V_{slip}}\right]\right\}+K_{OP,p}x\,, \tag{7.1}$$

where V_{slip} is the slip resistance, previously given as A in Chapter 5, and $K_{OP,i}$ is the initial stiffness, which was previously defined by B, i.e., $K_{OP,i}=V_{slip}B^{-1}$. $K_{OP,p}$ is the hardening stiffness, which is introduced to reflect the small increase in the friction resistance after slip, but before the bearing stage.

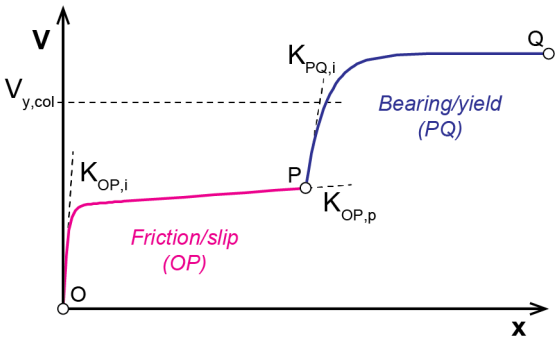

Figure 7.11. Proposed shear force-displacement model

Equation (7.1) was fitted to the numerical data, and the resulting V_{slip}, $K_{OP,i}$, and $K_{OP,p}$ values are shown in Table 7.1. Hence, from the numerical results, the slip load can be estimated as

$$V_{slip} = C_{slip}\mu_p F_{clamp}, \tag{7.2}$$

where C_{slip} = 1.087 is a coefficient obtained by curve fitting to the numerical results, μ_p is the column-plate slip factor, and F_{clamp} is the effective clamping force, which will be derived in Section 7.5.3.1 (p.182) as Equation (7.23). In the numerical model, the penalty method was adopted for the tangential behaviour. The slip factor (μ) and elastic slip (γ_{crit}) were input for each surface. This defined the critical shear stress (τ_{crit}) at which surfaces slide, and, hence, following Equation (5.7) (p.124) the stiffness in the sticking stage can be given as

$$k_{s,i} = \frac{\tau_{crit}}{\gamma_{crit}} = \frac{\mu_p p}{\gamma_{crit}}, \tag{7.3}$$

where p is the contact pressure. The overall initial stiffness is, therefore, expected to be a function of $\lambda = \mu_p F_{clamp}\gamma_{crit}^{-1}$. Hence, the overall initial stiffness ($K_{OP,i}$) can be estimated as

$$K_{OP,i} = c_1\lambda^2 + c_2\lambda, \tag{7.4}$$

where $c_1 = -2.272\times10^{-5}\,mm\,kN^{-1}$, $c_2 = 0.4203$, and $\lambda\left[kN\,mm^{-1}\right] = \mu_p F_{clamp}\gamma_{crit}^{-1}$. For preliminary design purposes, when the elastic slip is unknown, the initial stiffness can be estimated as

$$K_{OP,i} = c_3 V_{slip}^2 + c_4 V_{slip}, \tag{7.5}$$

where V_{slip} [kN] is the slip load calculated using Equation (7.2), c_3 = -0.04728 $kN^{-1}mm^{-1}$, and c_4 = 17.88 mm^{-1}. For the hardening stiffness, $K_{OP,p}$, a value equal to 0.3% of $K_{OP,i}$ is suggested.

The column wall thickness may have an effect on the force-displacement behaviour obtained from the simplified model. For example, in the previous experiments (Chapter 5), increasing the column cross-sectional area from 1530 to 3474 mm^2 increased the slip load by 8% for the Sa3-150 specimen. The increase in the slip load was explained by the fact that increasing the contact area reduced the contact pressure, thereby reducing flattening of the surface asperities

and increasing the slip load. Hence, increasing the column thickness will increase the cross-sectional area, which may have a small effect on the slip load.

It can be seen from Table 7.1 that the initial stiffness ($K_{OP,i}$) values in this chapter differ slightly from those in Chapter 5. For example, in this chapter, the NSB-150 specimen had a slip load of 22.1 kN and an initial stiffness of 378 kN/mm. Hence, the value of B (§5.6.4, p.134) can be calculated as 0.059 mm, which is greater than the value of 0.04 mm suggested in Chapter 5. The difference was caused by the different boundary conditions, as explained in Section 7.3.6 (p.168).

Table 7.1. Connection specimens and associated numerical curve fitting parameters
Positive axial load (N) indicates tension.

Specimen	μ_p	$F_{t,ini}$ (kN)	γ_{crit} (mm)	N (kN)	F_{clamp} (kN)	V_{slip} (kN)	$K_{OP,i}$ (kN/mm)	$K_{OP,p}$ (kN/mm)	$K_{PQ,i}$ (kN/mm)
NSB-150	0.5	45	0.025	0	45.0	22.13	377.8	1.449	443.6
NSB-250	0.5	81	0.025	0	81.0	40.98	619.1	1.998	415.5
Sa3-150	0.55	45	0.0225	0	45.0	25.47	448.1	1.435	431.7
Sa3-250	0.55	81	0.0225	46.38	40.5	21.76	388.1	1.388	443.1
Sa3-250	0.55	81	0.0225	0	81.0	46.72	736.0	1.378	419.3
Sa3-250	0.55	81	0.0225	-53.6	128.0	76.06	1080.0	3.559	346.8
Sa3-250	0.55	81	0.0225	-107	175.0	108.30	1387.0	5.626	215.0

7.4.2.2 Bearing/yield (PQ)

The shear force-displacement behaviour in the bearing/yield stage can be represented by the exponential function

$$V(x) = V_{friction} + V_{y,IMC}\left[1 - \exp\left(\frac{-K_{PQ,i}\left(x - x_P\right)}{V_{y,IMC}}\right)\right] \le V_{y,col}, \tag{7.6}$$

where V is the applied shear force, x is the displacement, $V_{friction}$ is the shear force transferred through friction between the column and the central plate, $V_{y,IMC}$ is the shear force which causes first yield of the components of the IMC, $V_{y,col}$ is the shear force which causes first yield of the column, and $K_{PQ,i}$ is the V-x stiffness at the start of the bearing stage. Equation (7.6) is valid for $x > x_P$, i.e., the displacement at point P, which is taken as the effective tolerance (4 mm).

The shear yield capacity of the column ($V_{y,col}$) represents the maximum load which can be transferred by the column to the IMC. It can be estimated by calculating the column shear yield capacity, which may be reduced by the axial load in the column. A conservative estimate of the reduced shear yield capacity can be obtained by applying the Von Mises yield criterion [217]. Hence, the shear yield capacity can be given as

$$V_{y,col} = A_{V,col}\sqrt{\frac{f_{y,col}^2 - \left[\max\left(N, F_{clamp}\right)A_{col}^{-1}\right]^2}{3}}\,, \tag{7.7}$$

where $f_{y,col}$ is the column yield strength, N is the applied axial tension force, and F_{clamp} is the clamp force. $A_{V,col}$ is the portion of the column cross-section which is active for shear, and it can be estimated as [166]

$$A_{V,col} = 0.5A_{col}\,. \tag{7.8}$$

The shear yield capacity of the IMC ($V_{y,IMC}$) represents the maximum load which can be transferred by the IMC. It can be estimated based on the possible shear yield of the column flange ($V_{y,col,flange}$), and yield of the shear key ($V_{y,key}$). Shear yield of the column flange can occur due to lateral pressure from the shear key. Applying Equation (7.7), the shear yield capacity of the column flange can be estimated as

$$V_{y,col,flange} = 2t_{col}h_{key}\sqrt{\frac{f_{y,col}^2 - \left(F_{clamp}A_{col}^{-1}\right)^2}{3}}\,, \tag{7.9}$$

where F_{clamp} is the clamp force, t_{col} is the thickness of the column section, and h_{key} is the height of the shear key above the central plate. For example, with t_{col} = 6 mm, h_{key} = 50 mm, $f_{y,col}$ = 350 MPa, F_{clamp} = 81 kN, and A_{col} = 1532 mm^2 the shear yield capacity of the column flange is 120 kN. After the column contacts the shear key, friction between the column and the key allows the transfer of axial load to the key. However, this axial load is concentrated in the flange of the key, while the shear resistance is developed predominantly in the webs. Hence, the shear yield capacity of the key can be estimated simply as [166]

$$V_{y,key} = 0.5A_{key}\frac{f_{y,key}}{\sqrt{3}}\,, \tag{7.10}$$

where $f_{y,key}$ is the yield strength of the key, and A_{key} is the cross-sectional area of the shear key. For example, with $f_{y,key}$ = 350 MPa, and A_{key} = 1200 mm^2 the shear yield capacity of the key is 121 kN. Hence, the shear yield capacity ($V_{y,IMC}$) can be given as

$$V_{y,IMC} = \min(V_{y,col,flange}, V_{y,key})\,. \tag{7.11}$$

After the column contacts the shear key, the clamping force can reduce due to friction between the column and the shear key. Allowing for the reduced clamping force, the friction resistance between the column and central plate can be given as

$$V_{friction} = V_P - \left(V^* - V_P\right)C_{slip}\mu_k\mu_p\,, \tag{7.12}$$

where C_{slip} is a coefficient from Equation (7.2) (p.173), μ_p is the column-plate slip factor, μ_k is the column-key slip factor, $V_P = V_{slip} + K_{OP,p}x_P$ is the slip resistance at the start of the bearing

stage, and $V^* > V_P$ is the applied shear force. Substituting Equation (7.12) into Equation (7.6), the exponential model can be given as

$$V(x) = V_P + \frac{V_{y,IMC}}{1 + C_{slip}\mu_k\mu_p}\left[1 - \exp\left(\frac{-K_{PQ,i}\left(x - x_P\right)}{V_{y,IMC}}\right)\right] \le V_{y,col}\,. \tag{7.13}$$

In the numerical model, the shear force was applied to the webs of the upper column, while the corresponding frictional resistance was generated around the column perimeter. Consequently, there was local bending deformation of the upper column flange, as shown in Figure 7.8(b). This reduced the contact area between the column flange and the shear key. The resulting deformation of the shear key, which can be idealised as a cantilevering column, was increased because the height of the applied lateral load was raised. At the start of the bearing stage, the axial load in the upper column had a lateral offset of 4 mm relative to the lower column. The resulting bending moment caused a small rotation which further reduced the contact area between the column flange and the shear key, thereby increasing deformation of the shear key as the height of the applied lateral load was raised. In this way, the axial load in the column caused a reduction in the bearing stiffness ($K_{PQ,i}$). Therefore, fitting a curve to the numerical results, the bearing stiffness ($K_{PQ,i}$) can be given as a function of the clamping force as

$$K_{PQ,i} = c_5 F_{clamp}^3 + c_6\,, \tag{7.14}$$

where F_{clamp} [kN] is the clamping force, $c_5 = -4.29\times10^{-5}\,kN^{-2}mm^{-1}$, and $c_6 = 441\,kNmm^{-1}$.

The bearing stiffness given in Equation (7.14) is the result of bending deformation of the column and shear key flanges, and combined bending and shear deformation of the shear key webs. Due to the restraint applied to the upper surface of the lower column, the deformation of the lower column and shear key was suppressed in the numerical model. These may be included by halving the stiffness given by Equation (7.14). In addition, the bending deformation of the column flange depends on the thickness of the column. Therefore, changes to the column thickness may affect the bearing stiffness.

7.4.2.3 Comparison with numerical results

Figure 7.12 shows the shear force-displacement curves from the numerical study, in addition to those which result from applying the simplified model. In the numerical model, the shear force was applied at the bottom of the upper column, which had the effect of suppressing the column shear yield. Therefore, the curves plotted in Figure 7.12 do not include the upper limit of $V_{y,col}$ as shown in Equation (7.13), i.e., the applied shear force is not limited to the shear yield capacity of the column. In the bearing/yield stage, it can be seen that the simplified model

predicts a smaller shear capacity than the numerical simulation, particularly for the specimen with an axial tension force (0.5Nt). This occurs because the model assumes that the ultimate shear capacity is reached when the applied shear force first causes shear yield of the inter-module connection. A positive hardening stiffness is not included because the resulting model could predict a shear capacity for the inter-module connection that is much larger than the column section could transfer. Therefore, the main interest is the accuracy of the model behaviour prior to the first shear yield.

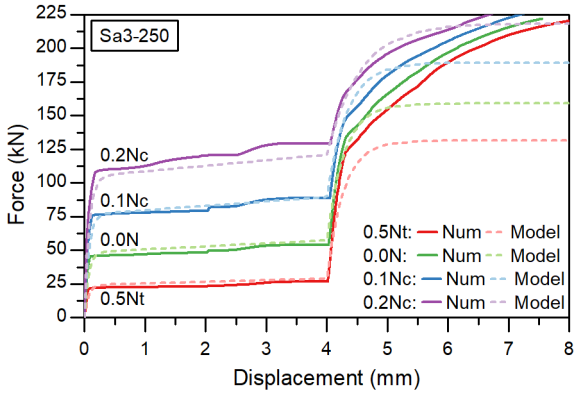

Figure 7.12. Comparison between simplified model and numerical results for shear behaviour

Referring to the Sa3-250 specimens in Figure 7.12, the predicted slip load was most accurate for the 0.1Nc specimen (0.67% error) and least accurate for the 0.5Nt specimen (11% error). For the value of C_{slip}=1.087, the slip load for the 0.1Nc and 0.2Nc specimens is predicted accurately. For smaller clamp loads, which may occur due to axial tension or a small initial bolt preload, a value of C_{slip}=1 is suggested. This would reduce the percentage error for the 0.5Nt specimen to 2.4%, while increasing that for the 0.1Nc specimen to 1.1%. The predicted initial stiffness ($K_{OP,i}$) was most accurate for the 0.2Nc specimen (0.47% error) and least accurate for the 0.5Nt specimen (1.5% error). While the predicted initial bearing stiffness ($K_{PQ,i}$) was most accurate for the 0.0N specimen (0.18% error), and least accurate for the 0.1Nc specimen (1.4% error). Overall, a good match is demonstrated between the numerical and model parameters for the behaviour prior to first yield.

7.5 Axial force-displacement behaviour

7.5.1 Numerical results

7.5.1.1 Axial force (N)

Figure 7.13 shows the numerical axial force-displacement curves for the four specimens. Figure 7.13(a) relates to the inter-module joint (IMJ) for which the vertical displacement was calculated as

$$y_{IMJ} = y_a - y_d \,, \tag{7.15}$$

where y_a and y_d were the vertical displacements at points *a* and *d* as shown in Figure 7.1 (p.164) and Figure 7.4 (p.167). For axial tension, a high force-displacement stiffness was observed which continued until the column started to lift and separate from the central plate at point 2 (Figure 7.13, p.179). Thereafter, a lower constant stiffness was observed which continued until the rod started to yield at point 3, resulting in a sudden increase in the displacement. For axial compression, a high stiffness was observed, which was relatively constant until the compression force was sufficient to cause yielding of the column at point 1.

Similarly, Figure 7.13(b) relates to the inter-module connection (IMC), for which the vertical displacement was calculated as

$$y_{IMC} = y_b - y_c \,. \tag{7.16}$$

For axial compression the displacement was negligible in comparison with that of the IMJ. For axial tension the displacement was negligible until the column started to separate from the central plate at point 2. After the column started to lift, the stiffness was relatively constant until the rod started to yield at point 3.

7.5.1.2 Moment – axial force interaction (M+N)

A bending moment of 1.35 kNm was applied, and the axial force was increased incrementally to establish the axial behaviour, as shown in Figure 7.14. For axial tension, the stiffness of the IMC was a constant and there was negligible vertical displacement, until the upper column separated from the central plate. The tension force at which the upper column started to lift was reduced in comparison with the Sa3-250 specimen, which was subjected to an axial force only. The applied moment affected the distribution of the clamping pressure such that a smaller tension force was required to cause separation. A P-Δ effect was also introduced, wherein the initial bending moment caused a lateral flexural displacement of the column and, hence, as the axial force was applied there was a corresponding secondary moment induced in the column. For axial compression, the ultimate capacity of the column was reduced due to the P-Δ effect. In the case of axial tension, the lateral flexural displacement of the column due to the initial

bending caused the rod to contact the central plate earlier, and the ultimate tension capacity of the connection was reduced due to the combined bending and tension in the rod.

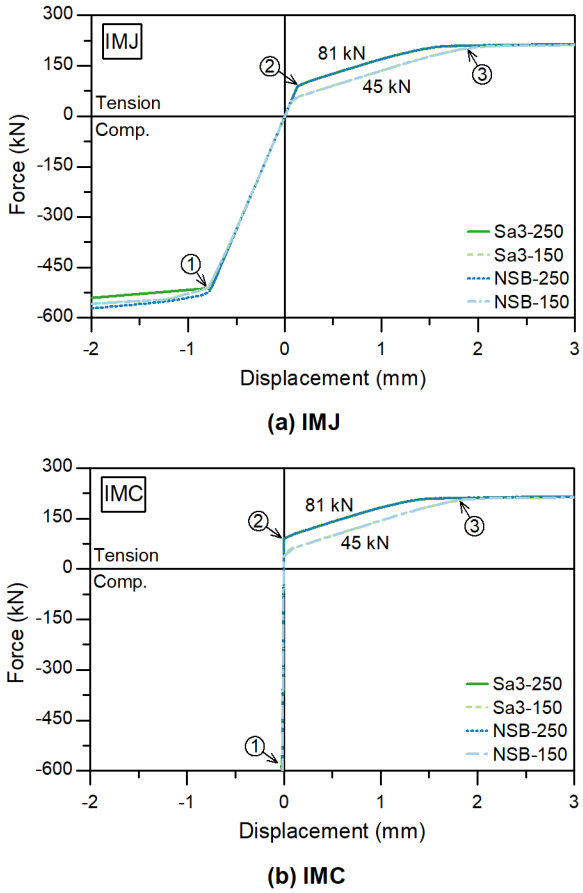

Figure 7.13. Numerical axial behaviour for (a) the inter-module joint (IMJ) and (b) the inter-module connection (IMC)

7.5.1.3 Shear – axial force interaction (V+N)

A shear force equal to half the slip resistance of the Sa3-250 specimen was applied, i.e., 23 kN. The axial force was then increased incrementally to establish the axial force-displacement curve, as shown in Figure 7.14. The applied axial tension force slowly reduced the clamp force and, hence, the slip resistance, until the connection eventually slipped. When the connection slipped there was a corresponding lateral displacement equal to the effective tolerance, i.e., the upper column moved across 4 mm relative to the lower column. The rod nuts did not immediately slip against the reacting plates (P2), therefore the centreline of the rod rotated relative to the column. As a result, a rotation was induced in the upper column due to the rotation of the line of action of the rod tension. Hence, the upper column separated from the central plate earlier due to the addition of the shear force. That is, the point at which the column started to lift was associated with the shear slip of the connection. The lateral displacement due to shear slip also caused a bending moment to be induced in the rod. This had the effect

of increasing the rod tension, and ultimately reduced the axial capacity of the rod due to the combination of bending and tension in the rod.

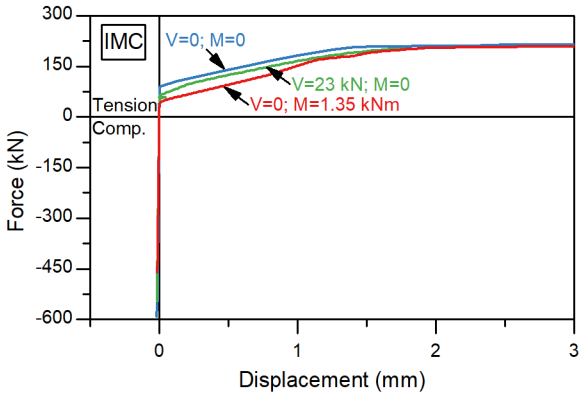

Figure 7.14. Numerical axial behaviour for Sa3-250 with shear and bending moment

7.5.2 Comparison with existing inter-module connections

Two existing inter-module connections (IMCs) with published axial force-displacement data were selected for comparison with the post-tensioned IMC. The selected existing IMCs are known as the VectorBloc (VB) connection [218] (Figure 7.15a) and the Self-lock (SL) connection [219] (Figure 7.15b). In the VectorBloc (VB) connection [218], an *upper bloc connector* joins the module ceiling beams to the column, and a *lower bloc connector* joins the module floor beams to the column. The bloc dimensions were defined to suit a 101.6 x 101.6 x 9.5 mm square hollow section (SHS) column. During the site assembly, a 12.7 mm thick *gusset plate* is screwed to the *upper bloc connectors*, thereby providing horizontal connection between adjacent modules. The 19.05 mm diameter screws have a countersunk flat head, and hence they are known as *flat head cap screws* (FHCS). A 50.8 mm diameter *registration pin*, which is fixed to the *gusset plate*, is inserted into the *lower bloc* of the upper module, and assists with the alignment of stacked modules during site assembly. Finally, two long screws are inserted through the *lower bloc* and *gusset plate*, and into the *upper bloc connector* of the lower module, thereby providing the vertical connection. The 25.4 mm diameter long screws have a socket head and are, therefore, known as *socket head cap screws* (SHCS).

The axial behaviour of the VB connection was tested experimentally, and the resulting force-displacement curves are shown in Figure 7.16. The curves, which were traced from the plots in the referenced work [218], show the axial behaviour for two similar specimens, i.e., *Specimen 1* and *Specimen 2*. In tension, the failure was determined by failure of the long socket head screws, and the average maximum load was 521 kN. The ultimate tension capacity of each of the long screws was approximately 654 kN, i.e., $N_{tf} = 506.7mm^2 \times 1290.9MPa = 654kN$ [218]. The long screws were offset from the column centreline and so they were subjected to

combined bending and tension. This explains why the connection failed at 521 kN, which was less than the tension capacity of the two screws (1,308 kN). In compression, the failure was due to buckling of the column, and the average maximum load was 1,830 kN. The ultimate capacity of the 101.6 x 101.6 x 9.5 mm SHS section was approximately 1935 kN, i.e., $3500mm^2 \times 552.9MPa$ [218].

In the Self-lock (SL) connection [219], a *joint box* joins the lower module ceiling beam to the column, and a similar *joint box* joins the upper module floor beam to the column. Referring to (Figure 7.15b), a *stud* (12) is fixed to the lower *joint box*, and it is inserted into the upper *joint box* during site assembly. The upper *joint box* includes female threaded parts, known as *cone-shaped latches* (10), which engage with the male threaded part of the lower joint box, i.e., the *stud* (12). In the upper joint box, springs allow the threaded parts to engage during site assembly, without requirement for physical access. The axial tension behaviour of the SL connection was tested experimentally, and the resulting force-displacement curve is shown in Figure 7.16. The force-displacement curve shows three stages. First, the behaviour was linear elastic, up to a load of 350 kN. Then, the behaviour was nonlinear, due to plastic deformation of the threads in the *stud* and *cone-shaped latches*. Finally, at a load of 690 kN, the *stud* failed in tension at the first thread, where the diameter of the *stud* cross-section was 40 mm. The failure load was approximately equal to the ultimate tensile capacity of the *stud*, i.e., $N_{tf} = 1257mm^2 \times 553.7MPa = 696kN$ [219].

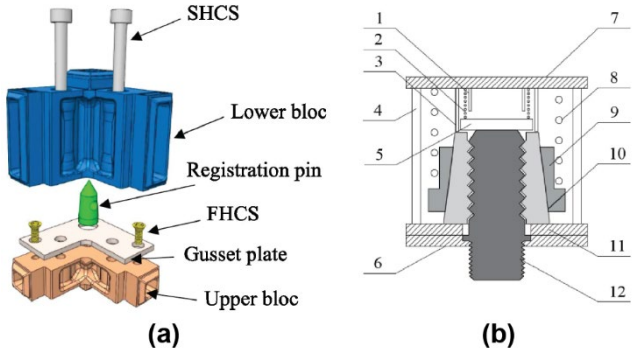

Figure 7.15. Existing inter-module connections: (a) VectorBloc (VB) connector [218], and (b) Self-lock (SL) connector [219]

Figure 7.16 shows the axial behaviours, and allows a comparison of the shape of the curve for the different IMCs. It can be seen that the behaviour of the PT connection is similar to the SL connection, which builds confidence in the numerical results of the present study. This is because the tension behaviour for the PT and SL connections was determined by the tension failure of a single threaded rod component. In comparison, the axial tension behaviour of the VB connection was determined by combined tension and bending in the long screws, which resulted in larger displacements.

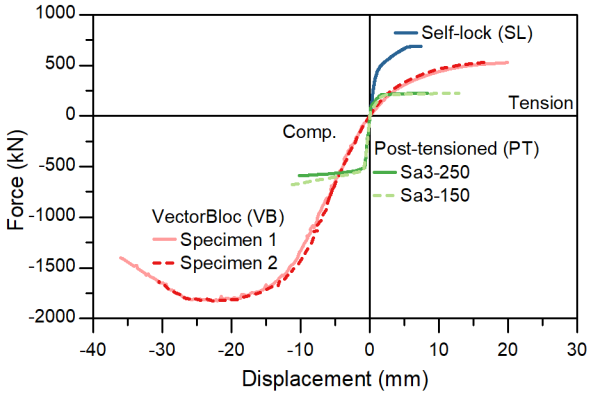

Figure 7.16. Axial behaviour of the VectorBloc (VB) [218], Self-lock (SL) [219], and Post-tensioned (PT) inter-module connections

7.5.3 Simplified analytical model

A simplified four stage model is proposed for the axial behaviour of the post-tensioned inter-module joint. The proposed model is defined by three key points, i.e., *F*, *G*, and *H*, as shown in Figure 7.17 for the inter-module joint (IMJ) and the inter-module connection (IMC), respectively. In this figure, a positive value for the applied force (N) indicates tension, and a positive displacement (y) indicates extension of the column length. For the compression behaviour, the proposed model has a linear behaviour until the ultimate compression capacity is reached at *F*. For the tension behaviour, the stiffness is constant until the applied tension is sufficient to separate the column from the central plate P1, which occurs at *G*. Prior to *G* the stiffness is high because the column and rod work in combination due to the initial preload in the rod. After *G* the stiffness is reduced as only the rod contributes to the resistance. Finally, at *H*, the ultimate tension capacity is reached.

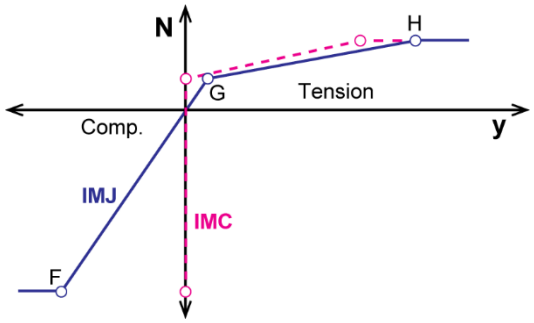

Figure 7.17. Proposed axial model for the inter-module joint (IMJ) and inter-module connection (IMC)

7.5.3.1 Inter-module joint (IMJ)

The following method can be used to derive the axial behaviour for the IMJ. First, the ultimate compression capacity of the column (N_F) is determined using the relevant design standard, for

example, AS4100 [139]. Next, the stiffness of the segment *FG* is calculated by combining the stiffness of the column (k_{col}) with the effective stiffness of the rod assembly ($k_{rod,eff}$) as

$$K_{FG} = k_{col} + k_{rod,eff} . \tag{7.17}$$

The stiffness of the column is approximated as

$$k_{col} = \frac{E_{col} A_{col}}{L_{ad}}, \tag{7.18}$$

where E_{col} is the elastic modulus, A_{col} is the cross-sectional area of the column, and L_{ad} is the grip length of the rod. The rod assembly consists of two plates (P2) and the rod in series, and the effective stiffness is calculated as

$$k_{rod,eff} = \left(\frac{1}{k_{P2}} + \frac{1}{k_{rod}} + \frac{1}{k_{P2}} \right)^{-1} = \frac{k_{P2} k_{rod}}{k_{P2} + 2k_{rod}}, \tag{7.19}$$

where k_{P2} is the stiffness of plate P2, and k_{rod} is the stiffness of the rod. The stiffness of the rod can be estimated as

$$k_{rod} = \frac{E_{rod} A_{rod}}{L_{ad}}, \tag{7.20}$$

where E_{rod} is the elastic modulus, and A_{rod} is the cross sectional area. For practical applications Equation (7.20) should be adjusted to allow for the threads in the rod, which were not included in the present numerical simulations. Plate P2 is assumed to be a square plate which is simply supported with the load applied to a small concentric circle. The effect of the bolt hole is neglected and the stiffness can be estimated as [220]

$$k_{P2} = \frac{E_{P2} {t_{P2}}^3}{\alpha b_{P2}^2}, \tag{7.21}$$

where E_{P2} is the elastic modulus, b_{P2} and t_{P2} are the width and thickness of the plate, respectively, and α is a coefficient equal to 0.1267 for a square plate with Poisson's ratio of 0.3 [221]. Hence, the displacement at point *F* (Figure 7.17) can be calculated as

$$y_F = \frac{N_F}{K_{FG}} . \tag{7.22}$$

For the post-tensioned connection, the rod is tensioned following the site installation during which the modules are stacked. If an external axial load is subsequently applied to the column then this has an effect on the clamp force between the faying surfaces and, hence, an effect on the tension in the rod (F_t). If an external force (N) is applied to the column, such that N greater than zero indicates tension, then the reduced clamp force (F_{clamp}) can be estimated as

$$F_{clamp} = F_{t,ini} - C_{clamp} N , \tag{7.23}$$

where $F_{t,ini}$ is the initial preload in the rod, and $C_{clamp} = \left(\frac{k_{col}}{k_{rod,eff} + k_{col}} \right)$. The corresponding rod tension can then be estimated as

$$F_t = F_{t,ini} + \left(1 - C_{clamp}\right) N \,. \tag{7.24}$$

To ensure the rod is limited to tension, and to account for the possible separation of the faying surfaces, the rod tension must be greater than or equal to zero, and the corresponding clamp force must be less than or equal to the applied load (N).

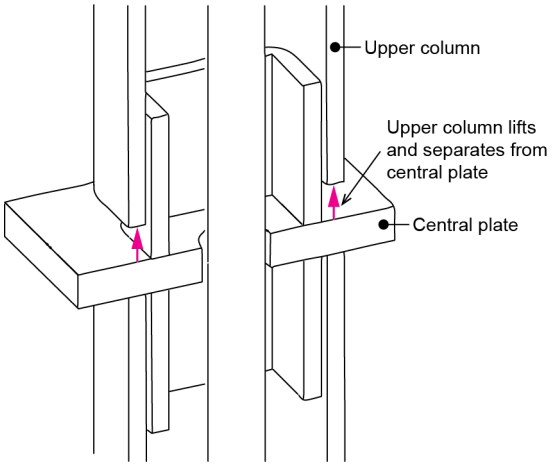

Figure 7.18. Column separates from central plate

G is the point at which the column separates from the central plate P1 (Figure 7.18). The load required to separate the column from the central plate can be found by setting the clamp force equal to zero, which gives

$$N_G = \frac{F_{t,ini}}{C_{clamp}} \,, \tag{7.25}$$

and the displacement at point G can then be calculated as,

$$y_G = \frac{N_G}{K_{FG}} \,. \tag{7.26}$$

H is the point at which the rod yields in tension, and the corresponding stiffness of segment K_{GH} can be estimated as,

$$K_{GH} = k_{rod,eff} \,. \tag{7.27}$$

Therefore, the displacement at point H can be calculated as,

$$y_H = y_G + \frac{N_H - N_G}{K_{GH}} \,. \tag{7.28}$$

7.5.3.2 Inter-module connection (IMC)

For use in the global simulation of the modular building, it is convenient to define the IMC as shown in Figure 7.1 (p.164). To derive the axial behaviour for the IMC, a simplification is proposed in which the displacement due to the IMC is considered to be insignificant until the applied tension is sufficient to separate the upper column from the central plate. Hence, for the IMC, the displacement at G is zero, and, after separation, the displacement at H is estimated as

$$y_{H,IMC} = \frac{N_H - F_{t,ini}}{k_{rod,eff}} . \tag{7.29}$$

7.5.3.3 Moment – axial force interaction (M+N)

If a constant bending moment is applied in combination with an increasing axial force, a change in the N-y stiffness is expected when the neutral axis reaches the centre of the column, where the rod is located. To ensure equilibrium, the applied moment (M^*) can be related to the initial rod tension ($F_{t,ini}$) and the applied axial force (N^*) as

$$M^* = \left(F_{t,ini} - N^*\right)\left(y_{Fc} - y_{Ft}\right) , \tag{7.30}$$

where y_{Fc} is the location of the equivalent compression force, and y_{Ft} is the location of the rod tension. Further explanation on the relevant parameters is provided in Section 7.6.3 (p.193). With the neutral axis located at the centre of the column, i.e., $y_{NA} = y_{Ft} = 0.5b$, the location of the equivalent compression force can be estimated as $y_{Fc} = 1.8y_{NA}$. Therefore, the tension force at which the N-y stiffness reduces can be estimated as

$$N_G = F_{t,ini} - \frac{M^*}{y_{Fc} - y_{Ft}} = F_{t,ini} - \frac{2.5M^*}{b} , \tag{7.31}$$

where b is the width of the column section. For design purposes the axial behaviour can be established based on the maximum design bending moment. In addition, the rod preload can be selected to ensure that the design bending moment does not exceed the decompression moment.

7.5.3.4 Shear – axial force interaction (V+N)

If a constant shear force is applied in combination with an increasing axial force, then a change in the N-y stiffness is expected when the connection slips in shear. Therefore, the tension force at which the connection slips can be estimated as

$$N_G = \left(F_{t,ini} - \frac{V^*}{\mu_p}\right) C_{clamp}^{-1} , \tag{7.32}$$

where V^* is the constant applied shear force. For design purposes, provided the tension force is limited to N_G, the shear force has little effect on the axial behaviour. That is, the maximum axial tension force can be set by selecting the maximum shear force ($V^*<V_{slip}$).

7.5.3.5 Comparison with numerical results

Figure 7.19 compares the simplified model with the numerical results for the axial behaviour of specimens Sa3-250 and Sa3-150, i.e., $F_{t,ini}$ = 81 and 45 kN. The behaviour of the IMJ is shown in Figure 7.19(a), and the behaviour of the IMC is shown in Figure 7.19(b). The simplified models can be seen to provide a reasonable estimate of the numerical behaviours. For example, the numerical result for Sa3-250, i.e., 81 kN preload, showed the column would separate from the central plate at a load of 89.3 kN. In comparison, the analytical model predicted the column would separate from the central plate at a load of 92.7 kN. This represented an error of approximately 3.8%, assuming the numerical result was the more accurate value.

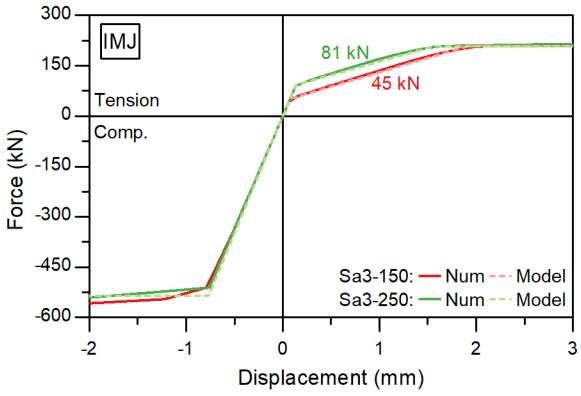

(a) IMJ

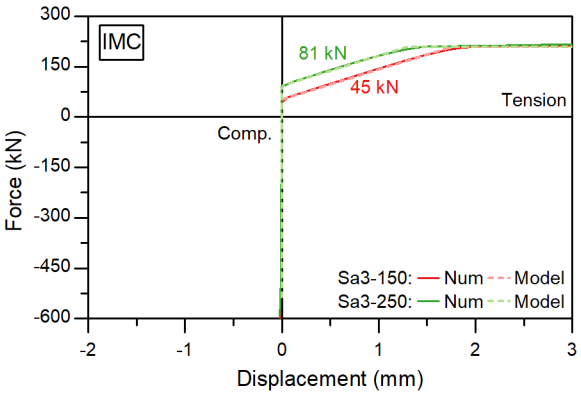

(b) IMC

Figure 7.19. Simplified model and numerical results for axial behaviour

For the rod tension, Equation (7.24) (p.184) was well matched to the numerical results, as shown in Figure 7.20. The accuracy of the estimated rod tension curve could be improved by

a more accurate estimate of the stiffness of plate P2, although a reasonable match was achieved with the present simplification. As shown in Figure 7.20, the tension in the rod increases in response to a tension force applied to the column. During the design, the size of the rod should be selected to ensure that sufficient additional tension capacity is available for the anticipated design tension force on the column. At the same time, the reduction in the slip resistance which results from the reduced clamping force, following Equation (7.23) (p.183), should be considered.

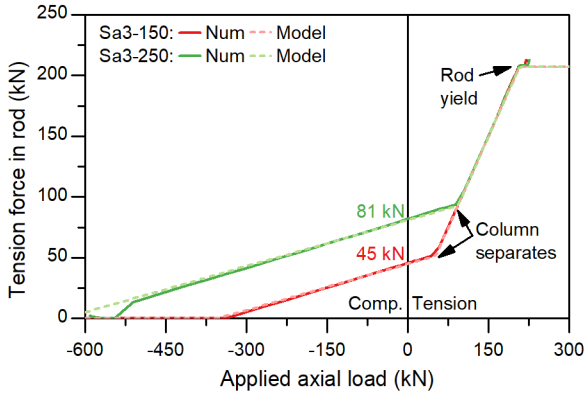

Figure 7.20. Plot of rod tension against column axial load

7.6 Moment-rotation behaviour

7.6.1 Numerical results

7.6.1.1 Moment (M)

Figure 7.21 shows the numerical moment-rotation (M-θ) curves for the four specimens. Figure 7.21(a) relates to the inter-module joint (IMJ) for which the total rotation (θ) was calculated based on the displacement of points 1 and 2 (Figure 7.5, p.167) as

$$\theta = \text{atan}\left(\frac{x_2 - x_1}{256.25mm + y_2 - y_1}\right), \tag{7.33}$$

where x_1 and y_1 indicated the displacement of point 1 in the x- and y-direction, respectively. Similarly, Figure 7.21(b) relates to the inter-module connection (IMC) for which the gap rotation (θ_{gap}) was calculated based on the displacement of the points 3 and 4 (Figure 7.5) as

$$\theta_{gap} = \text{atan}\left(\frac{y_3 - y_4}{75mm + x_3 - x_4}\right). \tag{7.34}$$

A similar behaviour was observed for each of the specimens. Initially, the rotation was caused by flexural displacement of the column. At point 1, which is also known as the decompression point, the clamp force due to the rod preload was reduced to zero at the leading edge of the

column flange. As a result, the column started to lift as illustrated in Figure 7.22. As the column started to lift there was a corresponding shift in the neutral axis, and the total rotation increased due to the opening of a gap between the upper column and the central plate. As the applied moment increased, there was a corresponding increase in the maximum stress in the compression flange of the upper column. At point 2 there was local yielding of the column flange which caused an increase in the rotation as the gap rotation increased. At point 3 the rod came into contact with the central plate which caused a small increase in the M-θ stiffness. As illustrated in Figure 7.23, the upper column came into contact with the shear key at point 4, which again caused a small increase in the M-θ stiffness. Then, at point 5, the shear key was effectively confined as the key came into contact with the lower column.

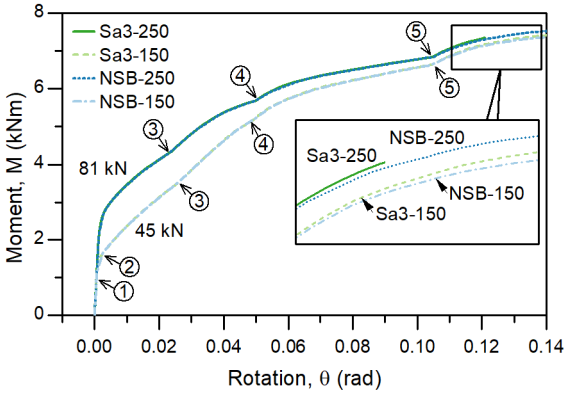

(a) Total Rotation

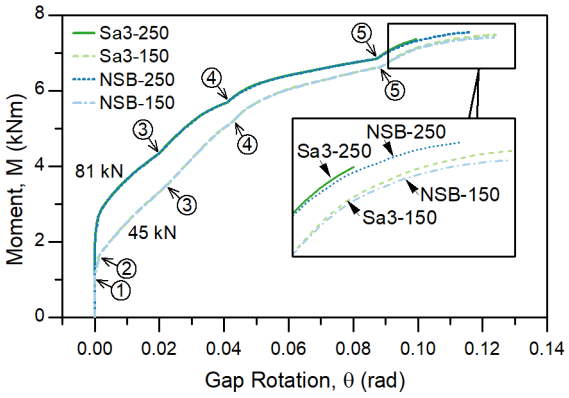

(b) Gap Rotation

Figure 7.21. Numerical M-θ curves for (a) the total rotation, and (b) the gap rotation

The ultimate moment capacity was controlled by the key points illustrated in Figure 7.24, which occurred after point 5 in Figure 7.21. Since the rod had come into contact with the central plate, the applied moment resulted in a combination of tension and bending in the rod, which resulted in yielding of the rod at point 6. Due to friction between the upper column and the central plate, the applied moment caused local deformation of the column flange, leading to contact between the upper column and the shear key at point 7. Friction at the new column

to shear key interface, i.e., point 7, then contributed to the ultimate moment resistance. Similarly, friction at the interface formed at point 4 (Figure 7.23) increased the moment capacity. In the ultimate state the friction resistance was exceeded and the upper column slid over the shear key as illustrated by point 8 in Figure 7.24.

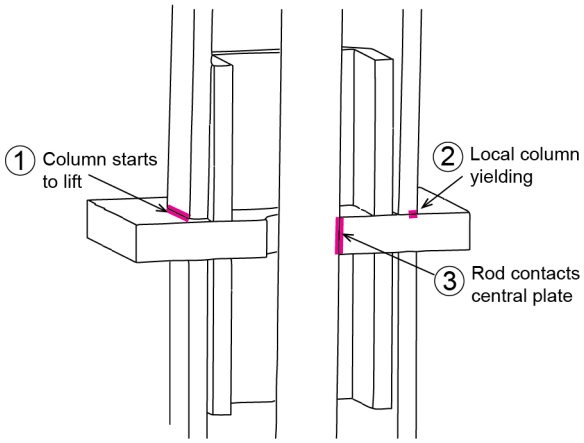

Figure 7.22. M-θ key points 1-3

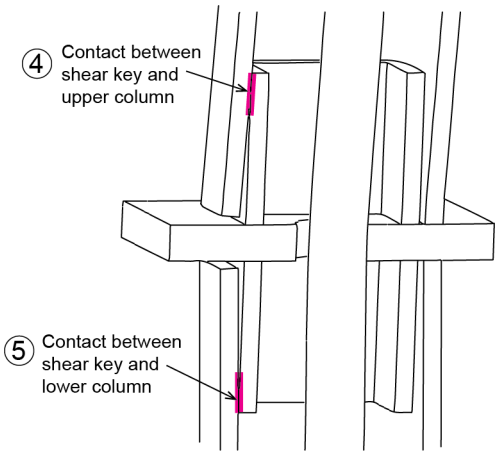

Figure 7.23. M-θ key points 4-5

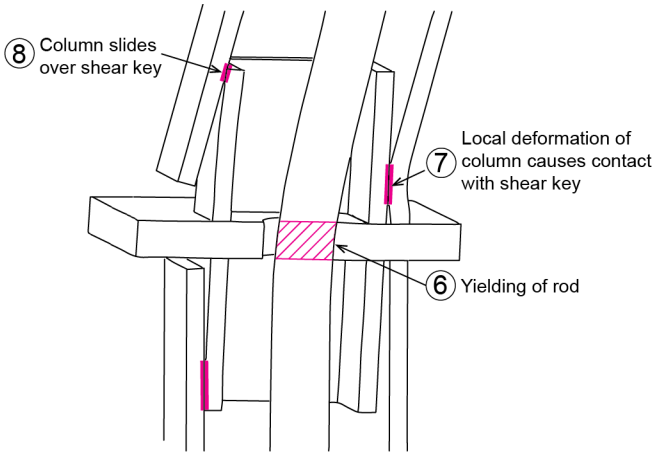

Figure 7.24. Key points for the ultimate M-θ behaviour

7.6.1.2 Axial force – moment interaction (N+M)

To determine the effect on the moment-rotation (M-θ) behaviour, an axial force (N) was applied to the upper column, after which the moment was applied, and incrementally increased. The axial forces considered included $0.5N_t$, $0.1N_c$, $0.2N_c$, and $0.3N_c$ where N_t was the tension capacity, and N_c was the ultimate compression capacity of the column. The resulting M-θ curves are shown in Figure 7.25. The axial tension force ($0.5N_t$) decreased the decompression moment, i.e., point 1 in Figure 7.21 (p.188), whereas the axial compression forces ($0.1N_c$ – $0.3N_c$) increased the decompression moment. The applied axial load changed the effective clamp force, which explains the difference in the decompression moment. In the case of axial compression, the applied axial force increased the effective clamp force, which increased the moment required for the column to start to lift. The increased initial clamp force also caused an increase in the column stress once the moment was applied. Hence, the specimens subjected to an axial compression force had a reduced gap rotation at failure due to the earlier yielding of the column flange. For preliminary design purposes, the bending behaviour may be established based on the design gravity load.

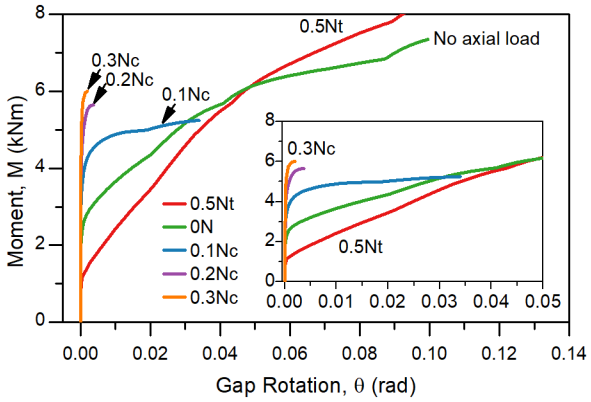

Figure 7.25. Numerical M-θ curves for the Sa3-250 specimen with varying axial force

7.6.1.3 Shear force – moment interaction (V+M)

To determine the effect on the moment-rotation (M-θ) behaviour, a shear force (V) was applied to the upper column at the same time as the moment (M) was applied. Following Section 7.4.1.3 (p.171), three cases were considered: M/V=1 m, M/V=0.5 m, and M/V=0.25 m. The resulting M-θ curves are shown in Figure 7.26. The M-θ behaviour in the early stages was not affected by the addition of the shear force. In the later stages, as the shear key was effectively confined at point 5 (Figure 7.23), the shear force increased the effective normal force, i.e., at point 8 in Figure 7.24, which increased the friction developed, and, hence, increased the ultimate moment capacity. Since the main interest in design is the early behaviour, the shear force may be considered to have negligible effect.

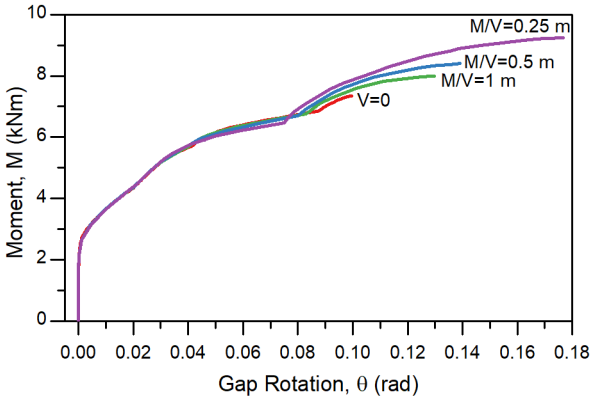

Figure 7.26. Numerical M-θ curves for the Sa3-250 specimen with varying shear force

7.6.2 Comparison with existing inter-module connections

Two existing connections with published moment-rotation (M-θ) data were selected for comparison with the post-tensioned inter-module connection (IMC): a Rotary connection (RC) [222] (Figure 7.27a), and a bolted moment end plate (EP) [165] (Figure 7.27b), also known as a beam splice connection in the referenced work. For the existing connections considered in Section 7.5.2 (p.180), experimental data for the moment-rotation behaviour of the isolated connection was not available. Hence, two different existing connections were selected. In Figure 7.27, the illustrations are taken from the referenced works, and text added for the present study is shown in red. In the Rotary connection (RC), upper and lower *corner fittings* are incorporated in the modules at the corners. The *corner fittings* are welded in place during fabrication of the module, joining the module column to the module beams. The *fittings* are 212 x 212 x 234 mm high and 16 mm thick, and suit a 200 x 200 x 18 mm square hollow section module column. Holes in the *corner fittings* allow insertion of a *connector* during site installation of the modules. The *connector* includes a threaded M58 rod which provides the connection between vertically stacked modules, and rotating parts which lock the connector in place after positioning of the modules on site. For the experiments [222], the corner fittings were fabricated from Q345B steel which had a yield stress of 355 MPa, and an ultimate strength of 515 MPa. The connector rod and rotating parts were fabricated from steel with a yield stress of 340 MPa and an ultimate strength of 590 MPa.

In the bolted moment end plate (EP), square hollow sections are joined by a bolted end plate. This is a traditional connection type which can be applied in modular buildings as a vertical IMC which joins the columns of stacked modules. Wheeler et al. [165] reported the M-θ behaviour for this connection type based on experiments completed at the University of Sydney. The connection had four M20 8.8/T bolts which were arranged in two rows, and tensioned to 145 kN. The yield and ultimate capacity of the bolts was measured as 195 and 230 kN, respectively. The end plates were grade 350, and had 22 mm diameter bolt holes

which were located with 30 mm from the plate edge to the centre of the hole. The 150 x 150 x 9 mm square hollow sections had nominal yield strength of 350 MPa, and were welded to the end plates via 8 mm fillet welds. Three experimental curves were selected for comparison with the post-tensioned IMC: *T17*, *T18*, and *T19*, referring to *Test 17*, *Test 18*, and *Test 19*, respectively. The end plate thicknesses were 12, 16 and 20 mm for *T17*, *18*, and *19*, respectively. For the 12 mm thick plate (*T17*) the test was stopped due to excessive deformation of the end plate. In comparison, for *T18* and *T19*, the test was stopped when the bolt fractured in tension.

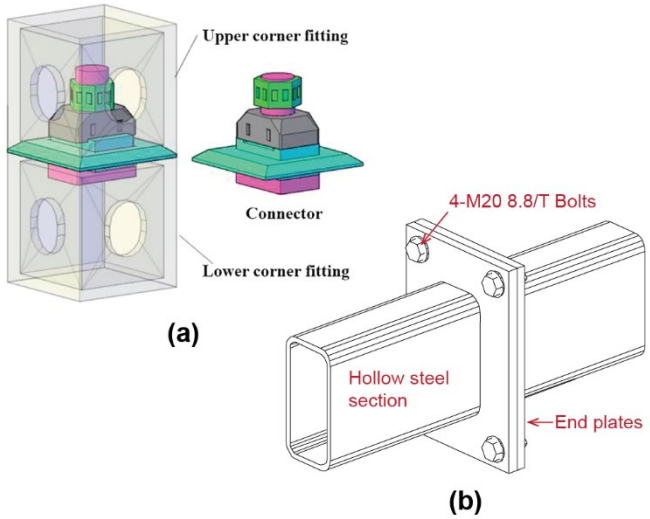

Figure 7.27. Existing inter-module connections: (a) Rotary connection (RC) [222], and (b) Bolted moment end plate (EP) [165]

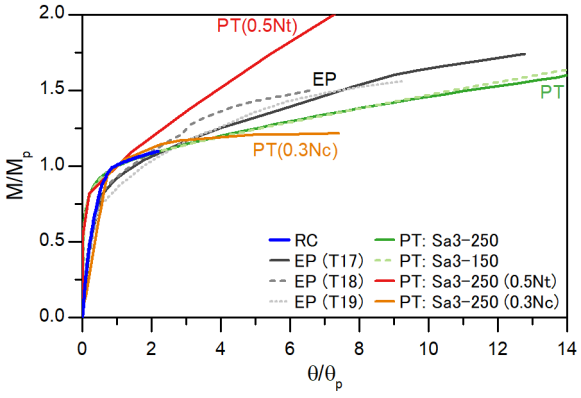

Figure 7.28. Normalised M-θ behaviour of the Rotary connection (RC) [222], Bolted moment end plate (EP) [165], and Post-tensioned (PT) inter-module connections

Figure 7.28 shows the normalised M-θ behaviour for the selected connections. The y-axis was normalised by dividing by the plastic moment, M_p, and the x-axis was normalised by the corresponding rotation, θ_p. The plastic moment was identified as the inflection point on the M-θ curve, which was located between the decompression point and the point at which the rod came into contact with the central plate. It can be seen that the behaviour of the PT connection

is similar to that of the rotary connection and the bolted moment end plate, which builds confidence in the numerical results of the present study.

7.6.3 Simplified analytical model

A simplified two stage model (OTU) is proposed for the moment-rotation (M-θ) behaviour, as shown in Figure 7.29. In the first stage (OT) the connection is compressed due to the rod preload. A linear model can be applied which has two parameters: K_{OT} and M_T. K_{OT} is the initial M-θ stiffness, which is due to flexure of the column, and can be estimated based on a fixed-free cantilever with a concentrated moment applied at the free end. Hence, assuming a rigid behaviour for the column, the stiffness can be given as

$$K_{OT} = \frac{2E_{col}I_{col}}{L_{12}}, \tag{7.35}$$

where L_{12} is the initial vertical distance between points 1 and 2 in Figure 7.5 (p.167), and E_{col} and I_{col} are the elastic modulus and area moment of inertia for the column cross-section, respectively.

The derivation of Equation (7.35) can be further explained as follows. Referring to Figure 7.5 (p.167) it can be seen that L_{12} is the joint length along the upper column. Moreover, that the column segment initially displayed a rigid behaviour, based on which the total rotation was given in Equation (7.33) (p.187). Following the fixed-free cantilever model with a concentrated moment (M) at the free end, the lateral displacement x can be given as a function of y as

$$x(y) = \frac{My^2}{2E_{col}I_{col}}. \tag{7.36}$$

Due to the initial preload, the column was effectively fixed at point 1 (Figure 7.5, p.167), hence, the lateral displacement at point 2 can be given as

$$x_2 = \frac{ML_{12}^2}{2E_{col}I_{col}}. \tag{7.37}$$

Since the column segment initially displayed a rigid behaviour, the total rotation can be given as

$$\tan\theta = \frac{ML_{12}^2}{2E_{col}I_{col}L_{12}} = \frac{ML_{12}}{2E_{col}I_{col}}. \tag{7.38}$$

Assuming a small angle, which will be the case for the initial stiffness, then

$$\theta = \frac{ML_{12}}{2E_{col}I_{col}}, \tag{7.39}$$

and the moment-rotation stiffness can be given as

$$\frac{M}{\theta} = \frac{M 2E_{col} I_{col}}{ML_{12}} = \frac{2E_{col} I_{col}}{L_{12}}. \tag{7.40}$$

T represents the point at which the applied moment is sufficient to cause first decompression of the column. The first decompression occurs when the tensile stress due to bending is equal to the compression stress due to the preload, plus any additional applied axial load. Hence, the moment at which the column edge starts to lift can be given as

$$M_T = \frac{F_{clamp} Z_{col}}{A_{col}}, \tag{7.41}$$

where F_{clamp} is the clamp force which is defined by Equation (7.23) (p.183), Z_{col} is the elastic section modulus of the column, and A_{col} is the gross area of the column cross-section. The rotation at T can then be calculated as

$$\theta_T = \frac{M_T}{K_{OT}}. \tag{7.42}$$

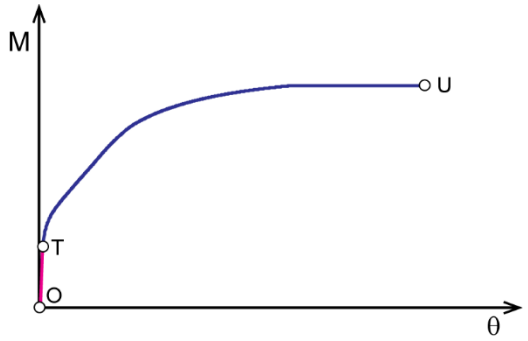

Figure 7.29. Proposed M-θ model

After decompression the M-θ behaviour is nonlinear and it is represented by the segment TU in Figure 7.29. The nonlinear M-θ behaviour can be estimated by following an iterative procedure as shown in Figure 7.30. First, an arbitrary rotation is applied to the connection, and the depth to the neutral axis (Figure 7.31) is guessed. The maximum compression strain in the column can then be calculated by adopting the *Monolithic Beam Analogy (MBA)* [223, 224]. In the present application, the *MBA* indicates that the lateral displacement of an equivalent monolithic column is equal to the sum of the lateral displacements due to the elastic flexural displacement of the column, and the gap opening between the column and the central plate. This analogy provides the second equation needed to determine the strain in the column, while ensuring strain compatibility, given the use of an unbonded post-tensioning rod [224].

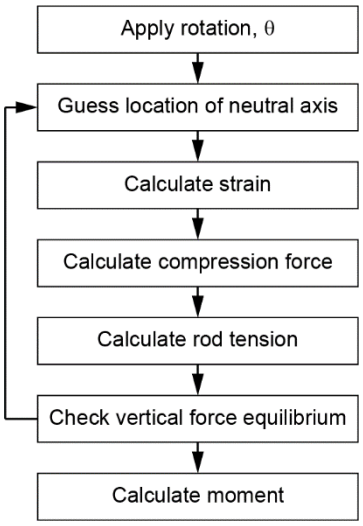

Figure 7.30. Iteration flow chart

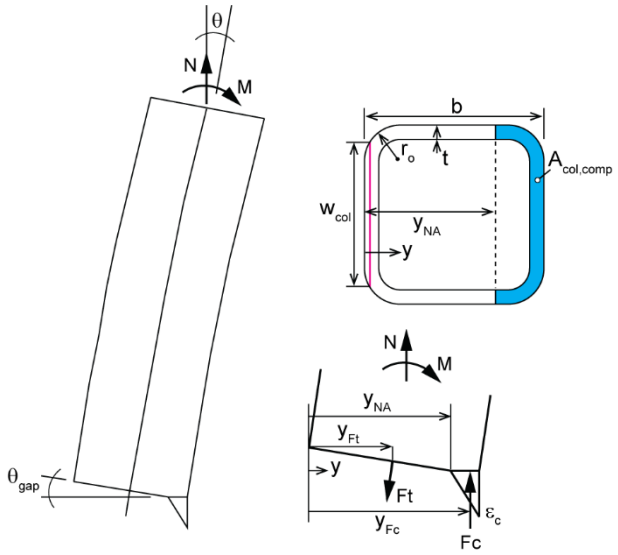

Figure 7.31. Free body diagram for iterative calculation of the M-θ behaviour

The lateral displacement of a monolithic column subjected to a bending moment M can be given as

$$\Delta_{mon} = \phi_{mon} \frac{L^2}{2}, \tag{7.43}$$

where $\phi_{mon} = \frac{M}{EI}$ is the curvature, and L is the height of the monolithic column. After decompression the lateral displacement can be given as

$$\Delta = \theta_{gap} L + \phi_{dec} \frac{L^2}{2}. \tag{7.44}$$

The decompression curvature can be given as [223]

$$\phi_{dec} = \frac{2(F_t - N)}{E_{col} A_{col} b}, \tag{7.45}$$

where N is the axial load, F_t is the rod tension, E_{col} is the elastic modulus, A_{col} is the column cross-sectional area, and b is the column width. Assuming $\Delta_{mon} = \Delta$, the curvature can be calculated as

$$\phi = \frac{2\theta_{gap}}{L} + \phi_{dec}. \tag{7.46}$$

Hence, the maximum compression strain can be calculated as

$$\varepsilon_c = \left(\frac{2\theta_{gap}}{L} + \phi_{dec} \right) (b - y_{NA}). \tag{7.47}$$

Assuming a linear distribution, the strain can be given as

$$\varepsilon(y \geq y_{NA}) = \frac{\varepsilon_c (y - y_{NA})}{b - y_{NA}}, \tag{7.48}$$

where b is the column width and y_{NA} is the distance to the neutral axis. The compression stress, f_c, can then be calculated based on the quad-linear material model [203] for the column steel. The strain in the rod can be estimated by summing the strain due to the initial rod tension with the strain due to the applied rotation (θ_{gap}). Hence, the total strain in the rod can be given as

$$\varepsilon_t = \frac{F_{t,ini} + (1 - C_{clamp}) N}{L_{ad} k_{rod}} + \frac{\theta_{gap} (y_{NA} - y_{Ft})}{L_{ad}}, \tag{7.49}$$

where L_{ad} is the grip length of the rod and k_{rod} is the axial stiffness of the rod. y_{Ft} gives the location of the rod tension force which can be estimated as

$$y_{Ft} \approx \begin{cases} 0.5b + \theta_{rod} L_{bd}, & 0 \leq \theta_{rod} \leq 0.5 d_{tol} L_{bd}^{-1} \\ 0.5b + 0.5 d_{tol}, & 0.5 d_{tol} L_{bd}^{-1} < \theta_{rod} \end{cases} \tag{7.50}$$

where L_{bd} is the length between points b and d in Figure 7.1 (p.164), d_{tol} is the bolt hole tolerance, and θ_{rod} is the rotation of the rod which can be estimated as

$$\theta_{rod} \approx \frac{L_{ab}}{L_{ad}} \theta. \tag{7.51}$$

Hence, the tension stress can then be calculated based on the quad-linear material model for the rod steel, and the tension in the rod can be calculated as

$$F_t = f_t A_{rod}. \tag{7.52}$$

The guessed neutral axis location can then be varied over several iterations, until vertical force equilibrium is achieved. Finally, the corresponding moment can be estimated based on moment equilibrium, after the position of the equivalent compression force is calculated.

Based on the column geometry, the total width of the square hollow section area, excluding the hollow internal area, can be expressed as a function of y as

$$w_{col}(y)=\begin{cases} b-2r_o+2r_o\sqrt{1-\lambda_1^2 r_o^{-2}}, & y\le t \\ 2r_o\sqrt{1-\lambda_1^2 r_o^{-2}}-2(r_o-t)\sqrt{1-\lambda_1^2(r_o-t)^{-2}}, & t<y\le r_o \\ 2t, & r_o<y\le b-r_o \\ 2r_o\sqrt{1-\lambda_2^2 r_o^{-2}}-2(r_o-t)\sqrt{1-\lambda_2^2(r_o-t)^{-2}}, & b-r_o<y\le b-t \\ b-2r_o+2r_o\sqrt{1-\lambda_2^2 r_o^{-2}}, & b-t\le y \end{cases} \tag{7.53}$$

where b, t, and r_o are the column section width, thickness and outer corner radius, respectively, and $\lambda_1 = r_o - y$ and $\lambda_2 = r_o - b + y$. Hence, the cross-sectional area of the column subjected to compression can be given as

$$A_{col,comp} = \int_{y_{NA}}^{b} w_{col}\,dy\,, \tag{7.54}$$

where y_{NA} is the distance to the neutral axis. The compression force can then be calculated as

$$F_c = \int_{y_{NA}}^{b} w_{col} f_c\,dy \tag{7.55}$$

and the location of the equivalent concentrated compression force can be calculated as

$$y_{F_c} = \frac{\int_{y_{NA}}^{b} y w_{col} f_c\,dy}{F_c}. \tag{7.56}$$

The corresponding moment values can be estimated as

$$\begin{aligned} M &= F_c\left(y_{Fc}-y_{Ft}\right)+L_{ab}\sin\theta_{gap}N \\ &= \left(F_t\cos\theta_{gap}-N\right)\left(y_{Fc}-y_{Ft}\right)+L_{ab}\sin\theta_{gap}N. \end{aligned} \tag{7.57}$$

Having followed an iterative procedure to obtain the M-θ curve, the plastic moment, which was used to normalise the behaviour in Section 7.6.2 (p.191), can be obtained directly. As shown in Figure 7.32, the plastic moment (M_P) is defined by the intersection between the initial and hardening stiffness, after the point of decompression (M_T).

Figure 7.32 compares the simplified model with the numerical results for the moment-rotation (M-θ) behaviour of specimens Sa3-250 and Sa3-150. A reasonable match is shown for the early stages. For example, for Sa3-250, the numerical results showed the column edge would start to lift at a moment of 1.64 kNm. In comparison, the analytical model predicted the column edge would lift at a moment of 1.63 kNm which, assuming the numerical value was more accurate, indicated an error of 0.55%. Considering the plastic moment, the numerical and analytical model values were 2.74 and 2.37 kNm, respectively, indicating an error of 14%. In

the later stages, the ultimate moment capacity is underestimated. For example, for Sa3-250, in the numerical model, the upper column came into contact with the shear key at a moment of 5.7 kNm. Thereafter, the simplified model underestimates the moment capacity because contact between the column and shear key is not accounted for.

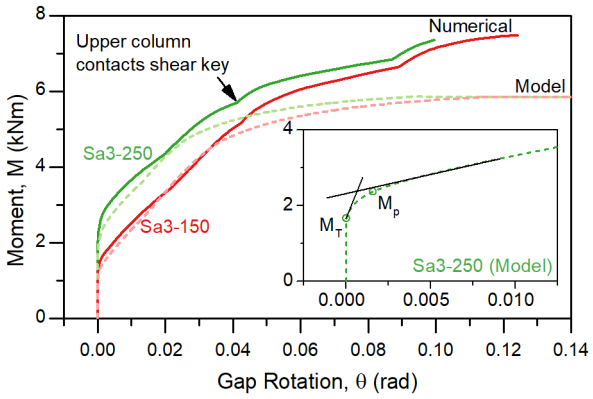

Figure 7.32. Simplified model and numerical results for M-θ behaviour

Figure 7.33 compares the model and numerical M-θ curves for specimen Sa3-250 with varying applied axial load. A reasonable match is shown, demonstrating that the model is able to capture the effect of the axial load. For example, with an axial load of 0.3Nc, the numerical result shows a plastic moment of 4.97 kNm, and an ultimate moment capacity of 6.00 kNm. The analytical model, however, predicts a plastic moment of 4.96 kNm, and an ultimate capacity of 5.73 kNm, indicating errors of 0.55 and 4.5%, respectively. Similar to the case with no axial load, the model underestimates the moment capacity if the gap rotation is large enough to cause contact between the column and the shear key.

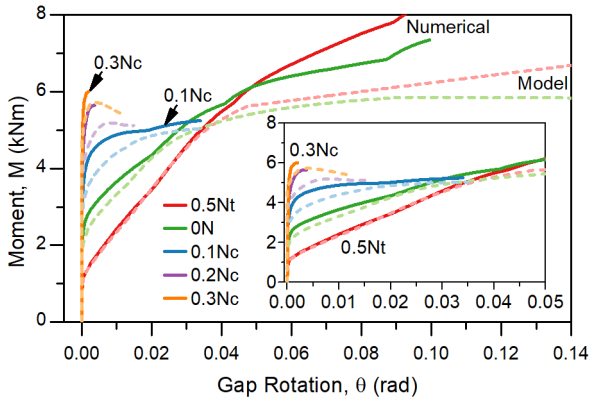

Figure 7.33. Simplified model and numerical results for M-θ behaviour with axial load

7.7 Summary

In this chapter, the shear, axial and bending behaviours of the newly developed post-tensioned inter-module connection were investigated by numerical simulations. Simplified models were

developed to predict the shear, axial and moment-rotation behaviours. The main findings are summarised as follows.

1. The important shear behaviour can be represented by a two stage model (Figure 7.11, p.173). Bending moments have negligible effect, while axial forces affect the effective clamp force and, hence, the slip resistance. For preliminary design, the shear behaviour may be based on the corresponding design gravity load.

2. The axial behaviour can be represented by a multi-linear model (Figure 7.17, p.182). Bending moments affect the clamping pressure and introduce a P-Δ effect, which affects the axial behaviour. For design, the axial behaviour can be established based on the maximum design moment. Shear forces affect the tension behaviour, causing the upper column to lift earlier, and reducing the capacity due to combined tension and bending in the rod. For design, the tension force may be limited depending on the maximum shear force, such that the shear force has negligible effect on the axial behaviour.

3. The moment-rotation behaviour can be represented by a two stage model (Figure 7.29, p.194). In the first stage the behaviour is linear, while in the second stage, the nonlinear behaviour is estimated by an iterative procedure. Axial forces affect the bending behaviour by reducing the gap rotation at failure due to earlier yielding of the column. For a preliminary design, the bending behaviour may be established based on the design gravity load. Shear forces affect the behaviour in the later stages due to the development of friction between the column and the shear key. Since the main interest is the early behaviour, the shear force can be considered to have negligible effect.

Chapter 8 Simplified models for the interlocking (IL) connection[1]

8.1 Introduction

A new interlocking (IL) inter-module connection (IMC) was proposed in Chapter 6, and experimental and numerical studies were undertaken to develop an empirical model for the shear behaviour. Numerical models were developed based on the experimental specimens which combined two connections to give a balanced load arrangement (Figure 8.1a). This was replicated in the numerical models (Figure 8.1b) which included symmetry boundary conditions in the X- and Z-directions. Penalty friction was adopted for the tangential behaviour in ABAQUS, and the elastic slip and friction coefficient were input based on the previous slip factor tests (Chapter 4). To validate the numerical models, the numerical and experimental shear force-displacement curves were matched. Hence, a simplified empirical model was proposed for the shear behaviour of the experimental specimens. However, it remains to investigate the shear behaviour of a single IL connection, which may be different to that of the experimental specimens due to the different loading and boundary conditions. Moreover, it remains to establish simplified models for the axial force-displacement and moment-rotation (M-θ) behaviours of the IL connection.

Therefore, in this chapter, an intermediate numerical simulation is undertaken to investigate the effect of the loading and boundary conditions on the shear behaviour. The intermediate model is different to the previous numerical models (Chapter 6) in three ways. First, the intermediate model has only one connection, as would be the case in a modular steel building, whereas the previous models included two connections (Figure 8.1). Second, the shear force is applied directly to the column in the intermediate model, whereas the shear force was applied to the bearings in the previous models. Third, the intermediate model has the bolts and locating pins positioned centrally in their respective holes, whereas in the previous models they were positioned at one side of the holes. Following the intermediate simulations, extended numerical models are developed based on a more realistic geometry which has two bolts per column to improve the resistance to in-plane rotation. The shear behaviour is similarly investigated, following which the simplified model developed for the shear behaviour in Chapter 6 is reviewed and improved. Then, the numerical models are further extended to establish the axial and M-θ behaviours. To verify the extended numerical results, simplified

[1] The related work in Chapter 8 was published in Engineering Structures:

Lacey AW, Chen W, Hao H, Bi K. New interlocking inter-module connection for modular steel buildings: Simplified structural behaviours. Eng Struct. 2021;227:111409. https://doi.org/10.1016/j.engstruct.2020.111409

analytical and semi-empirical models are developed, and the results are compared. Further, a comparison is made between the present numerical behaviours, and the experimental behaviours reported for other existing IMCs [165, 218, 219, 222]. The extended numerical results are shown to be similar to those from the previous experimental studies, which verifies the accuracy of the present numerical simulations.

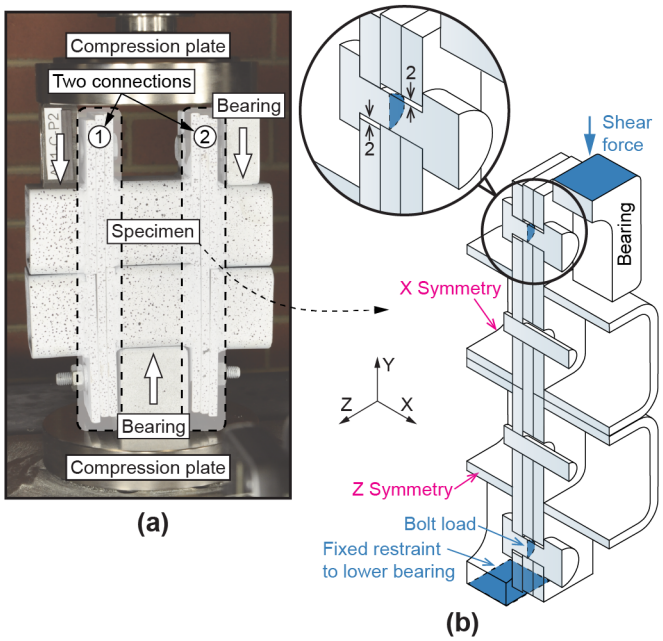

Figure 8.1. (a) Previous experimental setup and (b) numerical model
Adapted from Figure 6.5 (p.141) and Figure 6.18 (p.155).

8.2 Interlocking (IL) connection

The new interlocking IMC was introduced in Chapter 6. It was illustrated in Figure 6.1 (p.138) and described in Section 6.2 (p.137). In this chapter, the interlocking (IL) connection is limited to a configuration suitable for the connection of two upper and two lower modules (Figure 8.2). Although the IL connection supports the connection of eight modules, the present chapter is simplified by limiting the scope to two and four modules. As shown in Figure 8.3, these are the two cases which occur for a building comprised of modules placed either side of a central corridor, such as the case study building considered in Chapter 3.

8.3 Inter-module joint model

The development of joint models applicable to bolted IMCs was summarised in Section 2.2.3.1 (p.27). The IMC model adopted in the present work is shown in Figure 8.4. For the vertical connection between two modules, i.e., 2C (Figure 8.4b), points *a*, *b*, and *c* were defined along the column centreline, such that *ab* and *bc* represent two link elements, which may be combined into a single vertical link. In the following sections, nonlinear springs were defined

to reflect the shear, axial and moment-rotation behaviours of the links. For the connection between four modules, i.e., 4C, the vertical connection was defined similarly, with two points along each column centreline, as shown in Figure 8.4(c). Hence, *ab* and *bc* are vertical links on one side, and *de* and *ef* are vertical links on the other side. For the horizontal connection, a horizontal link was defined between points *b* and *e*. Then, in the following sections, the axial and shear springs were established based on the section properties of the central tie plate.

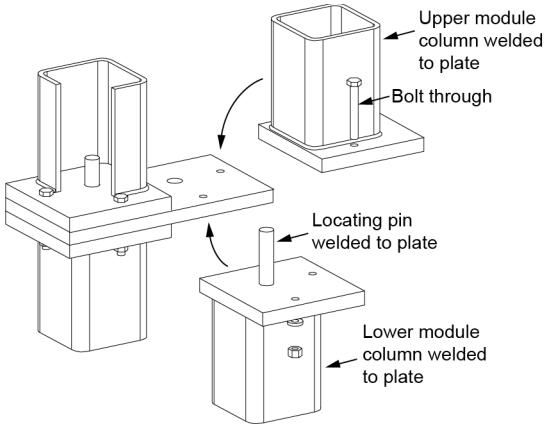

Figure 8.2. Interlocking inter-module connection
Adapted from Figure 6.1 (p.138).

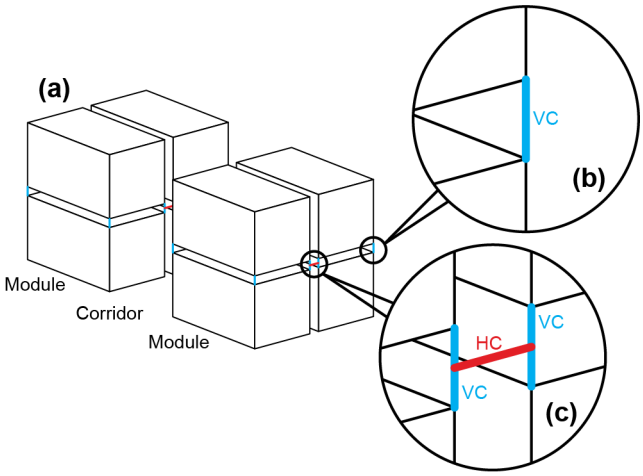

Figure 8.3. Typical modular layout showing (a) module, (b) 2 column connection, and (c) 4 column connection

The combination of the vertical and horizontal connections in the 4C geometry contributed significantly to the complexity. In the existing literature, a horizontal gap is generally provided between the adjacent columns. This gap simplifies the analysis by ensuring that there is no contact between horizontally adjacent columns, which might otherwise affect the behaviour. In the present work, the connections were modelled without a horizontal gap between the columns, which was considered a more realistic arrangement. Then, in the cases where contact

between the columns occurred, the effect on the connection behaviour is discussed, and a recommendation is made on whether the contact should be considered for design purposes.

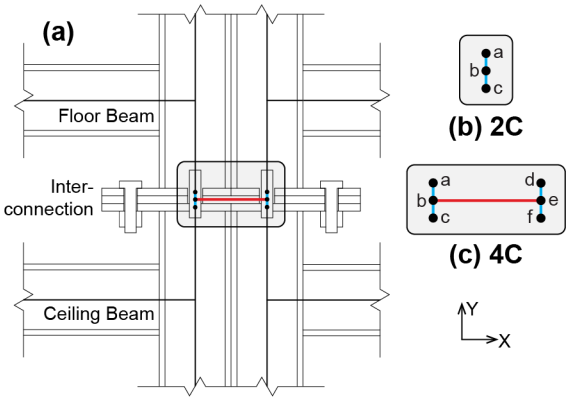

Figure 8.4. Inter-module connection model showing (a) XY section through connection, (b) connection between two module columns (2C), and (c) connection between four module columns (4C)

8.4 Numerical simulation

8.4.1 Intermediate numerical models

The finite element model was prepared using ABAQUS [206], and the geometry (Figure 8.5) was based on the experimental specimens A1 and A2 (Figure 6.2, p.139), for which the bolt preloads were 50 and 35 kN, respectively. The bolts and locating pins were positioned centrally in their respective holes, and a symmetry boundary condition was defined in the z-direction. The locating pins, L1 and L2, were tied to the lower plates, P3L and P3R, to match the experimental weld detail. Similarly, the column cross-sections were tied to the adjacent plates, i.e., C1 was tied to P1L, C2 to P1R, C3 to P3L, and C4 to P3R. The mesh consisted of first-order 8-node linear brick elements (C3D8R in ABAQUS) with a nominal size of 3 mm. The 3 mm size was selected following a sensitivity study, wherein the shear force-displacement behaviour was determined for mesh sizes of 6, 3, and 1.5 mm (Figure 8.6). The 3 mm mesh was found to be suitable, with little difference in the shear behaviour compared to the model with the 1.5 mm mesh.

Hard normal contact was input generally and separation was allowed. Penalty friction was adopted for the tangential behaviour, and the friction coefficient and elastic slip were input based on the numerical calibration carried out in Section 6.5 (p.154). Hence, the elastic slip was 0.001 mm for all of the contacting surfaces. Similarly, the friction coefficient was 0.3146, 0.05, 0.2, and 0.3 for the plate/plate, bolt head/plate, locating pin/plate, and column/column interfaces, respectively, while the bolt shank/plate contact was frictionless. The friction coefficient of 0.3146 for the plate/plate interface reflected the clean mill scale finish (Table

4.3, p.90), while the coefficient of 0.3 represented the painted finish applied by the manufacturer of the hollow steel sections (§5.5.2, p.123). The material properties were also matched to the previous study. The stress-strain curves were defined using the quad-linear model [203], and the elastic modulus and Poisson's ratio was input as 200 GPa and 0.25, respectively. Finally, the yield and tensile strengths were defined as shown in Table 6.2 (p.142).

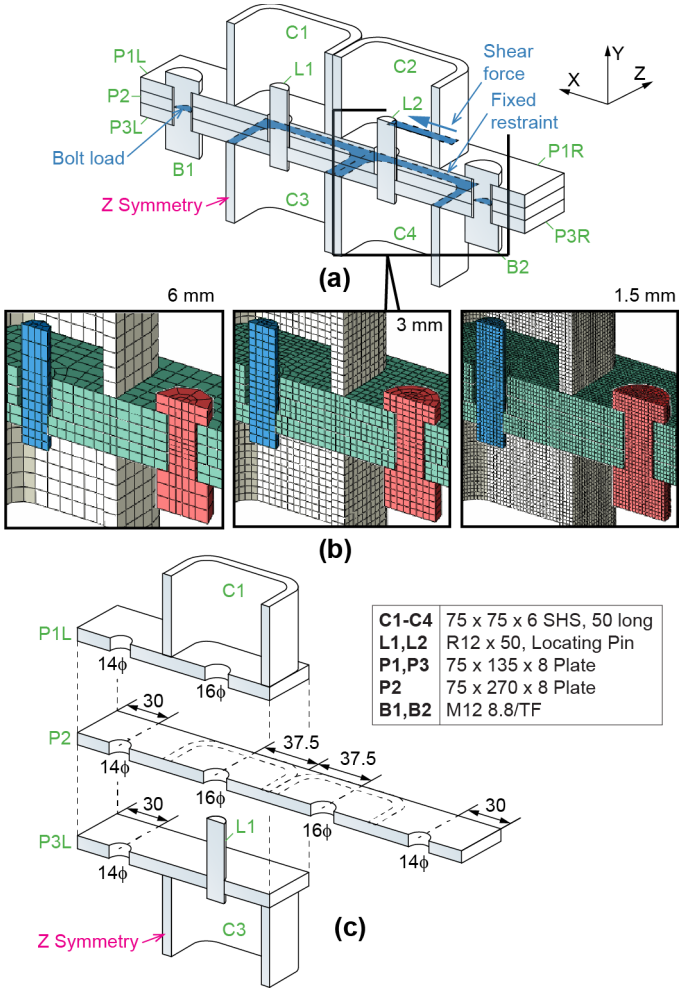

Figure 8.5. Intermediate numerical model
All dimensions in mm.

Three steps were defined for the analysis. First, the contact interactions were activated, after which the bolt preloads were generated using the *applied force method*. Finally, the bolt length was fixed, and the shear force was applied to the web of the upper column (C1), while the lower columns (C3 and C4) were restrained, as shown in Figure 8.5(a). Figure 8.7 shows the experimental and numerical shear behaviours from the previous study (Chapter 6), along with the numerical shear behaviours for the intermediate connection. Since the experimental setup included two connections, while the intermediate geometry had only one connection, the numerical force was multiplied by two for the intermediate connection curves. B1 and B2 refer

to the previous experimental specimens which were identical to A1 and A2 except that the locating pins were omitted.

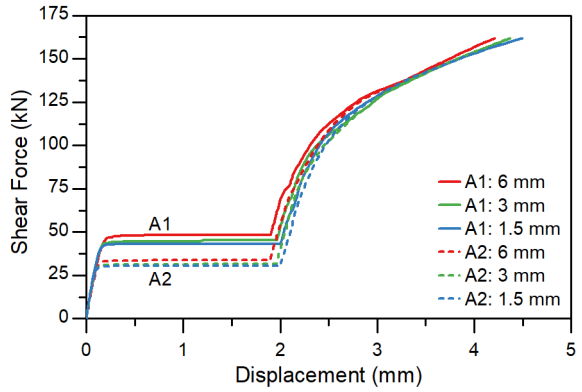

Figure 8.6. Numerical shear force-displacement behaviour for the intermediate connection with varying nominal mesh size

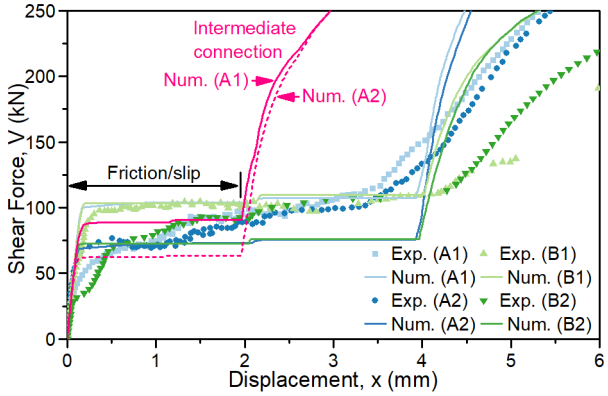

Figure 8.7. Shear force-displacement curves for the intermediate connection and previous experimental specimens (Chapter 6)

Referring to the friction/slip stage in the previous study (Chapter 6), the experimental shear force-displacement (V-x) curve differed from the numerical curve mainly due to the presence of gaps between the connection elements, which resulted from the fabrication and assembly tolerance. For the A2 and B1 specimens, for example, the initial gap was small and the numerical and experimental curves matched well in the friction/slip stage (Figure 8.7). In the following bearing stage, deformation of the bolt threads and rotation of the bolt shank relative to the nut increased the experimental displacement. In comparison, the numerical curve overestimated the stiffness as the numerical model did not include the bolt threads, and the nut and bolt shank were combined which reduced the rotation of the bolt shank. Moreover, while the numerical model resulted in a consistent slip sequence, the experimental slip sequence varied depending on the surface variation of the friction coefficient, which could result in eccentric loading of the bolt shank and further increase the experimental bearing displacement. Notwithstanding these differences, the previous study matched the friction/slip shear

behaviour neglecting the initial gaps, which validated the tangential behaviour in the ABAQUS numerical model. Although the previous experiments were not carried out until failure of the specimens, the deformed shape of the locating pins and bolts in the numerical results matched that observed in the experiments. For example, Figure 8.8(a) presents the numerical model of the A1 specimen showing the distribution of the Mises stress while Figure 8.8(b) and (c) show the post-experiment deformation of a locating pin and bolt, respectively.

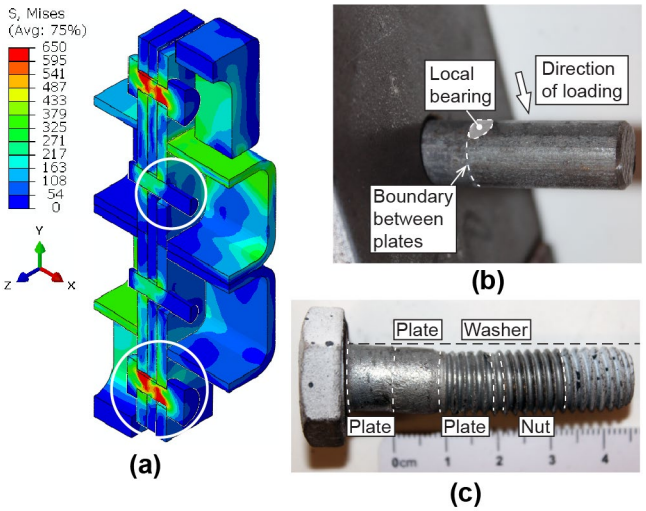

Figure 8.8. (a) Numerical model of the A1 specimen showing distribution of Mises stress, (b) post-experiment deformation of a locating pin, and (c) post-experiment deformation of a bolt

Similarly, in the present study, the main interest was the friction/slip portion of the V-x curve. Comparing the present numerical curves for the intermediate connection with the calibrated numerical curves for the experimental specimens (Figure 8.7), two main differences were observed. First, the displacement at the end of the friction/slip stage was smaller for the present intermediate connection which had an effective bolt hole tolerance of 2 mm, as compared with 4 mm in Chapter 6. Second, the numerical slip resistance for the intermediate connection was smaller than the numerical slip resistance for the related experimental specimen, i.e., 86.6 compared with 99.9 kN for A1 and 61.6 compared with 68.9 kN for A2. In the previous experiments, the shear force was simulated by applying a compression force to the upper bearing while the lower bearing was restrained, as shown in Figure 8.1(b). Therefore, the offset distance between the restraint and the applied shear force was larger in the previous study (Chapter 6). The bending moment caused by the offset shear force resulted in a different distribution of the contact pressure across the faying surfaces. This ultimately resulted in a larger slip resistance for the experimental specimens, as compared with a similar single connection in a modular building, based on the intermediate connection results. Therefore, the simplified model proposed for the shear force-displacement behaviour of the experimental specimens in Chapter 6 may over-estimate the slip resistance if applied to a single connection

in a modular building. Hence, further study of the shear force-displacement behaviour of a single interlocking connection was required.

8.4.2 Extended numerical models

While the experimental specimens were well suited to the experimental method adopted in Chapter 6, the geometry was not optimised for practical applications in real structures. As shown in Figure 8.5(a), the intermediate connections, which were based on the experimental specimens, had only one bolt per column. If a shear force was applied to the column in the Z-direction (Figure 8.5a), then rotation of the column about the Y-axis would be restrained only by friction due to the bolt preload. The moment about the Y-axis which could be restrained in this way would be small, as the friction is generated closely around the bolt. To resist in-plane rotation in practical applications, it is desirable that at least two bolts are provided per column. Therefore, following the intermediate numerical models, two extended numerical models were developed. For the first numerical model, 2C, the geometry allowed connection between two modules, as shown in Figure 8.9(a). Similarly, the geometry of the second model, 4C, allowed connection between four modules, as shown in Figure 8.9(b). The key dimensions of the parts are illustrated in Figure 8.9(c).

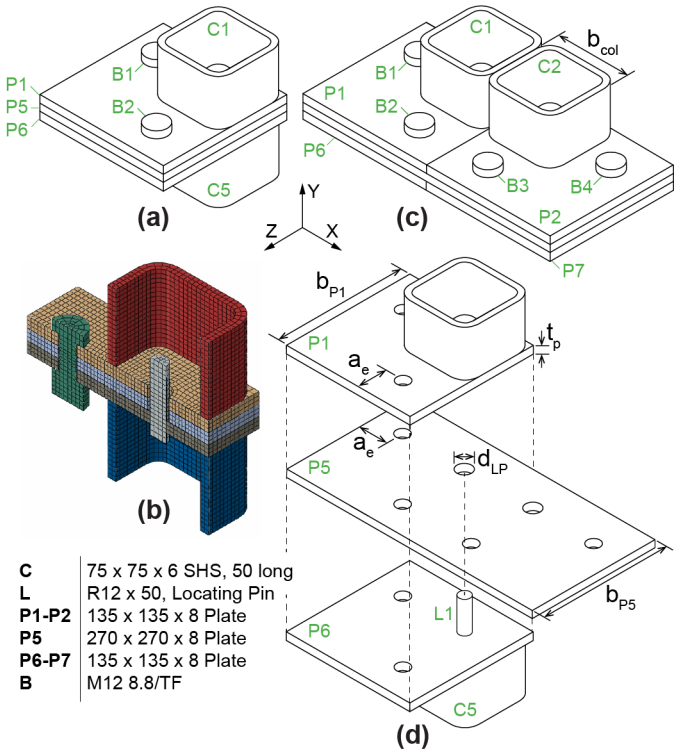

Figure 8.9. Numerical model showing (a) 2C geometry, (b) numerical model, (c) 4C geometry, and (d) partial 4C geometry

For the extended numerical models, the materials, contact interactions and constraints, and the mesh were defined in the same way as described in Section 8.4.1. The shear force was similarly

applied to the upper column webs, while the top surface of the lower column was restrained, as shown in Figure 8.10(a). The axial force was applied to the top surface of the upper column, as shown in Figure 8.10(b), and the bending moment was applied relative to a central reference point located at the top of the upper column, as shown in Figure 8.10(c). For 4C, the loads were first applied to only one of the two upper columns, while the effect of loading on each of the two upper columns is discussed as appropriate in the following sections.

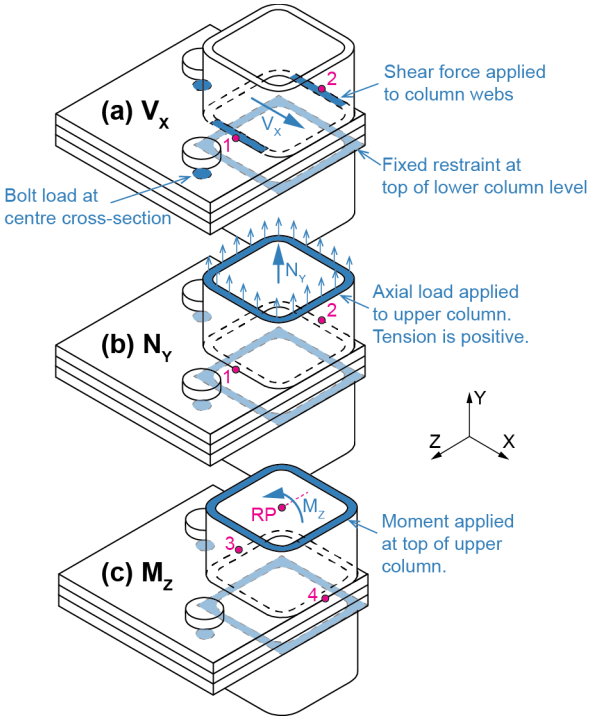

Figure 8.10. Loading and boundary conditions

8.5 Shear force-displacement behaviour

8.5.1 Numerical results

8.5.1.1 Shear (V)

A shear force was applied to the column webs, while the displacement was recorded at points 1 and 2, as shown in Figure 8.10(a) for the 2C geometry. For the 4C geometry, the shear force was similarly applied to column C1, while the two lower columns were restrained, as shown in Figure 8.13. Figure 8.11 shows the resulting numerical shear force-displacement (V-x) curves for two different bolt preloads, based on the average displacement. For example, the displacement in the x-direction was calculated as

$$x = \frac{x_1 + x_2}{2}, \tag{8.1}$$

where x_1 and x_2 were the x-displacement at points 1 and 2 (Figure 8.10a), respectively.

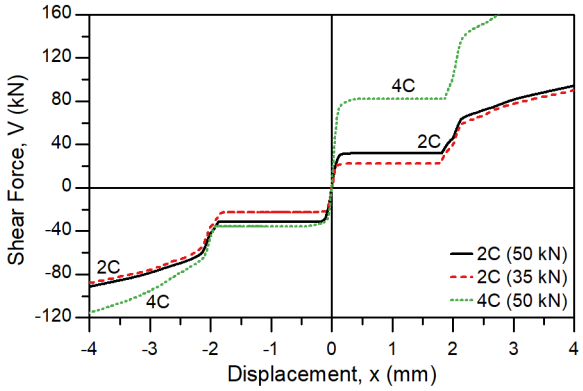

Figure 8.11. Numerical shear force-displacement curves corresponding to the 4C geometry, and the 2C geometry with different bolt preloads

For 2C, a similar V-x behaviour was observed for the positive and negative shear forces. The displacement slowly increased until the friction resistance was reached, and there was a large displacement corresponding to the slip between the plates. As the slip displacement reached 2 mm, i.e., the bolt hole tolerance, the bolts and the locating pin were confined and the V-x stiffness increased. B1 (see Figure 8.9, p.208) yielded first, although it was closely followed by the locating pin (L1), and finally by the second bolt B2. The bolt preload affected the slip resistance, and a higher preload resulted in a higher slip resistance due to the increased friction between the clamped plates. For example, two different bolt preloads, 35 and 50 kN, are shown in Figure 8.11.

Pressure between the plates was generated at the bolt locations due to the initial bolt preloads. The initial friction resistance was, therefore, concentrated at the bolt locations, while the shear force was applied to the column webs, as shown in Figure 8.10(a). That is, the centroid of the bolt group was offset from the line of action of the applied shear force. Therefore, once the friction resistance was exceeded the resulting slip permitted rotation of the upper plates P1 and P5 relative to P6, as shown in Figure 8.12. The eccentricity was resolved by the rotation, which collectively engaged the two bolts and the locating pin to resist additional shear force by direct bearing.

For 4C, the slip resistance for the positive shear force was greater than that for the negative shear force (Figure 8.11). When subjected to a positive shear force, C1 came into contact with C2, as shown in Figure 8.13(a). The frictional resistance was effectively doubled because all four of the bolts contributed. Moreover, the presence of P2 restrained rotation of P1, as friction developed at the interface between P1 and P2. Hence, the total slip resistance of 4C was greater than twice that for 2C. In contrast, when subjected to a negative shear force (Figure 8.13b), C1 moved away from C2, and only two of the four bolts contributed to the frictional resistance. The slip resistance for 4C was therefore more similar to 2C, although there was still a small

increase as P2 restrained the initial rotation of P1. After slip, contact between P1 and P2 resulted in a greater V-x stiffness and ultimate capacity for 4C, compared with 2C.

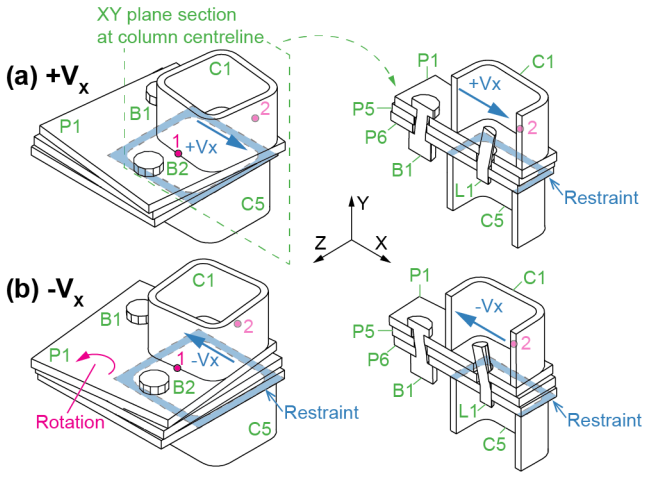

Figure 8.12. Deformed shape for 2C with shear force applied in the (a) positive and (b) negative x-direction

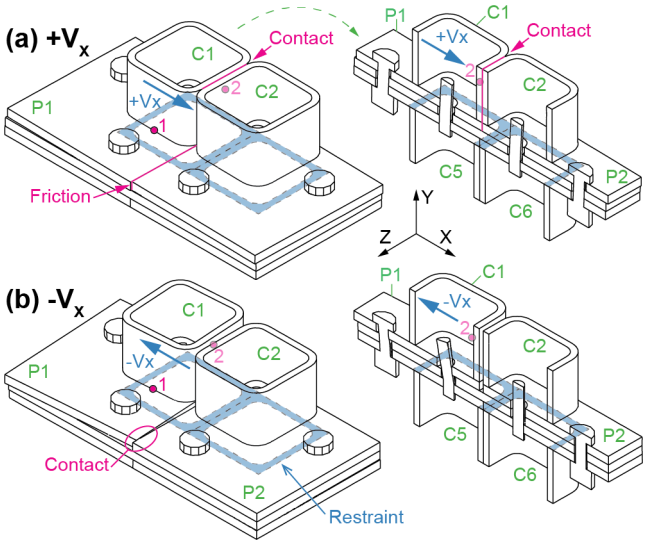

Figure 8.13. Deformed shape for 4C with shear force applied in the (a) positive and (b) negative x-direction

8.5.1.2 Axial – shear interaction (N+V)

An axial load was applied to the upper column C1, as shown in Figure 8.10(b), after which a shear force was applied and incrementally increased to establish the shear V-x curve. Axial forces of 0.5Nt, 0.1Nc, and 0.2Nc were considered, where Nt and Nc are the yield strength of the connection in tension and compression, respectively, based on visual inspection of the numerical results in Section 8.6. The resulting V-x curves for the 2C geometry are shown in Figure 8.14. When an axial compression force was applied, additional friction was generated by the resulting normal pressure between the columns. This friction resistance was aligned with the shear force such that the rotation of the plates following slip was less significant.

Consequently, the shear force was transferred predominantly to only one bolt (B1) and the locating pin (L1). Hence, only B1 and L1 contributed to the first shear yield capacity.

Applying a tension force 0.5Nt in this study caused the plates to separate from one another between the columns. P1 and P6 (Figure 8.12) were subjected to bending, while the normal pressure between P1 and the head of B1, and between P6 and the nut of B1 was increased. P1, P6 and B1 are labelled in Figure 8.12 which shows the deformed shape due to pure shear, while Figure 8.19 (§8.6, p.218) shows the deformed shape due to the axial tension force. For a positive shear force, as the friction resistance was reached P1 slipped 1 mm, and came into contact with the B1 bolt shank. However, due to the increased normal pressure between P6 and B1, B1 was unable to immediately slide across, and the V-x stiffness increased, i.e., the tension force changed the slip sequence. This affected the bearing/yield behaviour by changing the boundary conditions for B1. The shear yield capacity of the connection was increased, as the full shear yield capacity of B1 resisted the applied shear force, and the failure mechanism was changed to bearing in P1. In comparison, the connection subjected to a compression force had a lower shear capacity, as the combined shear and bending in the bolt reduced the effective bolt shear yield capacity. In contrast, for a negative shear force, the vertical offset of the shear force increased the rotation of P1. This altered the normal pressure distribution around B1 which allowed the bolt to slide. The subsequent shear yield of the connection was reduced due to the combined shear and bending in B1, and the failure mechanism included bending of P1 and P6.

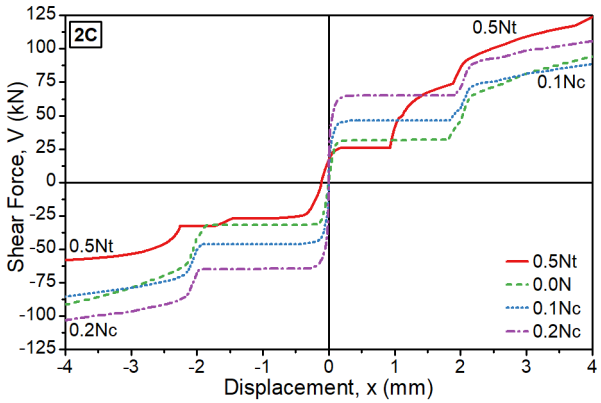

Figure 8.14. Numerical shear force-displacement curves with varying axial force

8.5.1.3 Moment – shear interaction (M+V)

A bending moment and shear force were applied to the upper column, as shown in Figure 8.10(c) and (a). The moment and shear force were applied simultaneously, as would be the case for a cantilevering column subjected to a lateral load. Three different bending moment to shear force ratios were considered, namely M/V=1 m, M/V=0.5 m, and M/V=0.25 m. A shear

force in the positive x-direction was assumed to correspond with a negative moment about the x-axis. Figure 8.15 shows the resulting V-x curves. Due to the relatively low M-θ stiffness, the V-x curves for each of the M/V combinations were related to the moment-rotation (M-θ) response of the connection. For M/V=0.25 m, for example, the V-x curve shows a large x-displacement at -7.2 kN. The corresponding moment was 1.8 kNm, which will be derived as the positive plastic moment capacity in Section 8.7.3.2 (p.232). Therefore, the large x-displacement at -7.2 kN was associated with yielding of the plates in bending, rather than shear slip at the plate interface. The negative M-θ stiffness was greater than the positive M-θ stiffness (see §8.7, Figure 8.27, p.228). Hence, the positive and negative V-x curves for the M/V combinations were not symmetric, as the x-displacement was mainly due to the rotation induced by the moment. In contrast, in the case of pure shear, the x-displacement was associated with the friction/slip shear behaviour, and so the positive and negative V-x curves were symmetric.

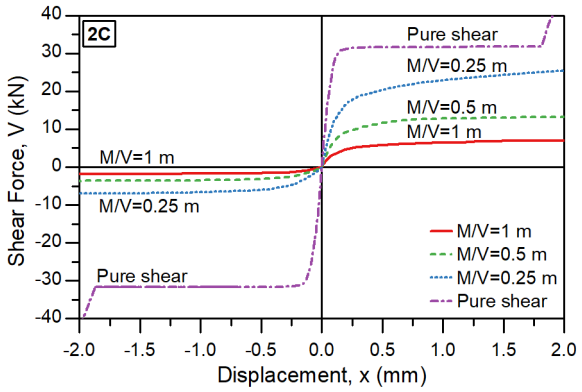

Figure 8.15. Numerical shear force-displacement curves with varying bending moment

Due to the low M-θ stiffness, it is unlikely that the connection will attract a large moment when incorporated in a modular structure. Moreover, if it does attract a large moment, then the friction/slip shear behaviour will be insignificant compared to the large rotation of the yielded connection. Therefore, it is suggested that the symmetric pure shear behaviour can be adopted for preliminary design purposes. If, however, the connection is to be adopted in applications where it will be subjected to bending moments approaching the moment capacity, then a reduction factor should be introduced to accommodate possible bending effects.

8.5.2 Simplified empirical model

8.5.2.1 Friction/slip (OP)

In Chapter 6, a model was proposed for the initial shear force-displacement behaviour of the experimental specimens as Equation (6.4) (p.159). In the present chapter, an improved function is proposed (Figure 8.16) as

$$V(x) = V_{slip}\left[1 - \exp\left(\frac{-K_{V,i}x}{V_{slip}}\right)\right], \tag{8.2}$$

where α is replaced by V_{slip}, and β is replaced by $V_{slip}K_{V,i}^{-1}$. Equation (8.2) is preferred over Equation (6.4), because the slip resistance (V_{slip}) and initial stiffness ($K_{V,i}$) are shown clearly. Equation (8.2) is limited to the range $0 \le x \le x_P$ where x_P is the effective tolerance. For x less than zero, V_{slip} is negative, while $K_{V,i}$ remains positive, resulting in a negative value for V, as expected.

Table 8.1 shows the results of fitting Equation (8.2) to the numerical data. To estimate the slip resistance, a function was fitted to the numerical values, assuming that, disregarding numerical error, the positive and negative values should be equal. Hence, the slip resistance can be estimated as

$$V_{slip} = C_{slip}\mu_p F_{clamp}, \tag{8.3}$$

where C_{slip} = 0.9915 with 95% confidence bounds of (0.9753, 1.008), μ_p is the slip factor, and

$$F_{clamp} = n_b F_{t,ini} - N \tag{8.4}$$

is the clamping force calculated based on the number of bolts (n_b), initial preload ($F_{t,ini}$), and applied axial force (N, tension positive). Similarly, the initial stiffness can be estimated as

$$K_{V,i} = c_1 + c_2\mu_p N\gamma_{crit}^{-1}, \tag{8.5}$$

where $c_1 = 497.3\ \text{kNmm}^{-1}$, N [kN] is the applied axial force (tension positive), and $c_2 = -0.03289$. γ_{crit} [mm] is the elastic slip which, in the numerical model, defined the maximum slip in the sticking phase of the tangential contact, and defined the local sticking stiffness as in Equation (7.3) (p.173). Hence, the stiffness in Equation (8.5) is proportional to $\mu_p N\gamma_{crit}^{-1}$. For preliminary design, γ_{crit} = 0.001 mm, i.e., the elastic slip input for all surfaces in this chapter, may be adopted in Equation (8.5).

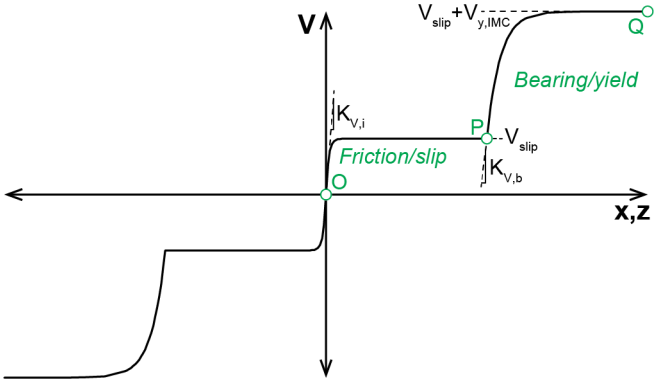

Figure 8.16. Proposed model for shear force-displacement behaviour

Table 8.1. Curve fitting parameters for the numerical shear behaviour of 2C
Positive axial load (*N*) indicates tension, μ_p = 0.3146, and γ_{crit} = 0.001 mm.

Direction	$F_{t,ini}$ (kN)	N (kN)	F_{clamp} (kN)	V_{slip} (kN)	$K_{V,i}$ (kN/mm)	$K_{V,b}$ (kN/mm)
+x	50	0	100	31.87	509.1	95.12
-x	50	0	100	-31.74	498.0	109.60
+x	35	0	70	22.31	504.3	91.18
-x	35	0	70	-22.4	492.8	106.40
+x	50	-53.6 (0.1Nc)	153.6	46.5	1039.0	79.36
-x	50	-53.6 (0.1Nc)	153.6	-46.01	1035.0	102.70
+x	50	-107.3 (0.2Nc)	207.3	65.32	1629.0	98.72
-x	50	-107.3 (0.2Nc)	207.3	-64.66	1601.0	130.40
+x	50	13.1 (0.5Nt)	86.9	26.3	251.2	100.80
-x	50	13.1 (0.5Nt)	86.9	-26.92	193.0	129.40

As the slip displacement was measured at the column, the axial load applied to the column (N), affected the initial stiffness ($K_{V,i}$). The centre of the bolt group was offset from the column. Therefore, the bolt preload caused the plates to separate underneath the column. Although the separation was small, it caused a reduction in the initial stiffness, because the shear force had to be transferred from the column to the bolts where the friction resistance was generated. That is, the slip displacement was increased by the axial elongation of the plate. Conversely, when a compression force was applied, the plates under the column were pushed together, and the friction resistance was generated directly underneath the column. This caused an increase in the stiffness ($K_{V,i}$), as the axial elongation of the plate did not add to the measured slip displacement. The axial tension force also caused a difference between the initial stiffness for the cases of a shear force in the positive and negative x-directions. In the positive x-direction, the shear force reduced the separation of the plates under the column. Once the initial separation was closed, the stiffness was increased, and, hence, the curve fitting process resulted in a higher stiffness. In the negative x-direction, the shear force increased the plate separation, and so the curve fitting resulted in a lower stiffness.

The simplified model for the friction/slip stage matched the numerical results for the 2C geometry (Figure 8.17). As shown in Table 8.2, the percentage error was calculated for the model slip resistance and initial stiffness, relative to the average numerical result. The largest error for the slip resistance was 3.6%. The error was mainly associated with the curve fitting process, which resulted in slightly different slip resistances for loading in the positive and negative x-directions. Except for the model subjected to axial tension, the largest error for the initial stiffness was 1.5%. In the case of axial tension, i.e., *N* equal to a positive value of 0.5Nt, the simplified model significantly overestimated the initial stiffness by 63%, as shown in

Figure 8.17(b). This occurred because the tension force caused the plates to separate underneath the column, reducing the initial stiffness. Therefore, Equation (8.5), which was based on the behaviour of the models with either zero axial force or an axial compression force, i.e., *N* equal to negative values of 0.1Nc and 0.2Nc, overestimated the initial stiffness. For preliminary design purposes, it is proposed that the shear behaviour can be established based on the design gravity load. Hence, the simplified model was matched to shear behaviour associated with 0.1Nc and 0.2Nc, while a comparison is made to the 0.5Nt behaviour to illustrate the limitations of the simplified model. As discussed in Section 8.5.1.3 (p.212), the simplified model reflects the symmetric pure shear behaviour, which is the main interest for preliminary design.

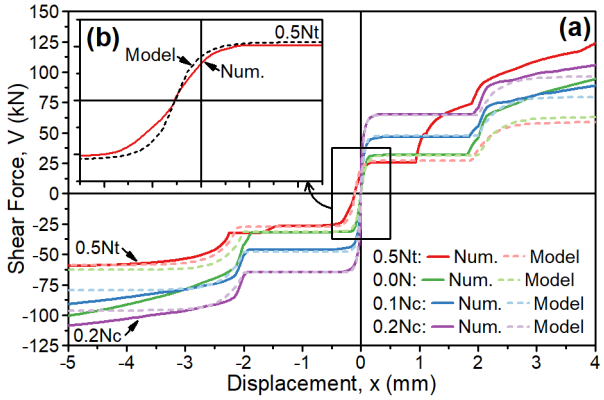

Figure 8.17. (a) Numerical (Num.) and model shear behaviour with varying axial force, and (b) closer view of the shear behaviour with axial tension (0.5Nt)

Table 8.2. Slip resistance (V_{slip}) and initial stiffness ($K_{V,i}$) from the simplified model (mod) and average numerical (num) results, with corresponding error (mod-num)/num
Positive axial load (*N*) indicates tension, μ_p = 0.3146, and γ_{crit} = 0.001 mm.

$F_{t,ini}$ (kN)	N (kN)	$V_{slip,mod}$ (kN)	$V_{slip,num}$ (kN)	V_{slip} Error (%)	$K_{V,i,mod}$ (kN/mm)	$K_{V,i,num}$ (kN/mm)	$K_{V,i}$, Error (%)
50	0	31.2	31.8	-1.93%	497.3	503.6	-1.241%
35	0	21.8	22.4	-2.33%	497.3	498.6	-0.251%
50	-53.6 (0.1Nc)	47.9	46.3	3.60%	1052.2	1037.0	1.468%
50	-107.3 (0.2Nc)	64.7	65.0	-0.504%	1607.6	1615.0	-0.461%
50	13.1 (0.5Nt)	27.1	26.6	1.90%	362.1	222.1	63.018%

8.5.2.2 Bearing/yield (PQ)

The behaviour in the bearing/yield stage can similarly be represented as

$$V(x) = V_{friction} + V_{y,IMC}\left[1-\exp\left(\frac{-K_{V,b}\left(x-x_P\right)}{V_{y,IMC}}\right)\right] \le V_{y,col}\,. \tag{8.6}$$

The first term, $V_{friction}$, is the force transferred through friction, which, after slip, is equal to the slip resistance (V_{slip}). The second term is the additional component transferred via bearing through the bolts and locating pins of the inter-module connection (IMC). Hence, the maximum value, $V_{y,IMC}$, refers to the shear yield capacity of the IMC. The combined terms are limited to the shear yield capacity of the column ($V_{y,col}$), which can be estimated, allowing for the applied axial load, as

$$V_{y,col} = 0.5 A_{col} \sqrt{\frac{f_{y,col}^2 - \left[\max\left(N, F_{clamp}\right) A_{col}^{-1}\right]^2}{3}}, \tag{8.7}$$

where $f_{y,col}$ is the yield strength, and A_{col} is the cross-sectional area of the column. The stiffness at the start of the bearing stage ($K_{V,b}$) varied between 79 and 130 kN/mm depending on the axial load and direction of the shear force (Table 8.1, p.215), and on average it was equal to 104 kN/mm. As indicated in Section 8.5.1.2 (p.211), the axial load can alter the slip sequence which can change the boundary conditions for the bolt and locating pins which are subjected to bending in the bearing phase. However, an empirical equation is not proposed in the present work, and further experimental studies are suggested to further establish and verify this aspect of the shear behaviour.

The bolts and the locating pins were subjected to combined shear and bending (§6.4.2, p.149). Both of these elements can be modelled as steel rods, although the boundary conditions are different. The shear yield capacity of a steel rod can be given as

$$V_{y,rod} = \frac{f_{u,rod} A_{rod}}{\sqrt{3}} = \frac{f_{u,rod} \pi d_{rod}^2}{4\sqrt{3}}, \tag{8.8}$$

where $f_{u,rod}$, A_{rod}, and d_{rod} are the tensile strength, cross-sectional area, and diameter of the rod cross-section, respectively. The plastic moment capacity can be calculated as,

$$M_{p,rod} = \frac{d_{rod}^3 f_{y,rod}}{6}, \tag{8.9}$$

where $f_{y,rod}$ is the yield strength of the rod steel. The interaction equation for combined shear and bending moment can be given as [225]

$$\left(\frac{V^*}{V_{y,rod}}\right)^2 + \frac{M^*}{M_{p,rod}} \leq 1, \tag{8.10}$$

where V^* and M^* are the applied shear force and bending moment, respectively. The applied bending moment can be estimated as

$$M^* = L_{eff} V^*, \tag{8.11}$$

where L_{eff} is the effective cantilever length. Solving Equation (8.10) for V^*, the reduced shear

capacity can be estimated as

$$V_{red,y,rod} = \frac{{d_{\text{rod}}}^4 {f_{u,rod}}^2 \pi^2}{96}\left(\sqrt{\frac{36{L_{\text{eff}}}^2}{{d_{\text{rod}}}^6 {f_{y,rod}}^2} + \frac{192}{{d_{\text{rod}}}^4 {f_{u,rod}}^2 \pi^2}} - \frac{6L_{\text{eff}}}{{d_{\text{rod}}}^3 f_{y,rod}}\right). \quad (8.12)$$

The locating pin can be idealised as a cantilever beam (Figure 6.24, p.161) and, hence, L_{eff} can be replaced by the plate thickness (t_p), and the reduced shear capacity can be estimated as 11.9 kN. Similarly, the bolt can be idealised as a fixed-guided beam with a span of $2t_p$ and, hence, L_{eff} can also be input as t_p, giving a reduced shear capacity of 19.8 kN per bolt. Due to the eccentricity of the shear force applied to the column with respect to the bolt group, the two bolts did not contribute equally to the overall shear resistance. The shear force resisted by bolt B1 was larger than that resisted by bolt B2, such that the shear yield capacity of the connection ($V_{y,IMC}$) can be estimated by summing the capacity of one bolt and locating pin. This assumption follows the numerical shear behaviour with an axial compression force applied to the column (§8.5.1.2, p.211).

As shown in Figure 8.17 (p.216), the simplified model, i.e., Equation (8.6) (p.216), was matched to the numerical results. Shear yield of the column was suppressed in the numerical model because the shear force was applied at the base of the column. Therefore, the shear force was not limited to the shear yield capacity of the column ($V_{y,col}$). To ensure the predicted capacity of the IMC did not significantly exceed $V_{y,col}$, the hardening stiffness was assumed to be zero in the model. Hence, the model curves fall below the numerical curves for larger displacements in the bearing/yield stage. The simplified model was most accurate for the models with an axial compression force, i.e., 0.1Nc and 0.2Nc, which were the main interest. For example, the shear yield force estimated by the simplified model had an error of 5.9% and 3.4% for 0.1Nc and 0.2Nc, respectively, in comparison with the numerical result. For 0.5Nt, as explained in Section 8.5.1.2 (p.211), the tension force changed the slip sequence, thereby altering the bearing/yield behaviour, which was not accounted for in the simplified model. Therefore, the simplified model significantly underestimated the shear capacity for x-displacements larger than 1 mm.

8.6 Axial force-displacement behaviour

8.6.1 Numerical results

8.6.1.1 Axial (N)

An axial force was applied to the upper surface of the column, as shown in Figure 8.10(b) (p.209) for the 2C geometry. For the 4C geometry, the axial force was similarly applied to column C1, while C5 and C6 were restrained (Figure 8.19b). The average y-displacement was

recorded based on points 1 and 2. As shown in Figure 8.18, the y-displacement was small in the case of axial compression, and, hence, 2C and 4C had a similar behaviour, and the bolt preload had little effect. For axial tension, however, the behaviours were different. As shown in Figure 8.19(a), the axial tension behaviour was determined by bending of the plates, which were restrained by the offset bolt group. The bolt preload had an effect on the initial stiffness, wherein decreasing the preload reduced the stiffness. As shown in Figure 8.19(b), the 4C geometry was able to resist larger tension forces than the 2C geometry due to the friction developed between C1 and C2, and P1 and P2. Due to the possibility of horizontal gaps between C1 and C2 (§6.4.5, p.152), it is recommended that, for preliminary design purposes, the axial behaviour should be established based on the 2C behaviour.

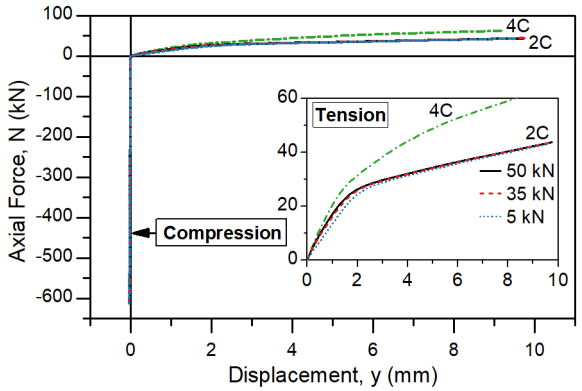

Figure 8.18. Numerical axial force-displacement curves

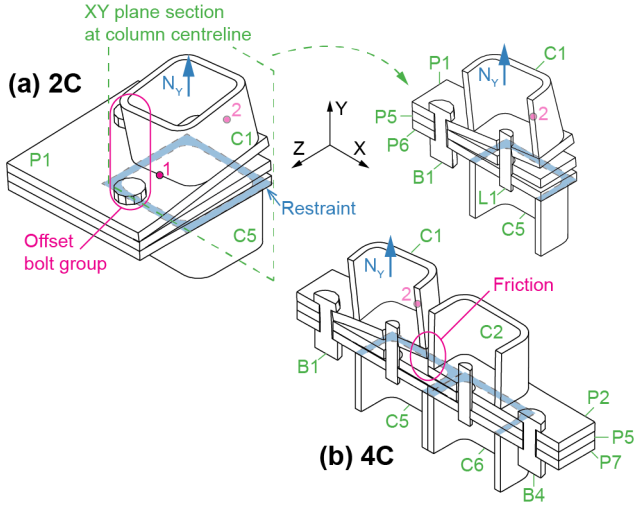

Figure 8.19. Deformed shape for (a) 2C and (b) 4C with axial tension force (N_Y) in the y-direction

8.6.1.2 Moment – axial force interaction (M+N)

A bending moment about the z-axis was applied to the upper column, as shown in Figure 8.10(c) (p.209), after which an axial force was applied and incrementally increased to establish

the axial F-d curves (Figure 8.20). Bending moments of 0.79 and -2.3 kNm were considered. These values were approximately half the plastic moment capacity for the 2C geometry with 50 kN bolt preload, for positive and negative bending, respectively, based on visual inspection of the numerical results. Both the positive, and the negative moment caused an initial displacement in the y-direction. For the negative bending, the rotational stiffness was greater than for the positive bending, hence, the initial y-displacement was smaller for the negative moment. The reason for the different rotational stiffness was the different deformed geometry, which can be seen by comparing Figure 8.27(a) and (b) (p.228). It can also be seen that the bending caused lateral displacement at the top of the column C1. As the axial force was applied at the top of C1, there was a corresponding P-Δ effect, which caused the different axial F-d stiffness for positive and negative bending in Figure 8.20.

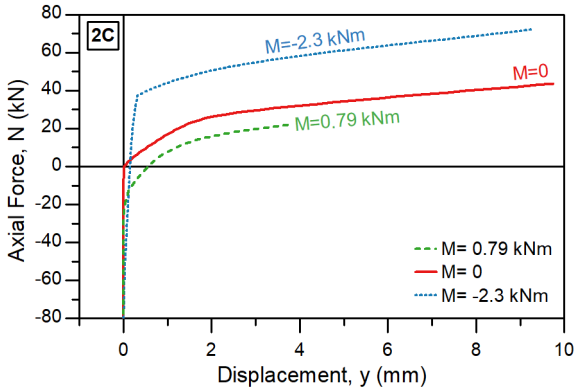

Figure 8.20. Numerical axial force-displacement curves with varying applied moment

8.6.1.3 Shear – axial force interaction (V+N)

A shear force of ±15 kN was applied to C1 in the x-direction, after which the axial force was applied to establish the axial F-d curves (Figure 8.21). As the bolts were offset from the column, the bolt preload caused the plates to separate underneath the column, resulting in a small positive displacement in the y-direction, i.e., 0.013 mm. The shear force was offset from the upper surface of the lower column by a distance equal to the combined thickness of the plates, i.e., $3t_p$. Therefore, the positive shear force generated a small negative moment, which resulted in a negative y-displacement. This reduced the initial y-displacement due to the bolt preload to 0.0075 mm. Conversely, the negative shear force resulted in a positive y-displacement, which increased the initial y-displacement to 0.11 mm. The effect on the initial displacement was greater, as the positive bending stiffness was smaller than the negative bending stiffness. In the same way, the positive shear force gave a small increase in the axial tension capacity, while the negative shear force gave a small decrease. The tension force caused the upper column to lift which resulted in bending in P1. For a positive shear force, for example, the y-displacement resulting from the tension force was reduced by the initial y-

displacement from the positive shear force. Moreover, as the y-displacement increased due to the tension force, the corresponding lever arm for the moment due to the shear force increased, such that the effect of the shear force was amplified.

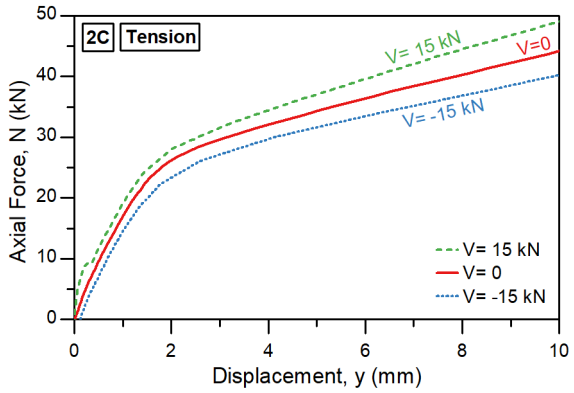

Figure 8.21. Numerical axial force-displacement curves with varying applied shear force

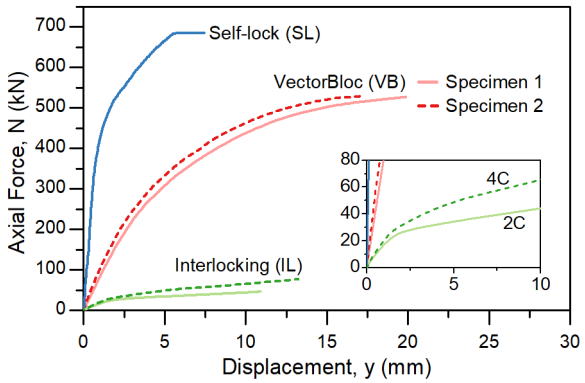

Figure 8.22. Axial behaviour of the interlocking (IL), Self-lock (SL) [219], and VectorBloc (VB) [218] connections

8.6.2 Comparison with existing inter-module connections

Two existing IMC's were selected from the literature: the VectorBloc (VB) connection [218], and the Self-lock (SL) connection [219]. As introduced in Section 7.5.2 (p.180), the selected connections had published experimental results for the axial behaviour, which was compared with the axial behaviour of the interlocking (IL) connection with a bolt preload of 50 kN (Figure 8.22). The tension capacity of the SL connection was the largest, followed by the VB connection, and, finally, the IL connection. For the SL connection, the capacity was associated with tensile failure of a 40 mm diameter threaded stud. Whereas, for the VB connection, the capacity was limited by the combination of tension and bending in two 25.4 mm diameter screws, which were offset from the centre of the 101.6 x 9.5 mm SHS column. Similarly, the tension behaviour of the IL connection was determined by bending of the plates, and combined

tension and bending in two bolts which were offset from the centre of the 75 x 6 mm SHS column. Despite the different magnitude of the tension capacity, the shape of the axial N-y curves for the IL connection were similar to those for the VB connection, which builds confidence in the present numerical results.

8.6.3 Simplified model

8.6.3.1 Axial compression

The axial force-displacement (N-y) behaviour can be divided into two stages as shown in Figure 8.23. The axial behaviour for compression, i.e., FG, can be represented by a linear function as

$$N(y) = \begin{cases} -N_F, & y < -N_F K_{FG}^{-1} \\ K_{FG} y, & -N_F K_{FG}^{-1} \le y \le 0 \end{cases} \tag{8.13}$$

where $N_F = A_{col} \min\left(f_{y,p}, f_{y,col}\right) = 536$ kN is the yield force, A_{col} is the column cross-sectional area, $f_{y,p}$ and $f_{y,col}$ are the yield strength of the plate and column steel, respectively, and K_{FG} is the axial compression stiffness of the plates. The width subject to compression increases through the thickness of the plates, reaching a maximum at the centre of P5, as shown in Figure 8.24(a). For a given half-apex angle (α), the maximum width can be given as

$$w_{\max} = t_{col} + 3t_p \tan\alpha \,, \tag{8.14}$$

where t_{col} is the column thickness, and t_p plate thickness. Hence, the average width through the plate thicknesses, which is reduced allowing for the plate edge constraints, can be estimated as

$$w_{av} = 0.25\left(4t_{col} + 4.5t_p \tan\alpha\right) = t_{col} + 1.125t_p \tan\alpha \,. \tag{8.15}$$

The column cross-sectional area (A_{col}) can be considered as the product of the column thickness (t_{col}) and a perimeter length,

$$L_{col,perimeter} = A_{col} t_{col}^{-1} \,. \tag{8.16}$$

Therefore, the average area through the plate thicknesses can be estimated as

$$A_{av} = L_{col,perimeter} w_{av} = A_{col} t_{col}^{-1} \left(t_{col} + 1.125t_p \tan\alpha\right), \tag{8.17}$$

and the corresponding axial stiffness is

$$K_{FG} = \frac{E_s A_{av}}{3t_p} = \frac{E_s A_{col}\left(t_{col} + 1.125t_p \tan\alpha\right)}{3t_{col} t_p}, \tag{8.18}$$

where E_s is the elastic modulus of the plate steel.

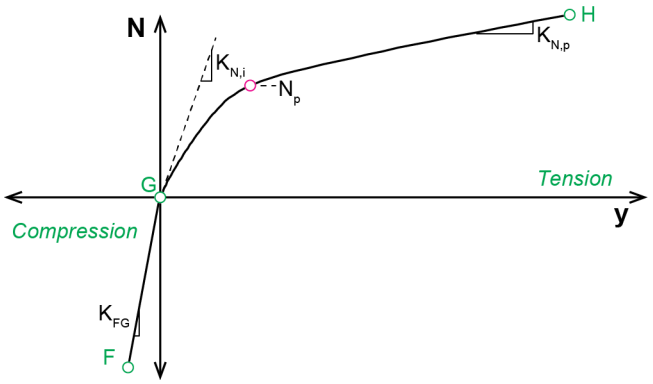

Figure 8.23. Proposed model for axial force-displacement behaviour

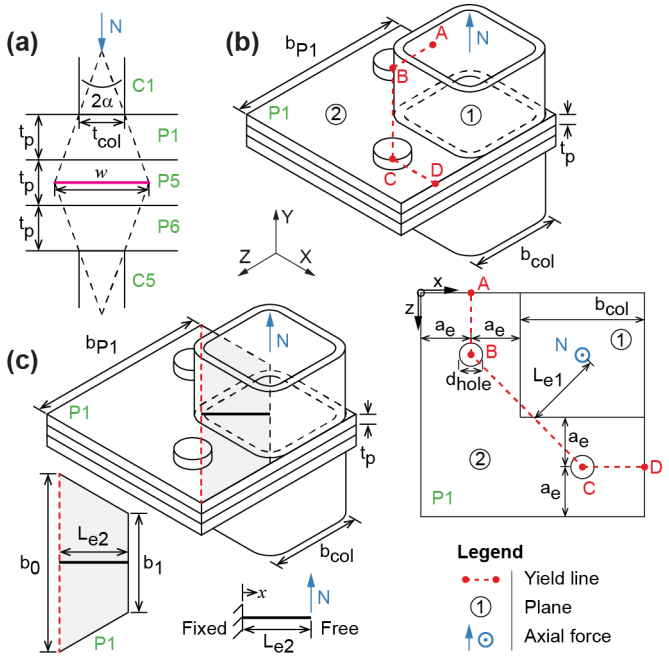

Figure 8.24. (a) Compression stiffness model, (b) yield line analysis model, and (c) cantilever beam model

Assuming a half-apex angle of 30° [226], the stiffness can be estimated as 2.38×10^4 kN/mm. Thus, the model overestimates the stiffness in comparison with the numerical result (2.01×10^4 kN/mm). In the numerical model, although a half-apex angle of 30° was observed through P1 and P6, slip at the interfaces, i.e., P1-P5 and P5-P6, reduced the angle. Therefore, a reduced half-apex angle of 21° is suggested.

8.6.3.2 Axial tension

The axial behaviour for tension, i.e., GH, can be estimated as

$$N(y) = N_p\left\{1-\exp\left[\frac{-\left(K_{N,i}-K_{N,p}\right)y}{N_p}\right]\right\}+K_{N,p}y\,, \tag{8.19}$$

where N is the axial force, y>0 is the y-displacement, N_p is the tensile yield force, $K_{N,i}$ is the

initial stiffness, and $K_{N,p}$ is the hardening stiffness. Fitting Equation (8.19) to the numerical results for 2C yields the values shown in Table 8.3.

Table 8.3. Curve fitting parameters for the numerical axial behaviour of 2C

$F_{t,ini}$ (kN)	K_{FG} (kN/mm)	N_p (kN)	$K_{N,i}$ (kN/mm)	$K_{N,p}$ (kN/mm)
50	2.01e4	24.22	26.15	2.003
35	2.01e4	24.08	24.37	2.006
5	2.00e4	24.18	19.62	2.005

The tensile yield force, N_p, can be estimated by yield line analysis. Three yield lines were apparent in the numerical results, as shown in Figure 8.24(b), i.e., AB, BC and CD. The normal vectors defining the corresponding planes 1 and 2 can be given as

$$n_1 = \left(-\delta, 0.5b_{col} + a_e, \delta\right), \text{ and} \qquad (8.20)$$
$$n_2 = \left(0,1,0\right),$$

where δ is a vertical virtual displacement applied at the centre of the column, b_{col} is the column width, and a_e is the plate edge dimension shown in Figure 8.24(b). The yield line rotation can then be estimated as [217]

$$\theta_{12} = \frac{\left|n_1 \times n_2\right|}{n_1 \bullet n_2}. \qquad (8.21)$$

The corresponding internal work for plate yielding can be given as

$$U_{p,uv} = l_{uv}\theta_{uv}m_p, \qquad (8.22)$$

where l_{uv} is the length of the yield line uv, θ_{uv} is the corresponding rotation, and m_p is the plastic moment per unit length, which can be given as

$$m_p = \frac{1}{4}t_p^2 f_{p,p}, \qquad (8.23)$$

where t_p is the plate thickness, and $f_{p,p}$ is the plate design stress. The plate design stress allows for the effect of strain-hardening, and is calculated as [165]

$$f_{p,p} = \frac{f_{y,p} + 2f_{u,p}}{3}, \qquad (8.24)$$

where $f_{y,p}$ is the yield strength, and $f_{u,p}$ is the ultimate tensile strength. Hence, the internal work for each yield line can be assembled, and the total internal work due to plate yielding can be given as

$$U_{Int.} = \sum_{\substack{\text{yield} \\ \text{lines}}} U_p = \frac{\left(1+\sqrt{2}\right)b_{col} + 2a_e}{0.5b_{col} + a_e}\delta m_p. \qquad (8.25)$$

Referring to Figure 8.24(b), the external work can be given as

$$U_{Ext.} = N_p L_{e1} \frac{\delta}{L_{e1}} = N_p \delta, \tag{8.26}$$

where N_p is the tensile yield force, and $L_{e1} = \frac{\sqrt{2}}{4}\left(b_{col} + 2a_e\right)$ is the effective lever arm. Setting the external work equal to the internal work, the tensile yield force can be given as

$$N_p = \frac{\left(1+\sqrt{2}\right)b_{col} + 2a_e}{0.5b_{col} + a_e} m_p. \tag{8.27}$$

Therefore, for the 2C geometry, the tensile yield force can be estimated as 24.0 kN. Thus, the model underestimates the force in comparison with the numerical result (24.2 kN) by approximately 1%.

It is recommended that the initial preload should be selected to ensure the plates do not separate between the bolts when subjected to the design tension force. The initial stiffness can then be estimated using the cantilever beam analogy shown in Figure 8.24(c). The vertical displacement along the cantilever can be derived as

$$y = \iint \frac{M}{EI} dx dx, \tag{8.28}$$

where E is the elastic modulus, I is the moment of inertia of the P1 cross-section, and M is the moment which can be given as

$$M(x) = N\left(L_{e2} - x\right), \tag{8.29}$$

where $L_{e2} = a_e\sqrt{2}$. The width of the P1 cross-section varies with x according to the equation

$$\begin{aligned} b(x) &= b_0 + \left(b_1 - b_0\right)\frac{x}{L_{e2}} - b_{holes} \\ &= \left(b_{col} + 2a_e\right)\sqrt{2} - 2x - b_{holes}. \end{aligned} \tag{8.30}$$

The width missing due to the two bolt holes (b_{holes}) can be derived as

$$b_{holes}\left(x\right) = 2\sqrt{2d_{hole}\ell - \ell^2}\left(\ell - 2x\right)\ell^{-1}, \tag{8.31}$$

where $x \le 0.5\ell$, d_{hole} is the bolt hole diameter and $\ell = d_{hole} - \sqrt{2}\left(0.5b_{col} - a_e\right)$. The moment of inertia can, therefore, be given as

$$I(x) = \frac{b(x)t_p^3}{12}. \tag{8.32}$$

Hence, the vertical displacement can be derived from Equation (8.28), and the stiffness can be calculated based on the maximum vertical displacement as

$$k_{P1} = \frac{N}{y(x = L_{e2})} = 56.3 \text{ kN/mm} . \tag{8.33}$$

Finally, the axial stiffness of the bolt can be estimated as

$$k_{bolt} = \frac{EA_{bolt}}{L_{bolt}}, \tag{8.34}$$

where E is the elastic modulus, A_{bolt} is the cross-sectional area of a single bolt, and L_{bolt} is the grip length plus half the height of the bolt head and nut. The initial stiffness can then be estimated by combining the relevant plate and bolt springs, i.e.,

$$K_{N,i} = \left(\frac{1}{k_{P1}} + \frac{1}{2k_{bolt}} + \frac{1}{k_{P6}} \right)^{-1} . \tag{8.35}$$

Therefore, for the 2C geometry, the initial stiffness can be estimated as 27.5 kN/mm. Thus, the model overestimates the stiffness in comparison with the numerical result (26.2 kN/mm) by approximately 5%.

While the yield line was assumed to be located along the main diagonal of P1, in reality, it was located along the diagonal line passing through the bolts. Therefore, the actual yield line was slightly shorter, and the lever arm was slightly greater in the numerical model, than in simplified model. By assuming the yield line was located on the main diagonal, the width of P1 could be expressed as a single linear function (Equation (8.30)), whereas otherwise a piecewise function would have been needed. This simplified the equation for the moment of inertia and, hence, the integration for the stiffness. Although the initial stiffness was overestimated, the model was well matched to the numerical result as shown in Figure 8.25.

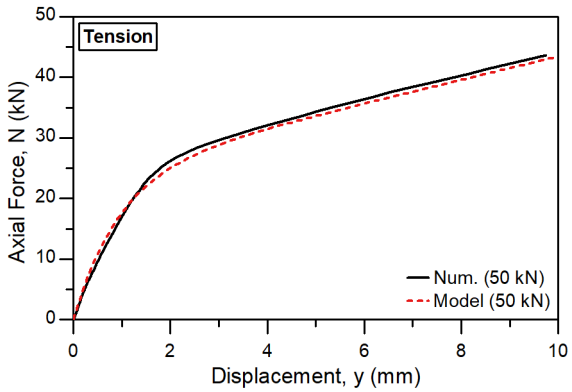

Figure 8.25. Model and numerical axial behaviour for axial tension

For large displacement the slope asymptotically tends to [227]

$$K_{N,p}^{\text{limit}} = \frac{E_{sh}}{E} K_{N,i} , \tag{8.36}$$

where E is the elastic modulus, and E_{sh} is the strain hardening modulus, which was determined following the quad-linear material model [203] in the numerical analyses. The hardening stiffness input into the simplified model should be larger than the limiting value [227]. An empirical factor of 6 is proposed following the numerical results, such that the hardening stiffness can be estimated as

$$K_{N,p} = 6\frac{E_{sh}}{E}K_{N,i} \approx 0.071K_{N,i}\,. \tag{8.37}$$

8.7 Moment-rotation behaviour

8.7.1 Numerical results

8.7.1.1 Moment (M)

Figure 8.26 shows the numerical moment-rotation (M-θ) curves for the 2C, and 4C geometries. The rotation about the z-axis was calculated based on the x- and y-displacements as

$$\theta_z = \text{atan}\left(\frac{y_3 - y_4}{b_{col} + x_4 - x_3}\right), \tag{8.38}$$

where x_3 and y_3 were the x- and y-displacement of point 3, and x_4 and y_4 were the x- and y-displacement of point 4, as shown in Figure 8.27. b_{col} represents the width of the column section (Figure 8.9, p.208), i.e., the initial distance between points 3 and 4 in the x-direction.

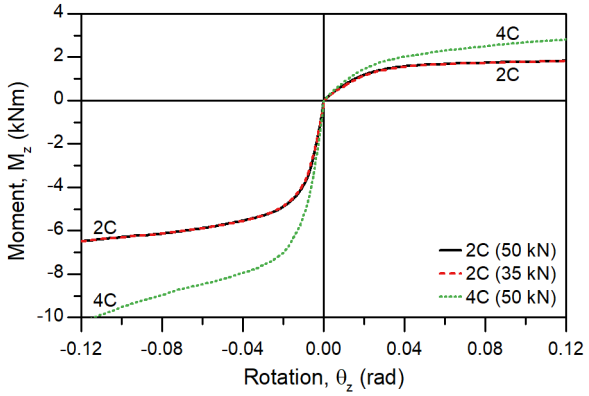

Figure 8.26. Numerical bending moment-rotation curves

For 2C subjected to a positive moment, the deformed shape is illustrated in Figure 8.27(a). The first yielding occurred in P1, and it was centred on the corner of C1 which was subjected to tension. The yielded zone spread across P1, and a diagonal yield line was formed, as shown in Figure 8.32(a) (p.234). The deformed shape for a negative moment is illustrated in Figure 8.27(b). The yielding occurred in both P1 and B1, and yield lines were formed as illustrated in Figure 8.32(b). Figure 8.26 shows the numerical M-θ curves for 2C with bolt preloads of

35 and 50 kN. The M-θ behaviour was determined mainly by the bending of the plates and, hence, the bolt preload had little effect.

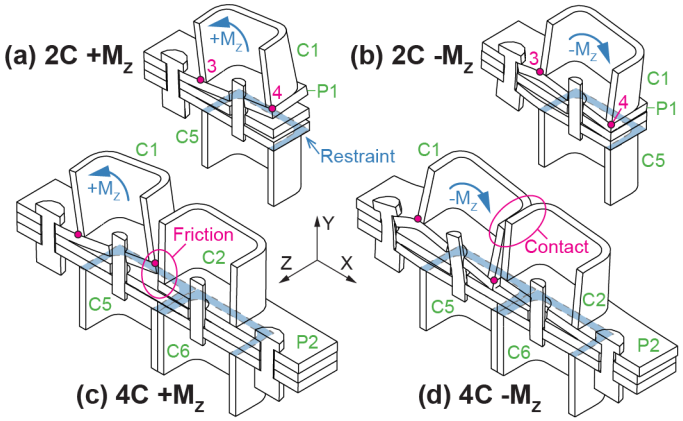

Figure 8.27. Deformed shape due to applied bending moment

4C had a higher yield moment than 2C. For positive moment about the z-axis, friction between C1 and C2 increased the yield moment capacity (Figure 8.27c). For a negative moment, C1 contacted C2, which substantially increased the capacity (Figure 8.27d). Reliance on contact between the columns may not be appropriate for design purposes. Both C1 and C2 may be subjected to a bending moment in the same direction. Hence, considering negative applied moment, for example, C2 would move away from C1, such that contact between the columns would not occur. Therefore, design based on the moment-rotation behaviour of 2C is recommended.

8.7.1.2 Axial force – moment interaction (N+M)

An axial load was applied, as shown in Figure 8.10(b) (p.209), after which a bending moment was applied and incrementally increased to establish the moment-rotation (M-θ) curve. Following Section 8.5.1.2 (p.211), axial forces of 0.5Nt, 0.1Nc, and 0.2Nc were considered. The resulting M-θ curves are shown in Figure 8.28. For axial tension, i.e., 0.5Nt, the applied axial force opened a gap between the plates, causing an initial rotation. When a negative moment was subsequently applied, the M-θ behaviour proceeded as follows. The initial rotation due to the axial load slowly reduced, until the applied moment was sufficient to completely close the gap, after which the M-θ stiffness increased. The first yield occurred in the top plate, P1. This was followed by tension yielding of the upper column, C1, yielding of P1 around the bolt head, and finally compression yielding of C1 and P1. In comparison, when a positive moment was applied, the initial gap did not close, but continued to open as the applied moment increased. The first yield occurred in the top plate, P1, and the yielding quickly spread across P1, forming a diagonal yield line. The moment capacity, i.e., the maximum applied moment, was reduced as a result of the initial moment induced by the

tension force. For axial compression, i.e., 0.1Nc and 0.2Nc, the compression force generated a bending moment which delayed separation of the plates. Hence, the initial stiffness and moment capacity were increased, compared to the case with no axial load. As the axial compression stiffness was larger than the tension stiffness, the initial rotation due to the axial load did not have a significant effect on the M-θ curves.

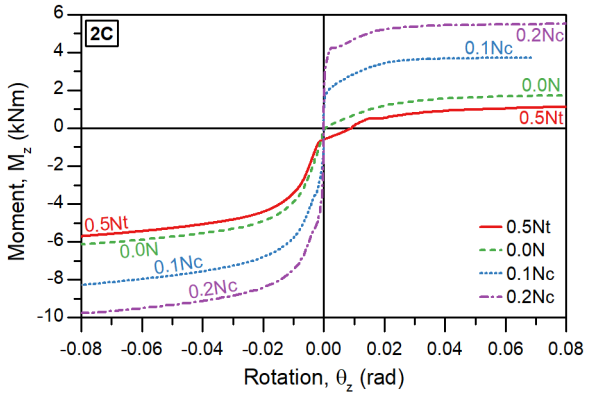

Figure 8.28. Numerical bending moment-rotation curves with varying axial force

8.7.1.3 Shear – moment interaction (V+M)

Following Section 8.5.1.3 (p.212), a bending moment and shear force were applied to C1 simultaneously, and three shear force ratios were considered: M/V=1 m, M/V=0.5 m, and M/V=0.25 m. A positive shear force was applied in combination with a negative moment. Whereas Section 8.5.1.3 presented the shear behaviour, this section presents the resulting moment-rotation (M-θ) behaviour (Figure 8.29). The shear force had only a small effect on the M-θ behaviour. A small bending moment was generated by the shear force, which was offset from the restrained lower column by the thickness of the plates. For a positive moment, the moment capacity was reduced due to the small positive moment generated by the negative shear force. Similarly, for a negative moment, the moment capacity was reduced due to the small negative moment generated by the positive shear force. As the moment decreased, the resulting rotation increased the offset of the shear force from the lower column. Therefore, the effect of the shear force on the M-θ behaviour was more significant for larger rotations. However, for preliminary design purposes, the main interest is the initial M-θ behaviour, for which the shear force had negligible effect.

8.7.2 Comparison with existing inter-module connections

Two existing IMCs were selected: the Rotary connection (RC) [222], and the bolted moment end plate (EP) [165]. As introduced in Section 7.6.2 (p.191), the selected connections had published experimental moment-rotation (M-θ) curves, which were normalised and plotted alongside the present numerical curves for the interlocking (IL) connection (Figure 8.30). The

applied moment was divided by the plastic moment and plotted on the y-axis. Similarly, the connection rotation was divided by the rotation corresponding with the plastic moment, and plotted on the x-axis. For the IL connection, the 2C geometry was adopted with a bolt preload of 50 kN. Axial loads of N= 0 and N= -53.6 kN, i.e., 0.0N and 0.1Nc, were considered, and normalised M-θ curves are given for positive and negative bending. For the RC connection, the M-θ behaviour was associated with yielding of an M58 rod which was located centrally inside a 200 x 18 mm SHS column. Whereas, for the EP connection, the M-θ behaviour was associated with bending of the end plates which were welded to the 150 x 9 mm SHS columns, and yielding of the tensioned M20 bolts. T17, for example, failed due to large deformation of the 12 mm thick plate. In contrast, T19 had 20 mm thick plates, and the connection failed due to tensile fracture of the bolts. The M-θ behaviour of the IL connection was determined by bending of the plates, and yielding of the bolts in tension. Hence, the M-θ behaviour of the IL connections was similar to that of the EP connection, which builds confidence in the present numerical results.

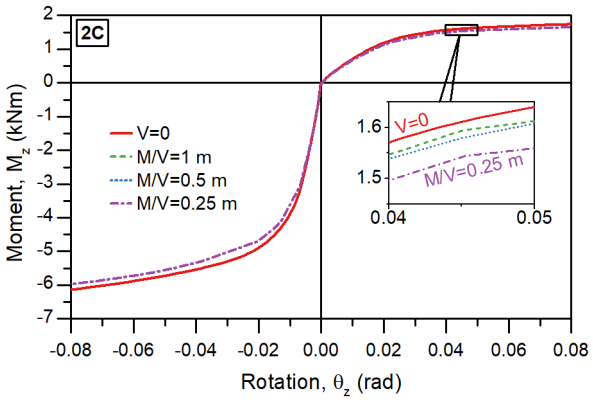

Figure 8.29. Numerical bending moment-rotation curves with varying shear force

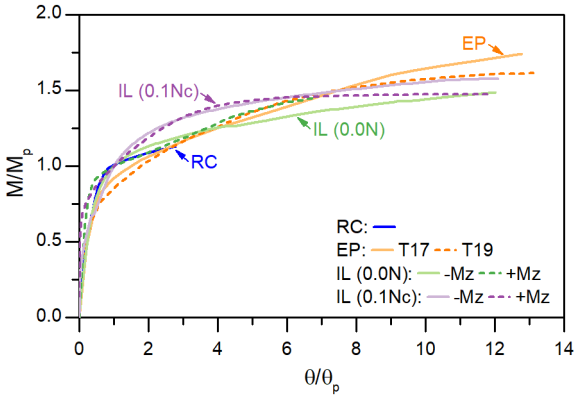

Figure 8.30. Normalised moment-rotation behaviour of the interlocking (IL), Rotary (RC) [222], and bolted moment end plate (EP) [165] connections

8.7.3 Simplified model

8.7.3.1 First stage (OT, OR)

The moment-rotation behaviour can be divided into two stages as shown in Figure 8.31. In the first stage, i.e., OR and OT, the behaviour is linear. When the upper column is subjected to an axial compression force, a bending moment is generated which delays rotation caused by separation of the plates. The moment at which the column starts to lift can be estimated as

$$M_R = -M_T = \frac{-NZ_{col}}{A_{col}}, \tag{8.39}$$

where N is the applied axial tension force, and Z_{col} and A_{col} are the elastic section modulus and cross-sectional area of the column, respectively. For example, for the 2C geometry, M_R and M_T can be estimated as ±1.08 kNm and ±2.16 kNm, for an axial load of -53.6 kN and -107 kN, respectively. Thus, the model underestimates the moment in comparison with the average numerical result (1.11 and 2.24 kNm) by 2.7 and 3.6%, respectively.

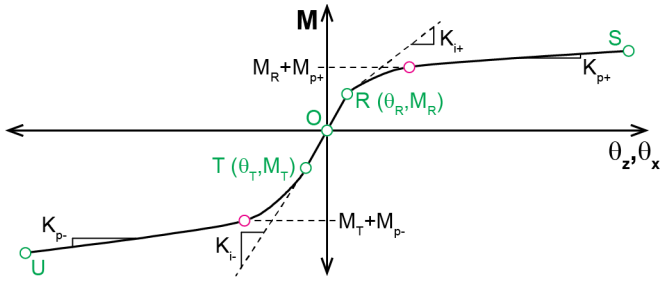

Figure 8.31. Simplified model for bending moment-rotation behaviour

The rotation in this stage is associated with the axial stiffness of the plates below the column. The applied moment is assumed to be transferred via the column flanges, resulting in a compression force on one side, and a tension force on the other side. Similar to Section 8.6.3.1 (p.222), the corresponding axial stiffness on each side, allowing for the plate edge constraint, is

$$k_{axial} = \frac{EA}{L} = \frac{Eb_{col}w_{av}}{3t_p}, \tag{8.40}$$

where E is the elastic modulus, b_{col} is the column width, w_{av} is the average width through the plate thicknesses calculated using Equation (8.15) (p.222), and t_p is the plate thickness. Then, the moment-rotation stiffness is estimated as

$$K_{TR} = 2L^2 k_{axial}, \tag{8.41}$$

where $L = 0.5(b_{col} - t_{col})$, and b_{col} is the column width. Therefore, for the 2C geometry, K_{TR} can be estimated as 14,100 kNm/rad. Thus, the model underestimates the stiffness in comparison

with the average numerical result (14,600 kNm/rad) by 3.4%.

8.7.3.2 Second stage (TU, RS)

In the second stage, i.e., RS and TU, the behaviour is nonlinear, and, for positive bending, it can be represented by an exponential function as

$$M(\theta) = M_R + M_{p+}\left\{1-\exp\left[\frac{-\left(K_{i+}-K_{p+}\right)\left(\theta-\theta_R\right)}{M_{p+}}\right]\right\} + K_{p+}\left(\theta-\theta_R\right), \tag{8.42}$$

where $\theta_R = M_R K_{TR}^{-1}$, M_{p+} is the plastic moment capacity, and K_{i+} and K_{p+} are the initial and hardening stiffness, respectively. Similarly, for negative bending, the behaviour can be represented as

$$M(\theta) = M_T + M_{p-}\left\{1-\exp\left[\frac{-\left(K_{i-}-K_{p-}\right)\left(\theta-\theta_T\right)}{M_{p-}}\right]\right\} + K_{p-}\left(\theta-\theta_T\right), \tag{8.43}$$

where $\theta_T = M_T K_{TR}^{-1}$, and M_{p-}, K_{i-} and K_{p-} are the plastic moment, initial and hardening stiffness, respectively. Fitting equations (8.42) and (8.43) to the numerical data yields the parameters summarised in Table 8.4. In the absence of axial loading, the average initial stiffness was 89.9 and 676 kNm/rad for positive and negative bending, respectively. On average, the hardening stiffness was equal to 0.024 times the initial stiffness for negative bending.

Table 8.4. Curve fitting parameters for the numerical bending moment-rotation behaviour of the 2C geometry

Direction	$F_{t,ini}$ (kN)	N (kN)	K_{TR} (kNm/rad)	θ_R, θ_T (x10^{-4} rad)	M_R, M_T (kNm)	M_p (kNm)	K_i (kNm/rad)	K_p (kNm/rad)
+Mz	50	0	-	0	0	1.808	92.42	0
-Mz	50	0	-	0	0	-4.904	693.9	16.02
+Mz	35	0	-	0	0	1.808	87.36	0
-Mz	35	0	-	0	0	-4.909	658.5	16.29
+Mz	50	-53.6 (0.1Nc)	14460	0.8022	1.16	2.522	308.7	0
-Mz	50	-53.6 (0.1Nc)	14380	-0.7371	-1.06	-5.286	1108	24.88
+Mz	50	-107 (0.2Nc)	14815	1.580	2.34	3.077	455.1	0
-Mz	50	-107 (0.2Nc)	14820	-1.444	-2.14	-5.947	1285	21.25

To verify the numerical results, the plastic moment capacity can be calculated by yield line analysis. For positive bending moment $+M_z$, three yield lines were apparent in the numerical

results, i.e., AB, BC, and BD, as shown in Figure 8.32(a). The corresponding normal planes, i.e., 1 through to 3, can be defined by the normal vectors

$$\begin{aligned} n_1 &= (-\delta, b_{col}, 0), \\ n_2 &= (-\delta, 2a_e, \delta), \text{ and} \\ n_3 &= (0,1,0), \end{aligned} \tag{8.44}$$

where δ is a virtual displacement applied at the tension flange of the column. The yield line rotations and corresponding internal work for plate yielding can then be calculated, following the same procedure as in Section 8.6.3.2 (p.223). For the plastic moment per unit length (m_p), the yield strength ($f_{y,p}$) is adopted, rather than the design stress ($f_{p,p}$), because strain hardening did not have a significant effect on the numerical M-θ behaviour for positive bending. Hence, the rotation and internal work for each yield line can be assembled, and the total internal work due to plate yielding can be given as

$$U_{Int.} = U_p = \lambda_1 \delta m_p , \tag{8.45}$$

where

$$\lambda_1 = 1 + \frac{\sqrt{2b_{col}^2 - 4a_e b_{col} + 4a_e^2} + \sqrt{2b_{col}^2 + 8a_e^2} - \sqrt{2}d_{hole}}{2a_e}. \tag{8.46}$$

The external work can be given as

$$U_{Ext.} = M_p \frac{\delta}{b_{col}}, \tag{8.47}$$

and, hence, the plastic moment capacity (M_{p+}) can be given as

$$M_{p+} = \lambda_1 b_{col} m_p . \tag{8.48}$$

Therefore, for the 2C geometry, M_{p+} can be estimated as 1.82 kNm. Thus, the model overestimates M_{p+} in comparison with the numerical result (1.80 kNm) by 1%.

When an axial force is applied the plastic moment is increased. The bending moment due to the axial load can be calculated as

$$M_N = -(0.5a_e + 0.25b_{col})N , \tag{8.49}$$

where N is the applied axial tension force, and $(0.5a_e + 0.25b_{col})$ represents the x- or z-component of the distance between the centre of the column and the centre of the bolt group. The increase in the plastic moment can then be given as $M_N - M_R$. Hence, for an axial load of -53.6 kN, the plastic moment can be estimated as 2.55 kNm. Thus, the model overestimates M_{p+} in comparison with the numerical result (2.52 kNm) by 1%.

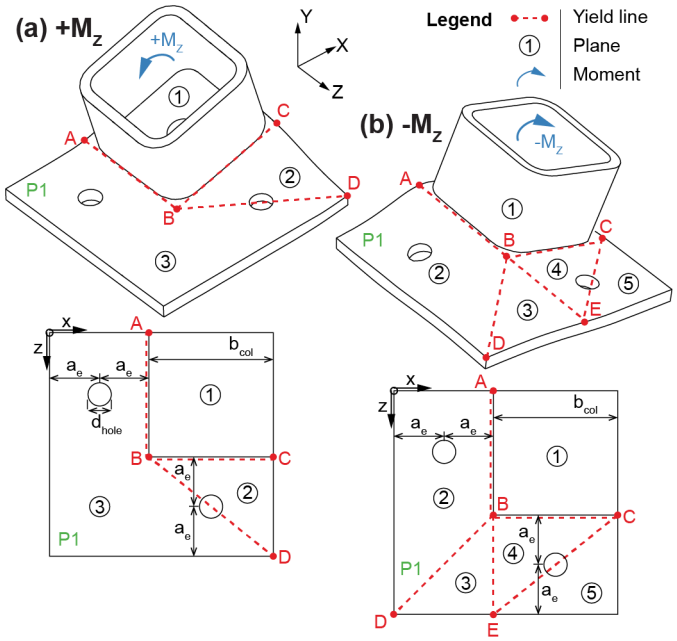

Figure 8.32. Definition of yield lines for yield line analysis

A different yielding mechanism applies in the case of negative bending, as shown in Figure 8.32(b). Five yield lines are defined, and the corresponding planes are named 1 through 5. Following the same procedure, the internal work due to plate yielding can be given as

$$U_p = \lambda_2 \delta m_p \,, \tag{8.50}$$

where

$$\lambda_2 = \frac{2a_e + b_{col} + \sqrt{2b_{col}^2 + 4a_e^2 - 4b_{col}a_e} + \sqrt{2b_{col}^2 + 8a_e^2} - \sqrt{2}d_{hole}}{2a_e} + \sqrt{2} + 2 \,. \tag{8.51}$$

For the plastic moment per unit length (m_p), the design stress ($f_{p,p}$) is adopted, because strain hardening had an effect on the numerical moment-rotation behaviour for negative bending. The internal work due to the bolt yielding can be given as

$$U_b = f_{y,b}\delta_b = 0.5 f_{y,b}\delta \,, \tag{8.52}$$

where $f_{y,b}$ is the bolt yield stress, δ_b is the compatible displacement induced in the bolt, and δ is the vertical virtual displacement. Therefore, the total internal work is

$$U_{Int.} = U_p + U_b = \lambda_2 \delta m_p + 0.5 f_{y,b}\delta \,, \tag{8.53}$$

which results in a plastic moment capacity of

$$M_{p-} = \left(\lambda_2 m_p + 0.5 f_{y,b}\right) b_{col} \,. \tag{8.54}$$

Therefore, for the 2C geometry, M_{p-} can be estimated as -4.496 kNm. Thus, the model underestimates M_{p-} in comparison with the numerical result (4.907 kNm) by 8%. This error

can be attributed to the approximate nature of the numerical curve fitting process, and to the simplifications made to the geometry in the yield line analysis.

The simplified model is conservative, in that it neglects the contribution of the axial force after the column starts to lift at M_T and M_R. In the model, the plastic moment was increased allowing for the axial load, following Equation (8.49). However, in reality, the effect of the axial load starts immediately after M_T and M_R, where it causes an increase in the moment-rotation stiffness. However, in the model, the effect of the axial load is incorporated in the plastic moment. Therefore, although the plastic moment is well matched to the numerical result, the stiffness of the moment-rotation curve immediately following M_T and M_R is underestimated. That is, this portion of the moment-rotation curve is conservatively estimated by the model, as shown in Figure 8.33. Overall, the simplified model was well matched to the numerical results, and it is recommended for preliminary design, where the moment-rotation behaviour may be determined based on the design gravity load.

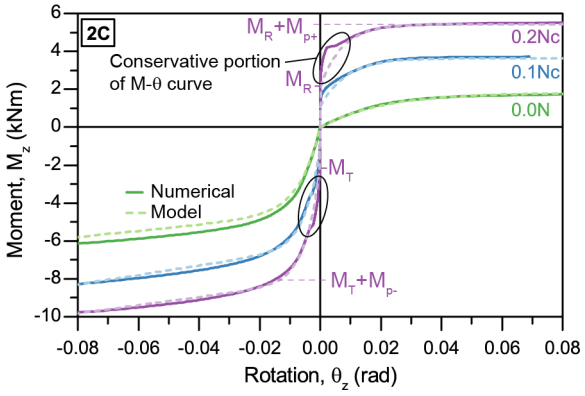

Figure 8.33. Comparison between model and numerical moment-rotation behaviour

8.8 Spring model

8.8.1 VC

The proposed spring model is shown in Figure 8.34. For the vertical connections (VCs), the shear behaviour is based on the 2C geometry (Figure 8.9). Each VC is composed of two equal springs in series, i.e., $K_{VC,V}$. The model for the shear behaviour (Figure 8.16) represents the behaviour of two springs in series. Hence, for positive displacement, combining Equation (8.2) (p.214) and (8.6) (p.216), the shear behaviour associated with $K_{VC,V}$ can be given as

$$V_{VC,V}(x)=\begin{cases} V_{slip}\left[1-\exp\left(\dfrac{-2K_{V,i}x}{V_{slip}}\right)\right], & 0\le x\le 0.5x_P \\ V_{slip}+V_{y,IMC}\left[1-\exp\left(\dfrac{-2K_{V,b}\left(x-0.5x_P\right)}{V_{y,IMC}}\right)\right]\le V_{y,col}, & 0.5x_P<x \end{cases} \tag{8.55}$$

and the negative displacement behaviour can be given as $-V_{VC,V}$. Due to the symmetry of the connection, Equation (8.55) can be adopted for the z-direction, with z substituted for x.

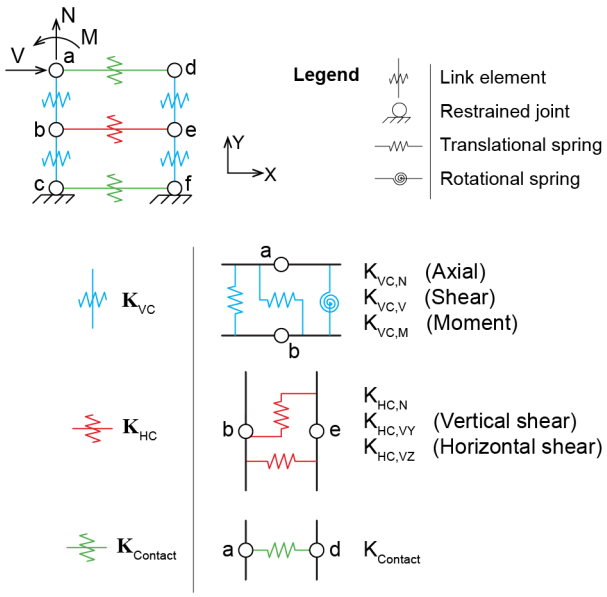

Figure 8.34. Proposed spring model

The increase in the shear slip resistance due to contact between the upper column plates is included by the compression only spring $K_{Contact}$. The axial stiffness can be estimated based on the P1/P2 cross-section (Figure 8.9, p.208) as

$$K_{Contact} = \frac{EA}{L} = \frac{Eb_{P1}t_p}{b_{col} - d_{LP}}, \tag{8.56}$$

where E is the elastic modulus, b_{P1} is the width of P1/P2, t_p is the plate thickness, b_{col} is the column width, and d_{LP} is the diameter of the hole in P1/P2 for the locating pin.

To ensure that the $K_{Contact}$ spring is limited to compression forces less than the yield strength of P1/P2, the force-displacement behaviour can be given as

$$N_{Contact}(x) = \begin{cases} -f_{y,p}b_{P1}t_p, & x < -x_L \\ K_{Contact}\left(x + x_{gap}\right), & -x_L \le x \le -x_{gap} \\ 0, & x > -x_{gap} \end{cases} \tag{8.57}$$

where $x_L = \frac{f_{y,p}b_{P1}t_p}{K_{Contact}} + x_{gap}$, $f_{y,p}$ is the plate yield strength, N is the axial tension force, and x is the axial elongation. x_{gap} is the initial gap due to the fabrication and assembly tolerance. In the present study the gap is assumed to be zero, following the numerical model. However, in the previous experiments (Chapter 6), the largest initial gap was approximately 2 mm, i.e., 1.9 mm. Therefore, a gap of 2 mm is suggested for design purposes.

Similarly, combining Equation (8.13) (p.222) and (8.19) (p.223), and allowing for the two springs in series, the axial behaviour associated with $K_{VC,N}$ can be given as

$$N_{VC,N}(y)=\begin{cases}-N_F, & y<-0.5y_F\\ 2K_{FG}y, & -0.5y_F\le y\le 0\\ N_p\left\{1-\exp\left[\dfrac{-2\left(K_{N,i}-K_{N,p}\right)}{N_p}y\right]\right\}+2K_{N,p}y, & y>0\end{cases} \tag{8.58}$$

where $y_F=N_FK_{FG}^{-1}$.

Finally, assembling Equation (8.39) and (8.41) to (8.43), the moment-rotation behaviour associated with $K_{VC,M}$ can be given as

$$M_{VC,M}(\theta)=\begin{cases}M_T+M_{p-}\left\{1-\exp\left[\dfrac{-2\left(K_{i-}-K_{p-}\right)\left(\theta-\dfrac{\theta_T}{2}\right)}{M_{p-}}\right]\right\}+2K_{p-}\left(\theta-\dfrac{\theta_T}{2}\right), & \theta<\dfrac{\theta_T}{2}\\ 2K_{TR}\theta, & \dfrac{\theta_T}{2}\le\theta\le\dfrac{\theta_R}{2}\\ M_R+M_{p+}\left\{1-\exp\left[\dfrac{-2K_{i+}\left(\theta-\dfrac{\theta_R}{2}\right)}{M_{p+}}\right]\right\}, & \dfrac{\theta_R}{2}<\theta\end{cases} \tag{8.59}$$

where $\theta_R=M_RK_{TR}^{-1}=-\theta_T$. As a result of the connection symmetry, Equation (8.59) can be adopted for rotation about the z-axis, and for rotation about the x-axis.

8.8.2 HC

For the horizontal connection (HC), following the previous study [140], the translational stiffnesses associated with the central tie plate (P5) are incorporated in the model. The axial contribution of P5 is included by the spring $K_{HC,N}$, and the axial behaviour can be estimated as

$$N_{HC,N}(x)=\begin{cases}-f_{y,p}A_{P5}, & x<-x_L\\ K_{HC,N}x, & -x_L\le x\le x_L\\ f_{y,p}A_{P5}, & x>x_L\end{cases} \tag{8.60}$$

where $K_{HC,N}=\dfrac{EA_{P5}}{2b_{col}}$, $A_{P5}=b_{P5}t_p$, $x_L=\dfrac{f_{y,p}A_{P5}}{K_{HC,N}}$, and b_{P5} is the width of P5 (Figure 8.9, p.208). $2b_{col}$ is an estimate of the effective length of P5. For example, it estimates the distance between the two bolt groups, where the friction resistance is generated. The horizontal shear contribution of P5 is included by the spring $K_{HC,VZ}$, and the shear behaviour can be estimated as

$$V_{HC,VZ}(z)=\begin{cases}-0.6f_{y,p}A_{P5}, & z<-z_L\\ K_{HC,VZ}z, & -z_L\le z\le z_L\\ 0.6f_{y,p}A_{P5}, & z>z_L\end{cases} \tag{8.61}$$

where $K_{HC,VZ}=\dfrac{GA_{P5}}{2b_{col}}$, $z_L=\dfrac{0.6f_{y,p}A_{P5}}{K_{HC,VZ}}$, and G is the shear modulus of the plate steel. Finally, the vertical shear contribution of P5 is included by the spring $K_{HC,VY}$, and the shear behaviour can be estimated as

$$V_{HC,VY}(y)=\begin{cases}-0.6f_{y,p}A_{P5}, & y<-y_L\\ K_{HC,VY}y, & -y_L\le y\le y_L\\ 0.6f_{y,p}A_{P5}, & y>y_L\end{cases} \tag{8.62}$$

where $K_{HC,VY}=\dfrac{GA_{P5}}{b_{col}}$, $y_L=\dfrac{0.6f_{y,p}A_{P5}}{K_{HC,VY}}$. b_{col} is the column width, which estimates the effective length of P5 for the calculation of the shear stiffness. For example, it estimates the distance between the bolt group on one side, and the edge of the column on the other side.

8.8.3 Validation of spring model by application to 4C

The accuracy of the spring model was demonstrated for the 2C geometry in the preceding sections 8.5.2 (p.213), 8.6.3 (p.222), and 8.7.3 (p.231). To demonstrate the application to the 4C geometry, a numerical model was prepared using SAP2000 [169]. The geometry was defined following Figure 8.34, and nonlinear links were created based on Equation (8.55) to (8.62). *c* and *f* were restrained, while a shear force, axial force, and bending moment were separately applied to *a*. The resulting F-d and M-θ behaviours were established by nonlinear static analyses, wherein the force or moment was increased linearly from zero.

The resulting shear behaviour is shown in Figure 8.35. The spring model underestimated the positive slip resistance in comparison with the numerical result, as the increase in the slip resistance due to the rotational restraint provided by P2 to P1 (refer §8.5.1.1, p.209) was not included. It was excluded because, during site assembly, a horizontal gap may occur between P1 and P2 (§6.4.5, p.152), such that reliance on the contact could result in an overestimate of the shear capacity. Similarly, the model underestimated the negative shear capacity in comparison with the numerical result. In the numerical results, contact between P1 and P2 increased the ultimate capacity, whereas the spring model did not include the effect of the contact. In this way, the proposed spring model gave a conservative estimate of the shear behaviour.

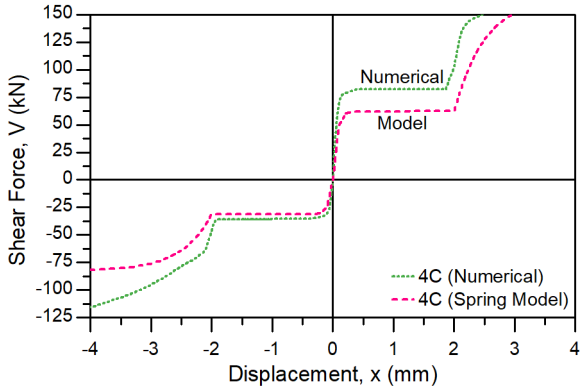

Figure 8.35. Numerical and spring model shear behaviour

Similarly, the axial behaviour (Figure 8.36) shows that the initial tension stiffness was slightly overestimated by the spring model in comparison with the numerical result for 4C. This was caused mainly by the yield line geometry assumed in the simplified model (see §8.6.3.2, p.223). After tensile yielding, the spring model underestimated the ultimate tension capacity in comparison with the numerical result, as contact between P1 and P2 was not included in the model. This was a conservative assumption which allowed for the possibility of gaps between the connection elements.

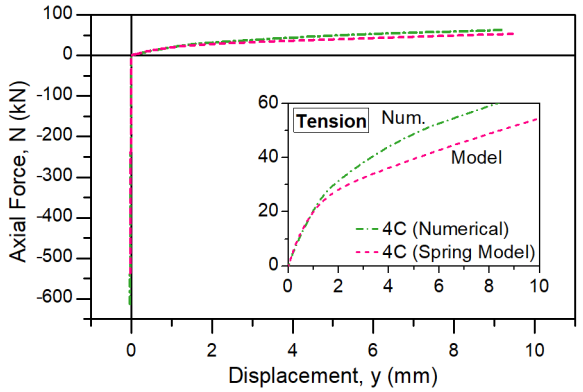

Figure 8.36. Numerical and spring model axial behaviour

Finally, for the M-θ behaviour (Figure 8.37), the numerical result showed that the negative moment capacity was increased due to contact between the upper columns. The spring model underestimated the negative moment capacity as this contact was not included in the simplified model (see §8.7.1.1, p.227). Similarly, the numerical result showed that the positive moment capacity was increased slightly due to friction between the upper column plates. This friction was not included in the simplified model, hence, the spring model underestimated the positive moment capacity. In this way, the spring model gave a conservative estimate of the M-θ behaviour, which was suitable for design purposes.

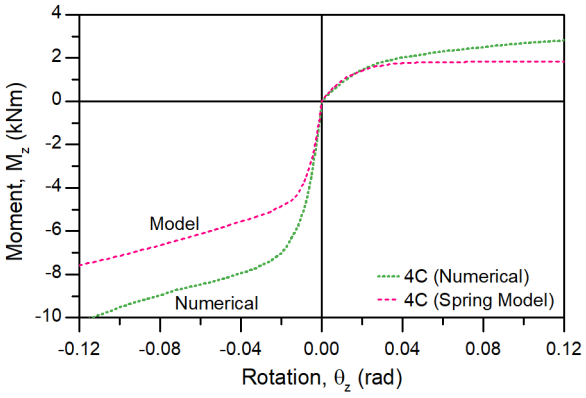

Figure 8.37. Numerical and spring model moment-rotation behaviour

8.9 Summary

Numerical simulations were carried out to investigate the shear, axial and moment-rotation behaviours of the interlocking (IL) inter-module connection (IMC). The simplified model developed previously for the experimental shear behaviour (Chapter 6) was reviewed, and numerical simulations were undertaken using ABAQUS to investigate the effect of the experimental loading and boundary conditions on the shear behaviour. Extended numerical models were developed for a more realistic IL connection with two bolts per column, and simplified empirical and analytical models were developed to predict the structural behaviours. Finally, a spring model which incorporated the structural behaviours was developed and evaluated. The main findings are summarised as follows.

1. The loading and boundary conditions in the previous experiments (Chapter 6) were different to those for a single connection in a modular building. The offset shear force in the experiments changed the contact pressure distribution and affected the friction resistance. Therefore, the shear behaviour of a single IL connection was investigated.

2. The structural behaviours of the single IL connection can be predicted by a spring model (Figure 8.34, p.236) which combines the vertical connection (VC) with the horizontal connection (HC). The HC shear and axial behaviours can be predicted based on the central tie plate geometry (Equation (8.60) to (8.62), p.237), whereas the structural behaviours of the VC can be predicted by simplified nonlinear models.

3. The VC shear behaviour can be represented by an exponential model (Equation (8.55), p.235). The addition of an axial force affects the shear behaviour by altering the slip resistance and shear yield capacity. The design gravity load can be adopted to establish the symmetric pure shear behaviour for design purposes. To account for the increase in the slip resistance due to contact between the upper columns, a compression only spring can be added to the spring model according to Equation (8.56) (p.236).

4. The VC axial behaviour can be predicted by a linear model for compression, and an exponential model for tension (Equation (8.58), p.237). The tensile yield force can be estimated by yield line analysis, while the initial stiffness can be estimated based on a cantilever beam model. The addition of a bending moment causes an initial y-displacement, and affects the tension stiffness due to a P-Δ effect, while the compression stiffness is relatively unaffected. Similarly, shear forces affect the tension behaviour, as a small moment is generated due to the initial plate separation.

5. The VC moment-rotation behaviour can be predicted by a two stage model (Equation (8.59), p.237). In the first stage, the behaviour is linear and depends on the applied axial load, and the compression stiffness of the plates. In the second stage, the behaviour is nonlinear and can be represented by an exponential function. The initial stiffness depends on the axial load and the bending direction, while the plastic moment can be estimated by yield line analysis.

6. In the future works the simplified models derived in this chapter will be applied in the overall numerical simulation of a case study building. In this way, the application of the proposed models will be demonstrated and evaluated for the typical load combinations. Following the numerical case study, the applicability of the simplified models may be verified and extended through further experimental studies on the shear (bearing/yield), axial and moment-rotation behaviours, and the response to combined actions. The application of the simplified models may also be extended by conducting further numerical simulations with different plate thicknesses, column sections, and bolt arrangements.

Chapter 9 Lateral behaviour of a modular steel building with simplified models of the new inter-module connections[1]

9.1 Introduction

In this chapter the simplified models for the structural behaviours of the new post-tensioned (PT) and interlocking (IL) inter-module connections (IMCs) are implemented in the overall numerical simulation of the case study building introduced in Chapter 3. In this way, the effect of the new simplified models on the overall building responses to wind and earthquake loads is examined. At the same time, the advantages and disadvantages of the innovative IMCs are determined by comparing the corresponding global building responses. Moreover, inter-storey drift ratio limits, which are not yet defined for modular steel buildings, are proposed from the perspective of the simplified IMC behaviours. To this end, this chapter reviews the numerical model of the case study building, and the geometry, and wind and earthquake actions. Then, the structural behaviours of the IMCs are reviewed, and the newly proposed simplified behaviours are outlined and compared. As the present chapter adopts full-scale connection geometries, discussion is provided on the application of the simplified models which were derived based on the half-scale connections. The associated IMC spring models are then discussed and related to the numerical model of the overall case study building. Finally, the numerical results are presented in two parts. The overall responses of the case study building incorporating different IMCs are presented first, followed by the structural responses of the IMCs.

9.2 Numerical model of the case study building

9.2.1 Geometry and gravity loads

To demonstrate the application of the simplified IMC behaviours derived in Chapter 7 and 8, a six-storey modular steel building was selected for further study. The selected apartment building was designed for a site located in Port Hedland, Western Australia. The building had modules stacked on each side of a central 2.5 m wide corridor. This corridor layout is common for modular buildings, and examples include a student residence in Bristol [8] and an apartment building in the Jinghai District of Tianjin Ziya circular economy park [170]. In Chapter 3, a numerical model of the building was built using the software SAP2000 [169].

[1] The related work in Chapter 9 is under review for publication in Engineering Structures:

Lacey AW, Chen W, Hao H, Bi K. Lateral behaviour of modular steel building with simplified models of new inter-module connections. (Under Review)

The numerical model used frame elements for the module structure and assumed rigid intra-module connections, while separate nonlinear links were included for the simplified behaviours of the vertical and horizontal IMCs. The modelling technique was verified in Chapter 3 by first modelling a different building and matching the overall building responses with those reported in a previous study [50], before extending the technique to the selected case study building. The present study adopts the same numerical model, which is referred to as the benchmark (BM).

Figure 9.1(a) shows the overall 30.3 x 26.29 x 21.15 m high benchmark numerical model and defines grid references for use in the following discussion. Grid lines 1 through 7 are parallel to the global Y-axis, and divide the structure along the X-axis. Similarly, grid lines A through D are parallel to the X-axis and divide the structure along the Y-axis. Figure 9.1(b) illustrates the structure of an individual ground level 4.95 x 11.885 x 2.95 m high, 26 t module. The numerical model included additional joint loads which allowed for the mass of the non-structural elements, and the bases of the main ground level columns (C1 in Figure 9.1) were restrained against translation. The corridor floor was made up of 150C24 joists which were placed 450 mm apart and spanned the 2.5 m width between the modules. The floor joists supported a 24 mm thick fibre cement sheet. This flooring was non-structural, hence, it was not included in the numerical model, although a load of 0.5 kPa was added to account for the self-weight (G). The roof was made up of 70x70x3 SHS stubs supporting C20a steel beams which in turn supported the purlins and roof cladding. The purlins and cladding were non-structural, and an additional 0.15 kPa was added for the self-weight. Uniformly distributed live loads (Q) were applied as area loads in the numerical model. The corresponding values were 0.25 kPa for the non-trafficable roof, 4.0 kPa for the corridor floors, 1.5 kPa for the general floor within the modules, and 2.0 kPa for the balcony portion of the module floor.

9.2.2 Wind actions

Equivalent static wind loads were calculated based on the Australian Standard [72]. The building was classified as importance level 3, and it was located within cyclonic region D and terrain category 2, indicating open terrain with well-scattered obstructions. The regional wind speeds were 93.5 and 53 m/s for the ultimate and serviceability limit states, respectively. Six levels were defined, i.e., z1 to z6 in Figure 9.1(a), and mean wind speeds were calculated using the Deaves and Harris model [173]. Equivalent joint loads were then assigned based on the tributary area. In Chapter 3, wind velocity time histories were simulated by combining the stationary mean with the fluctuating component, which was simulated using the method of Amirinia et al. [174]. The time varying joint loads were then calculated based on a nett drag coefficient of 1.3, and assigned in the numerical model based on the tributary area. These same

wind time histories were applied in this chapter, hence, a summary of the derivation is provided as follows. Three turbulence spectra were considered, namely the Kaimal et al. [175], Yu et al. [177] and Li et al. [178] spectra, which are referred to as Model A, B and C, respectively (Figure 3.19, p.67).

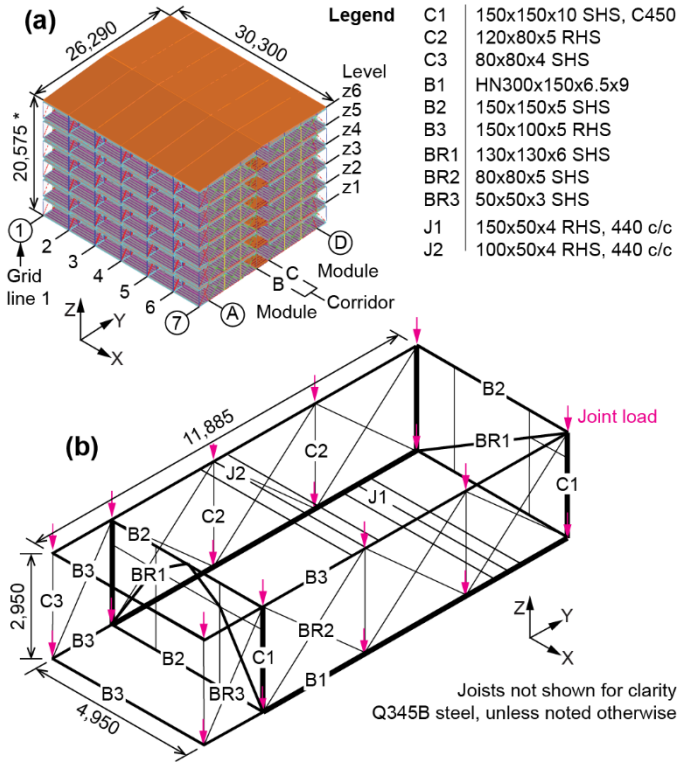

Figure 9.1. Case study building geometry showing (a) overall model and (b) structure of an individual module (adapted from Chapter 3)

All dimensions in mm. * The overall height is 20,575 and 21,150 mm at the lowest and highest points, respectively.

The Kaimal (A) power spectrum for the longitudinal wind velocity was based on neutral (non-cyclonic) conditions. In comparison, the Yu (B) spectrum was developed based on hurricanes at 10 m over land, and showed greater energy at lower frequencies. Finally, the Li (C) spectrum was related to the typhoon back eye-wall region and showed greater energy at higher frequencies. Hence, Models B and C represent two competing spectra for cyclonic conditions, while Model A represents non-cyclonic conditions for comparison. The height-wise spatial coherence of the fluctuating wind velocity was defined following the Davenport coherence function [228]. SAP2000 [169] was adopted for the nonlinear time history analyses. A constant modal damping of 3% was adopted in the analyses based on the existing empirical formula for steel buildings [82, 172] and the damping ratio estimated for a 2 x 2 stack of modules [98], as discussed in Chapter 3. In Section 9.4 (p.260) and Section 9.5 (p.264), the numerical results are presented for wind loading in the Y-direction (Figure 9.1a), which is the main interest as

the building adopts a corridor layout which is typically longer in the X-direction than in the Y-direction (Chapter 3).

9.2.3 Earthquake actions

The earthquake actions were calculated based on the Australian Standard [74]. First, a response spectrum analysis was conducted using the standard design spectrum [74] for a building with a probability factor (k_p) of 1.3 located in an area with a hazard factor (Z) of 0.12 and a sub-soil class of Ce. Then, time history analyses were carried out using ground motions which were simulated in Chapter 3. The spectral representation method was applied, in Chapter 3, to simulate acceleration time histories based on the design response spectrum [74]. Twenty horizontal acceleration time histories were simulated for the X- and Y-directions, and the same target design spectrum was adopted for each of the horizontal components. For example, Figure 3.15 (p.64) shows the simulated acceleration time histories, and Figure 3.16 (p.65) shows the response spectral acceleration for the first acceleration time history which matches the standard model [74]. The nonlinear time history analyses were carried out using SAP2000 [169]. For consistency with the design standard [74] and Chapter 3 (§3.3.4, p.60), a constant modal damping of 5% was adopted for the response spectrum and time history analyses. The numerical results are presented in Section 9.4 (p.260) to 9.6 (p.268) primarily for earthquake ground motions in the Y-direction, which was identified as generating the largest responses in Chapter 3. In Section 9.5.2.2 (p.266), however, numerical results for the X-direction are discussed in relation to the potential for contact between the modules in this direction.

9.3 Simplification of the inter-module connection (IMC) behaviour

In this section, the shear, axial and moment-rotation behaviours are estimated for three different IMCs, each of which includes associated horizontal connections (HCs) and vertical connections (VCs). First, there is the benchmark (BM), which refers to the IMC behaviours in Chapter 3. Next, there is the new post-tensioned (PT) IMC for which the structural behaviours are estimated based on the simplified models derived in Chapter 5 and Chapter 7 based on the half-scale connection. As this chapter adopts the full-scale connection, some of the previously derived equations are presented to facilitate discussion of the empirical parameters. Finally, there is the new interlocking (IL) IMC for which the structural behaviours are similarly estimated based on Chapter 6 and Chapter 8. The material properties for the PT and IL connections are summarised in Table 9.1, while the corresponding geometries are given in Section 9.3.2 (p.248) and 9.3.3 (p.251).

Table 9.1. Material properties

Description	Connection	Thickness / Diameter (mm)	Grade/Class	Min. yield stress (MPa)	Min. tensile strength (MPa)
Column	PT / IL	10	C450	450	500
Locating pin (round bar)	IL	24	300	300	440
Shear key	PT	12	350	360	450
Plate	PT / IL	25 / 12	350	350	450
Threaded rod	PT	36	8.8	660	830
Bolts	IL	24	8.8	660	830

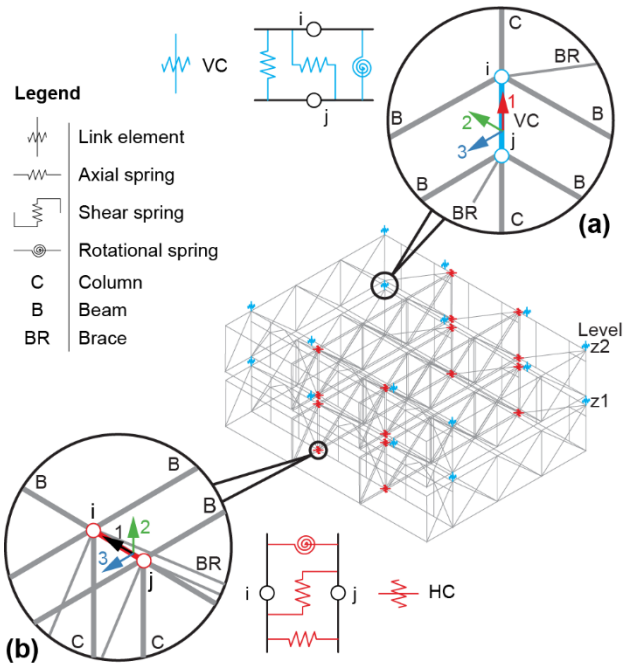

Figure 9.2. Inter-module connections in the benchmark model showing (a) vertical and (b) horizontal connection
Adapted from Figure 3.7 (p.55).

9.3.1 Previous benchmark (BM) case study

In the previous benchmark numerical model of the case study building (Chapter 3), the VCs and HCs were included as nonlinear links (Figure 9.2). The initial stiffness of the VCs was estimated assuming that the connection consisted of a 575 mm long 150x5 mm square hollow section (SHS) which was fixed at each end, i.e., the VCs were assumed to be rigid. While some of the VCs were located at the main columns (C1 in Figure 9.1b), other VCs were placed along the main beams (B2), and were offset from the centre of the columns. As the B2 beams were 150x5 mm sections, while the C1 columns were 150x10 mm sections, the smaller 5 mm thickness was adopted for the calculation of the initial stiffness. This simplified the numerical model by allowing the same stiffness to be adopted for all the VCs. For the HCs, which joined adjacent columns (C1), the initial stiffness was estimated based on the previous study by Styles

et al. [50], which adopted a similar connection detail. In this way, the benchmark stiffness properties were based on typical bolted connection details.

The resulting simplified bilinear translational behaviours are shown in Figure 9.3. In this figure, vc-u1, -u2, and -u3 refer to the translational behaviour of the vertical connection in the local 1-, 2-, and 3-directions as defined by the local axes shown in Figure 9.2(a). Similarly, hc-u1, -u2, and -u3 refer to the behaviour of the horizontal connection with respect to the local axes shown in Figure 9.2(b). In the same way, the trilinear rotational behaviours of the benchmark IMCs are shown in Figure 9.4, where r1, r2, and r3 denote rotation about the respective local axes.

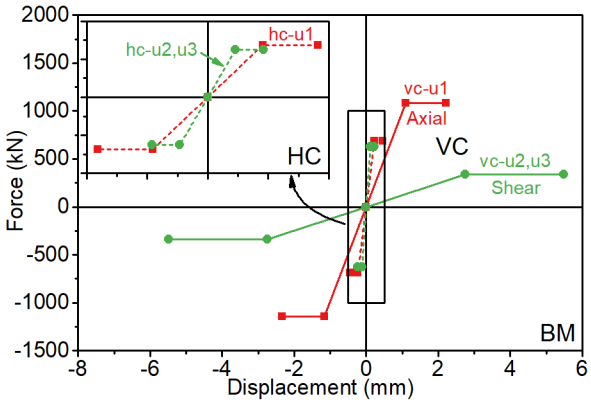

Figure 9.3. Translational behaviours of the benchmark (BM) horizontal (HC) and vertical (VC) connections
Adapted from Figure 3.10 (p 58).

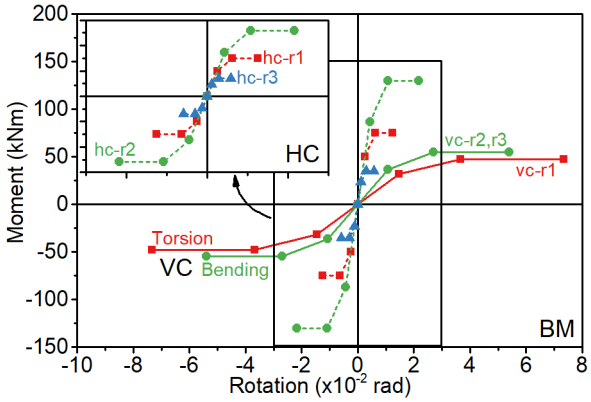

Figure 9.4. Rotational behaviours of the benchmark (BM) horizontal (HC) and vertical (VC) connections
Adapted from Figure 3.10 (p 58).

9.3.2 Post-tensioned (PT) inter-module connection

The VCs adopted in the benchmark numerical model were replaced with the post-tensioned IMC as shown in Figure 9.5, while the benchmark HCs were retained. To accommodate the new VC, the numerical model was adjusted as follows. First, the existing vertical links were removed and replaced with new links representing the PT connection. As the PT connection

must be positioned at the columns, new vertical links were created at each main column. Consequently, the total number of vertical links in the numerical model was increased, compared with the benchmark model. Comparing Figure 9.5(a) with Figure 9.2(a), it can be seen that the length of the new vertical links was reduced in comparison with the benchmark numerical model, and two short column lengths were added to account for the reduced length. For example, Figure 9.6 compares the simplified numerical models adopted for the benchmark (BM) and post-tensioned (PT) connections. The two additional column lengths can be seen in Figure 9.6(b).

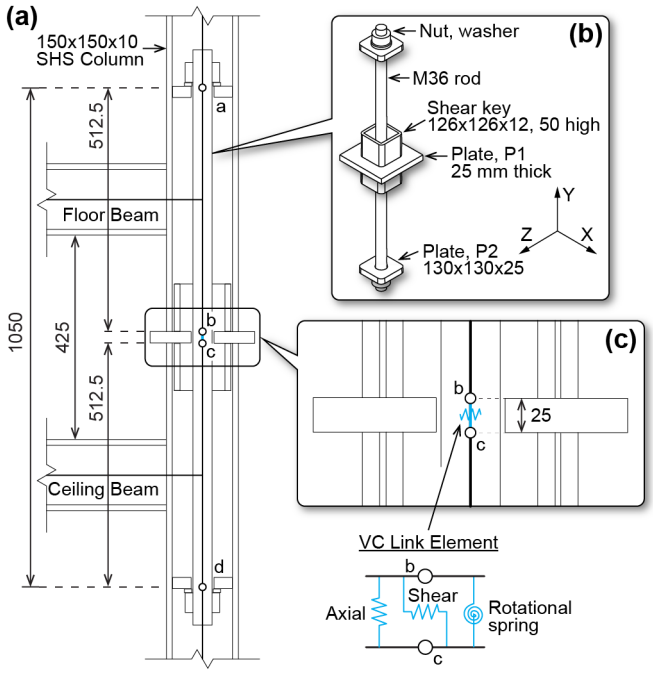

Figure 9.5. Post-tensioned inter-module connection: (a) XY plane section with superimposed link element *bc*, (b) illustration showing internal components, and (c) close-up showing link element and spring components

All dimensions in mm.

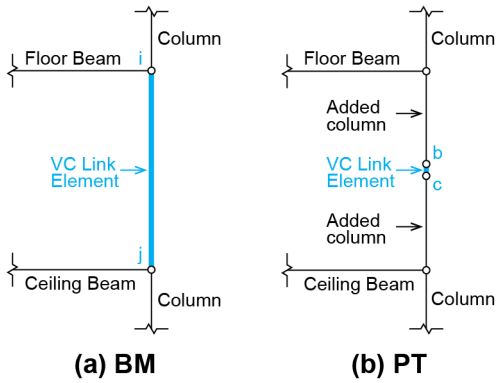

Figure 9.6. Comparison between simplified numerical model for (a) benchmark (BM) and (b) post-tensioned (PT) connections

9.3.2.1 Shear force-displacement behaviour

The estimated shear behaviours are shown in Figure 9.7 for a range of axial forces (N). The axial forces vary between 25 kN (tension) and -600 kN (compression) which reflects the range of axial forces to which the VCs were subjected in the following numerical simulations. The initial friction/slip behaviour was estimated based on Equation (7.1) (p.172) and the initial stiffness was estimated based on Equation (7.4) (p.173). The slip factor (μ_p) and elastic slip (γ_{crit}) were assumed to be constant regardless of the normal pressure, and the contact area, i.e., the cross-sectional area of the column, was assumed to have negligible effect (§7.4.2.1, p.172).

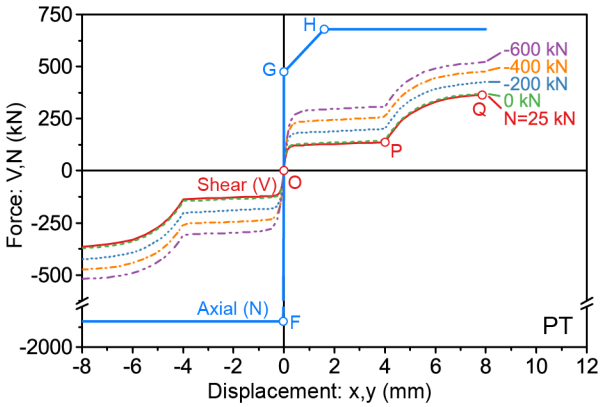

Figure 9.7. Translational behaviours of the post-tensioned (PT) vertical connection

For x larger than the effective tolerance (x_P=4 mm), the bearing/yield behaviour was estimated based on Equation (7.13) (p.176). In Chapter 7, the bearing stiffness ($K_{PQ,i}$) was associated with local deformation of the column flange and lateral deformation of the shear key, which could be idealised as a cantilever beam. In this chapter, compared to Chapter 7, the column was increased from a 75x6 SHS to a 150x10 SHS, and the shear key was increased from a 53x6 SHS to a 126x12 SHS. Consequently, in this chapter, $K_{PQ,i}$ was mainly associated with local bending of the column flange. While the thickness of the column flange (t_{col}) was increased from 6 to 10 mm, the span of the flange between the webs was also increased, such that $K_{PQ,i}$ was not significantly altered. However, in Chapter 7, local deformation of the lower column flange was suppressed in the numerical model. Therefore, in this chapter, $K_{PQ,i}$ was halved to allow for the deformation of both of the column flanges, i.e., $K_{PQ,i}$ = 221 kN/mm.

9.3.2.2 Axial force-displacement behaviour

Following Section 7.5.3 (p.182), the axial force-displacement behaviour (Figure 9.7) was estimated as

$$N(y)=\begin{cases} N_F, & y<y_F \\ K_{FG}y, & y_F \le y \le y_G \\ N_G+K_{GH}\left(y-y_G\right), & y_G<y\le y_H \\ N_H, & y>y_H \end{cases} \tag{9.63}$$

where y is the vertical displacement in the Y-direction (Figure 9.5), $N_F \le 0$ is the compression capacity, K_{FG} is the initial stiffness, $y_F = N_F K_{FG}^{-1}$, N_G is the tension force at which the column lifts from the central plate, $y_G = N_G K_{FG}^{-1}$, N_H is the tension capacity of the rod, $K_{GH} = k_{rod,eff}$ is the rod stiffness allowing for deformation of the P2 plates, and $y_H = y_G + \left(N_H - N_G\right)K_{GH}^{-1}$. K_{FG} was estimated based on the axial stiffness of the central plate as

$$K_{FG} = \frac{E_s A_{col}\left(t_{col} + 0.5t_p \tan\alpha\right)}{t_{col}t_p} \tag{9.64}$$

where E_s is the elastic modulus (200 GPa), A_{col} is the column cross-sectional area, t_{col} is the column thickness, t_p is the plate thickness (25 mm), and α is the half-apex angle for pressure distribution through the plate (30° [226]).

The shear force (V^*) has negligible effect on the axial behaviour provided that the tension force (N) is limited to the value given by Equation (7.32) (p.185). Similarly, bending moments (M^*) have negligible effect, provided that the tension force is limited to the value given by Equation (7.31) (p.185). In Section 9.5.1 (p.264) it will be confirmed that the tension force does not exceed the appropriate limits.

9.3.2.3 Moment-rotation behaviour

The moment-rotation behaviour (Figure 9.8) was estimated using the simplified analytical two stage model derived in Chapter 7. Following Section 7.6.3 (p.193), in the first stage, the behaviour was estimated as

$$M(\theta) = K_{OT}\theta, \quad 0 \le \theta \le \theta_T \tag{9.65}$$

where θ is the rotation about the Z-axis (Figure 9.5), $K_{OT} = \frac{2E_s I_{col}}{L_{ab}}$, I_{col} is the area moment of inertia, L_{ab} is the length between *a* and *b* in Figure 9.5(a), $\theta_T = \frac{M_T}{K_{OT}}$, $M_T = \frac{F_{clamp}Z_{col}}{A_{col}}$, and Z_{col} is the elastic section modulus. In the second stage, the nonlinear M-θ behaviour was estimated by applying the *Monolithic Beam Analogy* as described in Section 7.6.3 (p.193).

9.3.3 Interlocking (IL) inter-module connection

The IMCs adopted in the benchmark numerical model were replaced with the interlocking (IL) connection shown in Figure 9.9 and Figure 9.10. The vertical and the horizontal links were

replaced, as the IL connection provides vertical and horizontal connectivity. Like the PT connection, the VCs were positioned at every main column (C1 in Figure 9.1b, p.245). Therefore, the total number of vertical links in the numerical model was increased, compared with the benchmark model, although the total number was the same as in the model with the PT connections. In addition, the total number of horizontal links was reduced, compared with the benchmark model. In the benchmark numerical model four horizontal links were provided for each module, i.e., at the points where B2 intersects C1 in Figure 9.1. With the IL connections, however, one horizontal link was provided per IL connection as shown in Figure 9.9(b).

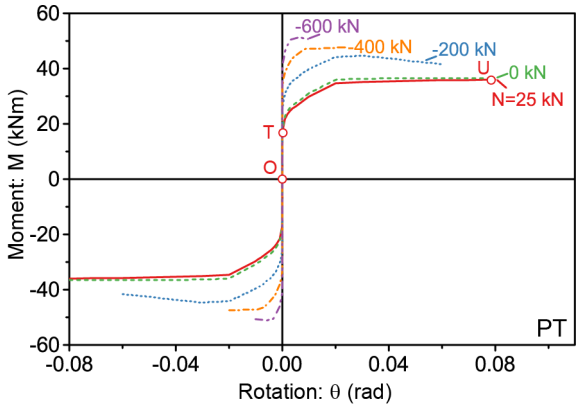

Figure 9.8. Rotational behaviours of the post-tensioned (PT) vertical connection

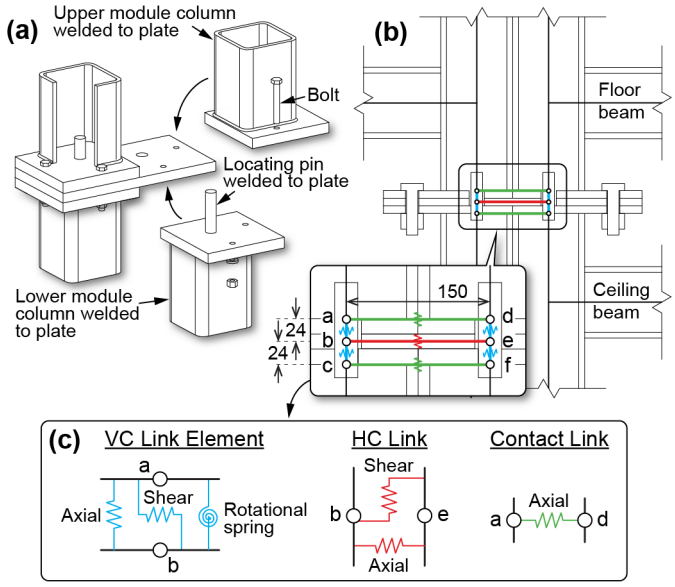

Figure 9.9. Interlocking inter-module connection: (a) illustration showing connection geometry, (b) XY plane section with superimposed link elements, and (c) component springs

Adapted from Figure 8.2 (p.203), Figure 8.4 (p.204), and Figure 8.34 (p.236).

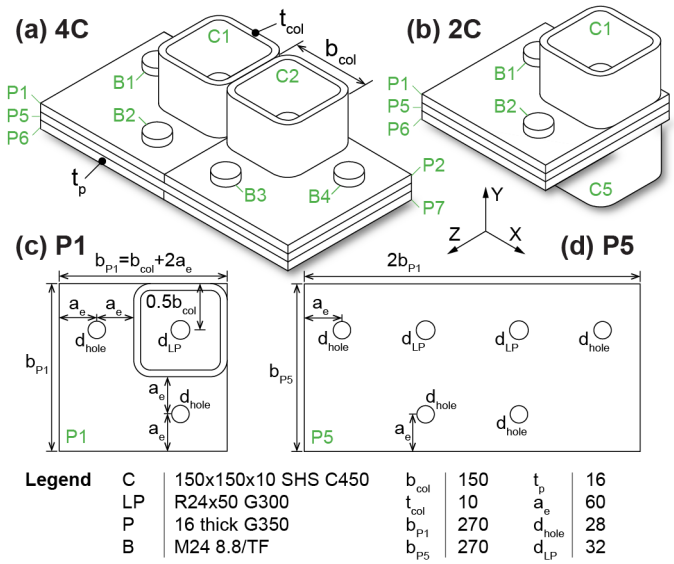

Figure 9.10. Key dimensions for the interlocking inter-module connection: (a) internal connection with four columns (4C), (b) end connection with two columns (2C), (c) plate P1, and (d) plate P5

Adapted from Figure 8.9 (p.208).

9.3.3.1 Horizontal connection (HC)

Following Section 8.8.2 (p.237), the translational shear and axial stiffness of the horizontal connection was calculated based on the geometry of the central plate P5 shown in Figure 9.10. That is, the axial behaviour was determined based on Equation (8.60), while the horizontal and vertical shear behaviours were evaluated based on Equation (8.61) and (8.62), respectively. The resulting behaviours are illustrated in Figure 9.11.

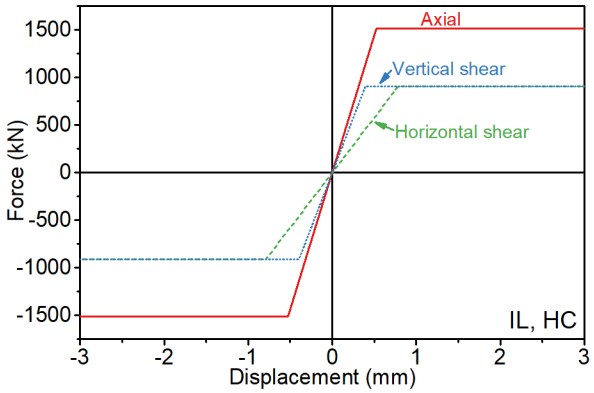

Figure 9.11. Translational behaviours of the interlocking (IL) horizontal connection (HC)

9.3.3.2 Vertical connection (VC) – Shear force-displacement behaviour

The shear behaviour (Figure 9.12) associated with the VC, e.g., *ab* in Figure 9.9(b), was estimated based on Equation (8.55) (p.235) and the initial friction/slip stiffness ($K_{V,i}$) was calculated using Equation (8.5) (p.214). In Chapter 8, the stiffness at the start of the bearing

stage ($K_{V,b}$) was associated with bending of the bolt and locating pin which could be idealised as a fixed-guided beam and a cantilever beam, respectively. Compared with Chapter 8, the diameter of the bolt and the locating pin were increased by a factor of 2. Similarly, the plate thickness, which determined the span of the model beam, was increased by a factor of 2. Therefore, based on the bending stiffness models, the stiffness in this chapter was increased by a factor of 2, i.e., $\frac{I_{new}}{I_{old}}\frac{L_{old}^3}{L_{new}^3}=2$. Hence, a constant value of 208 kN/mm was adopted for $K_{V,b}$.

A contact link was included in the spring model, e.g., *ad* in Figure 9.9(b), and the axial behaviour was estimated based on Equation (8.57) (p.236). The gap due to the assembly tolerance was initially set as zero and the contact stiffness was estimated using Equation (8.56).

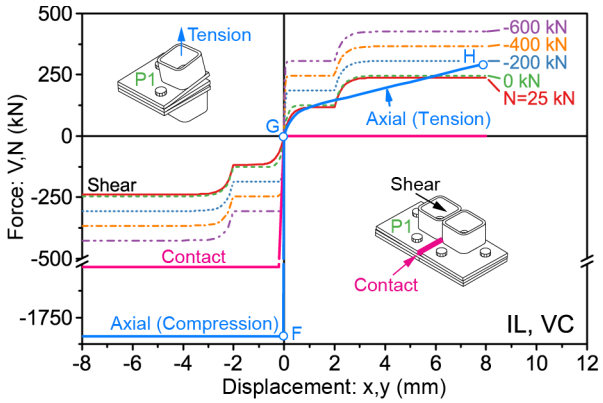

Figure 9.12. Translational behaviours of the interlocking (IL) vertical connection (VC)

9.3.3.3 Vertical connection (VC) – Axial force-displacement behaviour

The axial behaviour (Figure 9.12) associated with the VC, e.g., *ab* in Figure 9.9(b), was estimated based on Equation (8.58) (p.237) and the compression stiffness was estimated using Equation (8.18) (p.222). For the tension behaviour, following Section 8.6.3.2 (p.223), the tension yield force (N_p) was calculated by yield line analysis, the initial tension stiffness ($K_{N,i}$) was calculated based on the cantilever beam analogy, and the hardening stiffness ($K_{N,p}$) was estimated as 7% of $K_{N,i}$. In Section 9.5.2.1 (p.265) it will be confirmed that the axial force is limited to small tension forces, thereby ensuring that bending moments and shear forces have negligible effect on the axial behaviour.

9.3.3.4 Vertical connection (VC) – Moment-rotation behaviour

The moment-rotation behaviour (Figure 9.13) associated with the VC, e.g., *ab* in Figure 9.9 (c), was estimated based on Equation (8.59) (p.237). The M-θ stiffness before the column lifts (K_{TR}) was estimated using Equation (8.41) (p.231) and the moment at which the column lifts (M_R) was calculated from Equation (8.39) (p.231). The plastic moment capacities, i.e., M_{p+} and M_{p-}, were calculated by yield line analysis following Section 8.7.3.2 (p.232). The positive

and negative stiffnesses, i.e., K_{i+} and K_{i-}, were estimated empirically by fitting a curve to the numerical results from Chapter 8, and, for negative bending, the hardening stiffness was estimated as 2.4% of K_{i-}.

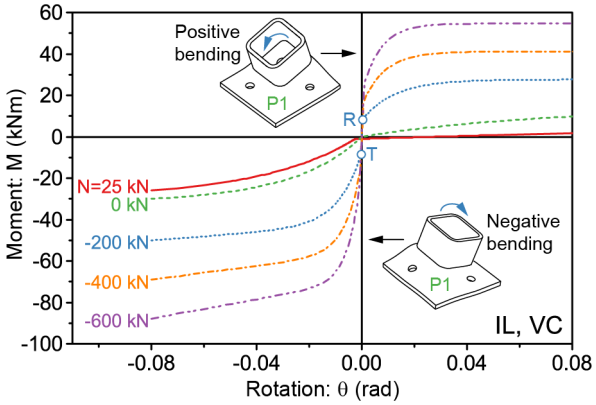

Figure 9.13. Rotational behaviours of the interlocking (IL) vertical connection (VC)

9.3.4 Comparison of inter-module connection behaviours

In this section, the structural behaviours of the PT and IL connections are compared. The purpose of this comparison is, firstly, to allow direct comparison of the structural behaviours of the PT and IL connections, which will inform the discussion of the global building responses in Section 9.4. In Section 9.3.3, the interlocking VC was divided into two links, e.g., *ab* and *bc* in Figure 9.9(b), and the structural behaviours were derived for just one of the links. In this section, the behaviours of the complete interlocking VC are estimated by combining the two VC links in series. In this way, the behaviours of the interlocking and post-tensioned VCs can be compared directly. The second purpose of this comparison is to explain how the connection geometries and key parameters, such as the bolt preload, were defined to ensure a fair comparison between the PT and IL connections.

9.3.4.1 Shear force-displacement behaviour

In the previous experiments on the PT connection (Chapter 5), the combination of the cut surface of the column with the clean mill scale plate surface resulted in a slip factor of 0.5. In comparison, in the previous experiments on the IL connection (Chapter 6), the faying surface was made up of two clean mill scale surfaces, which resulted in a slip factor of 0.31. As the slip factor for both connections can be controlled by varying the surface finish, a fair comparison was achieved in the present chapter by adopting a single slip factor of 0.3. Similarly, for each connection, the effective tolerance was set as 4 mm, the initial preload was set as 420 kN, and the slip resistance was calculated as $V_{slip} = C_{slip}\mu_p F_{clamp}$ where μ_p is the slip factor, F_{clamp} is the clamp force, and C_{slip}=1 is an empirical coefficient. For the PT connection, a small positive hardening stiffness was included in the friction/slip stage (§7.4.2.1, p.172),

whereas, for the IL connection, there was no hardening stiffness (§8.5.2.1, p.213) as shown in Figure 9.14.

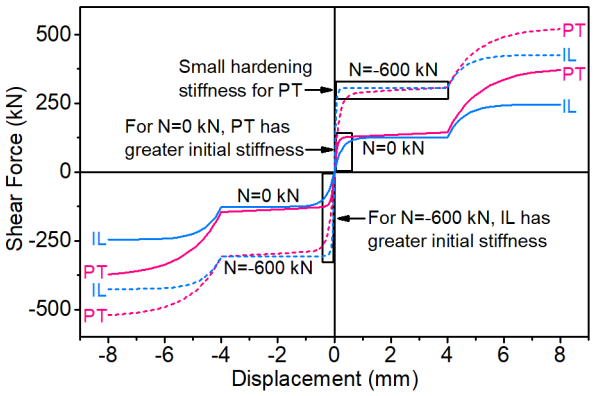

Figure 9.14. Shear behaviours of the post-tensioned (PT) and interlocking (IL) vertical connections

With no axial load (N=0 kN), the PT connection had greater initial shear stiffness than the IL connection, which matched the previous experiments (Chapter 5 and Chapter 6). When an axial compression force was applied (N=-600 kN), however, the IL connection had greater initial stiffness than the PT connection. In the PT connection, when a compression force is applied to the column, axial shortening of the column reduces the rod preload, and only part of the compression force affects the clamping force (§7.5.3.1, p.182). As the stiffness depends on the clamp force, the effect of the compression force on the initial stiffness is reduced. For the IL connection, the full compression force affects the initial shear stiffness (§8.5.2.1, p.213). As the bolt group is offset from the column, the initial preload causes the plates under the column to separate. The shear force applied to the column must then be transferred across to the bolts, and the resulting axial elongation of the plates reduces the shear stiffness. When a compression force is applied to the column, the plates under the column are pushed back together, which increases the shear stiffness. Hence, the full compression force affects the initial stiffness for the IL connection.

For the PT connection, the shear yield capacity was determined by shear yield of the column flange (§7.4.2.2, p.174). The column was relatively thick (10 mm), hence, the shear yield capacity was relatively large. The bearing stiffness (221 kN/mm) was associated with local deformation of the column flanges and was not affected by the axial load. For the IL connection, the shear yield capacity was determined by shear yield of a bolt and locating pin, which resulted in a smaller capacity than for the PT connection (§8.5.2.2, p.216). For the bearing stiffness, however, the value for the IL connection (208 kN/mm) was similar to that for the PT connection.

9.3.4.2 Axial force-displacement behaviour

For the PT connection, the half-apex angle for the pressure distribution through the central plate was 30° (§9.3.2.2, Eq. (9.64)), whereas, for the IL connection, the angle was only 21° due to slipping at the plate interfaces (§8.6.3.1, p.222). In addition, in the IL connection, the pressure distribution through the plates was constrained on two sides, while for the PT connection, the distribution was unconstrained. Furthermore, the length of the PT connection (25 mm, Figure 9.5) was smaller than the IL connection (48 mm, Figure 9.9). Therefore, the axial compression stiffness was larger for the PT connection than the IL connection (Figure 9.15). Comparing the tension behaviours, for the PT connection, the initial stiffness was high (72,000 kN/mm) due to the initial preload. After the column separated from the central plate at G (Figure 9.15), the stiffness (130 kN/mm) was associated with the axial stiffness of the rod, until the rod yielded at H. In contrast, for the IL connection, the initial tension stiffness was low (180 kN/mm), due to bending of the plates. The tension yield force was 95 kN, after which the stiffness reduced to the hardening stiffness of 13 kN/mm.

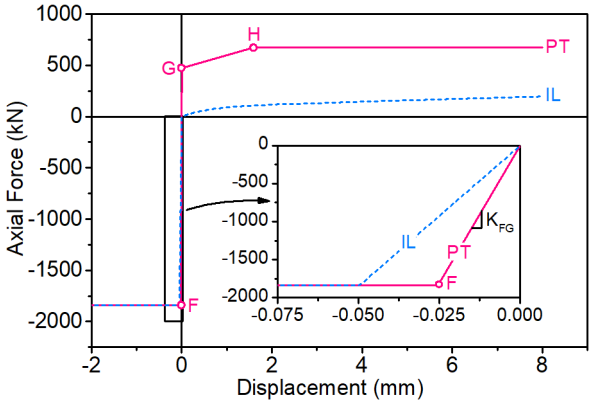

Figure 9.15. Axial behaviours of the post-tensioned (PT) and interlocking (IL) vertical connections

Positive axial force indicates tension.

The initial tension stiffness of the IL connection could have been increased by increasing the plate thicknesses. However, it was considered that the low tension stiffness was a feature of the IL connection. Moreover, if the plate thickness was increased for the IL connection, the axial compression stiffness would also have been affected. Although increasing the plate thickness would have reduced the compression stiffness in Figure 9.15, it would ultimately increase the overall compression stiffness in the numerical model. In the overall numerical model, the vertical IMC was modelled by a short length depending on the plate thicknesses, while the remaining length was modelled by two elements representing the column section properties (Figure 9.9). The axial stiffness for the IMC was greater than that for the column, due to the increased effective width resulting from the pressure distribution through the

thickness of the plates. As the IMCs were not subjected to large tension forces (§9.5, p.264), the compression behaviour was more important than the tension behaviour, and the plate thickness for the IL connection was retained as 16 mm. The larger overall compression stiffness was considered to be a feature of the IL connection, due to the presence of three plates, as compared with one plate for the PT connection.

9.3.4.3 Moment-rotation behaviour

For the PT connection, the initial moment-rotation (M-θ) stiffness was relatively high (Figure 9.16), due to the initial rod preload, and the plastic moment capacity was relatively large. Moreover, due to the connection symmetry, the M-θ behaviour was the same for positive and negative bending. In comparison, the IL connection had a low M-θ stiffness as the bolts were offset from the column resulting in bending of the plates, and the behaviour was asymmetric for positive and negative bending (§8.7.3.2, p.232). However, although the plastic moment capacity in the absence of an axial force was small, when a substantial compression force was applied, e.g., N=-600 kN, the plastic moment capacity was greater than that for the PT connection. For a small tension force, e.g., 25 kN, the stiffness and moment capacity were reduced, particularly for positive bending.

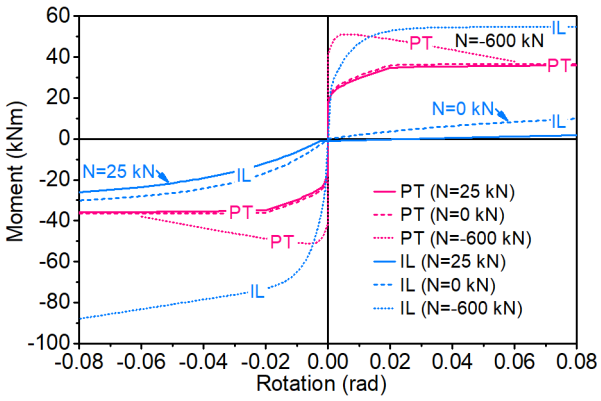

Figure 9.16. Rotational behaviours of the post-tensioned (PT) and interlocking (IL) vertical connections

The moment capacity and stiffness of the IL connection could have been improved by increasing the plate thickness, however, the low moment capacity and stiffness were features of the IL connection. Moreover, due to the relatively low M-θ stiffness, it was expected that, when incorporated in the overall numerical model, the connection would not attract bending moments approaching the plastic moment capacity, thereby justifying use of the symmetric pure shear behaviour (§8.5.1.3, p.212). Therefore, the plate thickness was retained as 16 mm, which was double that in Chapter 6 and Chapter 8. Similarly, the moment capacity and stiffness of the PT connection could have been reduced by decreasing the size of the rod.

However, the relatively high moment capacity and stiffness were considered to be features of the PT connection. Therefore, the M36 rod was retained based on Chapter 5 and Chapter 7 which adopted an M20 rod. From the available rod sizes of M36 and M42, an M36 rod was adopted as it most closely suited the 420 kN preload required to match the IL connection. That is, two M24 bolts were adopted for the IL connection as two M12 bolts were used in the previous half-scale studies (Chapter 6 and Chapter 8). The M24 bolts required a minimum bolt tension of 210 kN [139]. To match the shear slip resistance, the same total preload was required for the PT connection, i.e., 420 kN. Therefore, the M36 rod was adopted as the standard bolt preload (490 kN [139]) was closer to the intended preload of 420 kN, than for the M42 rod.

9.3.5 Implementing the inter-module connection spring models

The design gravity loads were calculated from the SAP2000 numerical model with VCs provided at each main column (C1 in Figure 9.1, p.245). In the case of wind loading, the axial forces associated with the self-weight (G) were combined with those due to the ultimate limit state wind load (Wu) as 0.9G+Wu. The axial forces due to the wind load were estimated based on the equivalent static load according to the Australian standard [72]. Similarly, for the earthquake loading, the axial forces resulting from the self-weight (G), live load (Q) and the ultimate earthquake (Eu) were combined as G+0.3Q+Eu. The axial forces due to the earthquake were estimated from the response spectrum analysis according to the Australian standard [74]. In this way, the calculated axial forces were an estimate of the maximum value (tension positive) to which each IMC may be subjected during the following time history analyses. The maximum value was adopted as it was associated, for example, with the smallest shear slip resistance, thereby ensuring a conservative estimate of the overall lateral response of the building.

For the IL connection, the local axes assigned to the VCs were varied to account for different orientations of the connection. For example, Figure 9.17(a) shows part of the building demonstrating subdivision of the grid lines parallel with the Y-axis, i.e., 2a and 2b, and Figure 9.17(b) shows the asymmetric IL connection geometry for grid reference A2. Figure 9.17(c) and (d) then show the local axes for grid references A2 and B2, respectively, highlighting the four VC orientations, i.e., VC-1 through VC-4. In Section 9.3.3.4 (p.254) the M-θ behaviours were estimated for rotation about the 2-axis in VC-1 (Figure 9.17c). The positive moment capacity for rotation about the 2-axis was less than the negative moment capacity due to the asymmetry of the connection. For rotation about the 3-axis, the behaviour was reversed, and the positive moment capacity was greater than the negative moment capacity. For the PT connections, the local axes were assigned consistently throughout the numerical model, as the structural behaviours of the VCs were symmetric.

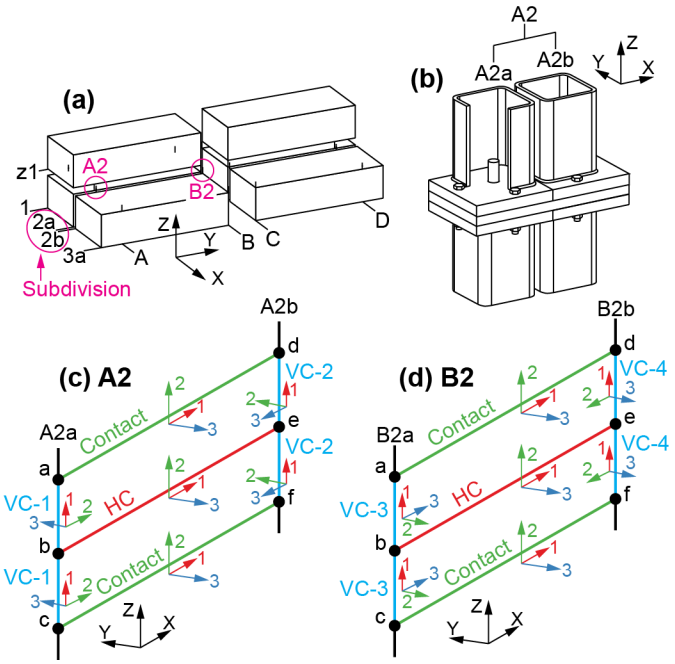

Figure 9.17. (a) Subdivision of grid lines parallel with the Y-axis, (b) asymmetric IL connection at grid reference A2, (c) local axes for IL connection at A2, and (d) local axes for IL connection at B2

9.4 Overall structural response of case study building

9.4.1 Response to wind

The PT and IL connections reduced the drifts and inter-storey drift ratios (IDRs) due to the wind loads in comparison with the building with the benchmark (BM) connections. Figure 9.18 shows the maximum drift for the case study building subjected to the ultimate wind load in the Y-direction. It can be seen, for example, that the maximum drifts associated with the Li et al. [178] turbulence spectrum were 34.9, 19.7 and 20.2 mm for the building with the BM, PT and IL connections, respectively. The main reason for the reduced drift was the larger number of VCs when using the PT and IL connections, compared with the BM connections (refer §9.3.2 & 9.3.3, p.248). The drifts for the building with the PT connection were slightly smaller than those for the building with the IL connection. The shear stiffness of the IL connection was slightly greater than that for the PT connection when the coincident axial compression force was large (Figure 9.14, p.256). However, when the compression force was small, such as at the top of the building, the shear stiffness of the IL connection was more substantially less than that for the PT connection, which resulted in slightly greater drifts at the top of the building with the IL connections.

The Li et al. [178] spectrum was associated with the largest responses as the peak of the normalised power spectral density (Figure 3.13) was closest to the normalised fundamental frequency of the building causing the largest resonant response. The normalised fundamental

frequencies, which were calculated by multiplying by the height and dividing by the mean wind velocity as in Figure 3.13, were 0.460, 0.612 and 0.608 for the building with the BM, PT and IL connections, respectively. Hence, the largest response was associated with the Li et al. [178] spectrum which had its peak at a normalised frequency of 0.0431. For the PT and IL connections which increased the stiffness of the building and, hence, increased the fundamental frequency, the resonant response associated with the Li et al. [178] spectrum was reduced compared with the benchmark analysis. As in Chapter 3, the aerodynamic admittance function was omitted to allow comparison of the resonant responses associated with the three turbulence spectra. The resonant response may be reduced if the aerodynamic admittance function is included.

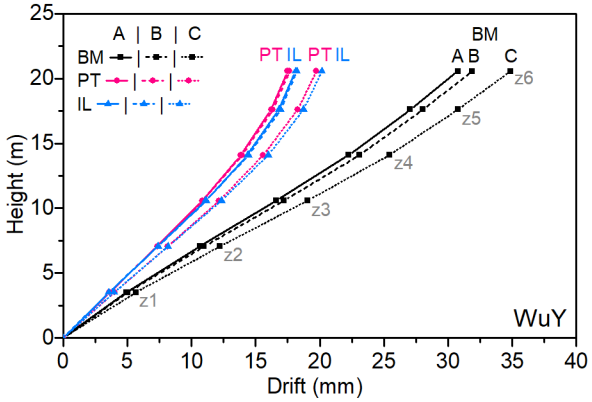

Figure 9.18. Overall drift due to the ultimate wind load in the Y-direction
A, B and C refer to the time histories simulated based on the Kaimal et al. [175], Yu et al. [177], and Li et al. [178] spectra, respectively.

Figure 9.19 shows the maximum IDRs for the case study building subjected to the ultimate wind load in the Y-direction. The PT connection was associated with a slightly larger IDR than the IL connection at the first level, i.e., 0.113 compared with 0.112%. At the second level, however, the IL connection was associated with the larger IDR, i.e., 0.118 and 0.120% for the PT and IL connection, respectively. In the case of a large axial compression force, the IL connection had a greater initial shear stiffness than the PT connection, hence, the IL connection was associated with the smaller IDR at the first level. As the axial load was reduced, the PT connection had greater initial shear stiffness, hence, the PT connection was associated with the smaller IDR at the second level.

The more accurate structural behaviours of the PT and IL connection, as compared with the benchmark analysis, resulted in a different height-wise variation of the IDR. For example, in the benchmark analysis, the predicted maximum IDRs showed a deviation in the profile at the top of the structure, which was attributed to the different storey height in Chapter 3. In the present chapter, however, with the more accurate models for the structural behaviours of the

PT and IL connections, the profile deviation was not observed, and the smallest IDR was recorded at the top of the structure. In addition, the more accurate IMC behaviours resulted in the maximum IDR occurring at the second level, rather than the third level, as in Chapter 3.

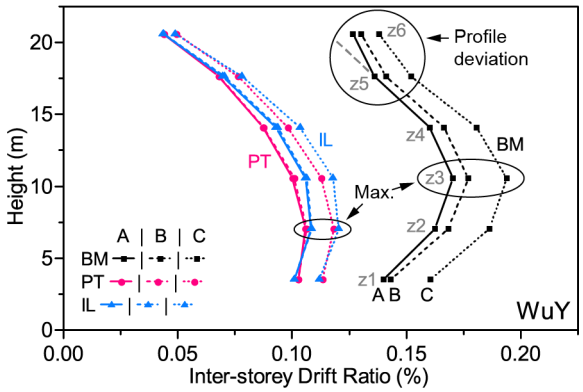

Figure 9.19. Maximum inter-storey drift ratios due to the ultimate wind load in the Y-direction

A, B and C refer to the time histories simulated based on the Kaimal et al. [175], Yu et al. [177], and Li et al. [178] spectra, respectively.

9.4.2 Response to earthquake

Figure 9.20 shows the maximum inter-storey drift ratios (IDRs) for the case study building subjected to the ultimate earthquake in the Y-direction. For each connection type, i.e., BM, PT, and IL, IDRs in the Y-direction are presented for the twenty acceleration time histories (TH), the mean time history (Mean TH) and the response spectrum analysis (RSA). In the benchmark (BM) analysis the maximum IDR for the mean time history was 0.265% at the third level. This was closely matched by the response spectrum analysis which resulted in a maximum value of 0.262%, although it occurred at the second level. With the more accurate models for the structural behaviours of the PT and IL connections, the height-wise variation of the drift ratio was different to that resulting from the benchmark analysis. For the building with the PT connections, the maximum IDR for the mean time history was 0.224% at the second level, while the response spectrum analysis gave a maximum of 0.220%, also at the second level. Similarly, for the building with the IL connections, the maximum IDR for the mean time history was 0.247% at the second level, while the response spectrum analysis gave 0.235 % at the second level. Overall, the PT and IL connections reduced the IDRs, compared with the benchmark analysis, except for the mean time history result for the IL connection at the first level. Similar to the wind loading, the result for earthquake loading showed a larger maximum IDR for the building with the IL connections (0.247%), as compared with the PT connections (0.224%).

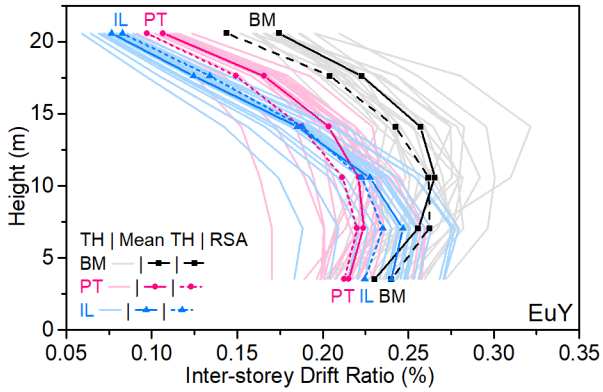

Figure 9.20. Maximum inter-storey drift ratios for the ultimate earthquake in the Y-direction

In Chapter 3, it was reported that the standard formula for the natural period, i.e.,

$$T_1 = 1.25 k_t H^{0.75}, \tag{9.66}$$

where k_t = 0.05 and H is the height to the uppermost seismic mass, could underestimate the period for braced modular steel buildings taller than 17 m. For example, in Chapter 3, the fundamental period was estimated as 0.6164 s using Eq. (9.66), and 0.7121 s by eigenvector analysis of the numerical model including the building self-weight and 30% of the imposed actions. As a result, the standard horizontal equivalent static base shear force [74] was estimated as 2,582 kN, whereas the more accurate response spectrum analysis resulted in a base shear force of 2,241 kN. Hence, the equivalent static analysis overestimated the base shear force by 15%, which was mainly due to the underestimated fundamental period. Using the correct period of 0.7121 s, for example, the horizontal equivalent static base shear force was estimated as 2,235 kN, which closely matched the response spectrum value of 2,241 kN.

In this chapter, eigenvector analysis of the numerical models, which included the more accurate inter-module connection models, yielded periods of 0.569 and 0.576 s for the building with the PT and IL connections, respectively. The estimated period of 0.6164 s (Eq. (9.66)) was more accurate, as the PT and IL connections increased the building stiffness and reduced the fundamental period, compared with the benchmark analysis. As the fundamental period was now overestimated, the standard horizontal equivalent static base shear force of 2,582 kN underestimated the response spectrum value of 2,670 kN. The equivalent static base shear force was underestimated by 3% and, hence, was more accurate than in the benchmark analysis. The PT and IL connections increased the building stiffness and increased the base shear force, thereby reducing the fundamental period and improving the accuracy of the standard [74] horizontal equivalent static base shear force.

9.5 Structural response of inter-module connections

The actions in the IMCs, i.e., shear force, axial force, and bending moment, were examined for the time history results in the Y-direction. For the wind loading, the time history results adopted were based on the Li et al. [178] turbulence spectrum. As shown in Section 9.4 (p.260), the Li et al. [178] spectrum was associated with the largest building responses, e.g., drift and inter-storey drift, as the spectrum peak (Figure 3.13, p.63) was closest to the fundamental frequency of the building, resulting in the largest resonant response. For use in the following discussion, Figure 9.1(a) (§9.2.1, p.243) shows grid references defined for the overall building, and Figure 9.17(a) (§9.3.5, p.259) illustrates subdivision of the grid lines parallel with the global Y-axis, i.e., 2a, and 2b.

9.5.1 Post-tensioned (PT) connection

The vertical connections (VCs) were subjected to the largest shear forces at the end of the building model, i.e., grid line 1 in Figure 9.1(a) (p.245). The shear force was the greatest at the bottom of the building, and it reduced moving up the height of the building. As the largest shear force occurred at the bottom of the building, it was associated with the VC with the largest axial compression force and, hence, the largest slip resistance. The VC with the largest shear force due to the wind load, i.e., PT-WuY in Figure 9.21, did not slip as the shear force was below the slip resistance. The largest shear force due to the ultimate earthquake loading (PT-EuY) was approaching the slip resistance, such that a small increase in the lateral load may have resulted in shear slip of the connection. Nevertheless, the IMCs did not slip in shear, demonstrating that shear slip of the IMCs can be avoided through the use of slip resistant connections, which have slip resistance greater than the largest shear force associated with the design wind and earthquake actions. As will be shown in Section 9.6 (p.268), however, the IMCs could slip if the lateral load exceeds the design value.

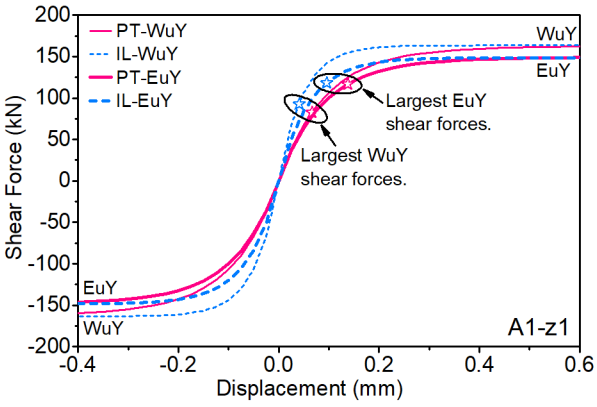

Figure 9.21. Shear behaviours of the vertical connections subjected to the ultimate wind and earthquake load in the Y-direction

The earthquake time history analyses resulted in the largest bending moments (Figure 9.22). The applied moments were less than the moment at which the column edge starts to lift, hence, the resulting rotations were small. Similarly, the earthquake time history analyses resulted in the largest axial compression force of -1,094 kN, and the largest axial tension force of 13 kN for the load combination G+EuY+0.3Q. These axial forces were well within the capacity of the PT connection which was -1,840 kN in compression and 678 kN in tension. As indicated in §9.3.2.2, the axial behaviour of the PT connection is unaffected by shear forces provided that the axial tension is limited to a small value. Following Equation (7.32) (p.185), for an applied shear force of 102 kN (B1-z1), a slip factor of 0.3, and an initial preload of 420 kN, the tension force limit can be estimated as 91 kN. Similarly, as per Equation (7.31) (p.185), the tension force limit to demonstrate bending moments having negligible effect can be estimated as 175 kN. As the largest tension force was only 13 kN, it can be concluded that shear forces and bending moments had negligible effect on the axial behaviour of the PT connection.

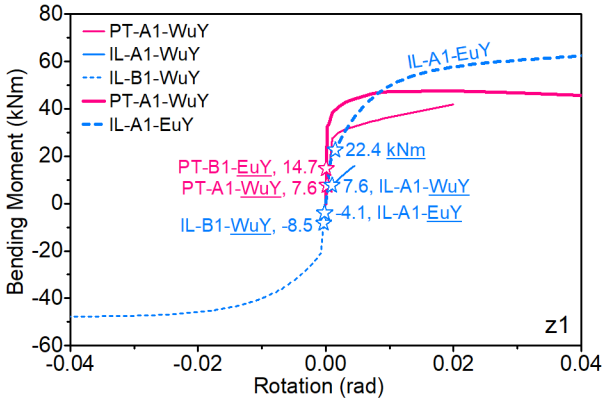

Figure 9.22. Rotational behaviours of the vertical connections subjected to the ultimate wind and earthquake load in the Y-direction

9.5.2 Interlocking (IL) connection

9.5.2.1 Vertical connection (VC)

The largest shear force in the interlocking VCs was due to the earthquake loading (Figure 9.21). Although the connections did not slip in shear, the shear force was approaching the slip resistance, and the connection may have slipped if the lateral load was slightly larger. The maximum shear forces were slightly larger for the IL connection, compared with the PT connection. For example, the maximum values due to wind loading were 86 kN and 92 kN for the PT and IL connections, respectively. For the earthquake loading, the maximum values were 116 kN and 118 kN for the PT and IL connections, respectively. The IL connection was associated with the larger shear force as it had the larger initial shear stiffness at the bottom of the building where the axial forces were greatest (§9.3.4.1, p.255). For the axial load, the VCs

were only subjected to small tension forces whereas the largest compression force was -1,036 kN which occurred at A1-z1 due to the earthquake loading. The compression force was less than the capacity of the VC which was -1,840 kN. As the axial forces were mainly limited to compression, with only small tension forces in some cases, the axial behaviour was unaffected by the addition of bending moments and shear forces (§9.3.3.3, p.254).

For wind loading, the largest negative moment was less than the moment which would cause the connection plates to separate, whereas the largest positive moment was close to the separating moment (Figure 9.22). As a result, the corresponding rotations were small, i.e., -0.00031 and 0.0010 rad, respectively. For the earthquake loading, the largest positive moment resulted in a slightly larger rotation, i.e., 0.0015 rad. In Chapter 8, when the applied moment reached the plastic moment capacity of the connection, the shear behaviour was significantly affected by the large lateral displacement associated with yielding of the plates in bending. In the present study, the largest ratio of the applied moment to the plastic moment capacity was 0.39, hence, yielding of the plates was not expected, and the analysis could proceed based on the symmetric shear behaviour (§9.3.4.3, p.258).

9.5.2.2 Horizontal connection (HC) and contact between columns

The HC associated with the IL connection was subjected to relatively small translational actions which were well within the capacities presented in Section 9.3.3.1 (p.253). The largest axial forces of 38.9 kN tension and -40.6 kN compression were associated with the earthquake loading in the Y-direction. The HCs were also subjected to vertical shear forces, and the largest force of 14.7 kN was due to the wind loading. If the wind load varied along the building width (X-direction) then a shear force in the 1-3 plane (V3), i.e., horizontal shear, would also be expected for the HC. However, as the wind load time history did not vary in the X-direction, i.e., along the building width, the main interest was the shear force in the 1-2 plane (V2), i.e., vertical shear.

The modules were initially located hard against one another in the numerical model, and the results showed compression-only axial forces up to -34 kN for the contact links. For example, Figure 9.23 shows the time history of the contact force (B2-z1 upper, Figure 9.17a & d, p.260) for the first earthquake acceleration time history in the Y- and X-directions, i.e., a1 and a21. When using the PT connection, the HCs guaranteed the proximity of the modules at the HC locations. This is because the HC bolts are initially tensioned, which pulls the modules together at the HC locations, thereby accounting for misalignment during site installation and normal deviations in the straightness of the steel elements. In the IL connection, however, the HC is integrated with the VC (Figure 9.9, p.252). The bolts pull the modules together vertically, but

not horizontally. If the modules are not placed hard against one another during site installation, then impact between the modules is prevented only by the friction generated between the vertically clamped plates. As a result, impact between the modules is possible if the VC slips in shear because the friction resistance is exceeded, or if the elastic displacement prior to slip exceeds the initial gap between the modules.

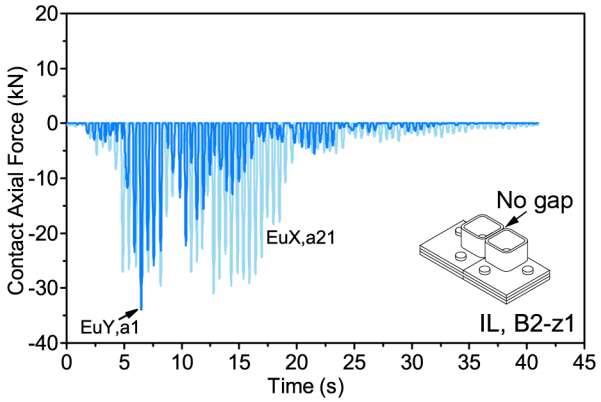

Figure 9.23. Contact force time history for a contact link with no gap for the first earthquake acceleration time history in the X- and Y-directions

When the gap between the modules was increased from zero to 2 mm in the numerical model, then the contact force due to earthquake accelerations were reduced to zero. As shown in Figure 9.24, although the axial displacement of the contact link varied in response to the earthquake ground motions the displacements were small, as the VCs did not slip in shear, and were not large enough to close the initial 2 mm gap. In this case the horizontal gaps between the modules may be an advantage, in that the horizontal gaps may permit out of phase vibration of the modules if they have different vibration frequencies, e.g., owing to different masses, which may dissipate energy and, hence, improve the overall performance of the building. Notwithstanding this potential advantage, impact between the modules is still possible if there is a large earthquake.

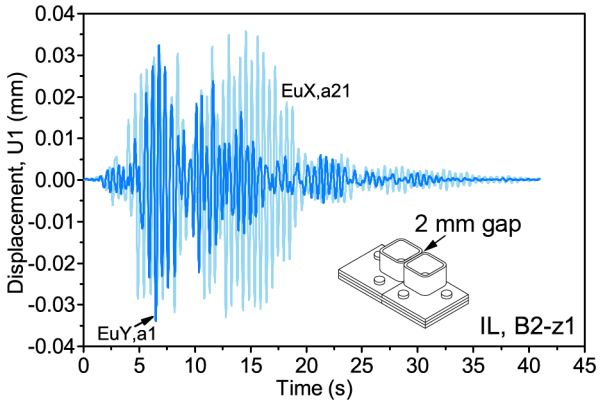

Figure 9.24. Axial displacement time history for a contact link with a 2 mm gap for the first earthquake acceleration time history in the X- and Y-directions

9.6 Drift limits

Drift limits of H/600 and h/500 are typically applied for the total and inter-storey drifts of traditional buildings due to the serviceability limit state wind, where H and h are the building and storey height, respectively (§2.1.6.2, p.15). The maximum total drifts of the case study building due to the serviceability wind simulated based on the Li et al. [178] spectrum were 6.3 and 6.6 mm for the PT and IL connections, respectively. These drifts were significantly less than the limit of H/600 which is equal to 34 mm. Similarly, the maximum inter-storey drift ratios (IDRs) were 0.0409 and 0.0398% for the PT and IL connections, respectively. These IDRs were less than the limit of 0.2% indicated by limiting the inter-storey drift to h/500. In the case of earthquake loading, displacement-based damage criteria such as an IDR limit of 1.5% [74] are applied to the ultimate limit state (§2.1.6.3, p.16). The maximum IDRs (mean time history) for the case study building were 0.224, 0.247, and 0.265% for the PT, IL, and BM connections, respectively. These drift ratios were well below the limit of 1.5%. However, the IMC responses were elastic (§9.5, p.264) and, for example, did not slip in shear (Figure 9.21, p. 264).

The above drift limits were developed for traditional building structures, and it is not clear if they are applicable to modular steel buildings (§2.1.6.3, p.16). The wind drift limits are related to serviceability issues including local damage to non-structural components [71]. Modular buildings may incorporate brittle exterior and interior cladding, for example, which may crack in response to large drifts. The existing drift limits [71] that where developed to prevent such cracking, i.e., H/600 and h/500, may reasonably be applied to modular buildings. For earthquake ground motions, however, the rocking and sliding responses of the modules due to the IMC connection behaviours may affect the inter-storey drift. Therefore, the conventional limit of 1.5% may not be applicable to modular buildings.

In this chapter, the inter-storey drifts were comprised of deformation of the modules and deformation of the IMCs. As the IMCs were the main interest, hinges were not incorporated for the intra-module connections, and the inelasticity was limited to the IMCs. The lateral displacement of the IMCs was made up of displacements associated with the IMC shear and moment-rotation behaviours. The ratio of the bending moment to the shear force varied with the magnitude of the lateral load, as the load was redistributed through the structure based on the inelastic IMC responses. To examine the relative contribution of the IMC shear and moment-rotation behaviours to the IDR, a series of time history analyses were carried out with incrementally increasing peak ground acceleration (PGA) in the Y-direction. The SAP2000 numerical models were subjected to gravity loading, followed by a nonlinear direct integration time history analysis. Second order P-Δ effects of the gravity loads acting on the deformed

structure were included in the simulations. The input IMC behaviours were based on zero axial force. This ensured that the IMC capacities were not overestimated as the axial force due to the earthquake ground motion cycled through positive and negative values.

The inelastic behaviours of the post-tensioned IMCs can be described as follows. For a PGA of 0.195g the IMC responses were elastic (§9.5.1, p.264). When the PGA was increased to 0.3g, local yielding of the IMCs was imminent. The IMCs at the braced end of the building, i.e., grid line 1 in Figure 9.1(a) (§9.2.1, p.245), slipped in shear, resulting in redistribution of the lateral load to the internal grids, e.g., grids 3a and 3b. The PT connections located along these internal grids were then subjected to the largest shear forces and, hence, had the largest lateral drifts. For example, Figure 9.25 shows the shear force and bending moment time histories for a PT connection at grid D3b-z1 due to the first earthquake acceleration time history (a1) with a PGA of 0.3g. Similarly, Figure 9.26 shows the drift associated with the IMC at grid D3b-z1 due to a1 with a PGA of 0.3g. For comparison, the total storey drift (Total) is shown along with the drift associated with the module, i.e., Total = Module + IMC. The maximum shear force and bending moment of 268 kN and 3.96 kNm, respectively, occurred at the same time as the maximum IDR of 0.5%. Referring to Figure 9.14 (p.256), it can be seen that, for zero axial load, a shear force of 268 kN corresponds to a displacement of 4.9 mm. Similarly, from Figure 9.16 (p.258), a bending moment of 3.96 kNm corresponds to 1.12×10^{-4} rad. The lateral displacement of the IMC due to the bending moment was small compared to that due to the shear force, hence, the IMC drift limits could be estimated based on the shear behaviour of the IMC.

For a PGA of 0.3g, the IMC was subjected to a maximum shear force of 268 kN, and the corresponding maximum IDR was 0.5% due to 4.9 mm displacement of the IMC and 12.7 mm displacement of the module (Figure 9.26). Referring to Figure 9.27, the corresponding point on the simplified shear behaviour for the PT connection is labelled as Y. This represents the point at which the shear force-displacement curve starts to deviate from the initial linear response defined by the stiffness $K_{PQ,i}$ due to yielding of the column flange. Following the simplified model, point Q represents the ultimate limit state. At this point the PT connection can accommodate displacements up to 9 mm (§7.4.1, p.170) as the shear force increases to 372 kN, representing complete failure of the connection. As hinges were not incorporated for the intra-module connections the module displacement was elastic. Therefore, as the shear force increases from 268 to 372 kN, the corresponding module displacement increases from 12.7 to 17.6 mm. By summing the IMC and module displacements, the total displacement can be estimated as 26.6 mm, i.e., 0.76% IDR. This IDR limit is a low estimate as the inelastic deformation of the module may, for example, increase the drift at the ultimate stage. A

corresponding upper bound estimate was made by combining the estimated inelastic module displacement with the IMC displacement. The inelastic module deformation was estimated as 62.4 mm based on a structural ductility of 1.84 and a structural performance factor of 0.52 [14]. Hence, the total displacement was 71.4 mm and the upper bound IDR limit was estimated as 2.0%.

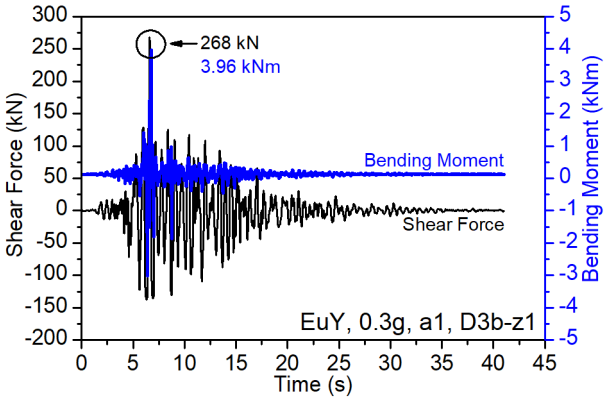

Figure 9.25. Shear force and bending moment time histories for PT connection at D3b-z1 due to earthquake acceleration time history a1 with PGA=0.3g

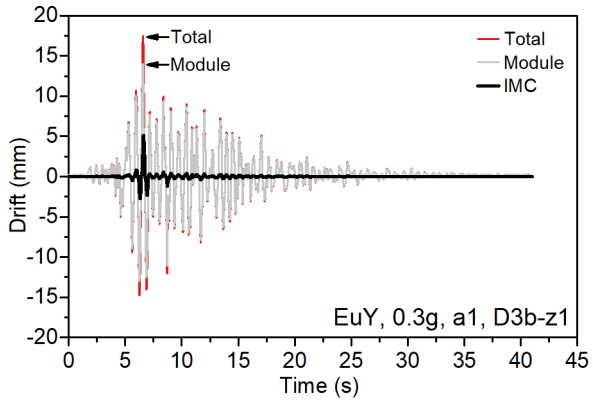

Figure 9.26. Drift in the Y-direction for PT connection at D3b-z1 due to earthquake acceleration time history a1 with PGA=0.3g

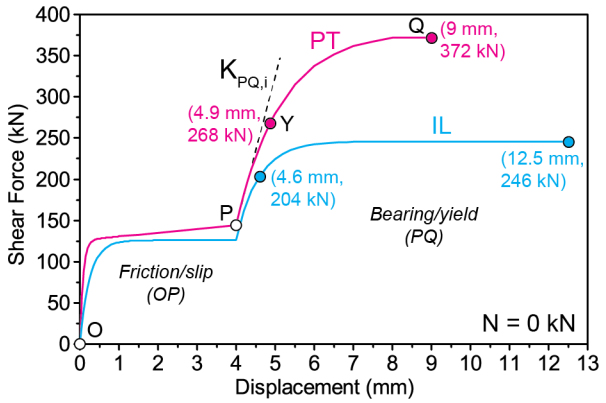

Figure 9.27. Shear behaviours of the post-tensioned (PT) and interlocking (IL) vertical connections for zero axial force

Similar inelastic responses were observed for the IL connection. The asymmetric M-θ behaviour of the VCs resulted in a less equal distribution of the moments among the IMCs, which ultimately caused larger maximum bending moments than for the PT connection. Although the maximum connection rotations were larger, the associated lateral displacements were still small in comparison with those due to the shear force-displacement behaviour. In Chapter 8, the average ultimate displacement was 10.5 mm for a 2 mm effective tolerance, i.e., the difference between the bolt and the bolt hole diameters. Therefore, for a 4 mm effective tolerance the ultimate displacement was estimated as 12.5 mm. Following the same procedure as for the building with the PT connections, as the shear force increases from 204 to 246 kN, the corresponding module displacement increases from 9.67 to 11.7 mm. Hence, by summing the IMC and module displacements, the total displacement can be estimated as 24.2 mm, i.e., 0.69% IDR. Finally, the inelastic module deformation was estimated as 41.2 mm, resulting in a total displacement of 53.7 mm and an upper bound IDR limit of 1.5%. Referring to Figure 9.27 it can be seen that, with zero axial force, the shear capacity of the IL connection was less than that for the PT connection. Consequently, the estimated ultimate module displacements were smaller in the case of the IL connections, as compared with the PT connections. If, for example, the IL connection shear capacity could be increased to 372 kN, i.e., to match the PT connection, then the IL connection IDR limits would increase. The IL connection lower limit would increase from 0.69 to 0.86% and the upper limit would increase from 1.5% to 2.1%.

Overall, the conventional IDR limit of 1.5% was not well related to the damage states of the IMCs. If inelastic deformation of the module is combined with that of the IMCs, then IDRs larger than 1.5% are possible, e.g., 2.0% for the PT connection. Conversely, if the modules respond elastically then the IMCs may fail at IDRs smaller than 1.5%, i.e., 0.76 and 0.69% for the PT and IL connections, respectively. For structural design purposes, it is recommended that the adequacy of the IMCs be established by comparing the design actions with the simplified connection behaviours as demonstrated in Section 9.5 (p.264), rather than relying on a single IDR limit which is unable to account for factors such as the IMC type, axial force, IMC shear capacity, and bolt hole tolerance. Moreover, global stability of the building, which was not considered in the suggested IDR limits, should also be assessed. For example, if a large IDR such as 2.0% was to occur for each storey, the total drift accumulated over the building height could be large, which may compromise the stability of a tall modular building.

9.7 Summary

Numerical simulations were carried out to investigate the overall responses of a selected modular steel building, incorporating new simplified models for the structural behaviours of the inter-module connections (IMCs). The application of the new simplified IMC behaviours was evaluated and the effect on the overall responses to wind and earthquake loading was examined. The main findings are summarised as follows.

1. The shear, axial and moment-rotation behaviours of the post-tensioned and interlocking IMCs are well-represented by the new simplified models, which in turn are well-suited to application in overall numerical simulations of modular steel buildings. Moreover, the simplified models can be applied to different IMC geometries, due to the analytical derivation of many of the parameters.

2. Compared with the previous benchmark analysis (Chapter 3) which adopted a rigid behaviour for the IMCs, the more accurate simplified models for the IMC connection behaviours leads to a more accurate understanding of the global responses of modular buildings, which facilitates the analysis and design of modular structures.

3. Shear slip of the IMCs can be avoided through the use of slip resistant post-tensioned and interlocking connections, which have slip resistance greater than the largest shear force associated with the design wind and earthquake loads. The potential for an IMC to slip, and for the slip to accumulate over the building height, can be assessed by comparing the design load with the simplified shear behaviour.

4. The conventional inter-storey drift limit of 1.5% was not related to the damage states of the IMCs. If the modules remain elastic then the IMCs may fail at smaller drift ratios, whereas larger drift ratios are possible if the response of the modules is inelastic. Therefore, for design purposes, it is recommended that the suitability of the IMCs is established by comparing the design actions with the respective simplified connection behaviour.

5. For the interlocking IMCs, the bolts pull the modules together vertically but not horizontally, creating the possibility of horizontal gaps between the modules and, hence, impact between the modules when subjected to lateral loads. At the same time, the horizontal gaps may permit out of phase vibration of the modules which may dissipate energy and improve the overall performance.

6. To further develop knowledge on the structural response of modular buildings, it is recommended that further numerical simulations are carried out considering different building layouts, inter-module connections, and intra-module connections. For the inter-module connections, further study of the cyclic response is recommended as the hysteretic shear behaviour may significantly affect the global response to earthquake actions, for example. For the intra-module connections, it is suggested that plastic hinges may be incorporated in the numerical models to account for the inelastic response of the beam-column joints considering the range of combined actions which may apply.

Chapter 10 Conclusion and recommendations

10.1 Main findings

This thesis studied the lateral responses of modular steel buildings subjected to wind and earthquake ground motion. In Chapter 2, the broad review of modular building structures highlighted that the structural response of modular buildings may be significantly affected by the inter-module connections (IMCs), and that the design and fabrication of reliable IMCs was a challenge for the existing industry. Moreover, through a focused review of bolted IMCs it was identified that the structural behaviours of the existing IMCs could not be accurately estimated by the existing simplified models. Hence, following the literature review, this study focused on the structural behaviours of the IMCs.

Chapter 3 introduced a six-storey case study building and carried out numerical simulations to investigate its response to wind and earthquake actions. The building responses to the lateral loads were established based on increasingly sophisticated design analyses. First, for the wind action, the building responses were estimated based on equivalent static analysis (ESA) and time history analyses (THA) using simulated load time histories. The wind loads were simulated based on the Kaimal et al. [175] turbulence spectrum which reflected non-cyclonic conditions, and the Yu et al. [177] and Li et al. [178] spectra, which were two competing models for cyclonic conditions. The ESA resulted in a reasonable estimate of the overall responses, while the Li et al. [178] spectrum was associated with the largest responses, as the spectrum peak was the closest to the fundamental frequency of the building. Second, for the earthquake action, equivalent static analyses (ESA) were conducted, followed by a response spectrum analysis (RSA), and finally time history analyses (THA) using simulated ground motion time histories. The RSA resulted in a reasonable estimate of the overall response. It was found, however, that the fundamental period of modular buildings may not be accurately estimated by the existing empirical formulae, which could result in an inaccurate estimate of the equivalent static earthquake base shear force. Therefore, it was recommended that the fundamental period should be determined from the overall numerical model, rather than relying on the existing empirical formulae. Finally, by varying the stiffness of the IMCs, it was found that the shear behaviour of the IMCs affected the overall building responses, while the moment-rotation behaviour had little effect. Therefore, the following Chapters 4 to 6 focused on the shear behaviour.

Chapter 4 established the short-term friction/slip shear behaviour associated with AS/NZS 3678-350 steel with clean mill scale and sand blasted (AS 1627.4 Sa 1 and Sa 3) surface finishes by conducting slip factor tests in accordance with Annex G of EN 1090-2. For the

sand blasted surfaces the characteristic slip factor was 0.5 which matched the EN 1090-2 standard value and was not sensitive to the degree of sand blasting defined by visual assessment to AS 1627.9 and ISO 8501-1. For the clean mill scale finish, however, the characteristic slip factor was dependent on the mill scale thickness and composition. A value of 0.27 was obtained which was 10% less than the EN 1090-2 standard value of 0.30. 95% confidence intervals were calculated for the experimental slip factor as 0.31 ± 4.9% and 0.55 ± 5.6% for the clean mill scale and Sa 3 sand blasted surfaces, respectively. The slip factor tests also served to demonstrate that the bolt preload could be well-controlled by the torque method, and that digital image correlation (DIC) could be used to effectively measure displacement of the specimens. Finally, numerical simulations were carried out to ensure the accuracy of the experimental load-slip behaviours and to establish the effect of the bolt preload and slip factor. Based on the calibrated numerical results, a more accurate empirical model was proposed for the friction/slip behaviour of the test specimens depending on the slip factor and bolt preload. In this way, Chapter 4 established the material friction/slip shear behaviour which was subsequently applied in the following studies on the IMCs (Chapter 5 to 8).

Chapter 5 introduced a new IMC known as the post-tensioned (PT) connection which allowed internal connection of the modules and, therefore, reduced the requirement for working at heights during the site installation. An experimental setup was developed which allowed the specimens to be tested using a universal testing machine. The bolt preloads were controlled by applying the torque method, and DIC was applied to determine the specimen displacement from photos taken during the loading sequences. Assembly tests were undertaken to determine the relationship between the preload in the threaded rod and the torque applied to the nut and, hence, 95% confidence intervals were obtained for the preload as 81 kN ± 3.8% and 45 kN ± 5.8% for an applied torque of 250 and 150 Nm, respectively. Allowing for variation of the surface and the preload, the maximum uncertainty of the slip resistance was calculated as ± 7.0% based on the sand blasted specimen with 150 Nm torque. The specimens had varying bolt preload (81 and 45 kN), surface finish (clean mill scale and Sa 3 sand blasted) and contact area (1530 and 3474 mm^2). Sand blasting the faying surfaces and increasing the bolt preload improved the slip resistance. Increasing the contact area, however, did not have a significant effect considering the experimental accuracy. The PT connection had a large initial friction/slip stiffness, which was greater than the selected existing IMCs. Numerical simulations were carried out and a new more accurate exponential model was proposed for the friction/slip shear behaviour of the PT connection specimens.

Chapter 6 introduced another new IMC known as the interlocking (IL) connection. The IL connection combined structural bolts with interlocking elements which assisted with site

assembly of the modules and improved the shear force-slip behaviour. Similar to the PT connection, an experimental setup was developed and the bolt preloads were controlled by the torque method, while displacements were determined using DIC. The accuracy of the experimental slip resistance was calculated as ± 4.8% allowing for variation of the clean mill scale surface and the bolt preload, which was calculated based on assembly tests conducted by the bolt manufacturer. The experimental specimens had varying bolt preload (50 and 35 kN), bolt hole tolerance (standard and slotted) and presence or absence of the interlocking element. The slip resistance was controlled mainly by the bolt preload and the slip factor. The bolt hole tolerance had a small effect on the experimental slip resistance. For the 35 kN preload, changing from the standard to the short slotted holes reduced the slip resistance by 13%, which was attributed to flattening of the surface asperities due to the greater contact pressure resulting from the slotted holes. The interlocking elements, i.e., the locating pins, were found to increase the shear resistance after the connection slipped. Similar to the PT connection, the IL connection exhibited a large initial friction/slip stiffness, which was greater than selected existing IMCs. Finally, numerical simulations were undertaken to facilitate further parametric study, based on which an empirical model was proposed for the friction/slip shear behaviour of the IL connection specimens.

In Chapter 7, simplified analytical and empirical models were derived which could be used to estimate the structural behaviours of the new PT connection and, hence, facilitate design. An extended numerical model was built based on the PT connection which was adjusted to suit a typical modular building structure. The numerical shear behaviour was established and calibrated based on the previous experiments (Chapter 5), and a two-stage simplified empirical model was proposed. The shear behaviour was unaffected by coincident bending moments, however, axial compression forces increased the slip resistance. The numerical axial force-displacement behaviour was similarly established, and a multi-linear model was proposed and matched to the analytically derived behaviour. The axial behaviour was affected by bending moments and shear forces, and appropriate axial force limits were proposed to ensure the effect was not significant. Finally, the numerical moment-rotation (M-θ) behaviour was established, and a simplified two-stage model was proposed and matched to the analytical behaviour. An iterative procedure was developed to estimate the nonlinear M-θ behaviour in the second stage. The M-θ behaviour was affected by the axial force which was accounted for in the iterative procedure. In contrast, shear forces had little effect on the early M-θ behaviour which was the main interest.

In Chapter 8, a spring model was developed for the IL connection, which combined the vertical and horizontal connection elements. Simplified models were proposed for the shear and axial

force-displacement behaviours of the horizontal connection based on the geometry of the central tie plate. For the vertical connection (VC), intermediate numerical simulations were undertaken to investigate the effect of the loading and boundary conditions on the shear behaviour. The results demonstrated that the empirical model proposed in Chapter 6 for the shear behaviour of the experimental specimens could over-estimate the slip resistance of a single IL connection in a modular steel building. The numerical shear behaviour of the VC was, therefore, established based on extended numerical models with two bolts per column, for which the tangential contact behaviour was validated with reference to the previous experiments (Chapter 6). A two-stage exponential model was then proposed, which accounted for the effect of axial forces. In addition, a compression only axial spring was incorporated into the spring model to account for the possibility of contact between the adjacent columns. Similarly, a two-stage analytical model was proposed for the VC axial behaviour. The model had a linear behaviour for compression and a nonlinear exponential behaviour for tension. The tension behaviour was affected by bending moments and shear forces, each of which caused an initial vertical displacement and affected the tension stiffness due to a P-Δ effect. For the moment-rotation (M-θ) behaviour, a two-stage semi-empirical model was proposed. The first stage was linear and was determined by the axial force and the stiffness of the clamped plates, whereas the second stage was nonlinear and suited an exponential model. The behaviour in the second stage was determined by the axial force and the asymmetric positive/negative plate bending behaviour.

Finally, in Chapter 9, the simplified models for the structural behaviours of the new PT and IL connections were applied in numerical simulations of the case study building first introduced in Chapter 3. Whereas Chapters 5 to 8 were based on the half-scale connections, in Chapter 9, the simplified models were applied to the larger full-scale connections. Hence, it was demonstrated that the simplified models can be applied to different connection geometries as a result of the analytical derivation of key parameters. The new simplified models were more accurate than the rigid behaviours assumed in Chapter 3 and, hence, the simplified models contributed to an improved understanding of the overall building responses to the lateral wind and earthquake actions. It was found that the vulnerability of IMCs to shear slip (§2.1.4.1, p.9) can be addressed through selection of slip resistant IMCs which have slip resistance larger than the maximum shear force expected due to the ultimate wind or earthquake event. In addition, it was found that the AS 1170.4 inter-storey drift ratio (IDR) limit of 1.5% did not match the damage states of either of the new IMCs. For the PT connection, for example, the ultimate IDR limit was estimated as 0.76% if inelasticity was limited to the IMC, or 2.0% if both the IMC and the module response was inelastic. Similarly, for the IL connection, the corresponding IDR limits were estimated as 0.86% and 2.1%, respectively. It was, therefore,

recommended that the IMC response should be determined with reference to the simplified models, rather than relying on the standard IDR limit. Finally, it was found that the IL connection permitted horizontal gaps between the modules which could occur depending on the site installation tolerance. These horizontal gaps were shown to be a potential hazard due to the possibility of impact between the modules, but also a potential advantage in that out of phase vibration of the modules could improve the overall performance.

10.2 Recommendations for future work

Chapter 2 presented the state-of-the-art with respect to modular buildings, and outlined several areas where the existing research was lacking. This thesis then studied the lateral responses of modular steel buildings, and the research led to a focus on the structural behaviours of the inter-module connections (IMCs). Consequently, some subjects identified as requiring further study in Chapter 2 remain to be investigated. This thesis may, therefore, be regarded as one of several initial studies on modular building structures, based on which many further works can be recommended. For brevity, however, only the works which directly follow this thesis are outlined below.

In this thesis, the simplified models for the new IMCs were established by numerical analyses for which the numerical models were calibrated with reference to the quasi-static shear behaviour (Chapter 4 to 6). The numerical axial force-displacement and moment-rotation (M-θ) behaviours of the new IMCs, however, were verified by comparison with the simplified analytical models and the experimental behaviours of other existing IMCs (Chapter 7 and 8). Hence, the validation of the tangential contact behaviours which controlled the friction/slip shear responses was more rigorous than that for the axial and M-θ behaviours. This was justified, in this thesis, by the relative importance of the IMC shear behaviour to the global building response. The IMC M-θ behaviour, for example, had negligible effect in the benchmark case study building analyses (Chapter 3). However, as it is possible that the axial and M-θ behaviours may be more influential in other modular structures, it is recommended that further study is undertaken to establish these components of the IMC behaviours experimentally.

Moreover, it is also recommended that further study of the cyclic shear behaviour may further improve the understanding of the response of modular buildings to earthquake actions. Similarly, experimental verification of the IMC post-yield shear behaviours may allow development of more precise models for this portion of the shear behaviour. Further work is also recommended to establish the behaviour of IMCs subjected to combined actions. Although combined actions were considered in Chapter 7 and 8, the works were specific to

the new PT and IL connections, respectively. Further work is recommended to establish the response of IMCs to combined actions more generally. For example, further investigation is required to verify the validity of standard interaction equations, such as equation (2.8) and (2.9) (p.47), in the case of IMCs.

It is suggested that, in future works, the study of modular buildings may be further advanced by conducting numerical simulations for different building layouts, different IMCs, different materials, different intra-module connections, and variation of the IMC structural behaviours. Considering the latter, for example, the variation of the structural behaviours of the IMCs can be estimated based on the simplified models proposed in this thesis. Mean and standard deviation values were reported, along with 95% confidence intervals, for the bolt preload and slip factor in Chapter 4 to 6. Hence, the corresponding variation of the slip resistance was reported. It can be seen, for example, that the variation of the shear behaviour could similarly be established based on the proposed simplified models. The variation of the bolt hole tolerance throughout the structure could also be considered and it could be randomly assigned. In the same way, the horizontal gap between the modules could be assigned randomly based on the maximum values reported in Chapter 6. Hence, the simplified models and associated parameter variations established in this thesis may be applied to estimate the corresponding variation of the IMC structural behaviours. The varying IMC behaviours could then be applied in a fragility analysis and, hence, the vulnerability of modular steel buildings to large lateral loads may be investigated including variation of the IMC behaviours.

In Chapter 9 it was found that interlocking IMCs may be vulnerable to impact between the modules due to horizontal gaps between the modules, which may occur depending on the site installation tolerance. However, it was also found that the horizontal gaps could allow out of phase vibration of the modules which may improve the overall building performance. Hence, the lateral response of a modular steel building may be improved due to the possibility of relative motion between each module and the surrounding modules. Thus, a new vibration control strategy is suggested which could be investigated further in future works.

References

[1] Ferdous W, Bai Y, Ngo TD, Manalo A, Mendis P. New advancements, challenges and opportunities of multi-storey modular buildings – A state-of-the-art review. Eng Struct. 2019;183:883-93. https://doi.org/10.1016/j.engstruct.2019.01.061

[2] Steinhardt DA, Manley K. Adoption of prefabricated housing–the role of country context. Sustainable Cities and Society. 2016;22:126-35. http://dx.doi.org/10.1016/j.scs.2016.02.008

[3] Navaratnam S, Ngo T, Gunawardena T, Henderson D. Performance review of prefabricated building systems and future research in Australia. Buildings. 2019;9(2):38 . https://doi.org/10.3390/buildings9020038

[4] White RB. Prefabrication : a history of its development in Great Britain. London, England: Her Majesty's Stationery Office; 1965.

[5] Gibb AGF. Off-site Fabrication: Prefabrication, Pre-assembly and Modularisation. Scotland, UK: Whittles Publishing; 1999.

[6] Smith RE. Prefab Architecture : A guide to modular design and construction. Hoboken, NJ, USA: John Wiley & Sons; 2010.

[7] Lawson RM, Ogden RG, Goodier C. Design in Modular Construction. Boca Raton, FL, USA: CRC Press; 2014.

[8] Lawson RM, Ogden RG, Bergin R. Application of Modular Construction in High-Rise Buildings. J Arch Eng. 2012;18(2):148-54. https://doi.org/10.1061/(asce)ae.1943-5568.0000057

[9] Kamali M, Hewage K. Life cycle performance of modular buildings: A critical review. Renewable Sustainable Energy Rev. 2016;62:1171-83. https://doi.org/10.1016/j.rser.2016.05.031

[10] Lopez D, Froese TM. Analysis of Costs and Benefits of Panelized and Modular Prefabricated Homes. Procedia Eng. 2016;145:1291-7. https://doi.org/10.1016/j.proeng.2016.04.166

[11] Annan CD. Applicability of Traditional Design Procedures to Modular Steel Buildings [PhD Thesis]. London, Ontario, Canada: The University of Western Ontario; 2008.

[12] Gorgolewski MT, Grubb PJ, Lawson RM. Modular Construction using Light Steel Framing: Design of Residential Buildings. Ascot, Berkshire, England: The Steel Construction Institute; 2001.

[13] Lawson RM, Ogden RG, Pedreschi R, Grubb PJ, Popo-Ola SO. Developments in pre-fabricated systems in light steel and modular construction. Struct Eng. 2005;83(6):28-35.

[14] Annan CD, Youssef MA, El Naggar MH. Seismic overstrength in braced frames of modular steel buildings. J Earthq Eng. 2008;13(1):1-21. https://doi.org/10.1080/13632460802212576

[15] Annan CD, Youssef MA, El Naggar MH. Seismic Vulnerability Assessment of Modular Steel Buildings. J Earthq Eng. 2009;13(8):1065-88. https://doi.org/10.1080/13632460902933881

[16] Annan CD, Youssef MA, El-Nagger MH. Effect of Directly Welded Stringer-to-Beam Connections on the Analysis and Design of Modular Steel Building Floors. Adv Struct Eng. 2009;12(3):373-83. https://doi.org/10.1260/136943309788708400

[17] Annan CD, Youssef MA, El Naggar MH. Experimental evaluation of the seismic performance of modular steel-braced frames. Eng Struct. 2009;31(7):1435-46. https://doi.org/10.1016/j.engstruct.2009.02.024

[18] Fathieh A, Mercan O. Seismic evaluation of modular steel buildings. Eng Struct. 2016;122:83-92. https://doi.org/10.1016/j.engstruct.2016.04.054

[19] Gunawardena T, Ngo TD, Mendis P, Alfano J. Innovative Flexible Structural System Using Prefabricated Modules. J Arch Eng. 2016;22(4):05016003. https://doi.org/10.1061/(asce)ae.1943-5568.0000214

[20] Gunawardena T, Ngo TD, Mendis P. Behaviour of Multi-Storey Prefabricated Modular Buildings under seismic loads. Earthquake Struct. 2016;11(6):1061-76. https://doi.org/10.12989/eas.2016.11.6.1061

[21] Lawson RM, Grubb PJ, Prewer J, Trebilcock PJ. Modular Construction using Light Steel Framing: An Architect's Guide. Ascot, Berkshire, England: The Steel Construction Institute; 1999.

[22] Lawson RM. Building Design Using Modules. Ascot, Berkshire, England: The Steel Construction Institute; 2007.

[23] Lawson RM, Ogden RG. 'Hybrid' light steel panel and modular systems. Thin Wall Struct. 2008;46(7-9):720-30. https://doi.org/10.1016/j.tws.2008.01.042

[24] Lawson RM, Byfield MP, Popo-Ola SO, Grubb PJ. Robustness of light steel frames and modular construction. Proc Inst Civ Eng Struct Build. 2008;161(1):3-16. https://doi.org/10.1680/stbu.2008.161.1.3

[25] Lawson RM, Richards J. Modular design for high-rise buildings. Proc Inst Civ Eng Struct Build. 2010;163(3):151-64. https://doi.org/10.1680/stbu.2010.163.3.151

[26] Lawson RM, Ogden RG, Popo-Ola SO. Design considerations for modular open building systems. Open House Int. 2011;36(1):44-53.

[27] Giriunas K, Sezen H, Dupaix RB. Evaluation, modeling, and analysis of shipping container building structures. Eng Struct. 2012;43:48-57. https://doi.org/10.1016/j.engstruct.2012.05.001

[28] Zha X, Zuo Y. Finite Element Study of Container Structure under Normal and High Temperature. Math Probl Eng. 2016;2016:2652149. https://doi.org/10.1155/2016/2652149

[29] Zha X, Zuo Y. Theoretical and experimental studies on in-plane stiffness of integrated container structure. Adv Mech Eng. 2016;8(3):1-20. https://doi.org/10.1177/1687814016637522

[30] Zuo Y, Zha X. FEM and experimental study on mechanical property of container building with holes. Int J Steel Struct. 2017;17(1):175-94. https://doi.org/10.1007/s13296-015-0132-y

[31] Boafo F, Kim J-H, Kim J-T. Performance of Modular Prefabricated Architecture: Case Study-Based Review and Future Pathways. Sustainability. 2016;8(6):558. https://doi.org/10.3390/su8060558

[32] Fathieh A. Nonlinear Dynamic Analysis of Modular Steel Buildings in Two and Three Dimensions [Master's Thesis]. Canada: University of Toronto; 2013.

[33] Gunawardena T. Behaviour of Prefabricated Modular Buildings Subjected to Lateral Loads [PhD Thesis]. Melbourne, Australia: The University of Melbourne; 2016.

[34] Gunawardena T, Ngo TD, Aye L, Mendis P. Innovative Prefabricated Modular Structures – An Overview and Life Cycle Energy Analysis. International Conference on Structural Engineering Construction and Management; December; Kandy, Sri Lanka. 2011.

[35] Manalo A. Structural behaviour of a prefabricated composite wall system made from rigid polyurethane foam and Magnesium Oxide board. Constr Build Mater. 2013;41:642-53. https://doi.org/10.1016/j.conbuildmat.2012.12.058

[36] Manalo A, Aravinthan T, Fam A, Benmokrane B. State-of-the-Art Review on FRP Sandwich Systems for Lightweight Civil Infrastructure. Journal of Composites for Construction. 2017;21(1):04016068. https://doi.org/10.1061/(asce)cc.1943-5614.0000729

[37] Satasivam S, Bai Y, Zhao X-L. Adhesively bonded modular GFRP web–flange sandwich for building floor construction. Compos Struct. 2014;111:381-92. https://doi.org/10.1016/j.compstruct.2014.01.003

[38] Satasivam S, Bai Y. Mechanical performance of bolted modular GFRP composite sandwich structures using standard and blind bolts. Compos Struct. 2014;117:59-70. https://doi.org/10.1016/j.compstruct.2014.06.011

[39] Satasivam S, Bai Y. Mechanical performance of modular FRP-steel composite beams for building construction. Mater Struct. 2016;49(10):4113-29. https://doi.org/10.1617/s11527-015-0776-2

[40] Satasivam S, Feng P, Bai Y, Caprani C. Composite actions within steel-FRP composite beam systems with novel blind bolt shear connections. Eng Struct. 2017;138:63-73. https://doi.org/10.1016/j.engstruct.2017.01.068

[41] Abeysinghe CM, Thambiratnam DP, Perera NJ. Dynamic performance characteristics of an innovative Hybrid Composite Floor Plate System under human-induced loads. Compos Struct. 2013;96:590-600. https://doi.org/10.1016/j.compstruct.2012.09.015

[42] Abeysinghe CM, Thambiratnam DP, Perera NJ. Flexural performance of an innovative Hybrid Composite Floor Plate System comprising Glass–fibre Reinforced Cement, Polyurethane and steel laminate. Compos Struct. 2013;95:179-90. https://doi.org/10.1016/j.compstruct.2012.06.019

[43] Loss C, Davison B. Innovative composite steel-timber floors with prefabricated modular components. Eng Struct. 2017;132:695-713. https://doi.org/10.1016/j.engstruct.2016.11.062

[44] Loss C, Piazza M, Zandonini R. Connections for steel–timber hybrid prefabricated buildings. Part I: Experimental tests. Constr Build Mater. 2016;122:781-95. https://doi.org/10.1016/j.conbuildmat.2015.12.002

[45] Loss C, Piazza M, Zandonini R. Connections for steel–timber hybrid prefabricated buildings. Part II: Innovative modular structures. Constr Build Mater. 2016;122:796-808. https://doi.org/10.1016/j.conbuildmat.2015.12.001

[46] Pedreschi R, Brennan J, Lawson RM. Preliminary studies of steel-plywood composite structures. In: Dubina D, Ungureanu V, editors. Steel - A New and Traditional Material for Building: Proceedings of the International Conference in Metal Structures. Romania: Taylor & Francis; 2006. p. 433-40.

[47] Lawson RM, Ogden RG, Pedreschi R, Popo-Ola SO. Developments of Cold-Formed Steel Sections in Composite Applications for Residential Buildings. Adv Struct Eng. 2008;11(6):651-60. https://doi.org/10.1260/136943308787543603

[48] Park KS, Moon J, Lee SS, Bae KW, Roeder CW. Embedded steel column-to-foundation connection for a modular structural system. Eng Struct. 2016;110:244-57. https://doi.org/10.1016/j.engstruct.2015.11.034

[49] Mills S, Grove D, Egan M. Breaking The Pre-fabricated Ceiling: Challenging the Limits for Modular High-Rise. In: Wood A, Malott D, editors. Proceedings of the CTBUH 2015 International Conference, New York, USA. Chicago: Council on Tall Buildings and Urban Habitat; 2015. p. 416-25.

[50] Styles AJ, Luo FJ, Bai Y, Murray-Parkes JB. Effects of joint rotational stiffness on structural responses of multi-story modular buildings. In: Mair RJ, Soga K, Jin Y, Parlikad AL, Schooling JM, editors. Proceedings of the International Conference on Smart Infrastructure and Construction. London: ICE Publishing; 2016. p. 457-62.

[51] Chen C, Cai YQ, Chiew S-P. Finite element analysis of up-down steel connectors for volumetric modular construction. In: Wald F, Chiew S-P, editors. Proceedings of the 12th International Conference on Steel, Space and Composite Structures. Prague, Czech Republic: Czech Technical University in Prague; 2014. p. 173-9.

[52] Choi K-S, Lee H-C, Kim H-J. Influence of Analytical Models on the Seismic Response of Modular Structures. J Korea Inst Struct Maint Insp. 2016;20(2):74-85. https://doi.org/10.11112/jksmi.2016.20.2.074

[53] Choi K-S, Kim H-J. An Analytical Study on Rotational Capacity of Beam-Column Joints in Unit Modular Frames. International Journal of Civil, Environmental, Structural, Construction and Architectural Engineering. 2015;9(2):100-3. https://doi.org/10.7734/COSEIK.2014.27.6.663

[54] Doh J-H, Ho NM, Miller D, Peters T, Carlson D, Lai P. Steel Bracket Connection on Modular Buildings. J Steel Struct Constr. 2017;2(2):121. https://doi.org/10.4172/2472-0437.1000121

[55] Lee S, Park J, Kwak E, Shon S, Kang C, Choi H. Verification of the seismic performance of a rigidly connected modular system depending on the shape and size of the ceiling bracket. Materials. 2017;10(3):263. https://doi.org/10.3390/ma10030263

[56] Chen Z, Li H, Chen A, Yu Y, Wang H. Research on pretensioned modular frame test and simulations. Eng Struct. 2017;151(Supplement C):774-87. https://doi.org/10.1016/j.engstruct.2017.08.019

[57] Chen Z, Liu J, Yu Y. Experimental study on interior connections in modular steel buildings. Eng Struct. 2017;147:625-38. https://doi.org/10.1016/j.engstruct.2017.06.002

[58] Deng E-F, Yan J-B, Ding Y, Zong L, Li Z-X, Dai X-M. Analytical and numerical studies on steel columns with novel connections in modular construction. Int J Steel Struct. 2017;17(4):1613-26. https://doi.org/10.1007/s13296-017-1226-5

[59] Deng E-F, Zong L, Ding Y, Dai XM, Lou N, Chen Y. Monotonic and cyclic response of bolted connections with welded cover plate for modular steel construction. Eng Struct. 2018;167:407-19. https://doi.org/10.1016/j.engstruct.2018.04.028

[60] Hong S-G, Cho B-H, Chung K-S, Moon J-h. Behavior of framed modular building system with double skin steel panels. J Constr Steel Res. 2011;67(6):936-46. https://doi.org/10.1016/j.jcsr.2011.02.002

[61] Ha TH, Cho BH, Kim H, Kim DJ. Development of an Efficient Steel Beam Section for Modular Construction Based on Six-Sigma. Adv Mater Sci Eng. 2016;2016:9687078. https://doi.org/10.1155/2016/9687078

[62] Jeyarajan S, Liew JYR, Koh CG. Enhancing the Robustness of Steel-Concrete Composite Buildings under Column Loss Scenarios. Int J Protective Struct. 2015;6(3):529-50. https://doi.org/10.1260/2041-4196.6.3.529

[63] Gill JC, Malamud BD. Reviewing and visualizing the interactions of natural hazards. Reviews of geophysics. 2014;52(4):680-722. https://doi.org/10.1002/2013RG000445

[64] Gill JC, Malamud BD. Hazard interactions and interaction networks (cascades) within multi-hazard methodologies. Earth Syst Dyn. 2016;7(3):659-79. https://doi.org/10.5194/esd-7-659-2016

[65] Gardoni P, LaFave JM. Chapter 1 - Multi-hazard Approaches to Civil Infrastructure Engineering: Mitigating Risks and Promoting Resilience. In: Gardoni P, LaFave JM, editors. Multi-hazard Approaches to Civil Infrastructure Engineering. Switzerland: Springer International Publishing; 2016.

[66] ASME. BTH-1 Design of Below-the-Hook Lifting Devices. New York, NY, USA: The American Society of Mechanical Engineers (ASME); 2017.

[67] Duerr D. ASME BTH-1 Pinned Connection Design Provisions. Pract Period Struct Des Constr. 2008;13(2):53-8. https://doi.org/10.1061/(ASCE)1084-0680(2008)13:2(53)

[68] Duerr D. Design Factors for Fabricated Steel Below-the-Hook Lifting Devices. Pract Period Struct Des Constr. 2008;13(2):48-52. https://doi.org/10.1061/(ASCE)1084-0680(2008)13:2(48)

[69] DNV GL AS. DNV-OS-H205 Lifting Operations (VMO Standard - Part 2-5). DNV GL AS; 2014.

[70] IMO. Code of Practice for Packing of Cargo Transport Units (CTU Code). International Maritime Organization (IMO); 2014.

[71] Griffis LG. Serviceability Limit States Under Wind Load. Eng J/AISC. 1993;30(1):1-16.

[72] Standards Australia. AS/NZS 1170.2:2011 Structural design actions, Part 2: Wind actions. Sydney, Australia: Standards Australia Limited; 2011.

[73] CTS. Simulated Windborne Debris Impact Testing of Building Envelope Components, Version 4. Townsville, Australia: Cyclone Testing Station (CTS), James Cook University; 2017.

[74] Standards Australia. AS 1170.4-2007(R2018) Structural design actions - Part 4: Earthquake actions in Australia. Sydney, Australia: Standards Australia Limited; 2007.

[75] Smith I, Asiz A, Gupta G. High Performance Modular Wood Construction Systems. Fredericton, Canada: Wood Science and Technology Centre; 2007.

[76] Holmes JD. Wind Loading of Structures. 3rd ed. Boca Raton, FL: CRC Press; 2015.

[77] Hao H. Predictions of Structural Response to Dynamic Loads of Different Loading Rates. Int J Protective Struct. 2015;6(4):585-605. https://doi.org/10.1260/2041-4196.6.4.585

[78] Aly MA, Abburu S. On the Design of High-Rise Buildings for Multihazard: Fundamental Differences between Wind and Earthquake Demand. Shock and Vibration. 2015:148681. https://doi.org/10.1155/2015/148681

[79] Mendis P, Ngo TD, Haritos N, Hira A, Samali B, Cheung J. Wind loading on tall buildings. EJSE. 2007;7:41-54.

[80] Holmes JD, Kwok KCS, Ginger JD. Wind Loading Handbook for Australia and New Zealand: Background to AS/NZS 1170.2 Wind Actions. Sydney, Australia: Australasian Wind Engineering Society (AWES); 2012.

[81] Jeary AP, Ellis BR. On predicting the response of tall buildings to wind excitation. J Wind Eng Ind Aerodyn. 1983;13(1):173-82. https://doi.org/10.1016/0167-6105(83)90139-3

[82] Tamura Y. Chapter 13 - Damping in Buildings and Estimation Techniques. In: Tamura Y, Kareem A, editors. Advanced Structural Wind Engineering. Tokyo, Japan: Springer; 2013.

[83] Gunawardena T, Ngo TD, Mendis P, Aye L, Alfano J. Structural performance under lateral loads of innovative prefabricated modular structures. In: Samali, Attard, Song, editors. Materials to Structures: Advancement through Innovation. London: Taylor & Francis; 2013.

[84] Minor JE. Windborne debris and the building envelope. J Wind Eng Ind Aerodyn. 1994;53:207-27. https://doi.org/10.1016%2F0167-6105%2894%2990027-2

[85] Wills JAB, Lee BE, Wyatt TA. A model of wind-borne debris damage. J Wind Eng Ind Aerodyn. 2002;90(4–5):555-65. https://doi.org/10.1016/S0167-6105(01)00197-0

[86] Minor JE. Lessons Learned from Failures of the Building Envelope in Windstorms. J Arch Eng. 2005;11(1):10-3. https://doi.org/10.1061/(ASCE)1076-0431(2005)11:1(10)

[87] Chen W, Hao H. Experimental and numerical study of composite lightweight structural insulated panel with expanded polystyrene core against windborne debris impacts. Mater Design. 2014;60:409-23. https://doi.org/10.1016/j.matdes.2014.04.038

[88] Chen W, Hao H, Du H. Failure analysis of corrugated panel subjected to windborne debris impacts. Eng Fail Anal. 2014;44:229-49. https://doi.org/10.1016/j.engfailanal.2014.05.017

[89] Chen W, Hao H. Performance of structural insulated panels with rigid skins subjected to windborne debris impacts – Experimental investigations. Constr Build Mater. 2015;77:241-52. https://doi.org/10.1016/j.conbuildmat.2014.12.112

[90] Meng Q, Hao H, Chen W. Experimental and numerical study of basalt fibre cloth strengthened structural insulated panel under windborne debris impact. J Reinf Plast Compos. 2016;35(17):1302-17. https://doi.org/10.1177/0731684416649787

[91] Meng Q, Hao H, Chen W. Laboratory test and numerical study of structural insulated panel strengthened with glass fibre laminate against windborne debris impact. Constr Build Mater. 2016;114:434-46. https://doi.org/10.1016/j.conbuildmat.2016.03.190

[92] NRCC. National Building Code of Canada (NBCC). Ottawa, Ontario, Canada: National Research Council of Canada (NRCC); 2005.

[93] Chopra AK. Dynamics of Structures, Theory and Applications to Earthquake Engineering. 5th ed. NJ, USA: Prentice Hall; 2016.

[94] Redwood RG, Channagiri VS. Earthquake resistant design of concentrically braced steel frames. Can J Civ Eng. 1991;18(5):839-50. https://doi.org/10.1139/l91-101

[95] Khatib IF, Mahin SA, Pister KS. Seismic behavior of concentrically braced steel frames (UCB/EERC-88/01). Berkeley, CA, USA: Earthquake Engineering Research Center, University of California; 1988.

[96] Asteris PG, Repapis CC, Repapi EV, Cavaleri L. Fundamental period of infilled reinforced concrete frame structures. Struct Infrastruct Eng. 2017;13(7):929-41. https://doi.org/10.1080/15732479.2016.1227341

[97] Shirokov VS, Kholopov IS, Solovejv AV. Determination of the Frequency of Natural Vibrations of a Modular Building. Procedia Eng. 2016;153:655-61. https://doi.org/10.1016/j.proeng.2016.08.218

[98] Malo KA, Abrahamsen RB, Bjertnæs MA. Some structural design issues of the 14-storey timber framed building "Treet" in Norway. Eur J Wood Wood Prod. 2016;74(3):407-24. https://doi.org/10.1007/s00107-016-1022-5

[99] ASCE. Design of Blast-Resistant Buildings in Petrochemical Facilities, 2nd ed. Reston, VA: American Society of Civil Engineers; 2010.

[100] Ngo TD, Mendis P, Gupta A, Ramsay J. Blast Loading and Blast Effects on Structures – An Overview. EJSE Special Issue: Loading on Structures. 2007.

[101] Summers PB. Design of Modular Blast-Resistant Steel-Framed Buildings in Petrochemical Facilities. In: Anderson DL, Bhatti MA, Foley CM, Charney FA, editors. Structures Congress 2008: Crossing Borders. Vancouver, Canada: American Society of Civil Engineers; 2008. p. 1557-63.

[102] Harrison BF. Blast resistant modular buildings for the petroleum and chemical processing industries. J Hazard Mater. 2003;104(1-3):31-8. https://doi.org/10.1016/s0304-3894(03)00232-2

[103] Maclachlan I. Standardization of location, design and specification of temporary modular buildings on petrochemical and process sites. Loss Prevention Bulletin. 2007;196(1):26-30.

[104] DoD. UFC 3-340-02 : Structures to Resist the Effects of Accidental Explosions. USA: Department of Defence (DoD); 2008.

[105] Hao H, Hao Y, Li J, Chen W. Review of the current practices in blast-resistant analysis and design of concrete structures. Adv Struct Eng. 2016;19(8):1193-223. https://doi.org/10.1177/1369433216656430

[106] DoD. UFC 4-023-03 : Design of Buildings to Resist Progressive Collapse. USA: Department of Defence (DoD); 2009.

[107] Cormie D. Whole-building response to blast damage. In: Cormie D, Mays G, Smith P, editors. Blast effects on buildings. 2nd ed. London: ICE Publishing; 2012.

[108] Byfield MP, Paramasivam S. Catenary action in steel-framed buildings. Proc Inst Civ Eng Struct Build. 2007;160(5):247-57.

[109] Lawson SH. *AFCEC conducts CONEX dorm field testing*. 2017 [cited 2017 April 21]; Available from: http://www.afcec.af.mil/News/Article-Display/Article/1157092/afcec-conducts-conex-dorm-field-testing/.

[110] Gallagher KA. The Dangers of Modular Construction. Fire Engineering. Tulsa: PennWell Corporation; 2009. p. 95-101.

[111] Gallagher KA. Modular Construction: Hidden Hazards Within. Fire Engineering. Tulsa: PennWell Corporation; 2013. p. 73-8.

[112] BBC. *London fire: A visual guide to what happened at Grenfell Tower*. 2017 [cited 2017 November 29]; Available from: http://www.bbc.com/news/uk-40301289.

[113] Ngo TD, Nguyen QT, Tran P. Heat release and flame propagation in prefabricated modular unit with GFRP composite facades. Build Simul. 2016;9(5):607-16. https://doi.org/10.1007/s12273-016-0294-3

[114] Nguyen QT, Ngo TD, Tran P, Mendis P, Zobec M, Aye L. Fire performance of prefabricated modular units using organoclay/glass fibre reinforced polymer composite. Constr Build Mater. 2016;129:204-15. https://doi.org/10.1016/j.conbuildmat.2016.10.100

[115] Nguyen QT, Tran P, Ngo TD, Tran PA, Mendis P. Experimental and computational investigations on fire resistance of GFRP composite for building façade. Composites Part B. 2014;62:218-29. https://doi.org/10.1016/j.compositesb.2014.02.010

[116] Nguyen QT, Ngo TD, Mendis P, Tran PA. Composite materials for next generation building facade systems. Civil Eng Arch. 2013;1(3):88-95. https://doi.org/10.13189/cea.2013.010305

[117] Monash University. Handbook for the Design of Modular Structures. Melbourne, Australia: Monash University; 2017.

[118] Biggs JM. Introduction to Structural Dynamics. New York, USA: McGraw-Hill, Inc.; 1964.

[119] Clough RW, Penzien J. Dynamics Of Structures, 3rd Ed. Berkeley, CA, USA: Computers & Structures, Inc.; 2003.

[120] Boughton GN. Tropical Cyclone Vance : damage to buildings in Exmouth. Perth, Australia: Dept. of Local Government; 1999.

[121] Boughton GN, Falck D. Tropical Cyclone George – Damage to buildings in the Port Hedland area. Queensland, Australia: Cyclone Testing Station, James Cook University; 2007.

[122] Hao H, Zhou Y. Dynamic Response of Rigid Blocks to Simultaneous Horizontal and Vertical Ground Shock. Adv Struct Eng. 2012;15(7):1069-82. https://doi.org/10.1260/1369-4332.15.7.1069

[123] Hao H, Zhou Y. Rigid Structure Response Analysis to Seismic and Blast Induced Ground Motions. Procedia Eng. 2011;14:946-55. https://doi.org/10.1016/j.proeng.2011.07.119

[124] Wu Z, Peng X, Zhang C. Overturning analysis of Harbor Containers based on wind tunnel test of rigid models. 2011 International Conference on Electric Technology and Civil Engineering (ICETCE). Lushan, China: IEEE; 2011. p. 544-8.

[125] ATC. Guidelines for Cyclic Seismic Testing of Components of Steel Structures, ATC 24. Redwood City, CA, USA: Applied Technology Council (ATC); 1992.

[126] ASTM. E564-06 : Standard Practice for Static Load Test for Shear Resistance of Framed Walls for Buildings. West Conshohocken, PA, USA: ASTM International; 2012.

[127] ASTM. E72-15 : Standard Test Methods of Conducting Strength Tests of Panels for Building Construction. West Conshohocken, PA, USA: ASTM International; 2015.

[128] Toro WM, Salenikovich A, Mohammad M, Beauregard R. Racking and Bending Tests for Prefabricated Wall Panels. MADERAS: Ciencia y technologia. 2007;9(1):3-14.

[129] ASTM. E1996-14a : Standard Specification for Performance of Exterior Windows, Curtain Walls, Doors, and Impact Protective Systems Impacted by Windborne Debris in Hurricanes. West Conshohocken, PA, USA: ASTM International; 2014.

[130] ASTM. E1886-13a : Standard Test Method for Performance of Exterior Windows, Curtain Walls, Doors, and Impact Protective Systems Impacted by Missile(s) and Exposed to Cyclic Pressure Differentials. West Conshohocken, PA, USA: ASTM International; 2013.

[131] Bayo E, Cabrero JM, Gil B. An effective component-based method to model semi-rigid connections for the global analysis of steel and composite structures. Eng Struct. 2006;28(1):97-108. https://doi.org/10.1016/j.engstruct.2005.08.001

[132] Uy B, Patel V, Li D, Aslani F. Behaviour and Design of Connections for Demountable Steel and Composite Structures. Structures. 2017;9:1-12. https://doi.org/10.1016/j.istruc.2016.06.005

[133] Fadden M, McCormick J. Cyclic Quasi-Static Testing of Hollow Structural Section Beam Members. J Struct Eng. 2012;138(5):561-70. https://doi.org/10.1061/(ASCE)ST.1943-541X.0000506

[134] Packer J, Sherman D, Lecce M. AISC Design Guide 24: Hollow Structural Section Connections. USA: American Institute of Steel Construction; 2009.

[135] Sultana P, Youssef MA. Seismic performance of modular steel-braced frames utilizing superelastic shape memory alloy bolts in the vertical module connections. J Earthq Eng. 2018;24(4):628-52. https://doi.org/10.1080/13632469.2018.1453394

[136] CEN. EN 1993-1-8:2005 Eurocode 3: Design of steel structures - Part 1-8: Design of joints. Brussels, Belgium: European Committee for Standardization (CEN); 2005.

[137] AISC. ANSI/AISC 360-16 Specification for Structural Steel Buildings. Chicago, Illinois, USA: American Institute of Steel Construction; 2016.

[138] RCSC. Specification for Structural Joints Using High-Strength Bolts. USA: Research Council on Structural Connections (RCSC); 2009.

[139] Standards Australia. AS 4100-1998 (R2016) Steel structures. Sydney, Australia: Standards Australia Limited; 1998.

[140] Chua YS, Liew JYR, Pang SD. Modelling of connections and lateral behavior of high-rise modular steel buildings. J Constr Steel Res. 2020;166:105901. https://doi.org/10.1016/j.jcsr.2019.105901

[141] AISC. ANSI/AISC 341-16 Seismic Provisions for Structural Steel Buildings. Chicago, Illinois, USA: American Institute of Steel Construction (AISC); 2016.

[142] AIK. Korean Building Code and Commentary - Structural. Seoul, Korea: Architectural Institute of Korea (AIK); 2009.

[143] Ministry of Construction. JGJ 101-96 Specification of testing methods for earthquake resistant building. Beijing, China: China Architecture & Building Press; 1996.

[144] SCI, BCSA. Joints in Steel Construction: Simple Connections. Ascot, Berkshire: The Steel Construction Institute (SCI) and The British Constructional Steelwork Association (BSCA); 2002.

[145] Shi Y, Wang M, Wang Y. Analysis on shear behavior of high-strength bolts connection. Int J Steel Struct. 2011;11(2):203-13. https://doi.org/10.1007/s13296-011-2008-0

[146] Luo FJ, Yang X, Bai Y. Member Capacity of Pultruded GFRP Tubular Profile with Bolted Sleeve Joints for Assembly of Latticed Structures. J Compos Constr. 2015;20(3):04015080. https://doi.org/10.1061/(ASCE)CC.1943-5614.0000643

[147] Crisinel M, Ren P, Carretero A. Practical Design Method for Semi-Rigid Composite Joints with Double Web Cleat Connections. IABSE Reports. 1996:185-96. https://doi.org/10.5169/seals-56909

[148] Karlsen FT, Aalberg A. Bolted RHS End-Plate Joints in Axial Tension. Proceedings of Nordic Steel Construction Conference; Oslo, Norway. 2012.

[149] Heistermann C, Veljkovic M, Simões R, Rebelo C, Simões da Silva L. Design of slip resistant lap joints with long open slotted holes. J Constr Steel Res. 2013;82(Supplement C):223-33. https://doi.org/10.1016/j.jcsr.2012.11.012

[150] CEN. EN 1090-2:2018 Execution of steel structures and aluminium structures - Part 2: Technical requirements for steel structures. Brussels, Belgium: European Committee for Standardization (CEN); 2018.

[151] Konkong N, Phuvoravan K. An analytical method for determining the load distribution of single-column multibolt connection. Adv Civil Eng. 2017;2017:1912724. http://doi.org/10.1155/2017/1912724

[152] Birkemoe PC, Packer JA. Ultimate Strength Design of Bolted Tubular Tension Connections. Proceedings of Steel Structures - Recent Research Advances and their Applications to Design; Budva, Yugoslavia. 1986. p. 153-68.

[153] Packer JA, Henderson JE. Hollow structural section connections and trusses - A design guide. Second ed. Toronto, Canada: Canadian Institute of Steel Construction; 1997.

[154] Mang F. Investigation of standard bolted flange connections for circular and rectangular hollow sections (CIDECT Report 8A-81/7-E). Germany: University of Karlsruhe; 1980.

[155] Kato B, Mukai A. Bolted tension flanges square hollow section members, Supplement in 1985: Bolted at two sides of flange (CIDECT Program 8B Report). Japan: University of Tokyo; 1985.

[156] Packer JA, Bruno L, Birkemoe PC. Limit Analysis of Bolted RHS Flange Plate Joints. J Struct Eng. 1989;115(9):2226-42. https://doi.org/10.1061/(ASCE)0733-9445(1989)115:9(2226)

[157] Willibald S, Packer JA, Puthli RS. Experimental Study of Bolted HSS Flange-Plate Connections in Axial Tension. J Struct Eng. 2002;128(3):328-36. https://doi.org/10.1061/(ASCE)0733-9445(2002)128:3(328)

[158] Willibald S. Bolted Connections for Rectangular Hollow Sections under Tensile Loading [PhD Thesis]. Germany: University of Karlsruhe; 2003.

[159] Packer JA, Wardenier J, Kurobane Y, Dutta D, Yeomans N. Design guide for rectangular hollow section (RHS) joints under predominantly static loading. First ed: Comité International pour le Développement et l´Etude de la Construction Tubulaire (CIDECT); 1992.

[160] Packer JA, Wardenier J, Zhao X-L, van der Vegte GJ, Kurobane Y. Design guide for rectangular hollow section (RHS) joints under predominantly static loading. Second ed: Comité International pour le Développement et l´Etude de la Construction Tubulaire (CIDECT); 2009.

[161] Weynand K, Jaspart J-P, Steenhuis M. The Stiffness Model of revised Annex J of Eurocode 3 In: Bjorhovd R, Colso A, Zandonini R, editors. Connections in Steel Structures III - Behaviour, Strength and Design - Proceedings of the Third International Workshop. Trento, Italy: Elsevier; 1996.

[162] Egeland BE, Torstvedt I-M. Stivhet til endeplateforbindelser i hulprofil (Stiffness of end plate joints in hollow sections) [Master's Thesis]. Norway: Norwegian University of Science and Technology; 2013.

[163] Karlsen FT. Knutepunkter for staver med hulprofiltverrsnitt (Joints for elements of hollow sections) [Master's Thesis]. Trondheim, Norway: Norwegian University of Science and Technology; 2011.

[164] Steige Y, Weynand K. Design resistance of end plate splices with hollow sections. Steel Construction. 2015;8(3):187-93. https://doi.org/10.1002/stco.201510023

[165] Wheeler AT, Clarke MJ, Hancock GJ, Murray TM. Design Model for Bolted Moment End Plate Connections Joining Rectangular Hollow Sections. J Struct Eng. 1998;124(2):164-73. https://doi.org/10.1061/(ASCE)0733-9445(1998)124:2(164)

[166] Wardenier J, Packer JA, Zhao X-L, van der Vegte GJ. Hollow Sections in Structural Applications. 2nd ed. Geneva, Switzerland: Comité International pour le Développement et l´Etude de la Construction Tubulaire (CIDECT); 2010.

[167] Carr AJ. Ruaumoko Manual, Volume 3: User Manual for the 3-Dimensional Version, Ruaumoko3D. New Zealand: University of Canterbury; 2012.

[168] Aalberg A, Uhreb AM, Larsena PK. End Plate Connection for Rectangular Hollow Section in Bending. Proceedings of The 13th Nordic Steel Construction Conference (NSCC-2015); 23-25 September; Tampere, Finland. 2015.

[169] CSi. CSI Analysis Reference Manual For SAP2000, ETABS, SAFE and CSiBridge. Berkeley, California: Computers & Structures, Inc. (CSi); 2015.

[170] Yu Y, Chen Z. Rigidity of corrugated plate sidewalls and its effect on the modular structural design. Eng Struct. 2018;175:191-200. https://doi.org/10.1016/j.engstruct.2018.08.039

[171] Srisangeerthanan S, Hashemi MJ, Rajeev P, Gad E, Fernando S. Numerical study on the effects of diaphragm stiffness and strength on the seismic response of multi-story modular buildings. Eng Struct. 2018;163:25-37. https://doi.org/10.1016/j.engstruct.2018.02.048

[172] Tamura Y. Amplitude dependency of damping in buildings and critical tip drift ratio. Int J High-Rise Build. 2012;1(1):1-13. https://doi.org/10.21022/IJHRB.2012.1.1.001

[173] Deaves DM, Harris RI. A mathematical model of the structure of strong winds, CIRIA Report 76. London: Construction Industry Research and Information Association (CIRIA); 1978.

[174] Amirinia G, Jung S. Along-Wind Response of High-Rise Buildings Subjected to Hurricane Boundary Layer Winds. J Struct Eng. 2017;143(9):04017087. https://doi.org/10.1061/(ASCE)ST.1943-541X.0001816

[175] Kaimal JC, Wyngaard JC, Izumi Y, Coté OR. Spectral characteristics of surface-layer turbulence. Quarterly Journal of the Royal Meteorological Society. 1972;98(417):563-89. https://doi.org/10.1002/qj.49709841707

[176] Simiu E, Scanlan RH. Winds Effects on Structures: Fundamentals and Applications to Design. New York: John Wiley & Sons; 1996.

[177] Yu B, Gan Chowdhury A, Masters FJ. Hurricane Wind Power Spectra, Cospectra, and Integral Length Scales. Boundary-Layer Meteorology. 2008;129(3):411-30. https://doi.org/10.1007/s10546-008-9316-8

[178] Li L, Xiao Y, Kareem A, Song L, Qin P. Modeling typhoon wind power spectra near sea surface based on measurements in the South China sea. J Wind Eng Ind Aerodyn. 2012;104:565-76. https://doi.org/10.1016/j.jweia.2012.04.005

[179] Deodatis G. Simulation of Ergodic Multivariate Stochastic Processes. Journal of Engineering Mechanics. 1996;122(8):778-87. https://doi.org/10.1061/(ASCE)0733-9399(1996)122:8(778)

[180] Lam NTK, Wilson JL. The new response spectrum model for Australia. EJSE. 2008;8:6-24.

[181] Bi K, Hao H. Modelling and simulation of spatially varying earthquake ground motions at sites with varying conditions. Probabilistic Engineering Mechanics. 2012;29:92-104. https://doi.org/10.1016/j.probengmech.2011.09.002

[182] Stranghöner N, Afzali N, Vries P, Glienke R, Ebert A. Optimization of the test procedure for slip factor tests according to EN 1090-2. Steel Construction. 2017;10(4):267-81. https://doi.org/10.1002/stco.201710040

[183] Cruz A, Simões R, Alves R. Slip factor in slip resistant joints with high strength steel. J Constr Steel Res. 2012;70(Supplement C):280-8. https://doi.org/10.1016/j.jcsr.2011.11.001

[184] Stranghöner N, Afzali N, de Vries P, Schedin E, Pilhagen J. Slip factors for slip-resistant connections made of stainless steel. J Constr Steel Res. 2019;152:235-45. https://doi.org/10.1016/j.jcsr.2018.07.005

[185] Maiorana E, Zampieri P, Pellegrino C. Experimental tests on slip factor in friction joints: comparison between European and American Standards. Frattura ed Integrità Strutturale. 2018;12(43):205-17. https://doi.org/10.3221/IGF-ESIS.43.16

[186] Hogan TJ, Munter SA. Design Guide 1: Bolting in structural steel connections. North Sydney, NSW, Australia: Australian Steel Institute; 2007.

[187] Kulak GL, Fisher JW, Struik JHA. Guide to Design Criteria for Bolted and Riveted Joints. 2nd ed. Chicago, IL, USA: American Institute of Steel Construction, Inc.; 2001.

[188] Annan C-D, Chiza A. Slip resistance of metalized–galvanized faying surfaces in steel bridge construction. J Constr Steel Res. 2014;95:211-9. https://doi.org/10.1016/j.jcsr.2013.12.008

[189] Standards Australia. AS/NZS 3678 Structural steel - Hot rolled plates, floorplates and slabs. Sydney, Australia: Standards Australia Limited; 2016.

[190] Standards Australia. AS/NZS 1252.1:2016 High-strength steel fastener assemblies for structural engineering - Bolts, nuts and washers, Part 1: Technical requirements. Sydney, Australia: Standards Australia Limited; 2016.

[191] Hutchings I, Shipway P. Tribology: Friction and Wear of Engineering Materials. Second ed. Oxford: Butterworth-Heinemann; 2017.

[192] Key PW. Technical Note TN001: High Strength Structural Bolt Assemblies to AS/NZS 1252:2016. Pymble, NSW, Australia: Australian Steel Institute; 2017.

[193] Standards Australia. AS 1627.4-2005 (R2017) Metal finishing - Preparation and pretreatment of surfaces, Part 4: Abrasive blast cleaning of steel. Sydney, Australia: Standards Australia Limited; 2005.

[194] Standards Australia. AS 2312.1 Guide to the protection of structural steel against atmospheric corrosion by the use of protective coatings, Part 1: Paint coatings. Sydney, Australia: Standards Australia Limited; 2014.

[195] Standards Australia. AS 1627.9 Metal finishing—Preparation and pretreatment of surfaces, Part 9: Pictorial surface preparation standards for painting steel surfaces. Sydney Australia: Standards Australia International; 2017.

[196] SIS. The Rust Grade Book, ISO 8501-1: Preparation of steel substrates before application of paints and related products - Visual assessment of surface cleanliness - Part 1: Rust grades and preparation grades of uncoated steel substrates and of steel substrates after overall removal of previous coatings. Switzerland: Swedish Standards Institute (SIS); 2007.

[197] CEN. EN 14399-3:2005 High-strength structural bolting assemblies for preloading - Part 3: System HR - Hexagon bolt and nut assemblies. European Committee for Standardization; 2005.

[198] Blaber J, Adair B, Antoniou A. Ncorr: Open-Source 2D Digital Image Correlation Matlab Software. Exp Mech. 2015;55(6):1105-22. https://doi.org/10.1007/s11340-015-0009-1

[199] Yuan C, Chen W, Pham TM, Hao H. Bond behavior between basalt fibres reinforced polymer sheets and steel fibres reinforced concrete. Eng Struct. 2018;176:812-24. https://doi.org/10.1016/j.engstruct.2018.09.052

[200] Yuan C, Chen W, Pham TM, Hao H. Effect of aggregate size on bond behaviour between basalt fibre reinforced polymer sheets and concrete. Composites Part B. 2019;158:459-74. https://doi.org/10.1016/j.compositesb.2018.09.089

[201] Loo WY, Quenneville P, Chouw N. The influence of surface preparation and the lubricating effect of mill scale on the performance of slip-friction connectors. Constr Build Mater. 2017;155:1025-38. https://doi.org/10.1016/j.conbuildmat.2017.08.100

[202] Khoo H-H, Clifton C, Butterworth J, MacRae G, Ferguson G. Influence of steel shim hardness on the Sliding Hinge Joint performance. J Constr Steel Res. 2012;72:119-29. https://doi.org/10.1016/j.jcsr.2011.11.009

[203] Yun X, Gardner L. Stress-strain curves for hot-rolled steels. J Constr Steel Res. 2017;133:36-46. https://doi.org/10.1016/j.jcsr.2017.01.024

[204] Krolo P, Grandić D, Bulić M. The guidelines for modelling the preloading bolts in the structural connection using finite element methods. J Comput Eng. 2016;2016:4724312. https://doi.org/10.1155/2016/4724312

[205] Husson W. Friction Connections with Slotted Holes for Wind Towers [Licentiate Thesis]. Lulea, Sweden: Lulea University of Technology; 2008.

[206] Abaqus Analysis User's Guide, Version 6.14. Providence, RI, USA: Dassault Systemes Simulia Corp; 2014.

[207] Zheng T, Lu Y, Usmani A, Seeam A, Laurenson D. Characterization and monitoring of seismic performance of post tensioned steel modular structures. Proceedings of the 15th World Conference on Earthquake Engineering (15 WCEE); 24 - 28 Spetember; Lisbon, Portugal. 2012. p. 19457-64.

[208] Standards Australia. AS 2193 Calibration and classification of force-measuring systems. Sydney, Australia: Standards Australia Limited; 2005.

[209] Harilal R, Ramji M. Adaptation of Open Source 2D DIC Software Ncorr for Solid Mechanics Applications. 9th International Symposium on Advanced Science and Technology in Experimental Mechanics; 1-6 November; New Delhi, India. 2014.

[210] Yuan C, Chen W, Pham TM, Hao H. Bond behaviour between hybrid fiber reinforced polymer sheets and concrete. Constr Build Mater. 2019;210:93-110. https://doi.org/10.1016/j.conbuildmat.2019.03.082

[211] Oberg E, Jones FD, Horton HL, Ryffel HH. Machinery's Handbook 30th Edition. South Norwalk, CT, USA: Industrial Press Inc.; 2016.

[212] Walpole RE, Myers RH, Myers SL, Ye K. Probability & Statistics for Engineers & Scientists. 9th ed. Harlow, Essex, England: Pearson Education Limited; 2016.

[213] CEN. EN 14399-2:2015 High-strength structural bolting assemblies for preloading - Part 2: Suitability for preloading. Brussels, Belgium: European Committee for Standardization (CEN); 2015.

[214] Bevington PR, Robinson DK. Data Reduction and Error Analysis for the Physical Sciences. 3rd ed. New York, NY, USA: McGraw-Hill; 2003.

[215] Abaqus Theory Guide, Version 6.14. Providence, RI, USA: Dassault Systemes Simulia Corp; 2014.

[216] Liu X, Cui X, Yang Z, Zhan X. Analysis of the seismic performance of site-bolted beam to column connections in modularized prefabricated steel structures. Adv Mater Sci Eng. 2017;2017:1932730. https://doi.org/10.1155/2017/1932730

[217] Bruneau M, Uang C-M, Sabelli R. Ductile Design of Steel Structures. 2nd ed. New York, NY, USA: McGraw-Hill; 2011.

[218] Dhanapal J, Ghaednia H, Das S, Velocci J. Structural performance of state-of-the-art VectorBloc modular connector under axial loads. Eng Struct. 2019;183:496-509. https://doi.org/10.1016/j.engstruct.2019.01.023

[219] Dai X-M, Zong L, Ding Y, Li Z-X. Experimental study on seismic behavior of a novel plug-in self-lock joint for modular steel construction. Eng Struct. 2019;181:143-64. https://doi.org/10.1016/j.engstruct.2018.11.075

[220] Young WC, Budynas RG, Sadegh AM. Roark's Formulas for Stress and Strain. 8th ed. New York, NY, USA: McGraw-Hill; 2012.

[221] Timoshenko S, Woinowsky-Krieger S. Theory of Plates and Shells. 2nd ed. New York, NY, USA: McGraw-Hill; 1959.

[222] Chen Z, Liu Y, Zhong X, Liu J. Rotational stiffness of inter-module connection in mid-rise modular steel buildings. Eng Struct. 2019;196:109273. https://doi.org/10.1016/j.engstruct.2019.06.009

[223] Rahmzadeh A, Alam MS, Tremblay R. Analytical Prediction and Finite-Element Simulation of the Lateral Response of Rocking Steel Bridge Piers with Energy-Dissipating Steel Bars. J Struct Eng. 2018;144(11):04018210. https://doi.org/10.1061/(ASCE)ST.1943-541X.0002216

[224] Pampanin S, Nigel Priestley MJ, Sritharan S. Analytical modelling of the seismic behaviour of precast concrete frames designed with ductile connections. J Earthq Eng. 2001;5(3):329-67. https://doi.org/10.1080/13632460109350397

[225] McBride KE. Steel strength of anchor bolts in stand-off base plate connections [PhD Thesis]. Gainesville, FL: University of Florida; 2014.

[226] Budynas RG, Nisbett JK. Shigley's Mechanical Engineering Design. 10th ed. New York, NY, USA: McGraw-Hill; 2014.

[227] De Stefano M, Astaneh A. Axial force—Displacement behavior of steel double angles. J Constr Steel Res. 1991;20(3):161-81. https://doi.org/10.1016/0143-974X(91)90030-5

[228] Davenport AG. The spectrum of horizontal gustiness near the ground in high winds. Quarterly Journal of the Royal Meteorological Society. 1961;87(372):194-211. https://doi.org/10.1002/qj.49708737208

Appendix A Statement of contribution of co-authors

To whom it may concern,

I, Andrew William Lacey, carried out the literature review, experimental investigation, numerical simulation, data processing and analysis, and wrote the manuscripts for the papers titled as follows. The co-authors reviewed and edited the manuscripts and contributed intellectual input towards the experiments, simulations, data processing and analysis.

1. **Structural response of modular buildings - an overview**
2. **Review of bolted inter-module connections in modular steel buildings**
3. **Effect of inter-module connection stiffness on structural response of a modular steel building subjected to wind and earthquake load**
4. **Experimental and numerical study of the slip factor for G350-steel bolted connections**
5. **New interlocking inter-module connection for modular steel buildings: Experimental and numerical studies**
6. **Simplified structural behaviours of post-tensioned inter-module connection for modular buildings**
7. **New interlocking inter-module connection for modular steel buildings: Simplified structural behaviours**
8. **Lateral behaviour of modular steel building with simplified models of new inter-module connections**

…….

I, as a co-author, endorse that this level of contribution by the candidate indicated above is appropriate.

Dr Wensu Chen …….

Prof. Hong Hao …….

Dr Kaiming Bi …….

To whom it may concern,

I, Andrew William Lacey, provided intellectual input towards planning the experiments, assisted with the specimen assembly, carried out formal analysis including digital image correlation, derivation of the force-slip curves, and statistical analysis of the experimental accuracy, planned and completed the assembly tests, carried out the numerical simulations, proposed the load-slip model and prepared the original manuscript for the paper titled "**Shear behaviour of post-tensioned inter-module connection for modular steel buildings**". The fifth author proposed the post-tensioned connection, and planned and carried out the experiments. The second, third and fourth authors reviewed and edited the manuscript and contributed intellectual input towards the experiments, simulations, data processing and analysis.

…….

I, as a co-author, endorse that this level of contribution by the candidate indicated above is appropriate.

Dr Wensu Chen …….

Prof. Hong Hao …….

Dr Kaiming Bi …….

Mr Forrest Tallowin …….

Appendix B Copyright clearance

The proof of the right granted by Elsevier to include the respective publications in this thesis is provided below.

Chapter 2

Lacey AW, Chen W, Hao H, Bi K. Structural response of modular buildings - an overview. J Build Eng. 2018;16:45-56. https://doi.org/10.1016/j.jobe.2017.12.008

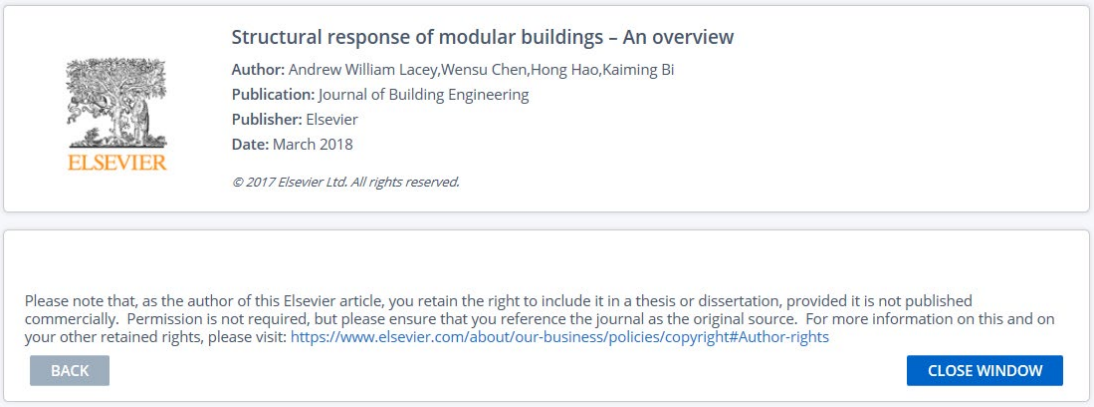

Lacey AW, Chen W, Hao H, Bi K. Review of bolted inter-module connections in modular steel buildings. J Build Eng. 2019;23:207-19. https://doi.org/10.1016/j.jobe.2019.01.035

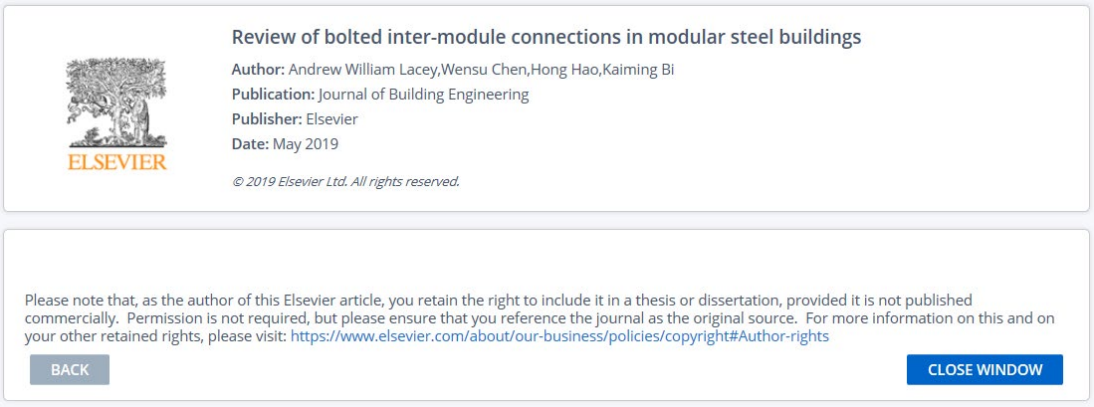

Chapter 3

Lacey AW, Chen W, Hao H, Bi K. Effect of inter-module connection stiffness on structural response of a modular steel building subjected to wind and earthquake load. Eng Struct. 2020;213:110628. https://doi.org/10.1016/j.engstruct.2020.110628

Chapter 4

Lacey AW, Chen W, Hao H, Bi K. Experimental and numerical study of the slip factor for G350-steel bolted connections. J Constr Steel Res. 2019;158:576-90. https://doi.org/10.1016/j.jcsr.2019.04.012

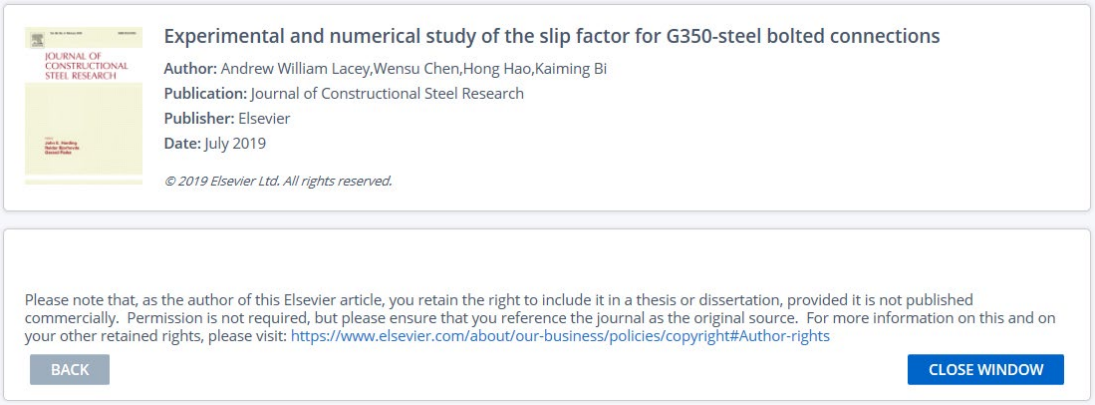

Chapter 5

Lacey AW, Chen W, Hao H, Bi K, Tallowin FJ. Shear behaviour of post-tensioned inter-module connection for modular steel buildings. J Constr Steel Res. 2019;162:105707. https://doi.org/10.1016/j.jcsr.2019.105707

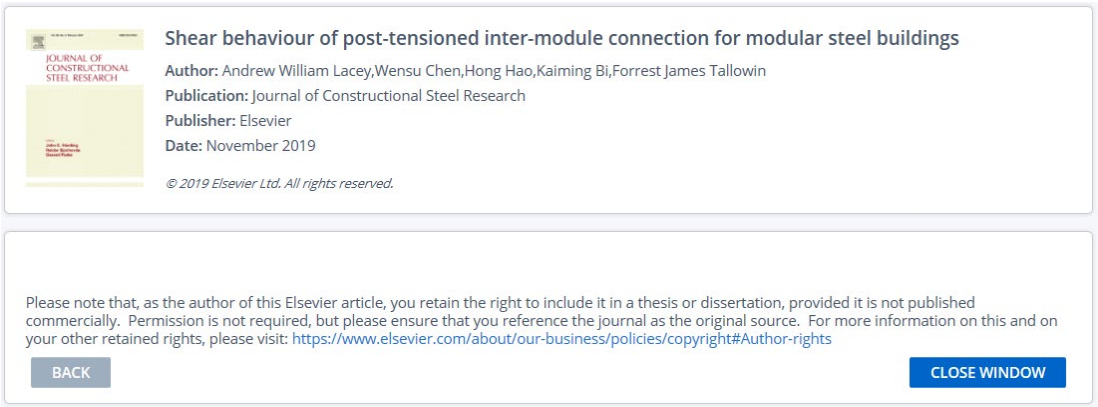

Chapter 6

Lacey AW, Chen W, Hao H, Bi K. New interlocking inter-module connection for modular steel buildings: Experimental and numerical studies. Eng Struct. 2019;198:109465. https://doi.org/10.1016/j.engstruct.2019.109465

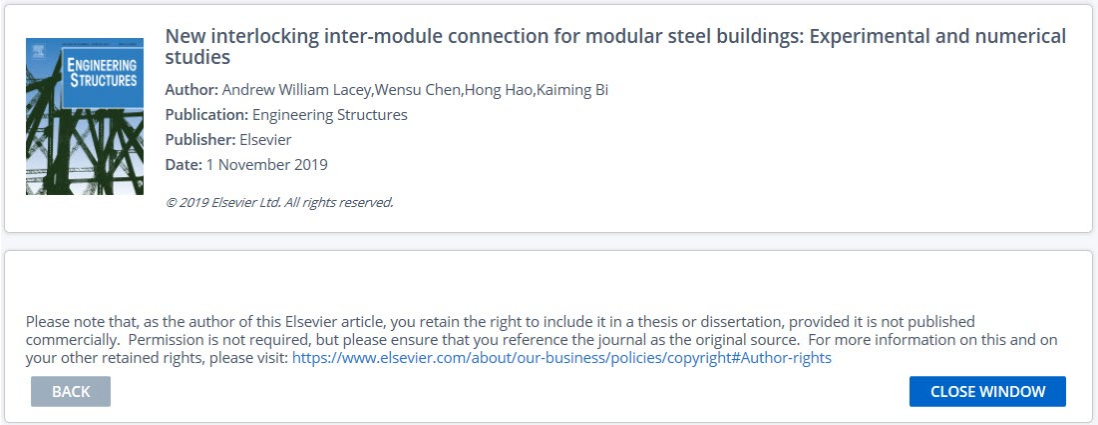

Chapter 7

Lacey AW, Chen W, Hao H, Bi K. Simplified structural behaviours of post-tensioned inter-module connection for modular buildings. J Constr Steel Res. 2020;175:106347. https://doi.org/10.1016/j.jcsr.2020.106347

Chapter 8

Lacey AW, Chen W, Hao H, Bi K. New interlocking inter-module connection for modular steel buildings: Simplified structural behaviours. Eng Struct. 2021;227:111409. https://doi.org/10.1016/j.engstruct.2020.111409